Master of Science Thesis

A numerical study of delamination propagation in post-buckled single stringer compression specimens using the virtual crack closure technique

S.A. Doesburg

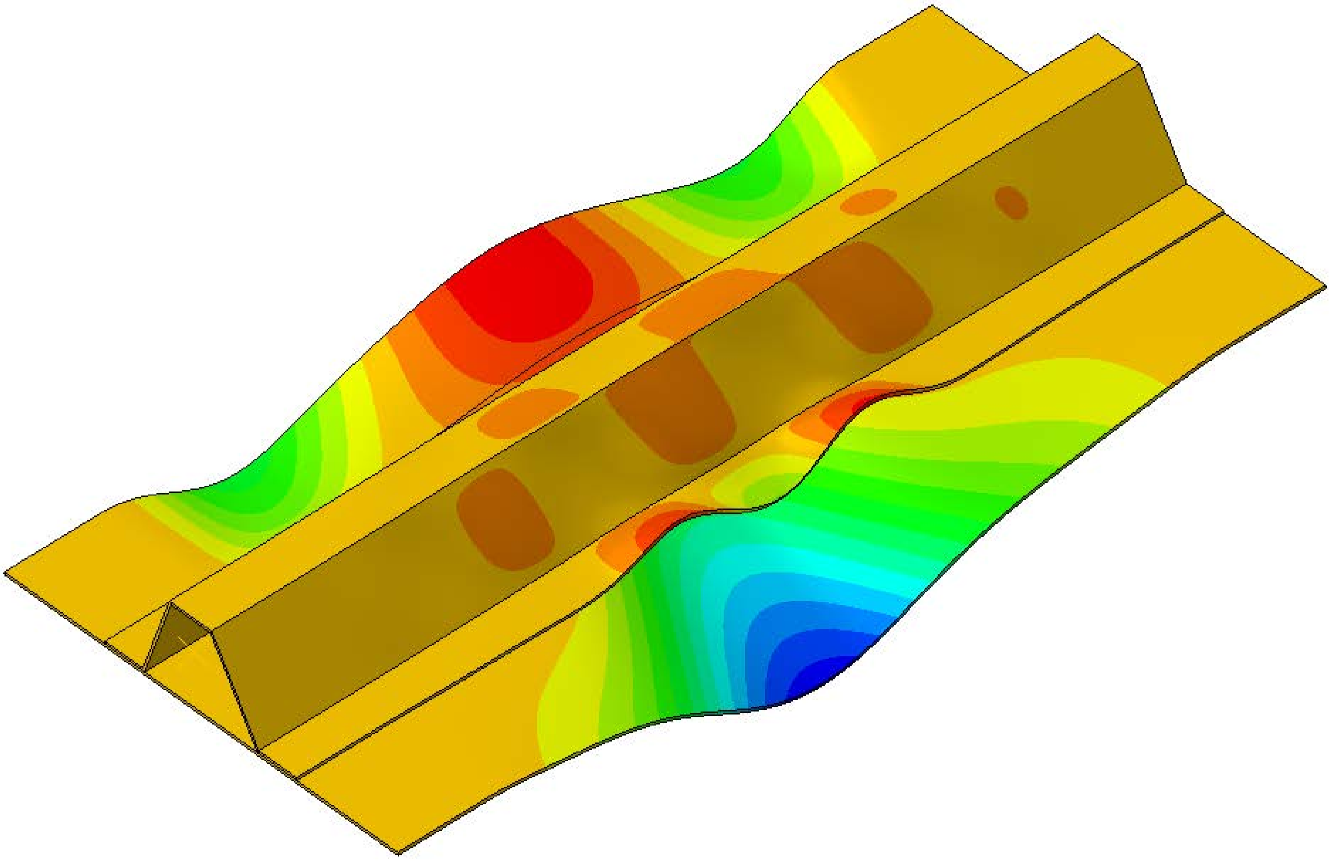

Faculty of Aerospace Engineering · Delft University of Technology

A numerical study of delamination propagation in post-buckled single stringer compression specimens using the virtual crack closure technique

MASTER OF SCIENCE THESIS

For obtaining the degree of Master of Science in Aerospace Engineering at the Delft University of Technology

S.A. Doesburg

8 March 2019

Faculty of Aerospace Engineering · Delft University of Technology

TU Delft Delft University of Technology

DELFT UNIVERSITY OF TECHNOLOGY
FACULTY OF AEROSPACE ENGINEERING
DEPARTMENT OF AEROSPACE STRUCTURES AND MATERIALS

GRADUATION COMMITTEE

Dated: 22 March 2019

Committee chair and thesis supervisor: ____________________
Prof. Dr. Chiara Bisagni

Committee members: ____________________
Dr.Ir. Roeland de Breuker

____
Dr.Ir. René Alderliesten

____
Dr.Ing. Saullo Castro

Contents

I Literature review 5

II Double Cantilevered Beam (DCB) and Mixed Mode Bending (MMB) specimen analyses 41

III Single Stringer Compression Specimen (SSCS) analyses 75

List of Figures

List of Tables

Abstract

The goal of the present research is to contribute to the understanding of the delamination growth behaviour of Single Stringer Compression Specimens with an initial delamination loaded in post-buckling. The Virtual Crack Closure Technique (VCCT) is used to study the delamination growth between the skin and the stiffener using the finite element software Abaqus. Both quasi-static and fatigue delamination propagation are studied. Two recently introduced fatigue delamination methods based on the Virtual Crack Closure Technique, the Constant Amplitude Fatigue method and the Simplified Fatigue method, are investigated.

The two VCCT based methods are first verified using Double Cantilevered Beam and Mixed Mode Bending specimen models before they are used to investigate the delamination growth behaviour in Single Stringer Compression Specimen specimens. Both the Constant Amplitude Fatigue and Simplified Fatigue methods produced excellent results when used to predict fatigue delamination growth in Double Cantilevered Beam and Mixed Mode Bending specimen models. At an element size of 1 mm the error when compared to benchmark data was less than 3% for the Double Cantilevered Beam specimen results and less than 5% for the Mixed Mode Bending specimen results. The Constant Amplitude Fatigue and Simplified Fatigue methods produced results with similar accuracy for a given element size. Using the Simplified Fatigue method a 25 to 50% reduction in computational time was observed compared to the Constant Amplitude Fatigue method.

Two element types have been used to construct the specimen models: S4R conventional shell elements and SC8R continuum shell elements. SC8R elements exhibited better solution convergence and better mesh convergence than S4R elements for quasi-static delamination growth analyses. The computational time required using SC8R elements was a factor 2 to 3 lower for the 1 mm and 3 mm element sizes evaluated.

In the quasi-static delamination growth analyses of the Single Stringer Compression Specimen a clear correlation has been observed between the local buckling of the stiffener flange, sudden delamination extensions, and load drops. In the fatigue delamination growth analyses of the Single Stringer Compression Specimen a correlation has been observed between local buckling of the stiffener flange and a sharp increase in the delamination growth rate. Initially, the stiffener flange does not buckle locally at the maximum applied load. The rate at which the delamination propagates increases by three to four orders of magnitude after the stiffener flange begins to buckle locally.

Predicting fatigue delamination growth in post-buckled Single Stringer Compression Specimen using the Virtual Crack Closure Technique is, in principle, achievable. The obtained results are similar to experimental results in a qualitative sense, but quantitatively the predicted delamination growth rates were off by one to three orders of magnitude. Limitations that should be addressed are the reliability of the cycle jumping mechanism included to speed up the analyses, the fixed mode-mixity ratio used for the fatigue delamination growth relation parameters, and the omission of the mode III contribution in determining these propagation relation parameters. In addition to addressing these limitations more experimental data of fatigue delamination growth in post-buckled Single Stringer Compression Specimens is needed to validate numerical results. Test data of only two specimens was available, and these exhibit substantial scatter in the observed delamination growth rates.

Nomenclature

ANS Assumed Natural-coordinate Strain

CAF Constant Amplitude Fatigue

CBT Corrected Beam Theory

CCT Crack Closure Technique

CMM Coordinate Measuring Machine

CZM Cohesive Zone Model

DCB Double Cantilevered Beam

DIC Digital Image Correlation

ENF End Notch Flexure

FNM Floating Node Method

LCF Low-Cycle Fatigue

LEFM Linear Elastic Fracture Mechanics

MMB Mixed Mode Bending

SERR Strain Energy Release Rate

SF Simplified Fatigue

SIF Stress Intensity Factor

SSCS Single Stringer Compression Specimen

UT Ultrasonic Testing

VCCT Virtual Crack Closure Technique

XFEM Extended Finite Element Method

Chapter 1

Introduction

Contemporary load bearing thin walled aerospace structures such as fuselage and wing structures make extensive use of stiffened skin panels. These panels consist of a thin skin stiffened with several L-, T-, I-, Z-, or Ω- profile stiffeners. The stiffeners are typically joined to the skin through riveting or adhesive bonding for metallic structures and adhesive bonding or co-curing for fibre epoxy composites. Many of these stiffened skin panels see considerable compressive or shear loads during service. For example, compressive loads are exerted on the lower fuselage panels of an aircraft in flight.

Thin walled panels loaded in compression or shear are prone to buckling. When the panel buckles the skin bulges in the out-of-plane direction and the in plane structural response of the panel becomes non-linear. The buckling load is typically much lower than the failure load of a panel; the failure load may exceed the buckling load by a factor of 4 to 7 [1].

If a stiffened panel is loaded beyond its buckling load, it enters the post-buckling regime. The out of plane deformation of the skin in the post-buckling regime may become considerable and can cause stresses that induce separation in the interface between the skin and the stiffeners.

To avoid the occurrence of these separation stresses the buckling load may be used as the panel's limit or design load. However, allowing buckling to occur in service means that the same structure can carry higher loads. By extension, allowing the panel to buckle means that a lighter structure may be constructed to carry a given load.

If buckling is allowed during service the skin-stiffener interface will be subject to repeated separation stresses. In this case due consideration must be given to fatigue delamination initiation and propagation in this interface to ensure the panel does not fail prematurely.

Over the past four decades the usage of fibre epoxy composites in aerospace structures has risen from single digit percentages of structural weight to just over 50% of aircraft structural weight in recent airliners such as the Airbus A350XWB and the Boeing 787 Dreamliner as shown in figure 1.1.

The prediction of fatigue delamination propagation in post-buckled stiffened composite panels is currently an underdeveloped field. Fatigue delamination propagation in fibre composites has been studied extensively at the coupon level. However, due to the expense and complexity involved investigations at the structural panel level of complexity have been far less prevalent. The prediction of fatigue delamination propagation at the panel complexity level is a key enabler for the weight reduction of contemporary composite aircraft designs.

The Single Stringer Compression Specimen (SSCS) has been developed [3] to be representative of the response of large multi stringer panels such as aircraft fuselage structures. In the building block approach the specimen fits between the coupon specimen level and the large multi-stringer stiffened panel level. It was developed to improve the ease and affordability with which the response of stiffened panels can be determined experimentally and analysed numerically. This enables the study of the failure behaviour and damage tolerance of skin stiffened structures in the post-buckling regime. Additionally the Single Stringer Compression Specimen provides the opportunity to verify and validate state of the art quasi-static and fatigue damage models due to its small size, making it computationally tractable, and its relatively complex geometry compared to coupon specimens.

The goal of the present research is to contribute to the understanding of the delamination growth

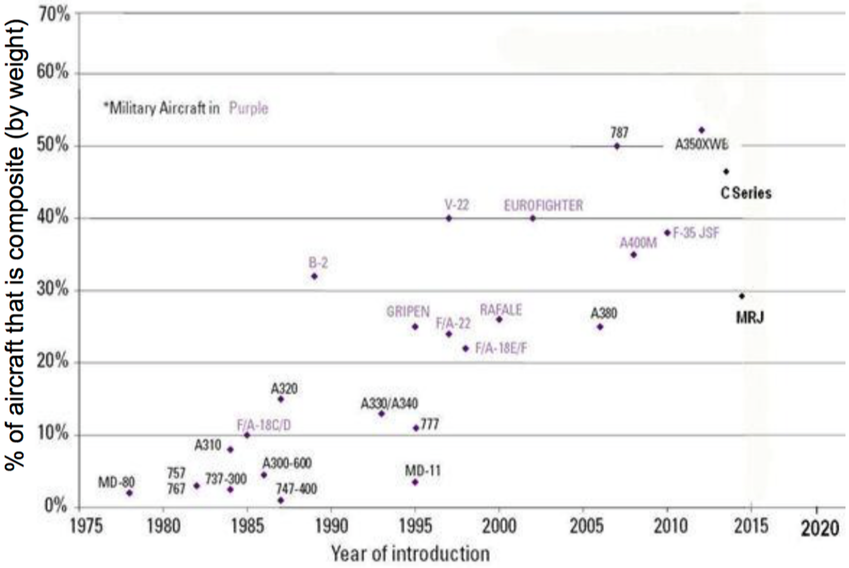

Figure 1.1: *Aircraft composite content, % of structural weight. From [2].*

behaviour of a Single Stringer Compression Specimen with an initial delamination loaded in post-buckling. The study will focus on the numerical analysis of delamination growth between the skin and the stiffener as this is a dominant failure mode identified in experimental investigations of compression loaded stiffened composite panels. The single stringer compression specimen, made of uni-directional carbon fibre epoxy composite, will be modelled in Dassault Systèmes Abaqus FEA 2017. Both quasi-static and fatigue delamination propagation will be studied. The scope of the study is limited to the use of the Virtual Crack Closure Technique for delamination growth prediction. Two fatigue delamination methods based on the Virtual Crack Closure Technique, the Constant Amplitude Fatigue method and Simplified Fatigue method available in Abaqus FEA 2017, will be investigated.

To operationalise the research goal it has been broken down into four concrete objectives:

- Investigate the delamination growth behaviour of Single Stringer Compression Specimens loaded in post-buckling.
- Identify any limitations of the Constant Amplitude Fatigue and Simplified Fatigue methods in predicting delamination growth in post-buckled Single Stringer Compression Specimens.
- Evaluate the efficacy of the Constant Amplitude Fatigue method provided with Abaqus FEA when applied to post-buckled Single Stringer Compression Specimens.
- Evaluate the use of SC8R elements for the analysis of Single Stringer Compression Specimens loaded in post-buckling.

In addition to the objective to investigate the delamination growth behaviour of a Single Stringer Compression Specimen, objectives to investigate fatigue delamination growth methods have been defined. Two new methods have been introduced in Abaqus FEA 2017, the Constant Amplitude Fatigue and Simplified Fatigue methods. It is currently unknown if and how well these methods work when they are applied to post-buckled Single Stringer Compression Specimens. Lastly, an objective to investigate the use of a different element type has been included. Previously, quasi-static delamination growth in post-buckled Single Stringer Compression Specimens has been investigated with a parametric S4R conventional shell element model. SC8R continuum shell elements have been shown to be preferable in some applications. It is of interest to investigate whether the same holds in this application.

A set of research questions have been formulated to guide the research and to ensure that the research objectives are met. They are listed as follows:

- How does a delamination front grow in Single Stringer Compression Specimen specimens loaded in post-buckling under quasi-static loading?
- How does a delamination front grow in Single Stringer Compression Specimen specimens loaded in post-buckling under fatigue loading?
- Are the Constant Amplitude Fatigue and Simplified Fatigue methods capable of predicting fatigue delamination growth in Single Stringer Compression Specimen models loaded in post-buckling?
- What are the limitations of the Constant Amplitude Fatigue and Simplified Fatigue methods that affect Single Stringer Compression Specimen delamination growth models?
- How does the performance of SC8R elements relate to S4R elements for VCCT based delamination growth in Single Stringer Compression Specimen models?

To answer the research questions a staged approach will be adopted where later work builds on the previous work to develop confidence in the obtained results. The work will be split into five distinct parts. First, a literature review will be conducted. This will be followed by the numerical analysis of simple specimens loaded quasi-statically to verify the adopted modelling approach. These specimens are then used to investigate and verify the selected fatigue delamination growth methods. Models of the Single Stringer Compression Specimen will be constructed and loaded quasi-statically to verify their construction. Finally the Single Stringer Compression Specimen models will be loaded in fatigue to investigate the delamination growth method and the delamination growth behaviour.

In the literature review the academic context of the research will be explored. The fundamentals of fracture mechanics based delamination growth will be detailed. After these fundamentals have been covered implementations of fracture mechanics based methods will be investigated. Both implementations used in research settings as well as implementations in Abaqus FEA will be considered. Finally, the experimentally observed post-buckling and delamination growth behaviour of Single Stringer Compression Specimens will be treated.

After the literature review has been concluded two simple specimens will be analysed. The Double Cantilevered Beam specimen and the Mixed Mode Bending specimen have been selected for this phase of the research. These are accepted standard specimens and have been used to investigate delamination growth both experimentally and numerically. Both are used in test standards to determine material toughness properties [4–6]. Numerical benchmark data are available for verification of the analysis results [7–10] of both specimens. The specimen models will be analysed under quasi-static loading conditions to verify the modelling approach using both conventional shell S4R elements and continuum shell SC8R elements. After this quasi-static verification the Double Cantilevered Beam and Mixed Mode Bending specimens will be analysed under fatigue loading using both the Constant Amplitude Fatigue and Simplified Fatigue methods to evaluate the methods' performance. The obtained fatigue results will be verified against available benchmark data.

Following the simple specimen phase of the study, models of the Single Stringer Compression Specimen will be constructed using both S4R and SC8R elements. These models will be analysed under quasi-static loading to verify the modelling approach against an available parametric S4R model, to compare the performance of the S4R and SC8R elements, and to investigate the delamination growth behaviour of the specimen. Finally the Single Stringer Compression Specimen models will be analysed under fatigue loading to investigate the performance of the Constant Amplitude Fatigue method and to investigate the delamination growth behaviour of the specimen.

The report is split into three parts. In part I the background of the Virtual Crack Closure Technique and the Single Stringer Compression Specimen is explored. In chapter 2 the linear elastic fracture mechanics approach is covered. Implementations of VCCT based methods are discussed in chapter 3. The Single Stringer Compression Specimen is treated in chapter 4.

In part II, analysis results using simple Double Cantilevered Beam and Mixed Mode Bending specimens are presented. The construction of the specimen models is discussed first in chapter 5 followed by the results obtained under quasi-static loading in chapter 6 and the results obtained under fatigue loading in chapter 7.

In part III, analysis results of the Single Stringer Compression Specimen are presented. The construction of the specimen models is discussed first in chapter 8 followed by the results obtained under quasi-static loading in chapter 9 and the results obtained under fatigue loading in chapter 10.

This is followed by the conclusions presented in chapter 11 and the recommendations given in chapter 12.

Part I

Literature review

Chapter 2

Fracture mechanics based fatigue crack propagation prediction

In the field of fracture mechanics a number of tools are employed to study and predict crack propagation in structural components. They allow the strength of a component in the presence of a given crack, the expected service life of a newly designed part, or the remaining life of a part in service to be determined. These tools can also be used to study and analyse the delamination propagation behaviour in post-buckled stiffened panel structures. Contemporary approaches to the study of fracture mechanics may be divided into three distinct categories: linear elastic fracture mechanics approaches, cohesive zone modelling, and XFEM based approaches. Cohesive zone modelling and XFEM approaches are outside the scope of the present research. Instead, the focus will be on linear elastic fracture mechanics based approaches.

Linear elastic fracture mechanics approaches are based on Griffith's [11] and Irwin's [12] work on quasi-static crack growth. Using an energy balance approach the decrease in elastic strain energy for a given amount of crack extension, the strain energy release rate, is equated to the increase in surface energy of the crack surface and the plastically dissipated energy. For fatigue crack propagation the amount of crack extension per load cycle is related empirically to the strain energy release rate through a propagation relation. Typically a Paris type relation is used as discussed below.

The propagation relations used to relate the strain energy release rate to the crack extension per load cycle are discussed first in section 2.1 followed by a discussion on the effect of mode mixity on these relations in section 2.2. The suitability of the strain energy release rate is discussed in section 2.3 and finally the virtual crack closure technique is presented and discussed in section 2.4.

2.1 Propagation relations

Fracture mechanics based approaches relate delamination growth rate to the Stress Intensity Factor (SIF) K or the Strain Energy Release Rate (SERR) G. These two quantities are equivalent [13] and they may be exchanged at will although obviously the values of the fitting parameters of a semi-empirical propagation relation with the SIF are not the same as the values associated with the SERR and vice-versa. Use of the SERR is generally preferred due to the challenges associated with determining the SIF for laminated orthotropic materials.

The majority of fracture mechanics based fatigue crack propagation approaches use a variation of the Paris relation to relate the SERR to the delamination propagation rate. The Paris relation [14, 15] in its most basic form is shown in equation 2.1 where C and n are fitting parameters and $f(G)$ is a function of the Strain Energy Release Rate G. Typical delamination growth rate behaviour is shown in a qualitative sense in figure 2.1. This behaviour can be divided into three distinct regions numbered I, II, and III. In region one threshold behaviour is shown where a sharp drop in growth rate occurs for a reduction in Strain Energy Release Rate. In region two an almost log-linear behaviour is shown. It is

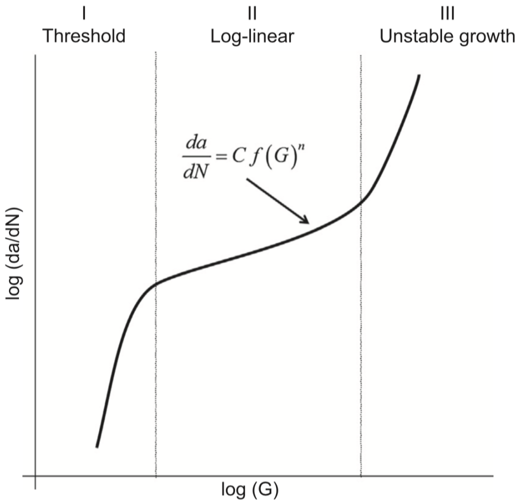

Figure 2.1: *Qualitative behaviour of the delamination growth rate. From [16].*

this log-linear behaviour that is captured by the Paris relation. In region three the behaviour becomes asymptotic as the SERR reaches its critical value and the propagation mechanism shifts from fatigue to quasi-static propagation.

$$\frac{da}{dN} = Cf(G)^n \tag{2.1}$$

The fracture mechanics approach was originally adopted to predict fatigue delamination growth in fibre-polymer composites based on its success in predicting fatigue crack growth in metals. "It is notable that in all these early investigations, the use of the Paris relation to correlate the delamination growth rate was not motivated by a consideration of the physics of the delamination problem itself. Instead, a model of the form of [equation 2.1] was chosen based on its earlier success in correlating fatigue crack growth in metals." [16, p.76]. Later works referred to these earlier studies and treated the use of a Paris type relation as a given.

No clear consensus on which function of G gives the best results can be derived from literature. Formulations tend to use G_{max} or ΔG where the former is the peak Strain Energy Release Rate and the latter is the SERR range, or they use some combination of the two. Pascoe et al [16] argue that, since the delamination growth is ultimately driven by the applied fatigue cycles which cannot be fully characterised by either one of these parameters, any equation using only one of the parameters will not fully capture the delamination growth behaviour.

To uniquely define a fatigue cycle, at least two parameters are needed, the minimum and maximum stress, or the mean stress and stress amplitude, or the stress range and stress ratio [17, p.142]. Consequently, a combination of two corresponding parameters, for example both G_{max} and ΔG, would also be needed to predict the fatigue delamination behaviour. Since G_{max} and ΔG can be related to the mean SERR G_m and the load ratio R through equations 2.2 and 2.3 [16] any two of these four may be used equivalently to characterise the delamination growth behaviour. That either G_{max} or ΔG alone is insufficient can also be seen from the R-ratio effect that has been reported extensively in literature where response curves at different load ratios would not collapse to a single curve using a propagation relation with a single parameter. When the fatigue cycle is properly characterised the R-ratio effect tends to disappear and the response curves collapse to a single curve [18].

$$G_{max} = \frac{2}{(1+R^2)} G_m \tag{2.2}$$

$$\Delta G = \frac{2\left(1-R^2\right)}{\left(1+R^2\right)} G_m \tag{2.3}$$

For the parameter ΔG it has been pointed out by Rans et al [19] as well as by Jones et al [20] that to correctly apply the similitude principle the SERR should be calculated through $\Delta G = \left(\sqrt{G_{max}} - \sqrt{G_{min}}\right)^2$ rather than the previously common $\Delta G = G_{max} - G_{min}$. This new equation may also be referred to as $\Delta\sqrt{G}$ in literature to distinguish it from the earlier equation.

An abundance of propagation relations have been proposed in literature featuring either one or two SERR parameters in some form of a Paris or Hartmann-Schijve type equation. For a selection the interested reader is referred to the work of Pascoe et al [16] and Khan et al [21]. For the research that follows use will be made of the propagation relations provided with Abaqus/Standard 2017 discussed in section 3.2.

2.2 Effect of mode-mixity

There is a distinct lack of consensus in literature as to what would be the most appropriate method to determine the fatigue crack growth rate under mixed mode opening, even more so than for single mode propagation relations. Most mixed mode propagation relations tend to fall in one of two categories. The first is where the crack propagation is assumed to depend on the total SERR, typically either G_{max} or ΔG, some form of a Paris type relation is assumed and the fitting parameters of the Paris relation become variables of the mode mixity. The second category is where the individual modal contributions are used directly in some Paris type relation.

Blanco et al [22] have presented an overview of mixed mode fatigue propagation relations up to approximately the turn of the century shown here in figure 2.2. They observe that these propagation relations all use a monotonic dependence of the Paris relation parameters on the mode mixity. They claim that the parameters should vary non-monotonically and construct their own progression relation based on second order polynomial curve fits shown in equations 2.4 where c_i, r_i, and g_i (i=1,2,3) are fitting parameters.

$$\begin{aligned}
\log C &= c_1 + c_2\left(\frac{G_{II}}{G}\right) + c_3\left(\frac{G_{II}}{G}\right)^2 \\
r &= r_1 + r_2\left(\frac{G_{II}}{G}\right) + r_3\left(\frac{G_{II}}{G}\right)^2 \\
G_c &= g_1 + g_2\left(\frac{G_{II}}{G}\right) + g_3\left(\frac{G_{II}}{G}\right)^2 \\
\frac{da}{dN} &= C\left(\frac{\Delta G}{G_c}\right)^r
\end{aligned} \tag{2.4}$$

The mixed mode relation proposed by Blanco et al appears to agree fairly well with experimental data as shown in figure 2.3. It should be noted that the relation uses only the SERR range as a similitude parameter and therefore does not use a complete specification of a load cycle. Consequently some variation with the load ratio R is expected. Additionally Blanco et al normalise the fatigue SERR range using the quasi-static critical SERR, a practice questioned by Yao et al [23] as discussed in section 2.3.

In the relations presented before only mode I and mode II contributions are used. Typically mode III contributions are either ignored, neglected or lumped in with mode II contributions because they are both due to in-plane shear. The practice of lumping mode II and mode III contributions together may be questionable as there appears to be no well founded reason why these should affect the crack propagation rate in an identical way, let alone that they should do so in an additive manner. Borrowing from the field of cryomechanics, Takeda et al [24, 25] have investigated the fatigue delamination of glass fibre polymer composites under combined mode II/III opening as well as under combined mode I/III opening at room temperature and at cryogenic temperatures. They have found that the growth rate varies with the mode mixity ratio $\frac{G_{III}}{G_{II}+GIII}$ and with the mode mixity ratio $\frac{G_{III}}{G_I+GIII}$ indicating that mode III loading does not affect the crack front the same as mode II loading.

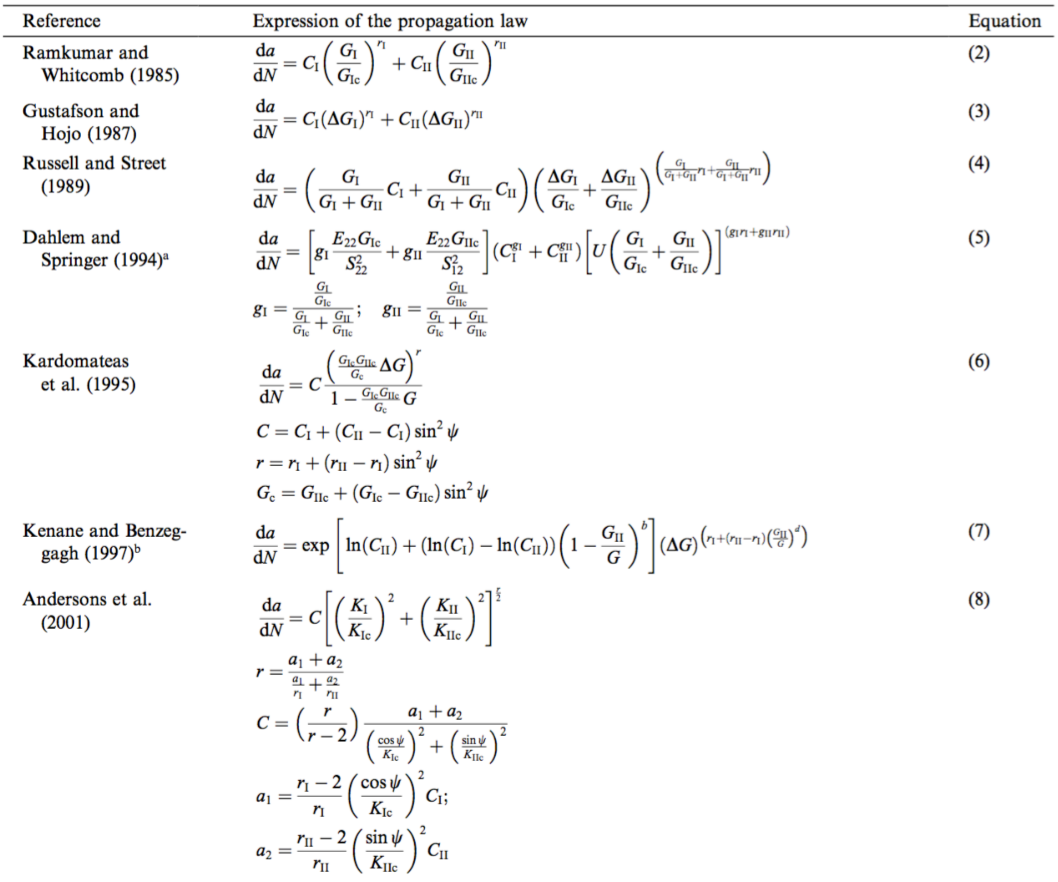

Reference	Expression of the propagation law	Equation
Ramkumar and Whitcomb (1985)	$\frac{\mathrm{d}a}{\mathrm{d}N}=C_{\mathrm{I}}\left(\frac{G_{\mathrm{I}}}{G_{\mathrm{Ic}}}\right)^{r_{\mathrm{I}}}+C_{\mathrm{II}}\left(\frac{G_{\mathrm{II}}}{G_{\mathrm{IIc}}}\right)^{r_{\mathrm{II}}}$	(2)
Gustafson and Hojo (1987)	$\frac{\mathrm{d}a}{\mathrm{d}N}=C_{\mathrm{I}}(\Delta G_{\mathrm{I}})^{r_{\mathrm{I}}}+C_{\mathrm{II}}(\Delta G_{\mathrm{II}})^{r_{\mathrm{II}}}$	(3)
Russell and Street (1989)	$\frac{\mathrm{d}a}{\mathrm{d}N}=\left(\frac{G_{\mathrm{I}}}{G_{\mathrm{I}}+G_{\mathrm{II}}}C_{\mathrm{I}}+\frac{G_{\mathrm{II}}}{G_{\mathrm{I}}+G_{\mathrm{II}}}C_{\mathrm{II}}\right)\left(\frac{\Delta G_{\mathrm{I}}}{G_{\mathrm{Ic}}}+\frac{\Delta G_{\mathrm{II}}}{G_{\mathrm{IIc}}}\right)^{\left(\frac{G_{\mathrm{I}}}{G_{\mathrm{I}}+G_{\mathrm{II}}}r_{\mathrm{I}}+\frac{G_{\mathrm{II}}}{G_{\mathrm{I}}+G_{\mathrm{II}}}r_{\mathrm{II}}\right)}$	(4)
Dahlem and Springer (1994)[a]	$\frac{\mathrm{d}a}{\mathrm{d}N}=\left[g_{\mathrm{I}}\frac{E_{22}G_{\mathrm{Ic}}}{S_{22}^{2}}+g_{\mathrm{II}}\frac{E_{22}G_{\mathrm{IIc}}}{S_{12}^{2}}\right](C_{\mathrm{I}}^{g_{\mathrm{I}}}+C_{\mathrm{II}}^{g_{\mathrm{II}}})\left[U\left(\frac{G_{\mathrm{I}}}{G_{\mathrm{Ic}}}+\frac{G_{\mathrm{II}}}{G_{\mathrm{IIc}}}\right)\right]^{(g_{\mathrm{I}}r_{\mathrm{I}}+g_{\mathrm{II}}r_{\mathrm{II}})}$ $g_{\mathrm{I}}=\frac{\frac{G_{\mathrm{I}}}{G_{\mathrm{Ic}}}}{\frac{G_{\mathrm{I}}}{G_{\mathrm{Ic}}}+\frac{G_{\mathrm{II}}}{G_{\mathrm{IIc}}}};\quad g_{\mathrm{II}}=\frac{\frac{G_{\mathrm{II}}}{G_{\mathrm{IIc}}}}{\frac{G_{\mathrm{I}}}{G_{\mathrm{Ic}}}+\frac{G_{\mathrm{II}}}{G_{\mathrm{IIc}}}}$	(5)
Kardomateas et al. (1995)	$\frac{\mathrm{d}a}{\mathrm{d}N}=C\frac{\left(\frac{G_{\mathrm{Ic}}G_{\mathrm{IIc}}}{G_{\mathrm{c}}}\Delta G\right)^{r}}{1-\frac{G_{\mathrm{Ic}}G_{\mathrm{IIc}}}{G_{\mathrm{c}}}G}$ $C=C_{\mathrm{I}}+(C_{\mathrm{II}}-C_{\mathrm{I}})\sin^{2}\psi$ $r=r_{\mathrm{I}}+(r_{\mathrm{II}}-r_{\mathrm{I}})\sin^{2}\psi$ $G_{\mathrm{c}}=G_{\mathrm{IIc}}+(G_{\mathrm{Ic}}-G_{\mathrm{IIc}})\sin^{2}\psi$	(6)
Kenane and Benzeggagh (1997)[b]	$\frac{\mathrm{d}a}{\mathrm{d}N}=\exp\left[\ln(C_{\mathrm{II}})+(\ln(C_{\mathrm{I}})-\ln(C_{\mathrm{II}}))\left(1-\frac{G_{\mathrm{II}}}{G}\right)^{b}\right](\Delta G)^{\left(r_{\mathrm{I}}+(r_{\mathrm{II}}-r_{\mathrm{I}})\left(\frac{G_{\mathrm{II}}}{G}\right)^{d}\right)}$	(7)
Andersons et al. (2001)	$\frac{\mathrm{d}a}{\mathrm{d}N}=C\left[\left(\frac{K_{\mathrm{I}}}{K_{\mathrm{Ic}}}\right)^{2}+\left(\frac{K_{\mathrm{II}}}{K_{\mathrm{IIc}}}\right)^{2}\right]^{\frac{r}{2}}$ $r=\frac{a_{1}+a_{2}}{\frac{a_{1}}{r_{\mathrm{I}}}+\frac{a_{2}}{r_{\mathrm{II}}}}$ $C=\left(\frac{r}{r-2}\right)\frac{a_{1}+a_{2}}{\left(\frac{\cos\psi}{K_{\mathrm{Ic}}}\right)^{2}+\left(\frac{\sin\psi}{K_{\mathrm{IIc}}}\right)^{2}}$ $a_{1}=\frac{r_{\mathrm{I}}-2}{r_{\mathrm{I}}}\left(\frac{\cos\psi}{K_{\mathrm{Ic}}}\right)^{2}C_{\mathrm{I}};$ $a_{2}=\frac{r_{\mathrm{II}}-2}{r_{\mathrm{II}}}\left(\frac{\sin\psi}{K_{\mathrm{IIc}}}\right)^{2}C_{\mathrm{II}}$	(8)

Figure 2.2: *Overview of selected mixed mode propagation relations up to the turn of the century. From [22].*

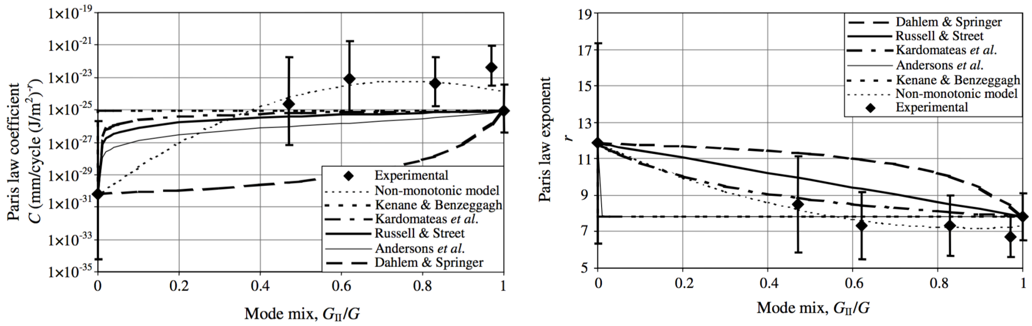

(a) *Paris relation coefficient C.*

(b) *Paris relation exponent r.*

Figure 2.3: *Paris parameters for various mode mixity relations. From [22].*

An overview of more mixed mode fatigue propagation relations up to 2013 is provided by Pascoe et al [16]. The recommended approaches suggested by Deobald et al [26] in their ”Guidelines for VCCT-Based Inter-laminar Fatigue and Progressive Failure Finite Element Analysis”, published September 2017, consist of the relation proposed by Ramkumar and Whitcomb shown in figure 2.2, the relation proposed by Kenane and Benzeggagh also shown in figure 2.2 and the relation proposed by Blanco et al discussed before. Deobald et al also present two other interpolation schemes based on the assumption that quasi-static mixed mode growth translates to mixed-mode fatigue growth.

2.3 Suitability of the Strain Energy Release Rate as similitude parameter

Although a fair correlation between the SERR and fatigue delamination growth has been established in literature, in a recent body of work Pascoe, Amaral, Alderliesten, Benedictus, Zarouchas, Yao, and Zhao [18, 23, 27–29] have questioned the suitability of the SERR as a similitude parameter for fatigue delamination propagation. Yao et al [23] have conducted an experimental campaign to investigate the similarity in damage state between quasi-static delaminations and fatigue delaminations as well as the effect of fibre bridging using unidirectional and multidirectional Double Cantilevered Beam (DCB) specimens. Pre-cracks of various lengths were introduced into the specimens either quasi-statically or using fatigue loading prior to fatigue testing. The results show a clear difference between the two sets of specimens in the relation between ΔG and da/dN as shown in figure 2.4. Because of this difference they deem the practice of normalising fatigue test results with quasi-static experimental data adopted in literature to be incorrect: ”Hence, quasi-static bridging clearly provides a different response under fatigue loading compared to fatigue bridging, As a result, it is deemed incorrect to use the quasi-static experimental data to normalize the fatigue test result with the purpose of decreasing scatter of fatigue data or establishing a fatigue prediction model.”[23, p.67].

Yao et al also note that the SERR originated from Griffith’s [11] and Irwin’s [12] work on quasi-static crack growth and relies on the assumption of fixed grips. ”In fixed grip condition, all energy is preserved within the specimen, because no additional work is applied. This implies that the total amount of energy absorbed by unit fracture surface should equate to the rate of loss of strain energy from the surrounding elastically strained material[...]. However, load and displacement change continuously during cyclic loading. Consequently, the assumption of fixed grip is inapplicable to fatigue loading conditions.” [23, p.67-68]. They claim that crack extension occurs over the entire load cycle rather than instantaneously at maximum load, a claim which is supported by the observations of Pascoe et al [30], and that therefore the applied work at which the crack advances continuously varies. This disagrees with the assumption of constant work by Irwin. They assert that for fatigue loading, instead of the SERR, the strain energy released in one load cycle is the difference between the work required to load the material and the work required to unload the material: the work dissipated per applied load cycle.

Yao et al compute the work dissipated per applied load cycle, dU/dN, and plot this against the crack propagation per load cycle, da/dN, as shown in figure 2.5 for unidirectional specimens F_1 and multidirectional specimens F_2. Both sets of specimens contain pre-cracks introduced through fatigue cycling ranging from 4.1 mm to 79.5 mm with a specimen length of 200 mm. It is evident that the different pre-crack lengths and layups have collapsed to a single curve with only a small difference observed for different amounts of fibre bridging being present. This is explained through the observation that bridging fibres are loaded and unloaded with the rest of the structure and do not contribute to any dissipation of strain energy unless they fail during the load cycle. Therefore the amount of strain energy that is dissipated is mostly unaffected by the amount of bridging present. The small change with the amount of bridging is attributed to there being more bridging fibres to break and contribute to the strain energy dissipation during a load cycle for a large amount of bridging compared to a small amount of bridging. Not duplicated here are the results which show that da/dN vs dU/dN of the quasi-statically pre-cracked specimens coincides with the fatigue pre-cracked specimens. Based on these findings Yao et al conclude that the SERR is not a ”[...] reasonable parameter to characterize

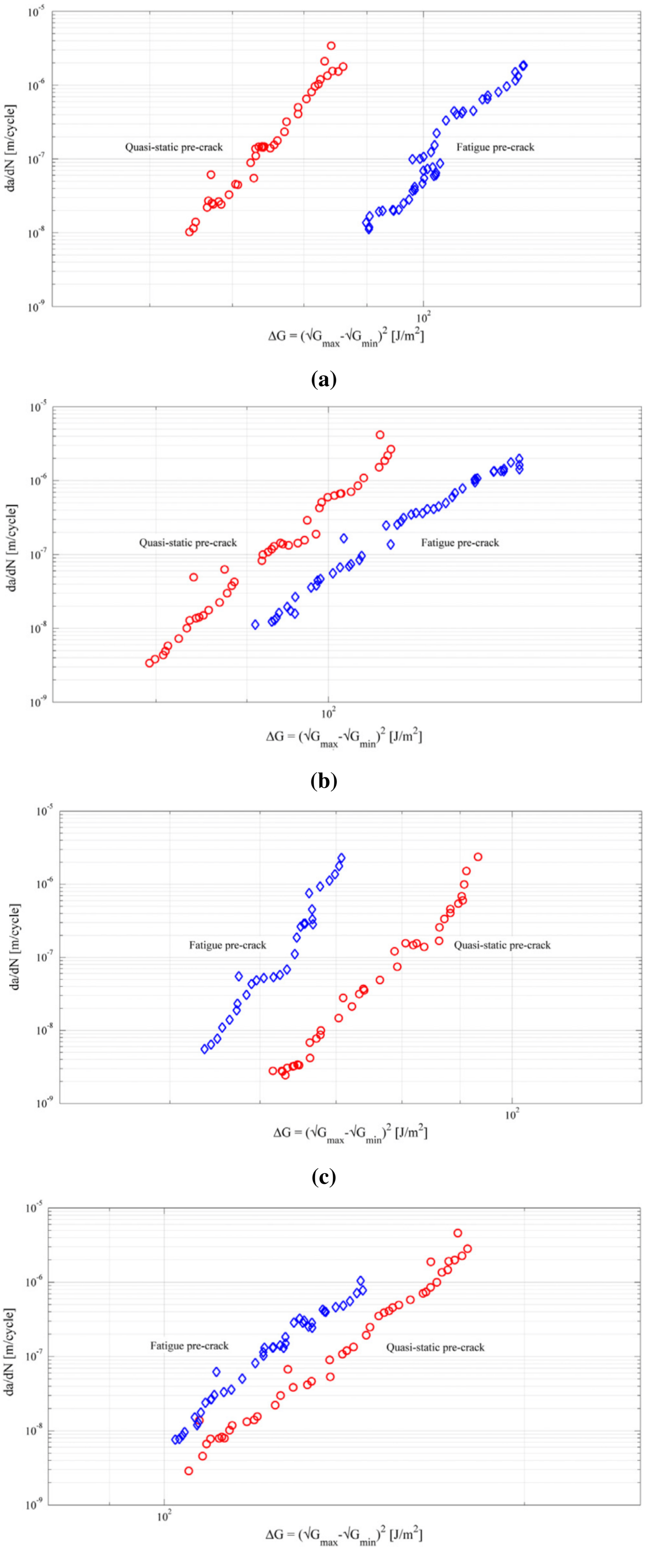

(a)

(b)

(c)

(d)

Figure 2.4: *Different damage in quasi-static and fatigue delamination. (a) Specimen F_1 and QS_1 (0//0 interface with 40 mm pre-crack). (b) Specimen F_1 and QS_2 (0//0 interface with 50 mm pre-crack). (c) Specimen F_2 and QS_3 (45//45 interface with 10 mm pre-crack). (d) Specimen F_2 and QS_4 (45//45 interface with 30 mm pre-crack). From [23].*

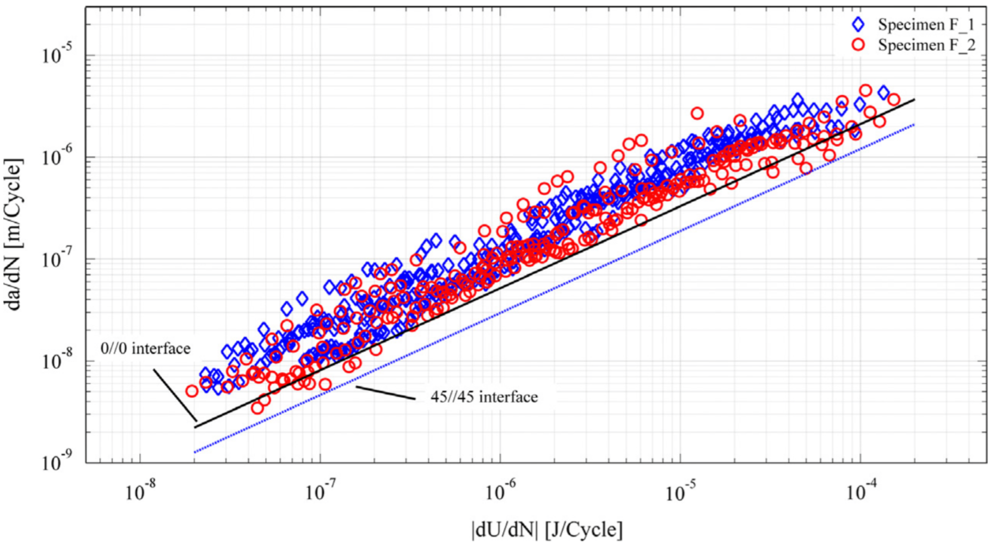

Figure 2.5: *Crack increment per cycle da/dN vs. work dissipated per cycle dU/dN for unidirectional specimens F_1 and multidirectional specimens F_2 with fatigue pre-cracks ranging from 4.1 mm to 79.5 mm. From [23].*

fatigue delamination growth."[23, p.71]. In more recent work Yao et al focus on developing a modified Paris relation to predict crack propagation in the presence of fibre bridging [31, 32] rather than on the implications of this conclusion for more general fatigue crack propagation.

These implications are, however, investigated further by Pascoe et al [28, 29] for fatigue delamination growth. They hypothesised, based on Griffith's energy principle, that the energy released during a single load cycle must be related to the amount of energy consumed for crack growth and thereby to the crack growth rate. They conducted 7 fatigue tests on aluminium DCB specimens bonded with epoxy adhesive to test their hypothesis. The specimens were manufactured with a pre crack of 50 mm and were loaded at 5 Hz with various R ratios. Fractographic analysis of the tested specimens showed that cohesive fracture of the adhesive occurred for all specimens. Adhesive failure between the adhesive and the adherents did not occur, nor did failure of the adherents. The delamination growth rate recorded during the fatigue testing is plotted in figure 2.6. Clearly visible are both the spread of the delamination rates when plotted against the maximum SERR and the SERR range as well as the R-ratio effect where the growth rates are shifted depending on the applied load ratio. When the delamination growth rates are plotted against the loss of cyclic strain energy they collapse rather well to a single curve. The only clear deviation from this curve is the data of test C-002-F1 which shows threshold behaviour. This anomaly is attributed by Pascoe et al to an artefact of the adopted measurement and data analysis techniques.

Pascoe et al note that the power relation fitted to the correlation of the delamination growth and the loss of cyclic strain energy has an exponent different from unity which implies that the energy required per unit delamination growth is not constant. As a potential explanation for this they cite the work of Broberg [33], and they speculate that small scale crack kinking or branching may cause such behaviour. On the applicability of this research to other materials they note that the results should hold for delamination growth which is continuous and correlates in a log-linear fashion with the SERR and SIF. Fatigue delamination growth in fibre reinforced polymer composites is explicitly mentioned as an example of such a case.

The correlation between the loss of cyclic strain energy and delamination growth rate is unfortunately of limited use in creating a predictive model. The loss of cyclic strain energy depends both on the continuously changing value of G during a load cycle and on the crack extension during the cycle and may be expressed as shown in equation 2.5 where G is the instantaneous SERR and a is the crack length along with suitable limits of integration. Determining G is straightforward using the VCCT

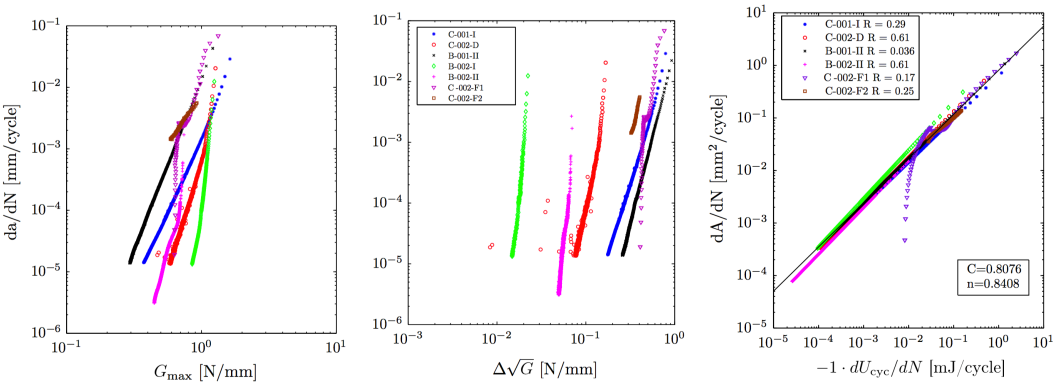

(a) **(b)** **(c)**

Figure 2.6: *Delamination growth rate versus maximum SERR (a), SERR range (b), and loss of cyclic energy (c).From [28].*

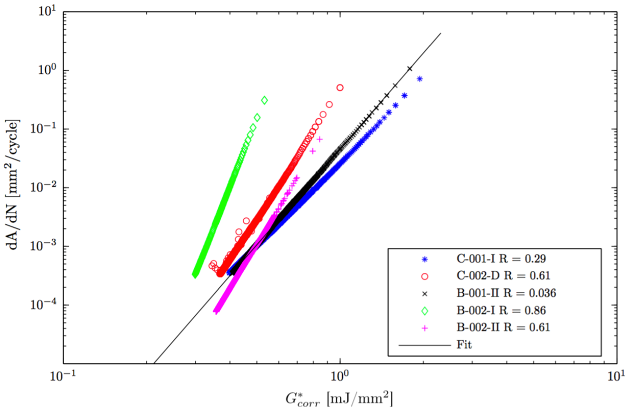

Figure 2.7: *Correlation between the crack growth rate dA/dN and the average strain energy release rate G^* including a correction for the released strain energy. From [28].*

discussed in section 2.4. However, determining the instantaneous crack length is not as it requires knowledge of da/dN. As such dU/dN can only be determined a posteriori.

$$\frac{dU}{dN} = \int G(a)da \tag{2.5}$$

As a solution Pascoe et al propose the parameter G^*, derived by assuming that crack growth and loss of energy are constant during a single cycle. They state ”[...] $G^*(N)$ can be understood as the average amount of strain energy released per unit crack extension during cycle number N.” [28, p.11]. The resulting correlation, shown in figure 2.7, is not unreasonable but is still quite a way off from the excellent correlation found using dU/dN. Pascoe et al indicate that the presented approximation is fairly crude and that future work will focus on refinement of the predictive model. In their most recent work Pascoe et al have focussed on understanding fatigue crack growth within a single load cycle [30] for just this purpose. Investigation into the correlation between mixed-mode fatigue disbond growth and the loss of cyclic strain energy has been conducted by Amaral et al [27, 34].

Although the correlation between fatigue crack growth and the loss of cyclic strain energy is excellent and the work on a predictive model based on this correlation is promising, the approach does not yet seem to have the maturity required to scale-up from specimen level to structural element level. More fundamental work at the specimen level is required before the approach can be depended on for larger scale structural fatigue disbond propagation prediction. As such, for the present research the Strain Energy Release Rate will be used as a similitude parameter.

2.4 Numerical determination of the Strain Energy Release Rate

The Virtual Crack Closure Technique (VCCT), presented by Rybicki and Kanninen [35], is a widely used technique to calculate the Strain Energy Release Rate (SERR). Its application relies mainly on two assumptions, the applicability of Irwin's crack closure integrals and the self-similarity assumption. The self-similarity assumption is the distinguishing factor between the VCCT and the earlier Crack Closure Technique (CCT). As such the CCT will be discussed first in section 2.4.1, before the extension to VCCT is discussed in section 2.4.2.

2.4.1 Crack Closure Technique

For the Crack Closure Technique (CCT) as presented by Irwin [36] it is asserted that the strain energy released by propagating a crack by a distance Δa from a to $a+\Delta a$ is equivalent to the energy required to close the crack over this same distance Δa. Although this may be evaluated analytically for some specific cases, such as those discussed by Irwin, with the computational resources currently available it is commonly evaluated numerically. A two dimensional representation of a crack propagating between two layers of a discretised solid is shown in figure 2.8 taken from [37]. The first step in the analysis is to calculate the nodal forces at node l, as shown in figure 2.8a, required to keep the node closed. For the second step, shown in figure 2.8b, the nodal forces at node I are reduced to zero and the corresponding displacements are calculated. The work ΔE required to close the crack is then calculated as shown in equation 2.6 from [37], where X_{1l} and Z_{1l} are the shear and opening forces at node l calculated in step 1 and where Δu_{2l} and Δw_{2l} are the shear and opening displacements at node l calculated in step 2 respectively.

$$\Delta E = \frac{1}{2}\left[X_{1l}\Delta u_{2l} + Z_{1l}\Delta w_{2l}\right] \tag{2.6}$$

2.4.2 Virtual Crack Closure Technique

Central to the Virtual Crack Closure Technique, also known as the Modified Crack Closure Technique, is the self-similarity assumption. Rybicki and Kanninen [35] argued that for a sufficiently small Δa the stress state of the crack tip at a crack tip location of $a+\Delta a$ is not substantially different from the crack tip stress state at a crack tip location of $a+2\Delta a$. This allows the SERR to be calculated in one step by calculating the nodal forces required to keep the node closed at, for example, node i and to combine these with the displacements of node l as shown in figure 2.9, halving the computational load. The work ΔE required to close the crack is then given by equation 2.7 from [37], where X_i and Z_i are the shear and opening forces at node i and where Δu_l and Δw_l are the shear and opening displacements at node l respectively.

$$\Delta E = \frac{1}{2}\left[X_i\Delta u_l + Z_i\Delta w_l\right] \tag{2.7}$$

The Strain Energy Release Rate, G, is calculated by normalising the work required to close the crack ΔE by the created crack surface ΔA. The expression of ΔE and ΔA depends strongly on the element type used. The aim of this study is not to present an exhaustive list. Instead only the formulation for shell elements relevant to the present research will be discussed. A selection of formulations for other element types is presented in [37], with more available from literature. A VCCT formulation for four noded elements, presented by Whitcomb and Shivakumar [38], and later extended to nine noded Assumed Natural-coordinate Strain (ANS) plate/shell elements by Wang et al [39] and subsequently by Wang and Raju [40] will be presented.

Two approaches were adopted by Wang and Raju to derive the VCCT formulations. In the first approach both the displacement and the rotation of the nodes at the crack front are constrained to be

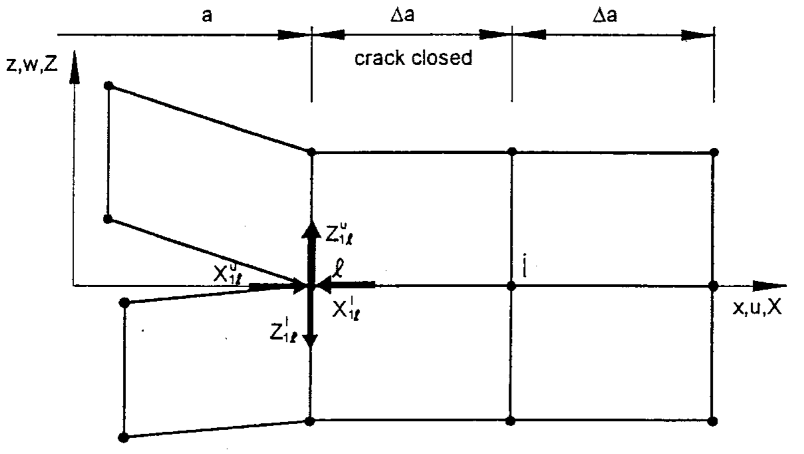

where $Z^l_{1\ell}=Z^u_{1\ell}$ and $X^l_{1\ell}=X^u_{1\ell}$ from equilibrium

(a) *First step - Crack closed*

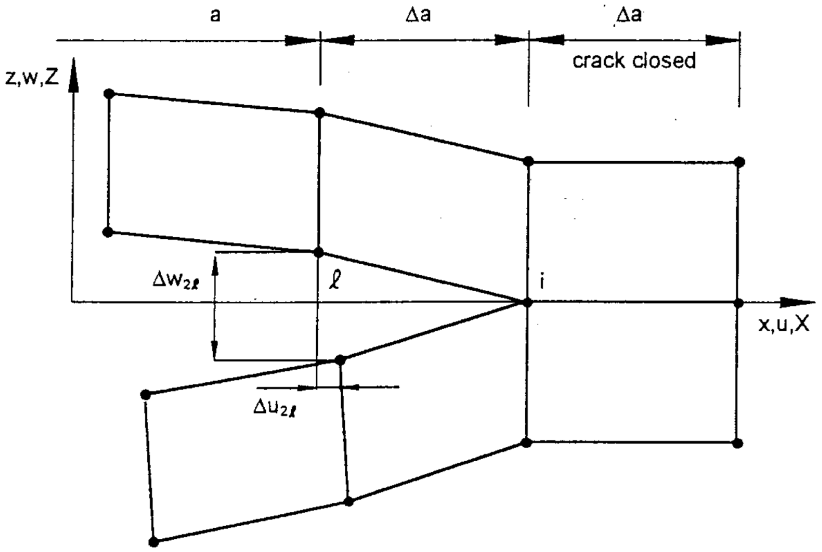

(b) *Second step - Crack extended*

Figure 2.8: *Crack Closure Technique (two-step method). From [37].*

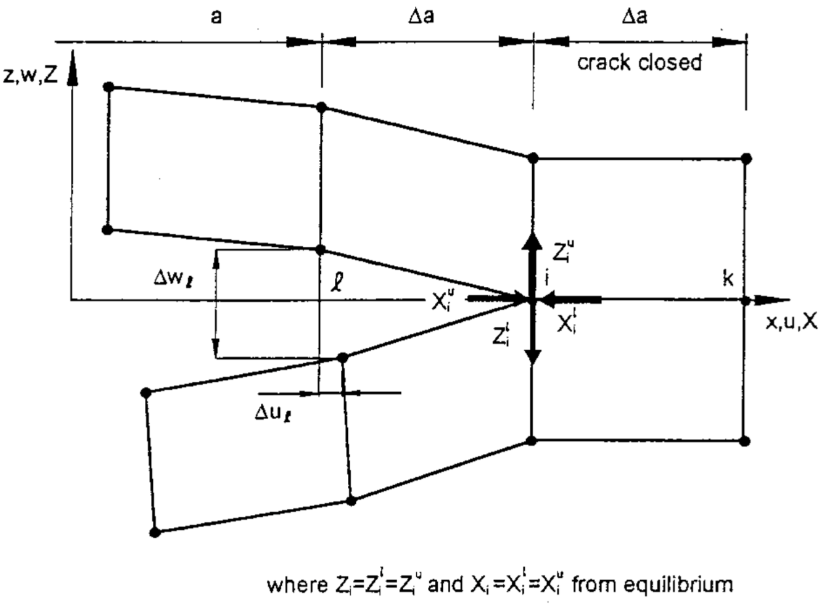

Figure 2.9: *Virtual Crack Closure Technique, (one step CCT). From [37].*

equal for the upper and lower sub-laminates. The second approach does not impose constraints on the node rotation, it only constrains the nodal displacement. For verification the VCCT formulations, along with suitable boundary conditions, were compared to existing plane strain solutions for the SERRs of DCB type specimens loaded with edge moments or shear loads. The results indicated that second approach agrees well with plane strain models, with an error of 1% for G_I and 7% for G_{II}. The first approach does not seem to agree as well, with an error of 22% for G_I and an error of 7% for G_{II}. Although it may be curious that both approaches show the same error for G_{II} this can be explained by the fact that no bending moment is involved in the formulation of the mode II SERR, and hence that both approaches lead to the same formulation.

The results of Wang and Raju [40] also indicate that there is no appreciable difference between four and nine noded plate/shell elements. As such it appears that 4 noded shell elements should be preferred due to the lower computational load associated with them relative to nine noded elements. The VCCT formulation for 4 noded plate/shell elements presented by Wang and Raju as shown in figure 2.10 for the Strain Energy Release Rate of mode I, II, and III are shown in equations 2.8. In these equations, $F_{z,i}$, $F_{x,i}$ and $F_{y,i}$ are the nodal forces of node i in z, x and y direction respectively and w_l, $w_{l'}$, u_l, $u_{l'}$, v_l, and $v_{l'}$ are the nodal displacements at node l and l' as indicated. The coefficients B_i are the equivalent widths apportioned to the node in question as shown in equation 2.9. Finally the total Strain Energy Release Rate (SERR) is calculated by summing the rates for the individual modes as shown in equation 2.10.

$$\begin{aligned} G_I &= -\frac{1}{2\Delta B_i}\left[F_{z,i}\left(w_l - w_{l'}\right)\right] \\ G_{II} &= -\frac{1}{2\Delta B_i}\left[F_{x,i}\left(u_l - u_{l'}\right)\right] \\ G_{III} &= -\frac{1}{2\Delta B_i}\left[F_{y,i}\left(v_l - v_{l'}\right)\right] \end{aligned} \tag{2.8}$$

$$B_i = \frac{1}{2}\left[b_{J-1} + b_J\right] \tag{2.9}$$

$$G_{total} = G_I + G_{II} + G_{III} \tag{2.10}$$

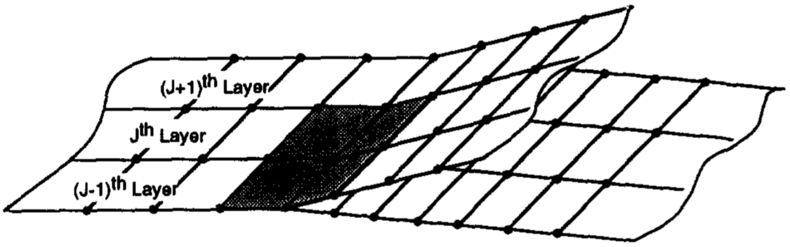

(a) *Plate element modelling near the crack front.*

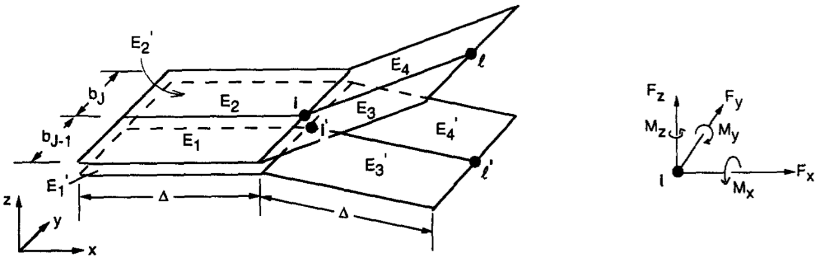

(b) *Details of the model near the crack front.*

Figure 2.10: *Crack Closure TechniqueModel with four noded AND plate elements. From [40].*

Implicitly assumed in the above formulation is the orthogonality between the mesh and the crack front as well as that the elements in front of the crack front have the same size as the elements behind the crack front. This orthogonality assumption holds quite well for test specimens such as the DCB specimen where the crack front largely remains straight and aligned with the mesh.

Nodal versus elemental formulations

The VCCT may be formulated either in a nodal sense as shown in section 2.4 to determine the SERR for every crack front node or in an elemental sense as shown in [41] to determine the SERR for every crack front element. The two formulations, although different in their details, are equivalent in use. The choice is one of convenience; for VCCT implementations based on a user element an elemental formulation is generally adopted and for implementations based on post-processing routines typically a nodal formulation is adopted.

2.4.3 Considerations

A number of issues with the original VCCT formulation by Rybicki and Kanninen [35] have been identified and addressed by a variety of researchers across a large number of publications. Some of these issues, with select solutions, are discussed in turn below. It is not the aim of this section to present an exhaustive list of all solutions or a full account of the history of these solutions.

Section continuity

Glaessgen et al [42] [43] have shown that the SERR tends to converge only when the section properties of the elements above and below the delamination plane are equal. In figure 2.11 the SERR is plotted against node spacing for an equidistant rectangular mesh and continuous section properties. Method one is the method of interest, with shear deformable elements and without rotational constraints at the crack front nodes.

The figure shows that the SERR is approximately 4% below the converged SERR when the nodal spacing is twice the plate thickness. With a nodal spacing around the plate thickness the SERR is

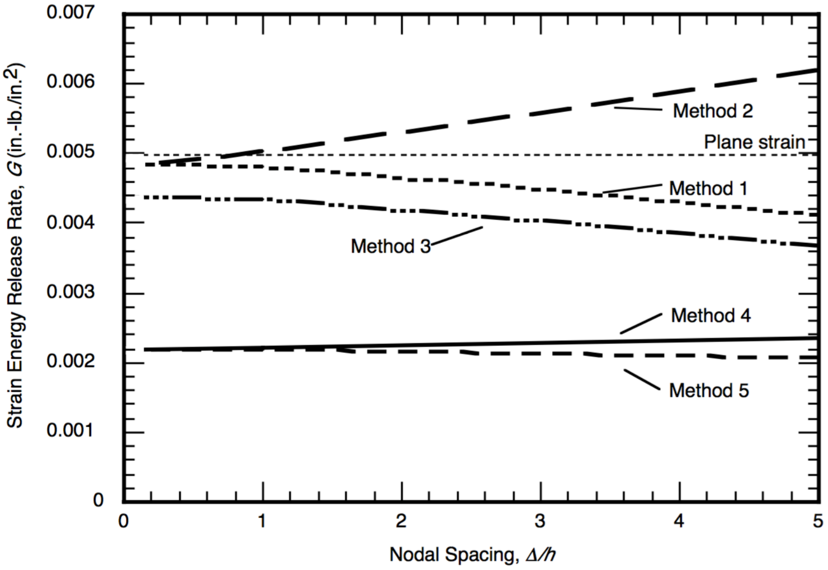

Figure 2.11: *Convergence of Strain Energy Release Rate. a=0.25", h = 0.025". From [43].*

indistinguishable from the converged value on the graph. The convergence behaviour of discontinuous section properties is shown in figure 2.12. Specifically the figure shows the mode I, Mode II and total SERR for a skin and stiffener flange with different stiffness. The total SERR shows little variation, but this is due to the change in Mode I and Mode II cancelling each other out. Figures for asymmetric layups of the skin and flange as well as those with different thicknesses for the flange and skin are not replicated here but show similar behaviour. Glaessgen et al remark "When the section properties above and below the crack plane are discontinuous, the total strain energy release rate is well behaved, but the modes do not converge or converge very slowly. Conversely, when the section properties are continuous, both the total strain energy release rate and the individual modes are well behaved." [42, p.6].

This effect is attributed to an oscillatory singularity which "[..] is an artefact of elastic modelling of cracks at bi-material interfaces"[42]. An excellent review of recent developments in bimaterial fracture mechanics analysis has been provided by Krueger, Shivakumar, and Raju [44].

Geometrically non-linear deformations

For geometrically non-linear deformations the displacements tend to be large. As such the nodal forces and displacements must be expressed in a local reference frame aligned with the crack front to determine the correct modal contributions to the total SERR. This local reference frame is also required to deal with arbitrary crack fronts. A method to construct such a frame is shown in next subsection on "Mesh and crack front orthogonality".

Mesh and crack front orthogonality

The VCCT formulation presented in section 2.4 implicitly assumed orthogonality between the crack front and the mesh. This assumption holds only for a select number of cases where the crack propagation direction is known a priori and the meshing can take this into account. In general, and for structural elements rather than specimens especially, it cannot be guaranteed that the crack front remains orthogonal to the mesh. One solution to this is to apply a re-meshing approach where the orthogonality of the mesh to the crack is enforced every time the mesh is refreshed. A more elegant, and more efficient, approach is to adjust the VCCT formulation to enable it to handle non-orthogonal meshes. Smith and Raju [45] have presented such a formulation of the VCCT. An example of a

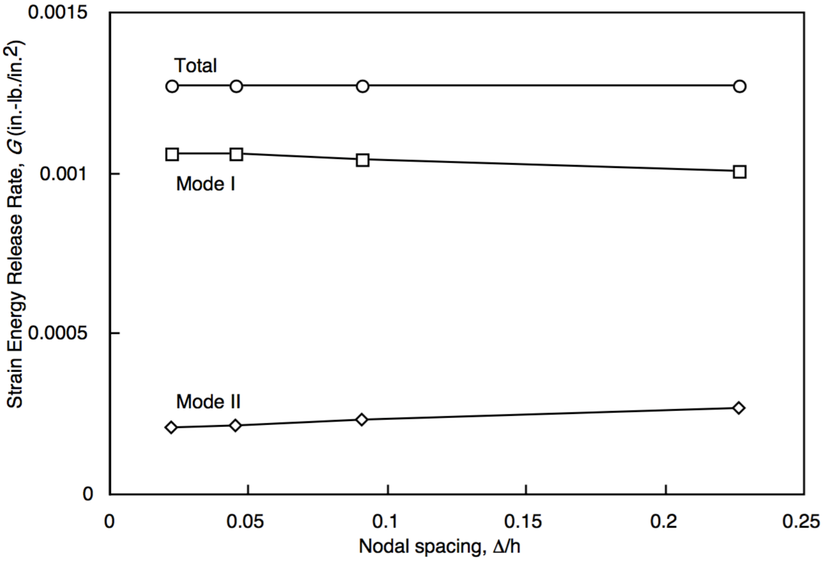

Figure 2.12: *Strain energy release rate for debond configuration with skin and flange with different stiffness. Flange,skin thickness: 0.11', flange layup: [$0_5/90_{10}/0_5$], skin layup: [0_{20}]. From [43].*

crack front with and without orthogonality is shown in figure 2.13. In figure 2.13a the nodes used to calculate the SERR using the VCCT are in plane with the crack and lie on the normals to the crack front. In figure 2.13b the nodes lie in the same plane, but not on the normals to the crack front. In the method proposed by Smith and Raju the nodes are projected onto the normals and these projected nodes, indicated by p* and p*', are subsequently used for the VCCT computation. The displacements at node p*' are computed through the elemental shape functions.

A general, non-orthogonal, mesh is shown in more detail in figure 2.14. In this figure the shaded area is cracked and the unshaded area is un-cracked The areas are separated by a piece-wise linear crack front as indicated. On this crack front exist the nodes j-1, j, and j+1 where the SERR is to be evaluated for node j. The normal to the crack front at node j, $\hat{\boldsymbol{n}}_j$, is computed by averaging the normals to the crack front line segments to either side of node j, $\hat{n}_{(-1)}$ and $\hat{n}_{(+1)}$. The radial distance r is determined by constructing a vector from node j to node p and projecting this vector onto the normal vector $\hat{\boldsymbol{n}}_j$. The node p*' is placed on the normal at the same radial distance r behind node j. Through this the method is also capable of handling differently sized elements in front of and behind the crack, the displacements at node p*' are computed through the elemental shape functions and the nodal locations of whichever element the node happens to coincide with.

The virtually closed area associated with node j required to calculate the SERR is shown as the hatched area in figure 2.15 marked with A_j. This area is computed by combining half the area of the quadrilateral formed by nodes j, j-1, p*, and (p-1)* with half of the area of the quadrilateral formed by nodes j, j+1, (p+1)*, and p* as shown in equations 2.11 and 2.12. In these equations t_i is the average width of one of the previously mentioned quadrilaterals and the quantity $\left[\hat{\boldsymbol{n}}_{(-1)} \cdot (\hat{\boldsymbol{n}}_{(j)} \cdot \bar{\boldsymbol{d}})\hat{\boldsymbol{n}}_{(j)}\right]$ is the length of the left quadrilateral found by projecting the vector from node j to p* onto the normal vector $\hat{\boldsymbol{n}}_{-1}$. This area A_j is comparable to the quantity ΔB_i of equations 2.8 of the orthogonal formulation.

$$A_j = \left[\hat{\boldsymbol{n}}_{(-1)} \cdot (\hat{\boldsymbol{n}}_{(j)} \cdot \bar{\boldsymbol{d}})\hat{\boldsymbol{n}}_{(j)}\right] \frac{t_i}{2} + \left[\hat{\boldsymbol{n}}_{(+1)} \cdot (\hat{\boldsymbol{n}}_{(j)} \cdot \bar{\boldsymbol{d}})\hat{\boldsymbol{n}}_{(j)}\right] \frac{t_{i+1}}{2} \tag{2.11}$$

$$t_i = \frac{(t_a)_i + (t_b)_i}{2} \tag{2.12}$$

The results of Wang and Raju show that the orthogonal VCCT formulation does not produce correct results for non-orthogonal meshes with differences up to 40% compared to orthogonal meshes.

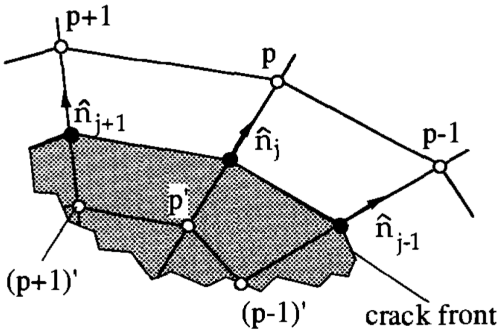

(a) *with orthogonality*

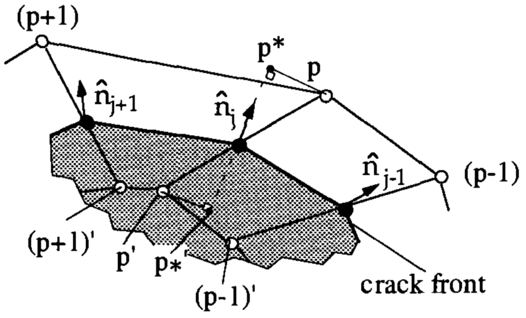

(b) *Without orthogonality*

Figure 2.13: *Crack fronts with and without orthogonality. From [45].*

It is also shown that the revised non-orthogonal formulation applied to a non-orthogonal mesh produces results within 3% of the original orthogonal formulation applied to an orthogonal mesh. The remaining three percent error is attributed to a very steep section of the elliptical crack front section in their verification case which is not well modelled by the quadrilateral mesh. They expect this error to decrease with further mesh refinement.

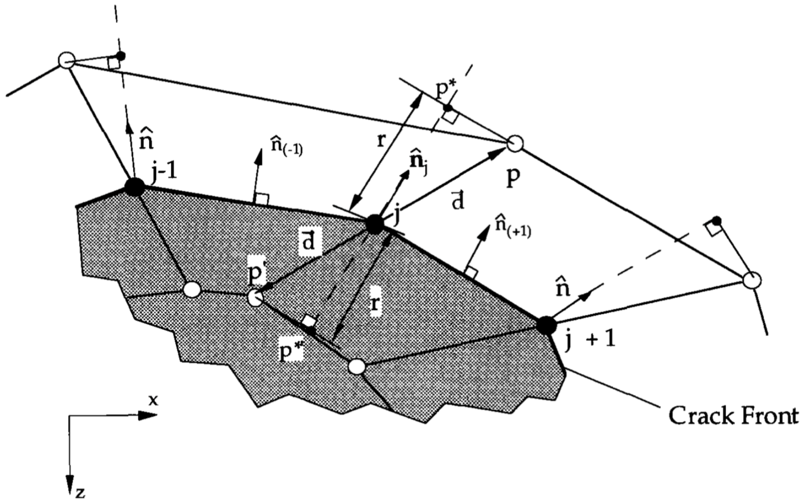

Figure 2.14: *The crack plane of a general model. From [45].*

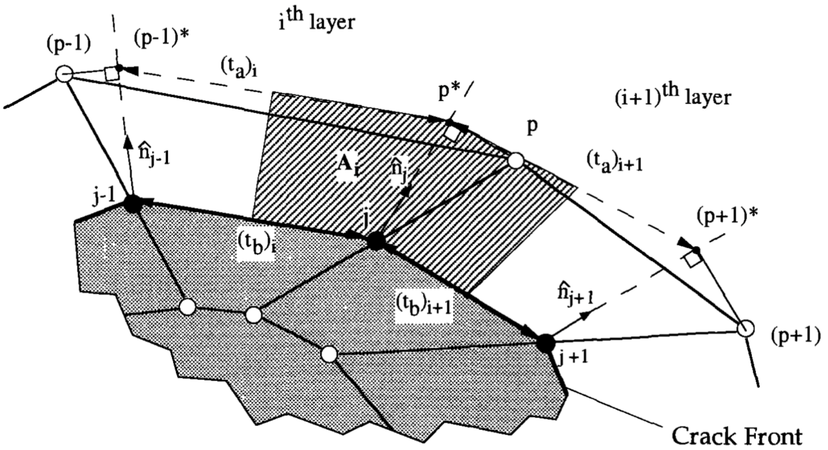

Figure 2.15: *Nodes and element boundaries on the crack plane near the crack front of a general finite-element model. From [45].*

Chapter 3

Implementations of fatigue propagation algorithms

Virtual Crack Closure Technique (VCCT) based fatigue propagation algorithms have been implemented in research settings as well as for commercially available finite element analysis software. These implementations are presented and discussed in this chapter. Implementations drawn from literature are discussed first followed by the implementations provided with the software Abaqus FEA 2017 by Dassault Systèmes SE. Many of the discussed research implementations are implemented in Abaqus through user elements or user subroutines. The distinction is made only to separate those implementations that are not provided with Abaqus from those that are.

3.1 Research implementations

Deobald et al [46] and Mabson et al [47] have presented a fracture interface element based on a fracture mechanics approach combined with the VCCT for fatigue delamination growth analysis. They have chosen to use a Paris type propagation relation using either G_{max} or ΔG of the form shown in equation 2.1, provided that the calculated Strain Energy Release Rate (SERR) exceeds the threshold G_{th} and does not exceed the critical SERR G_c. If the SERR does not exceed G_{th} no growth will occur, and if the critical SERR is exceeded quasi-static growth will occur. The parameters of the Paris relation are fitted to DCB specimen test data.

The process through which Deobald et al determine the fatigue delamination growth is shown in figure 3.1. The model is loaded and the VCCT is used to determine either the maximum SERR or the SERR range for every interface element at the crack front. Subsequently the crack growth rate is determined for every element and the cycles to failure are calculated for every element. The element with the lowest number of cycles to failure is failed, and the damage corresponding to the requisite number of cycles is added to every other crack front element. Finally the displacement of the model with the released element or elements is calculated and the cycle starts again. For both propagation parameters the model is loaded to P_{max} and used to determine G_{max}. For the SERR range G_{min} is then estimated linearly from G_{max} and the load ratio.

Deobald et al have implemented their approach for 2D analyses. The propagation parameters are based on the total SERR. As verification Deobald et al apply their method to the analysis of a DCB specimen and compare their results to an analytical DCB solution. Excellent agreement is shown for their fine mesh, although the corresponding mesh density is not specified.

De Carvalho and Krueger [41, 48] have implemented an element based VCCT approach combined with the Floating Node Method (FNM) through a user subroutine for fatigue damage onset and growth. For damage onset they have implemented a maximum principle stress criterion, a Weibull distribution for the material static strength, Weibull scaling to counter probabilistic mesh size effects, and the Palmgren-Miner rule for damage accumulation prior to crack onset. An exclusion zone

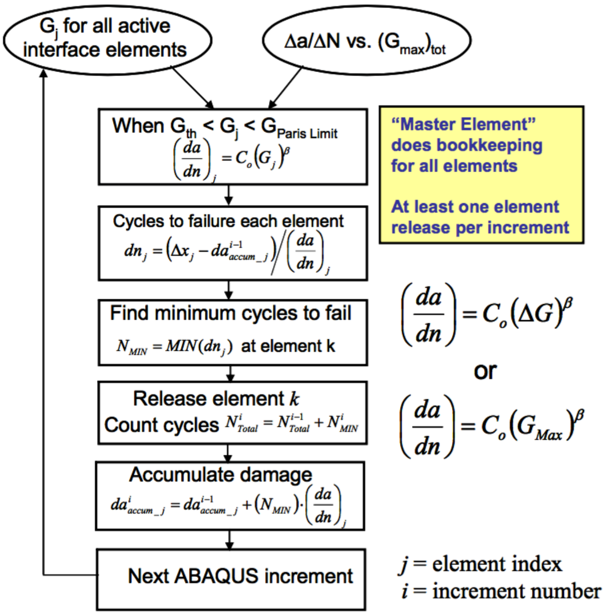

Figure 3.1: *Flow chart for Paris relation fatigue growth analysis. From [46].*

ahead of any existing crack fronts is used to prevent the onset criterion from dominating the fracture mechanics criterion due to the stress singularity at the crack front. For fatigue growth they have chosen a Paris type propagation relation using G_{max} as a similitude parameter. The modal contributions are summed to obtain G_{max}, and the mode-mixity ratio β is calculated separately and used to modify the parameters of the Paris relation to account for mode-mixity effects. A binary fail/release approach was adopted where elements are either in pristine condition or failed, no degradation of element properties occurs during damage accumulation. Delamination damage is accumulated by taking the original un-cracked area of an element and subtracting the cracked area increment for a given number of cycles. The same algorithm proposed by Deobald et al [46, 47] is used with the change that the algorithm looks for the lowest number of cycles for an element to fail or for the onset of a crack to occur. This number of cycles is then used to accumulate damage and progress crack fronts.

The VCCT implementations are verified separately for matrix cracks and for delaminations. To verify the predicted energy release rates for matrix cracks they are compared to analytical solutions. Convergence was observed, with an error of approximately 0.5% for mode I and approximately 1% for mode II loading at an element size of 0.125 mm. The predicted delamination energy release rates were verified by comparison to benchmark solutions developed by Krueger [8, 49]. Excellent agreement between the implementation and the benchmark was found, with results for mode I and mode II being indistinguishable.

The efficacy of the Palmgren-Miner rule, used here for crack onset damage accumulation, has been debated [50]. Nevertheless it is still widely applied in industry for its convenience. The matrix crack density predicted by the model is validated through comparison to experimental data of uniaxial tension-tension fatigue specimens. Qualitatively similar results are obtained from the simulation, where the crack density versus number of cycles show similar trends.

Krueger and De Carvalho [10] have quantified the accuracy and time efficiency of their approach in comparison to existing benchmark solutions and the LCF method provided with Abaqus/Standard by analysing DCB and MMB fatigue specimens. The FNM-VCCT approach adopted in this work by Krueger and De Carvalho does not include fatigue damage onset unlike the approach presented by De Carvalho and Krueger in [41, 48]. Otherwise the approach appears to be the same. A DCB specimen with pure mode I loading was analysed as well as an MMB specimen at 20%, 50%, and 80% Mode II mode mixity. As shown in figure 3.2 the results for the FNM-VCCT approach, the LCF approach and

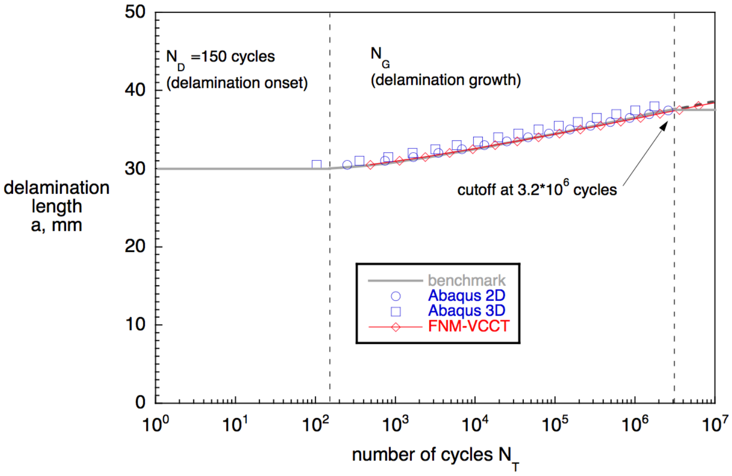

Figure 3.2: *Computed delamination onset and growth for DCB specimen. From [10].*

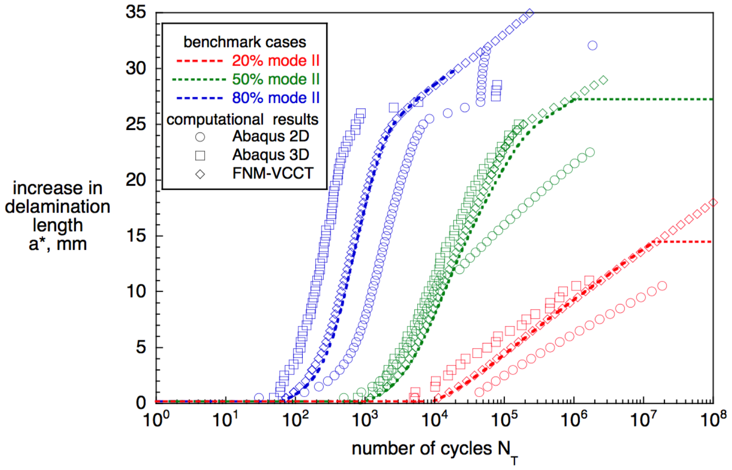

Figure 3.3: *Computed delamination onset and growth for MMB specimens. From [10].*

the benchmark agree very well. The 3D LCF approach tends to overestimate the delamination length slightly for any particular cycle count compared to the others, deviating not more than 4% from the benchmark.

Larger differences can be seen for the MMB specimens in figure 3.3. It should be noted that the FNM-VCCT results do not include a prediction for the number of cycles required for fatigue onset and have been offset using the number of cycles calculated for the benchmark. The LCF results do include such a prediction, either overestimating or underestimating the cycles required for the 2D analysis or the 3D analysis respectively. If this onset prediction were to be discarded and the benchmark onset cycle count were to be used for these the comparison with the FNM-VCCT results would be more comparable and the observed agreement would be better for the LCF results. That said, the 2D LCF results for the 50% mode II analysis deviate strongly from the other results. For the 20% mode II analysis the 2D results have a different slope compared to the other data, indicating incorrect propagation behaviour in addition to an inaccurate onset prediction.

The required computational time for the various analyses are shown in figure 3.4. The presented FNM-VCCT approach is approximately 2 orders of magnitude faster than the LCF approach implemented in Abaqus/Standard 6.14 across the presented analyses.

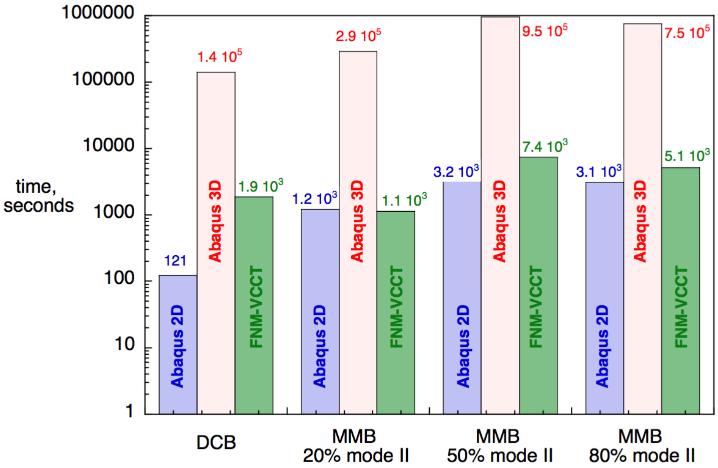

Figure 3.4: *Total CPU time required to calculate the propagation after 2e6 cycles for different models and implementations. From [10].*

3.2 Abaqus FEA implementations

Two fatigue delamination growth analysis methods are provided with Abaqus FEA from version 2017 onwards. The Low-Cycle Fatigue method will be discussed first in section 3.2.1 as it has been available the longest. The Constant Amplitude Fatigue method has only been available since Abaqus FEA 2017 and is discussed in section 3.2.2.

3.2.1 Low-Cycle Fatigue

The Low-Cycle Fatigue (LCF) analysis capability provided with Abaqus/Standard [51, ”Low-cycle fatigue analysis using the direct cyclic approach”] relies on the combination of the built in Direct Cyclic analysis [51, ”Direct cyclic analysis”] and the VCCT for fatigue delamination growth analyses. The Direct Cyclic analysis is used to determine the stabilised response of an elastic-plastic structure to cyclic loading without using a full transient analysis. A truncated Fourier series is used to represent the displacement response of the structure during a load cycle, the coefficients of which are solved for using a modified Newton method. A Fourier series expansion of the same form is used to expand the residual vector in the modified Newton method where the coefficients are obtained by time integration over a complete load cycle. The residual coefficients are used to refine the displacement coefficients in an iterative manner until convergence is achieved. A detailed explanation is available in the Abaqus documentation [51, ”Direct cyclic algorithm”].

Subsequent to the Direct Cyclic analysis the VCCT is applied to the stabilised response to determine the SERR range ΔG and the peak SERR G_{max} for all crack front nodes or elements. The LCF analysis includes a fatigue delamination onset criterion based on both ΔG and G_{max} as shown in equation 3.1 from [51, ”Crack propagation analysis”] where N is the total number of cycles, c_1 and c_2 are fitting parameters, ΔG is the SERR range, G_{max} is the peak SERR and G_{thresh} is the threshold SERR below which no fatigue growth occurs. The first part of the criterion is based on an exponential curve fit of experimental fatigue crack onset data for the material being tested. In addition to this the peak SERR must exceed the threshold SERR for onset to occur.

$$f = \frac{N}{c_1 \Delta G^{c_2}} \geq 1.0 \quad \wedge \quad G_{max} > G_{thresh} \tag{3.1}$$

The fatigue delamination growth rate is based on a Paris relation and uses ΔG as the similitude parameter as shown in equation 3.2 where c_3 and c_4 are fitting parameters. The delamination progression algorithm is the same as proposed by Deobald et al [46] where the crack growth rate is used to identify the node or element with the lowest number of cycles remaining to failure, that element is failed and the fatigue life of all other crack front elements/nodes is decreased by the required number of cycles.

$$\frac{da}{dN} = c_3 \Delta G^{c_4} \tag{3.2}$$

An LCF analysis is suitable to analyse the fatigue life of structures with non-linear material behaviour, such as elastic-plastic deformation, due to the inclusion of the Direct Cyclic analysis. Considering that thermoset fibre-composite delamination failure of tends to occur in a brittle fashion, without appreciable plasticity, the inclusion of the Direct Cyclic analysis seems unnecessary for such applications. This assessment is supported by the findings of Krueger and De Carvalho [10] who demonstrated that the computational load of the LCF was two orders of magnitude higher than their own VCCT implementation with similar accuracy. Because of the Direct Cyclic analysis the LCF analysis is also limited to geometrically linear structural responses. This makes the method unsuitable to determine fatigue delamination behaviour of composite panels loaded in the post-buckling regime.

3.2.2 Constant Amplitude Fatigue

The Constant Amplitude Fatigue (CAF) crack growth analysis [51, "Linear elastic fatigue crack growth analysis"] is a routine first introduced in Abaqus 2017 and first documented in the Abaqus 2018 Analysis guide. It uses the VCCT to determine both the SERR range ΔG and the peak SERR G_{max} for constant amplitude loading. The fatigue delamination onset and growth relations are identical to those used for the LCF analysis discussed in section 3.2.1. The main difference compared to the LCF approach is the lack of the Direct Cyclic analysis. This both substantially speeds up the fatigue delamination growth analysis for thermoset fibre-epoxy composite structures and eliminates the geometric linearity constraint. The CAF method is reported in the documentation to be capable of handling geometrically non-linear structural responses. The VCCT implementation must therefore have been implemented in a local reference frame aligned to the crack front to handle large deformations. The CAF analysis is also reported to handle changing contact conditions during a single load cycle. Any loads applied must have an amplitude definition that is cyclic over the analysis step. Although a single CAF analysis is constrained to a particular constant amplitude load cycle, the analysis may be repeated several times in a multi step analysis to represent a load spectrum with variable amplitudes. For the CAF analysis the specified load cycle is applied to the structure to determine the corresponding instantaneous strain energy release rate locally at the crack front. From that the local minimum and maximum SERR along the crack front are determined.

A standard fail-release approach has been adopted where elements are pristine until they reach a fatigue damage threshold and are then released instantaneously. If a gradual nodal release approach, through degrading element properties with the accumulation of fatigue damage similar to the method presented by De Carvalho et al [52], was available this would have been specified in the documentation. With a fail-release approach the CAF analysis may show delamination front straightening when analysing curved crack fronts on a rectilinear mesh. This would be visible as a tendency to straighten pre-defined curved crack fronts, a tendency for straight but oblique crack fronts to become orthogonal to the mesh, and a tendency for straight orthogonal crack fronts to grow exactly as they are even if crack rounding is observed in experimental campaigns.

Simplified Fatigue

The Simplified Fatigue (SF) analysis is a special case of the CAF analysis and is applicable when the maximum Strain Energy Release Rate (SERR) G_{max} and the minimum SERR G_{min} coincide with the peak applied load P_{max} and the minimum applied load P_{min} respectively, the SERR is proportional to the square of the applied load P, and the contact conditions are constant over a single load cycle. In this case a constant load P shown in equation 3.3 is applied to the structure instead of a cyclic load where $\alpha = P_{min}/P_{max}$.

$$P = P_{max}\sqrt{(1-\alpha^2)} \tag{3.3}$$

It would appear that the main distinguishing feature of the SF analysis is that the added complexity of computing the structural response to a load cycle and from that determining the local minimum and maximum SERR along the crack front has been eliminated. Instead a constant load is applied. From the proportionality assumption and a defined load ratio the maximum and minimum SERR can then be calculated. This approach would likely further reduce the computational load compared to the CAF analysis. Because the minimum and maximum SERRs are determined using a linear estimate from the applied constant load this analysis is not be expected to account for geometric non-linearity. In the post-buckling regime the Strain Energy Release Rate at the crack front of a stiffened panel will not generally be proportional to the square of the applied load due to global buckling and the interaction of skin buckles with the stiffener which itself may or may not have buckled flanges. Consequently it would appear that the SF analysis would be suitable mainly for structures made of linear-elastic materials loaded up to but not beyond the critical buckling load.

3.2.3 Analysis results of LCF and CAF

Di Memmo [53, 54] has investigated the LCF and CAF analyses included with Abaqus 2017 applied fatigue crack growth of DCB and MMB specimens. The numerical solutions are verified by comparison to the benchmark solutions presented by Krueger [8, 49]. SC8R continuum shell elements were used to model the 3D versions of both the DCB and the MMB specimens. Element length Δa is 0.5 mm in the crack propagation zone and the specimen, with a thickness of 3 mm, is modelled with 2 elements through the thickness.

The DCB specimen analysis results are shown in figure 3.5. DCB specimens have a geometrically linear response, linear-elastic material response, an almost straight crack front orthogonal to the rectilinear mesh that propagates orthogonally to the mesh, and have negligible mode II and Mode III SERR components. Since none of the distinguishing conditions discussed in sections 3.2.1 and 3.2.2 are present, all three analyses give nearly identical results for the 3D model. The corresponding CPU times are shown in figure 3.7 where the CAF analysis (indicated with ”Constant Amplitude”) took approximately 60% as long as the LCF analysis (indicated with ”Direct Cyclic Fatigue”). As expected the SF analysis was the fastest of the three at approximately 10% of the LCF analysis.

The crack front during the SF analysis is shown in figure 3.6. Clearly visible is the straight crack front and the tendency for the crack front to straighten out immediately after some crack growth has occurred somewhere along the crack front. This does not agree with typical experimental results where the crack front tends to have some curvature with the crack front at the middle of the specimen somewhat ahead of the crack front at the outer edges.

All three Abaqus analysis methods rely on the same Paris relation shown in equation 3.2 which uses only the total SERR range with two fitting parameters. These fitting parameters vary with mode mixity ratio [55]. To analyse the MMB specimen Di Memmo has used three different sets of fitting parameters, corresponding to a G_{II}/G_{total} ratio of 20%, 50% and 80% in addition to the fitting parameter values used for the DCB specimen analyses. As a consequence the mode-mixity must be known a-priori and is assumed to be constant along the entire crack front and for the duration of the entire analysis.

Di Memmo has only used the Simplified Fatigue (SF) analysis to determine the delamination behaviour of the MMB specimen under three mode mixity ratios. The results are shown in figure 3.8. The numerical results seem to agree fairly well with the analytical model by Krueger used for verification although they do not seem to agree quite as well as the DCB results.

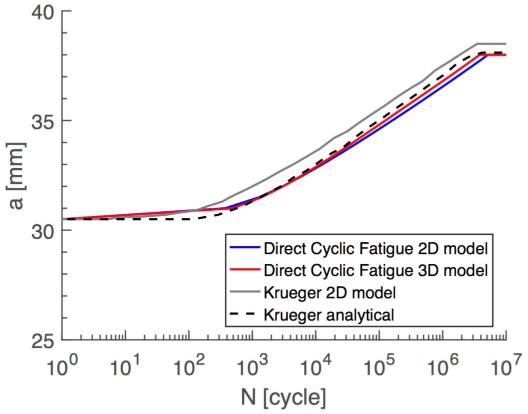

(a) *Crack length a versus fatigue cycles N for a DCB specimen analysed using the Low-Cycle Fatigue (LCF) analysis of Abaqus 2017 compared to the benchmark solution by Krueger [8].*

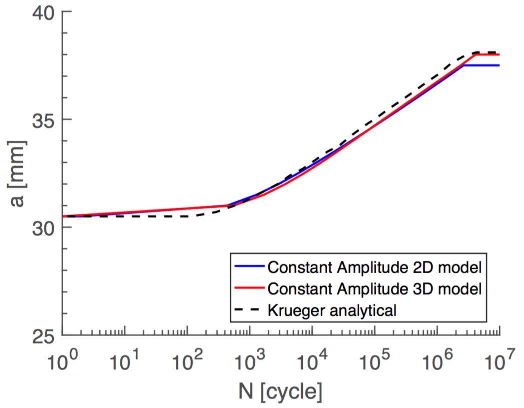

(b) *Crack length a versus fatigue cycles N for a DCB specimen analysed using the Constant Amplitude Fatigue (CAF) analysis of Abaqus 2017 compared to the benchmark solution by Krueger [8].*

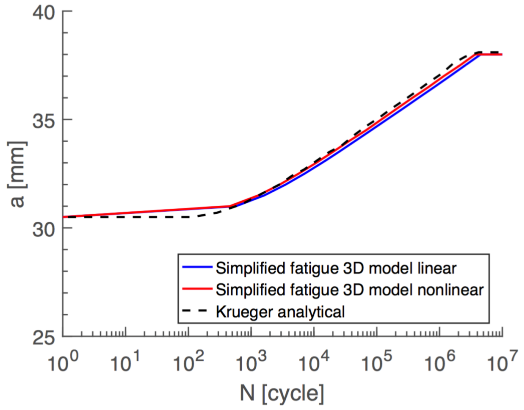

(c) *Crack length a versus fatigue cycles N for a DCB specimen analysed using the Simplified Fatigue (SF) analysis of Abaqus 2017 compared to the benchmark solution by Krueger [8].*

Figure 3.5: *Abaqus 2017 Analysis results for the DCB model using the LCF, CAF, and SF analyses. From [53].*

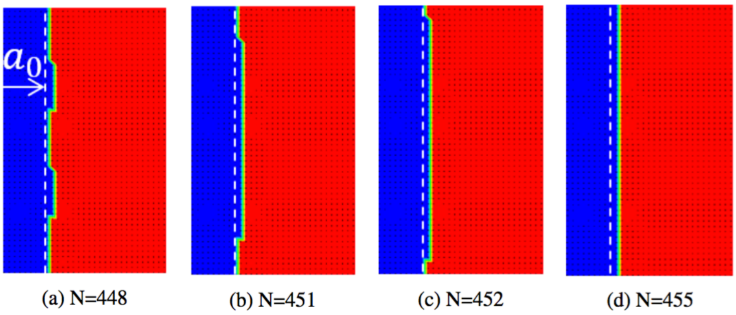

Figure 3.6: *DCB crack propagation during the SF analysis. From [53].*

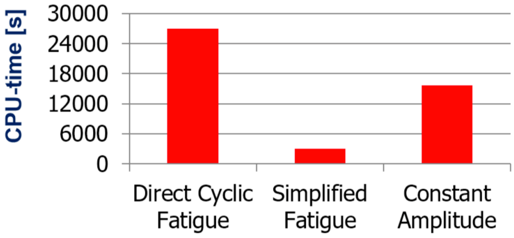

Figure 3.7: *3D DCB specimen analysis CPU time. From [53].*

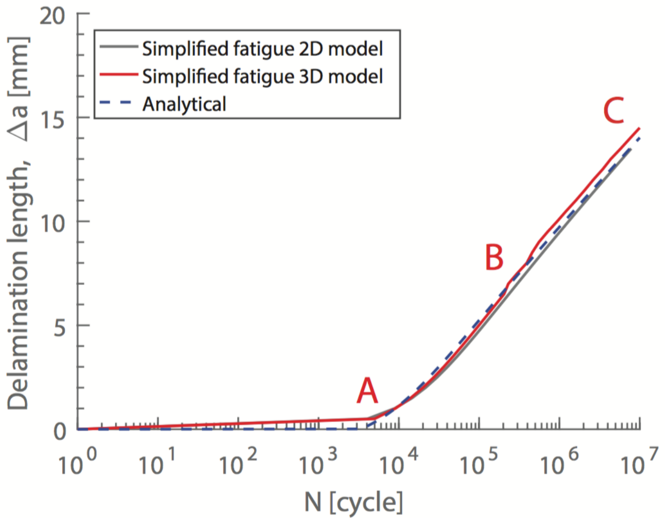

(a) *MMB Delamination propagation versus load cycles for 20% mode mixity.*

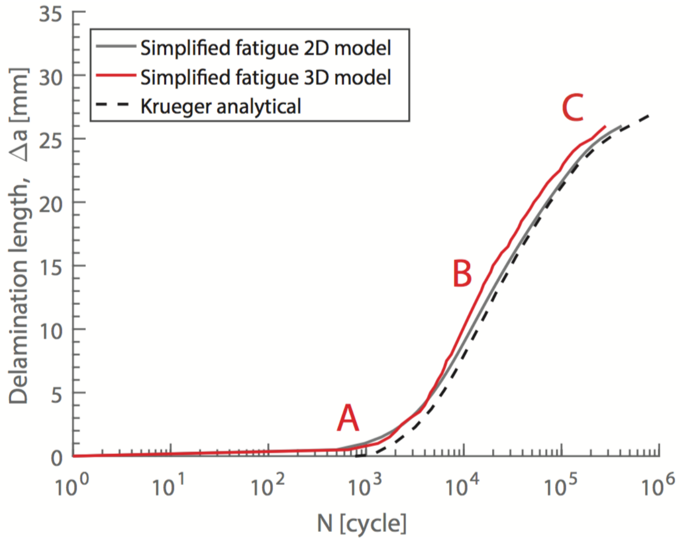

(b) *MMB Delamination propagation versus load cycles for 50% mode mixity.*

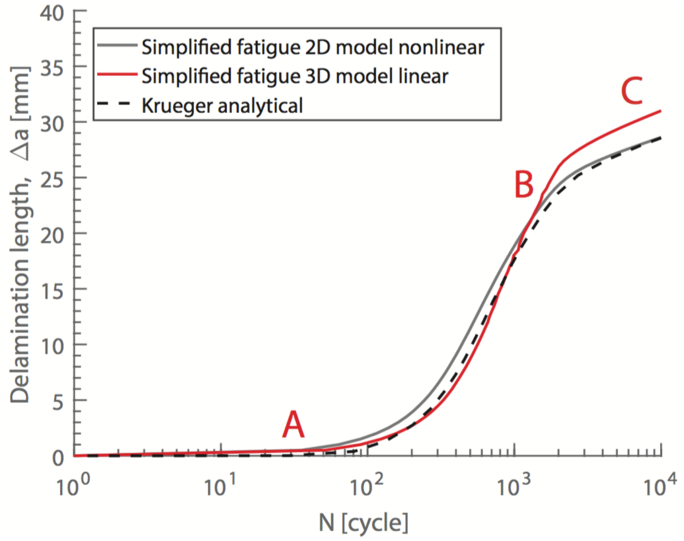

(c) *MMB Delamination propagation versus load cycles for 80% mode mixity.*

Figure 3.8: *Abaqus 2017 SF analysis results for the MMB specimen. From [53].*

Chapter 4

Single Stringer Compression Specimen

The Single Stringer Compression Specimen (SSCS) was developed by Bisagni, Vescovini, and Dávila [3] to be representative of the response of large multi stringer panels. In the building block approach the specimen fits between coupon specimen testing and the testing of large multi-stringer stiffened panels. The SSCS was designed to have a small size to ease handling, to have a relatively low manufacturing cost, and yet to have a structural complexity on the level of multi-stringer panels. The intent was to improve the ease and affordability with which the response of stiffened panels can be determined experimentally. This enables the study of their failure behaviour and damage tolerance in the post-buckling regime. In addition the SSCS provides the opportunity to verify and validate state of the art quasi-static and fatigue damage models due to its small size, making it computationally tractable, and its relatively complex geometry compared to coupon specimens.

The Single Stringer Compression Specimen developed by Bisagni et al is made of IM7/8552 carbon fibre reinforced epoxy and consists of a skin and a co-cured hat stiffener as shown in figure 4.1. Its geometry was determined by comparing the deformation and stress distribution of a quasi-static post-buckling analysis to the deformation and stress of a multi-stringer panel and choosing the width and length of the panel such that a good agreement was achieved. A stress contour plot comparing the two is shown in figure 4.2. Although the edge of the SSCS does not represent the behaviour of the multi-stringer panel exactly due to the free boundary condition compared to the symmetry boundary condition of the multi-stringer panel, excellent agreement is achieved at the foot of the hat stiffener. The membrane stresses that occur in thin panels subjected to transverse pressure loads, such as fuselage panels, are not represented by the SSCS due to the free edge boundary condition and the absence of transverse load application.

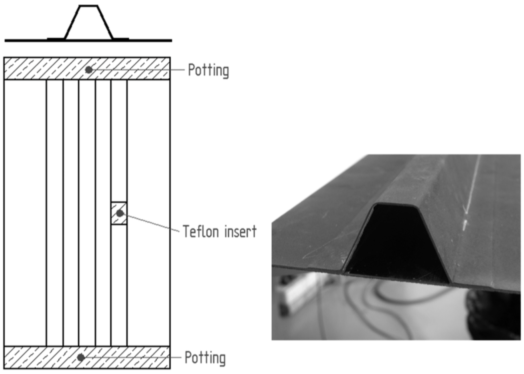

Figure 4.1: *Configuration of SSC specimen and close-up of hat stiffener. From [3].*

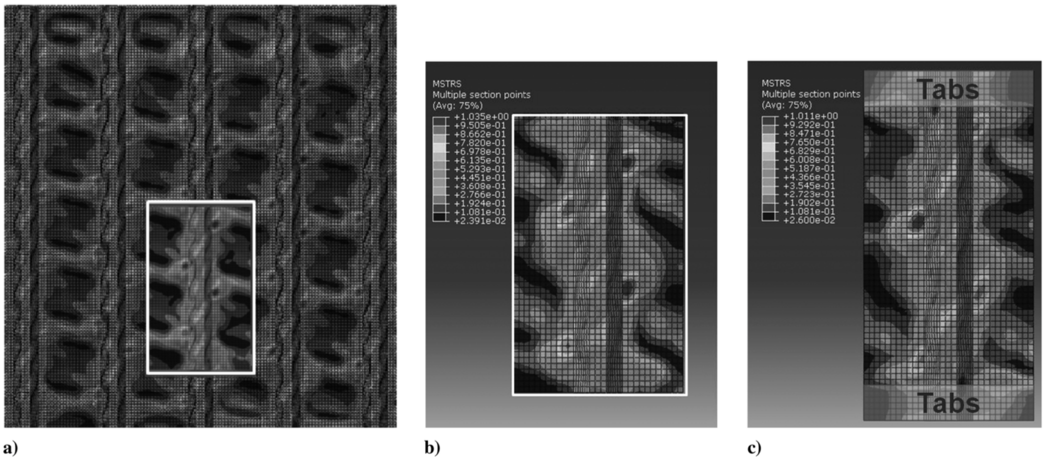

Figure 4.2: *Maximum stress contour plots for a) multi stringer panel; b) subunit of the multi stringer panel; c) SSC Specimen. From [3].*

In their study Bisagni et al investigate the quasi-static failure behaviour of SSC specimens with an initial delamination, both experimentally and numerically. Subsequent to this study, the specimen behaviour under fatigue loads was investigated numerically by Bisagni et al [56]. The LCF analysis, discussed in section 3.2.1, available in Abaqus/Standard was used to analyse DCB, MMB, and End Notch Flexure (ENF) specimens as well as the SSCS. The results for the DCB and MMB analyses agree well with the responses found by Di Memmo [53] discussed in section 3.2.3. The LCF analysis was unable to predict the fatigue delamination growth of the ENF specimen as it does not account for changing contact conditions during a load cycle.

The SSCS analysed by Bisagni et al was modelled using S4R shell elements and was assigned the material properties of IM7/8552 carbon epoxy composite. The layup of the skin was an 8 ply quasi-isotropic [45/90/-45/0]s stack and the stiffener was modelled with a 7 ply [-45/0/45/0/45/0/-45] stack. A 20 mm Teflon (polytetrafluoroethylene) film was inserted between the skin and one flange of the stiffener at the mid-length of the panel to serve as an initial delamination. The element size was 2.5 mm by 2.5 mm for a total of 9888 elements.

In the quasi-static failure analysis it was found that the Strain Energy Release Rate is not constant along the delamination front. In-plane shear components of the SERR (Mode II and III) were predominantly found towards the outside of the stiffener flange and the mode I component of the SERR was found to have a non-uniform distribution along the entire delamination front. Using the Low-Cycle Fatigue analysis for a cyclic fatigue load it was found that it does not determine the onset of buckling and the predicted response remained linear regardless of the load magnitude. The Constant Amplitude Fatigue and Simplified Fatigue analyses available in Abaqus 2017 and later were not yet available at the time of the study by Bisagni et al. Because of the changing mode mixity along the delamination front a single set of fitting parameters for the Paris relation implemented in Abaqus could not be determined.

The fatigue delamination growth behaviour of SSC specimens with Teflon inserts have been investigated experimentally by Dávila and Bisagni [57]. The SSC specimen geometry and layup were identical to their previous studies with the exception of the Teflon insert used to create a controlled pre-existing delamination. Where in the previous study they had used a 20 mm wide Teflon insert, in the latest studies they used a 40 mm wide insert still located between the skin and one flange of the stiffener at mid-length of the panel. This change has been made because no fatigue delamination growth was expected for specimens manufactured with a 20 mm insert. A fatigue load cycle with a peak load at 80% of the panel's quasi-static collapse load and a load ratio of R=0.1 was applied to the specimens with a frequency of 2 Hz. This corresponds to a peak load of 23 kN and a minimum load of 2.3 kN.

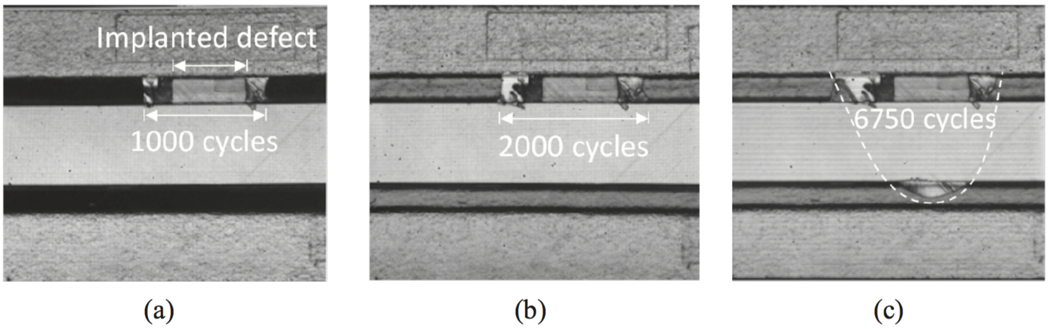

Figure 4.3: *Damage propagation measured by UT scan: a) 1000 cycles; b) 2000 cycles; c) 6750 cycles. Specimen F-40A. From [57].*

Three SSC specimens were tested, one was subjected to quasi-static compression until failure and two were subjected to the fatigue load described before. 3D Digital Image Correlation (DIC) was used to record the out of plane displacement of the specimen and an infra-red passive thermography camera was used to monitor the delamination front during testing. An in-situ UT scanner was used intermittently to determine the delamination progression. For the first fatigue specimen F-40A a delamination extension was observed from the 40 mm initial delamination to 68 mm in the first load cycle. In the subsequent 1000 cycles no delamination growth was observed. At 2000 cycles the delamination was observed to have propagated to a length of 72 mm. At 6750 cycles a delamination length of 88 mm was observed in the initially delaminated flange and a half moon delamination was observed in the in the other stiffener flange opposite the original delamination location. Complete skin-stringer delamination occurred at 6793 cycles. UT scans at 1000, 2000, and 6750 cycles for specimen F-40A are shown in figure 4.3. From the out of plane deformation shown in figure 4.4 it can be seen that the skin deformation is dominated by the delamination size. This is even more clear looking at figure 4.5 where the skin has buckled in three half waves before the initial defect has opened up. This reduces back to the single wave also visible in figure 4.4 after the initial delamination has opened. Also notable is that the half waves on the side opposite to the initial delamination reverse in sign after the initial delamination opens up. As a consequence the local fatigue load case at the interface between the skin and the stiffener flange at these half-waves switches from compression-compression fatigue to tension-tension fatigue and vice versa.

The second fatigue specimen, F-40B, was nominally identical to the other specimens and was tested under identical conditions and applied load. No delamination growth was observed until the 2002nd cycle, when the initial delamination suddenly opened up. The delamination had extended from its initial length of 40 mm to a length of 62 mm. At 11850 cycles the delamination had grown to 92 mm. At 24000 cycles the delamination length was 99 mm. At this point the peak load of the load cycle was increased to 85% of the quasi-static collapse load, or 24 kN. This was to speed up the delamination progression and final failure of the panel. At 25521 cycles the specimen failed suddenly through complete skin-stiffener separation. The progression of the delamination is shown in figure 4.6.

In figure 4.7 the dominant loading modes at the delamination front of the initial delamination are shown for all three tested specimens, both before and after the initial delamination opened up. Not only does the dominant loading mode change along the delamination front at any particular delamination length, it also changes during the delamination propagation. This change may occur suddenly and be quite substantial.

The very different loads and cycle counts at which the initial delaminations open are attributed by Dávila and Bisagni to minor imperfections in the skin. Because this appears to have a substantial influence on the propagation behaviour it may be prudent to include such imperfections in the analyses. This may either be done by incorporating the measured imperfections of manufactured specimens, such as those reported by Bisagni and Dávila [58], into the analyses or through a thermal analysis to

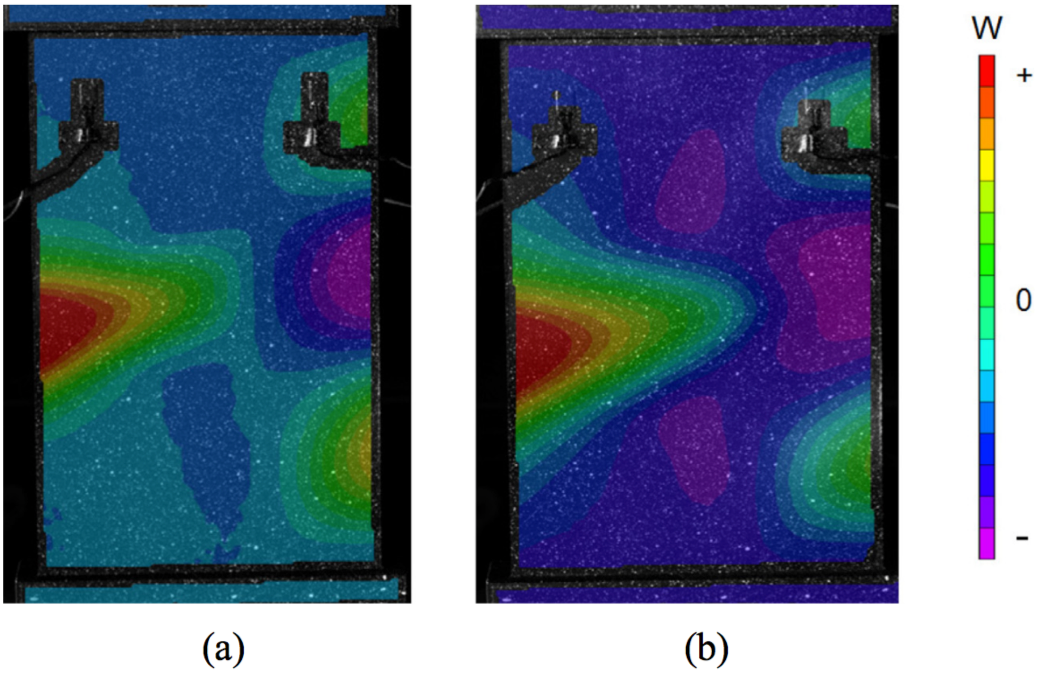

Figure 4.4: *Evolution of the out-of-plane deformation due to progression of skin-stiffener separation: a) at 1000 cycles; b) after 6500 cycles. Specimen F-40A. From [57].*

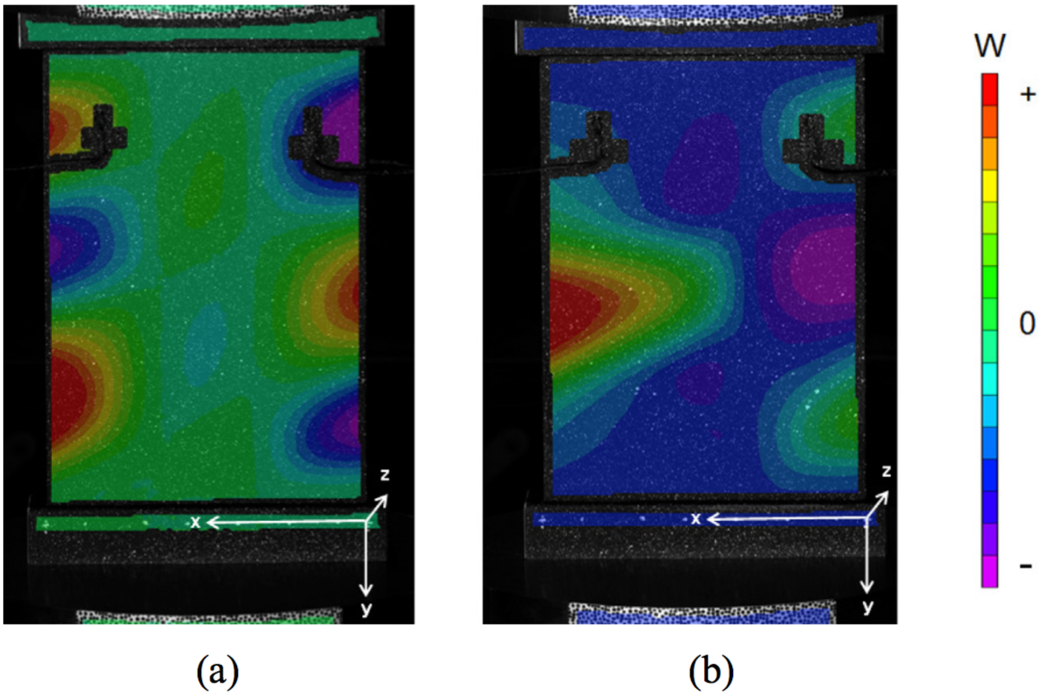

Figure 4.5: *Post-buckling mode before and after extension of the initial defect during second fatigue test: a) at 1000 cycles; b) after 2500 cycles. Specimen F-40B. From [57].*

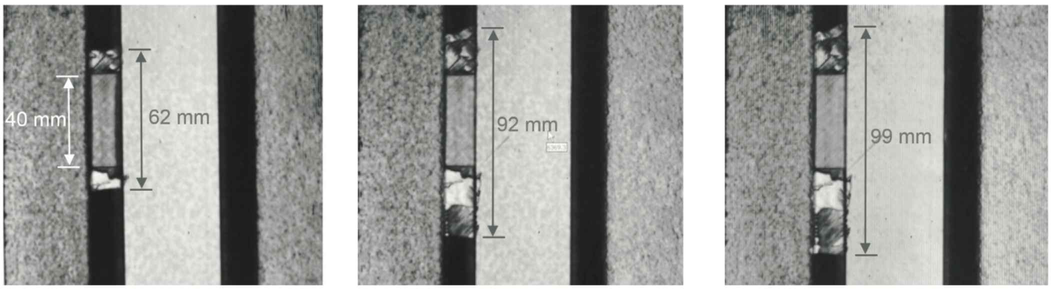

(a) (b) (c)

Figure 4.6: *Damage propagation measured by UT scan during the second fatigue test. Specimen F-40B. a) at 2002 cycles; b) at 11850 cycles; c) at 24000 cycles. From [57].*

account for residual thermal stresses combined with some sort of stochastic distribution in key model parameters.

Dávila and Bisagni [59] have also investigated the damage propagation of the SSCS subjected to indentation damage. Five SSC specimens were tested, one was loaded quasi-statically until collapse and four were subjected to a cyclic fatigue loading. The geometry of the SSC specimens was identical to the previous study with the exception that the Teflon insert was not included in the layup. All five specimens were indented from the skin side at the mid length of the panel. For two specimens, SSCS-1 and SSCS-5, the indentation was placed at the outside edge of one of the stiffener flanges. For the other three specimens the indentation was made at the centre of one of the stiffener flanges. A target indentation damage size of 40 mm was selected. The indenter was displaced by 1.65 mm after the first damage was detected to create the indentation damage. The resulting damage sizes were 45 mm, 32 mm, 56 mm, 37 mm, and 48 mm for SSCS-1 to 5 respectively. Specimen SSCS-3 was re-indented to achieve the final indentation size.

Based on the findings of the previous study the flatness of the specimens was measured after indentation using a DIC system and the indentations were measured in detail using a CMM. The amplitude of the measured out of plane deformations was approximately 0.4 mm or 40% of the skin thickness and was attributed mainly to residual thermal stresses. The residual indentation depth was measured to be approximately 0.1 mm. An example of the measured deformation is shown in figure 4.8 which shows the measurements taken of specimen SSCS-3.

For specimen SSCS-4 the UT image of the delamination is coloured based on the time of flight and shows the relative depth of the delaminations. The result is shown in figure 4.9 together with cross sections through the thickness. The large delamination exists at the interface between the skin and the stiffener, and one ply below in the stiffener flange. The smaller delamination exists at multiple depths in the skin. Looking at the damage growth of this specimen shown in figure 4.10 it can be seen that only the delamination between the skin and stiffener appears to grow. The delamination in the skin remains approximately the same over 78000 cycles. Specimen SSCS-4 collapsed suddenly at 78135 cycles. Infra-red thermographs indicated that in the failure sequence the delamination reached a critical size and subsequently both flanges of the stiffener de-bonded in an unstable fashion creating a ”tunnel” between the skin and the stiffener followed by stiffener crippling.

A considerable spread was observed in the cycle count at which the four fatigue specimens failed. Specimen 1 failed at 117506 cycles, specimen 3 at the initial cycle, specimen 4 at 33623 cycles and specimen 5 at 78135 cycles. This spread would make it challenging to use the experimental data as verification data for a numerical fatigue damage growth analysis of an SSC Specimen. Additionally the constant amplitude fatigue load amplitude was adjusted frequently to achieve a favourable delamination growth rate for specimens 1 and 4 which further increases the challenge for analysis. To analyse such a load case the loading spectrum must be taken in to account, likely as discrete chunks of constant amplitude loading applied in series. The importance of the imperfections and deformations determined in the previous study is further reinforced by the large spread of test results. Additionally

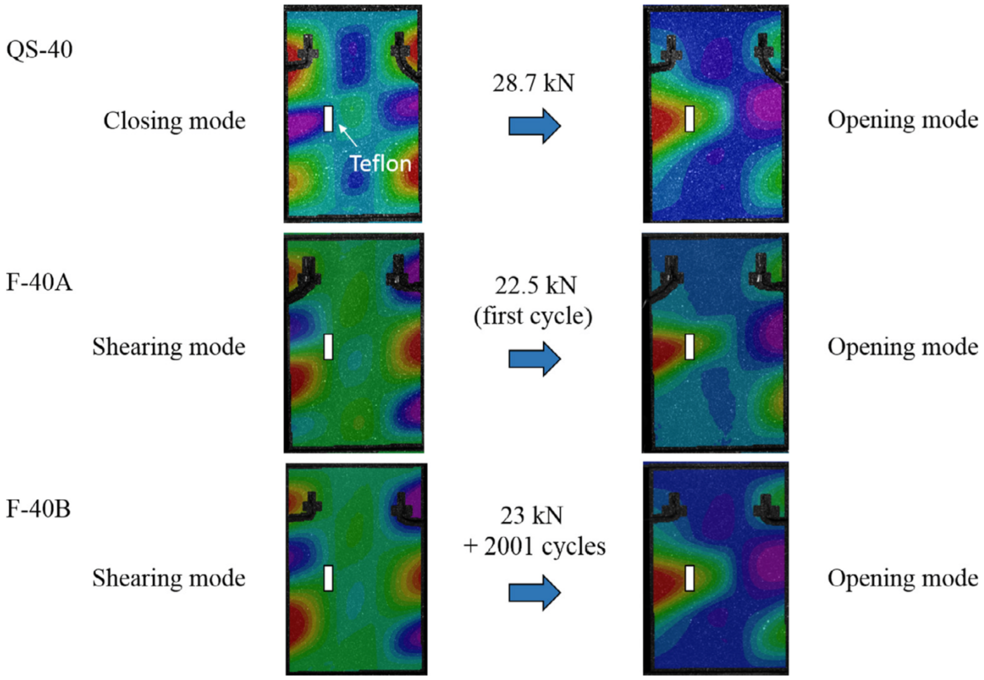

Figure 4.7: *Comparison of modes before and after opening for the three tested SSC specimens. From [57].*

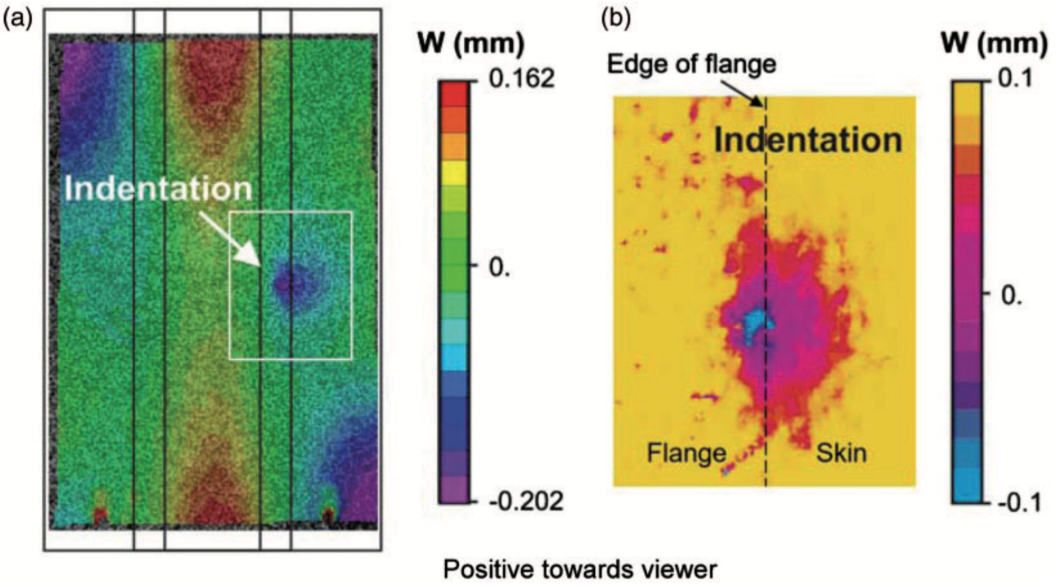

Figure 4.8: *Global and local out-of-plane deformation after indentation for specimen SSCS-3. a) Panel initial imperfection from VIC-3D and b) local indentation depth measured from CMM. From [59].*

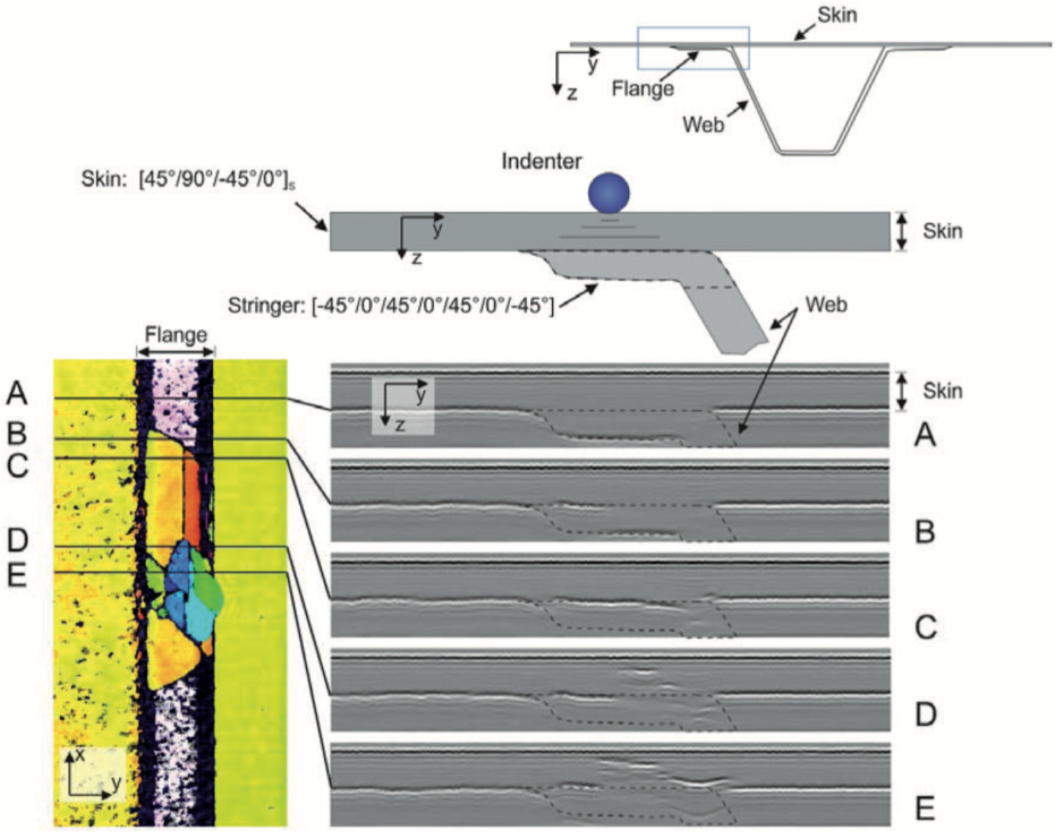

Figure 4.9: *UT images coloured using time-of-flight processing for depth location of delaminations in specimen SSCS-4. From [59].*

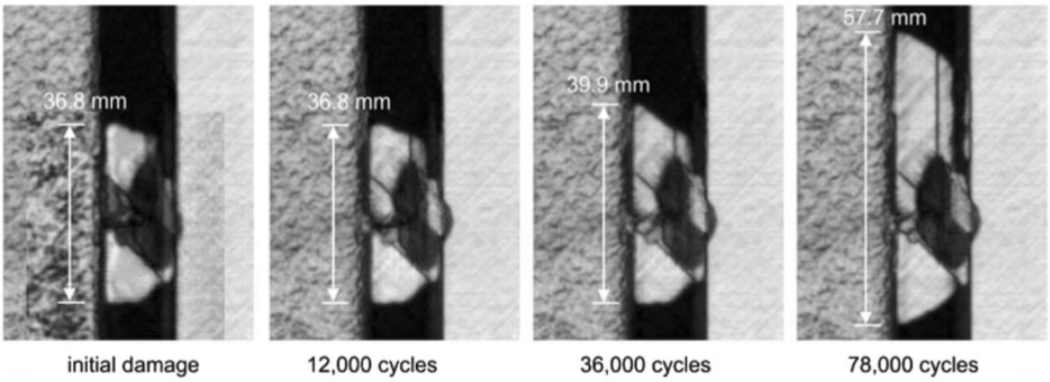

Figure 4.10: *UT images showing the damage propagation for specimen SSCS-4 at different life-cycle counts. From [59].*

the nature of the indentation damage appears to strongly affect the expected fatigue life considering that specimen 3, which was indented twice and which showed unstable delamination growth during the second indentation, failed upon the application of the first load cycle.

Part II

Double Cantilevered Beam (DCB) and Mixed Mode Bending (MMB) specimen analyses

Chapter 5

Model descriptions

To evaluate the efficacy of the Constant Amplitude Fatigue (CAF) and Simplified Fatigue (SF) methods specimen level models have been constructed. Two specimen types have been selected, the Double Cantilevered Beam (DCB) specimen and Mixed Mode Bending (MMB) specimen. The DCB specimen is an accepted standard to determine the mode one inter-laminar fracture toughness [4] and mode one fatigue crack growth onset [5] for uni-directional fibre composite materials. The specimen has also been used to characterise mode one fatigue crack propagation [60, 61] for unidirectional fibre composite materials. The Mixed Mode Bending (MMB) specimen is an accepted standard specimen to determine mixed mode one / mode two inter-laminar fracture toughness of unidirectional fibre composites [6]. The specimen has also been used to characterise mixed mode one/mode two fatigue crack propagation [55]. For both specimens numerical benchmark data are available for verification of the analysis results [7–10].

The modelling approach for the specimen models is verified through quasi-static delamination propagation analyses before the models are used to evaluate the CAF and SF methods. The efficacy of these fatigue methods is determined through comparison of the analysis results to established benchmark results.

The DCB models constructed for quasi-static and fatigue delamination propagation will be described first in section 5.1 followed by the MMB models in section 5.2. The analysis results will be shown and discussed in subsequent chapters.

5.1 DCB model

Double Cantilevered Beam (DCB) model specimen dimensions and material properties correspond to available verification data by Krueger [7, 8]. A schematic representation of a DCB specimen is shown in figure 5.1. Model dimensions for the quasi-static and fatigue delamination propagation models were the same except for the initial delamination length a_0 as shown in table 5.1. The layup of all the modelled specimens was $[0]_{24}$ where the initial delamination was located in the centre of this layup. The material properties used were for T300/1076 as shown in table 5.2.

For the present study the specimen was modelled using S4R conventional shell and SC8R continuum shell elements. For the S4R elements the two beams were modelled as a reference plane located at the bottom of the upper beam and the top of the lower beam. For the SC8R elements the beams were modelled as three dimensional geometry. Two element lengths were used for the delamination propagation zone: 1.25 and 0.5 mm. 25 elements were used across the width of the specimen for all meshes. The coarse mesh was a uniformly equidistant mesh of 25x120 elements as shown in figure 5.2. The mesh density of the fine mesh quasi-static delamination propagation model was reduced outside of the delamination propagation zone resulting in a 25x120 element mesh for the first 60 mm of the specimen and a 25x90 element mesh for the latter 90 mm as shown in figure 5.3. No mesh density reduction was used for the fine mesh fatigue delamination propagation model. An equidistant mesh with 25x300 elements was used as shown in figure 5.4. Only one element was used

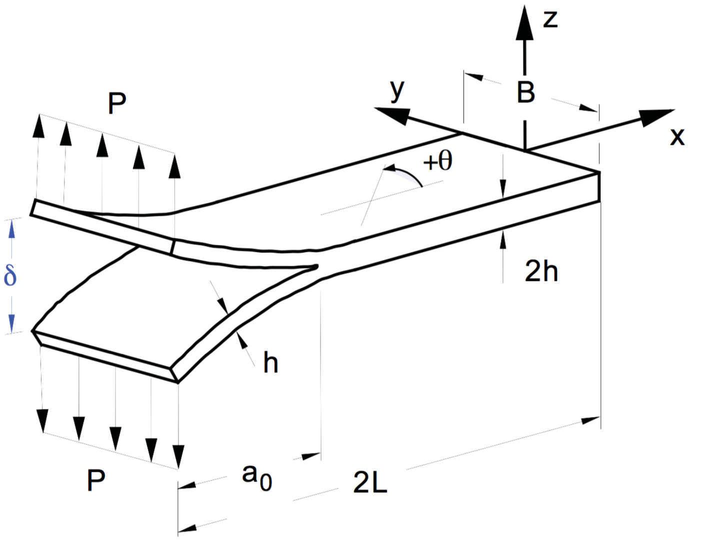

Figure 5.1: *Double Cantilevered Beam (DCB) specimen geometry. From [8, Fig. 1].*

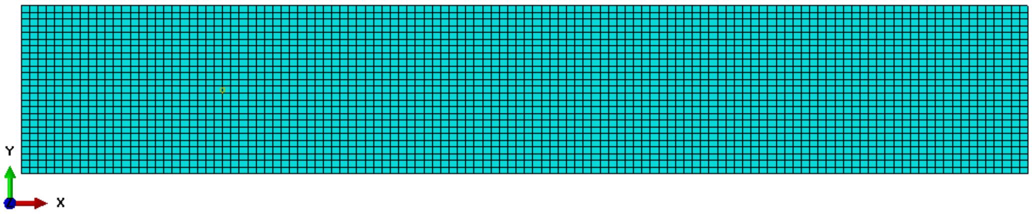

Figure 5.2: *Equidistant 25x120 element mesh. Element length 1.3 mm.*

through the thickness of each beam in all cases. The meshes were matched for the upper and lower beams such that the nodes used for the VCCT coincided. Since the VCCT implementation uses a surface to surface contact interaction it is not strictly necessary for the nodes to coincide, although better mesh convergence may be expected if they do.

A 'Debond using VCCT' type crack was specified between the two beams with a ramp debonding force for the quasi-static delamination propagation and a step debonding force for the fatigue analyses. The ramp debonding force was adopted for improved solution convergence. In literature DCB specimens have shown a slightly curved delamination front with a large radius [9, 56]. The ramp debonding force is better able to capture this delamination front rounding than a step debonding force as an added benefit. Ramp debonding is not currently supported for fatigue analyses and a step debonding force is the only available option. This is expected to cause delamination front straightening because sharp corners in the debonded delamination front created by releasing a node tend to attract load and fail shortly after the initial node failure that advanced the delamination front. This will continue until the nodes all the way out to the edge of the specimen have failed. The improved solution convergence of the ramp release would not be expected to benefit the fatigue propagation analysis since no quasi-static delamination growth occurs; the nodes are failed at the minimum displacement defined in the fatigue cycle and the load is redistributed over the new delamination front nodes before the displacement is increased in the subsequent fatigue cycle.

A surface to surface contact interaction was defined where the bottom surface of the upper beam served as the master surface and the top surface of the lower beam served as the slave surface. A small sliding formulation is adopted as the finite sliding surface to surface contact formulation is not supported for VCCT. No slave adjustment was used to prevent initial over or under closure since the

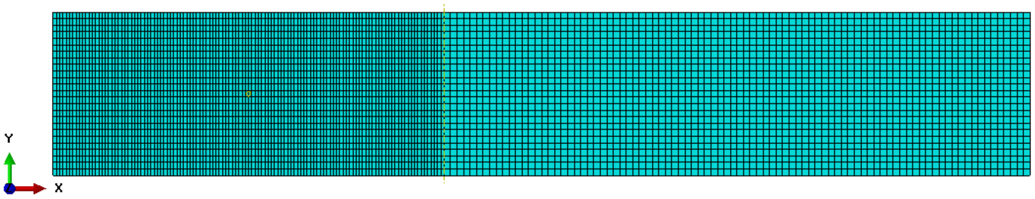

Figure 5.3: *Fine DCB mesh for quasi-static delamination propagation models. Equidistant 25x120 element mesh for the 60 mm of the specimen length with an equidistant 25x90 element mesh for the remaining 90 mm. Element length 0.5 mm in the propagation zone.*

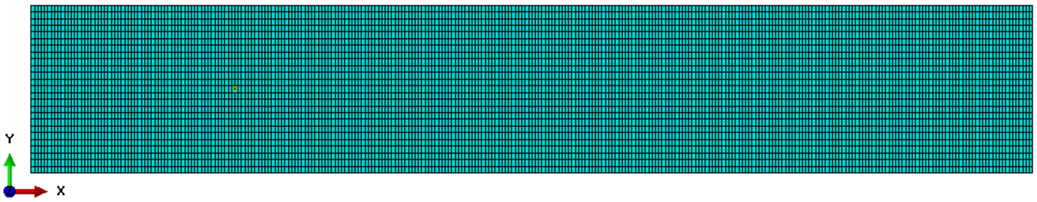

Figure 5.4: *Fine DCB mesh for fatigue delamination propagation models. Equidistant 25x300 element mesh. Element length 0.5 mm.*

specimen is modelled with flat surfaces which are assembled such that no under or overclosure exists. An initial clearance of $1.0 \cdot 10^{-8}$ mm is specified to prevent numerical round-off issues. A node set is specified on the top surface of the lower beam and the bonding of the slave nodes is limited to this subset. Automatic contact stabilisation was specified through standard contact controls with a value of $1.0 \cdot 10^{-6}$.

The pristine end of the specimen was encasted as shown in figure 5.5. On the delaminated end of the specimen two displacement boundary conditions were applied; one on the upper beam moving upwards and one on the lower beam moving downwards. All other displacements at the loaded end of the specimen were left unconstrained.

5.1.1 DCB quasi-static delamination propagation

For the quasi-static delamination propagation models a *VCCT* type fracture criterion contact property was specified with a Benzeggagh-Kenane mixed mode behaviour. The Benzeggagh-Kenane [62][51, ”Crack propagation analysis”] mixed mode critical Strain Energy Release Rate relation is given as follows

$$G_c = G_{Ic} + (G_{IIc} - G_{Ic}) \left(\frac{G_{II} + G_{III}}{G_I + G_{II} + G_{III}} \right)^{\eta} \tag{5.1}$$

where G_c is the calculated mixed mode critical strain energy release rate, G_{Ic} is the mode I critical strain energy release rate, G_{IIc} is the mode II critical strain energy release rate, G_I through G_{III} are

Table 5.1: *DCB model dimensions.*

Parameter	Value	Notes
B [mm]	25.0	
2L [mm]	150.0	
2h [mm]	3.0	
a_0 [mm]	30.0	Quasi-static propagation
a_0 [mm]	30.5	Fatigue propagation

Table 5.2: *T300/1076 material properties from [7, Table 1].*

Parameter	Value
E_{11} [GPa]	139.4
E_{22} [GPa]	10.16
E_{33} [GPa]	10.16
ν_{12} [-]	0.30
ν_{13} [-]	0.30
ν_{23} [-]	0.436
G_{12} [GPa]	4.6
G_{13} [GPa]	4.6
G_{23} [GPa]	3.54

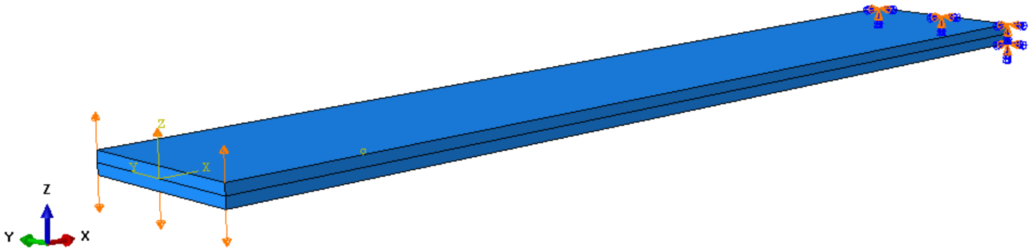

Figure 5.5: *View of an SC8R DCB model. Displacement boundary conditions have been applied to the loaded end of the specimen and the opposite end has been encasted.*

the SERRs calculated by the numerical analysis and η is a fitting parameter. All SERR parameters are in $[kJ/m^2]$, η is non-dimensional.

The VCCT tolerance was varied between 0.1 and 0.001 for the quasi-static delamination growth analyses. This tolerance governs how close the maximum computed strain energy release rate at any node must be to the specified critical strain energy release rate for an increment to have converged during quasi-static delamination propagation. The critical strain energy release rates and the Benzeggagh-Kenane exponent used are for T300/914C and were taken from [7, Table 1]. These properties were chosen for congruence with the available verification data from the same publication.

The analysis was split into a pre-load step where the specimen was displaced close to the onset of delamination growth in only a few increments and a delamination propagation step . A static general analysis was used for both the pre-load step and the quasi-static delamination propagation step.

For the quasi-static delamination propagation step the initial and maximum increment were 0.005 with a minimum increment of $1.0 \cdot 10^{-20}$. In the general solution controls the time incrementation parameter I_A was increased to 35 to increase the number of iterations allowed per increment. If this parameter is not increased the time increment cut-back settings do not allow the minimum increment size to be reached. Instead the analysis will error out with a message that the maximum number of iterations has been reached before the minimum increment size is reached.

Table 5.3: *T300/914C Critical Strain Energy Release Rates for mode 1 and mode 2, as well as the Benzeggagh-Kenane fracture criterion exponent from [7, Table 1].*

Parameter	Value
G_{Ic} $[\frac{kJ}{m^2}]$	0.1703
G_{IIc} $[\frac{kJ}{m^2}]$	0.4936
η [-]	1.62

Table 5.4: *T300/1076 fatigue delamination propagation parameters for pure mode one opening. From [8].*

Parameter	Value
c1	$2.8461 \cdot 10^{-9}$
c2	-12.415
c3	$2.44 \cdot 10^{6}$
c4	10.61
r1	0.353
r2	0.9

5.1.2 DCB fatigue delamination propagation

For the fatigue delamination propagation models a *Fatigue* type fracture criterion contact property was specified with a Benzeggagh-Kenane mixed mode behaviour. The mixed mode behaviour relation is used to determine the lower and upper thresholds for fatigue delamination propagation but is not used for the fatigue growth onset or propagation.

The analysis is split into a pre-load step where the specimen was displaced to the minimum displacement of the fatigue cycle in only a few increments and a cyclic load step where the delamination propagated. For the latter step either a Constant Amplitude Fatigue (CAF) step or a Simplified Fatigue (SF) step is used. The initial delamination length a_0 is 30.5 mm in the benchmark used for verification. For the coarse mesh model with an element length of 1.25 mm the closest available delamination length is 30.0 mm which is used for the analysis. The fine mesh model with an element length of 0.5 mm has an initial delamination length of 30.5 mm.

The fatigue parameters for T300/1076 which are used can be found in table 5.4. Here c1 and c2 are delamination growth onset parameters used in the delamination growth onset relation shown in equation 5.2 and c3 and c4 are fitting parameters for the ΔG based Paris relation shown in equation 5.3. For more information see section 3.2. r1 and r2 determine the lower and upper fatigue growth thresholds as $r1 = \frac{G_{thresh}}{G_c}$ and $r2 = \frac{G_{pl}}{G_c}$ respectively. The critical SERR G_c is determined using the Benzeggagh-Kenane mode mixity relation with the parameter values specified in table 5.3. If the calculated SERR is below G_{thresh} no delamination growth is assumed to occur. If the calculated SERR is above G_{pl} quasi-static delamination growth is assumed to occur and the fatigue delamination growth analysis is terminated.

$$f = \frac{N}{c_1 \Delta G^{c_2}} \geq 1.0 \quad \wedge \quad G_{max} > G_{thresh} \tag{5.2}$$

$$\frac{da}{dN} = c_3 \Delta G^{c_4} \tag{5.3}$$

For the CAF step a triangular load cycle was defined starting at the minimum applied displacement at step time 0, rising linearly to the maximum applied displacement at step time 0.5 and decreasing linearly back to the minimum applied displacement at step time 1. For more information on the Constant Amplitude Fatigue method see section 3.2.2. Three timepoints are defined, at step time 0, 0.5, and 1, to make sure that the minimum and maximum SERRs are captured. The applied displacements can be found in table 5.5. Due to the geometric linearity, the applied displacement ratio of 0.1 results in a load ratio R of 0.1 as well. The frequency specified is not used directly in the analysis, but all fracture toughness properties have originally been derived from testing conducted at this frequency.

For the SF step a constant displacement, shown in equation 5.4, is applied to the structure instead of a cyclic load. For equation 5.4 α is the load ratio R such that: $\alpha = R = P_{min}/P_{max}$. The constant displacement may be modified with the load ratio because of the geometric linearity. In the general case where the geometrical response is not linear this does not hold as the applied displacement no longer linearly relates to the applied load. For more information on the Simplified Fatigue method see section 3.2.2. In this case a pre-load step is used to load the specimen from zero displacement to the constant displacement used for the fatigue delamination growth.

Table 5.5: *DCB fatigue loading. From [8].*

Parameter	Value
$\frac{\delta_{max}}{2}$ [mm]	0.67
$\frac{\delta_{min}}{2}$ [mm]	0.067
R [-]	0.1
f [Hz]	10

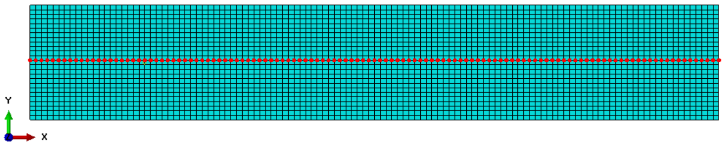

Figure 5.6: *Node set along the centre line of the specimen used to extract the crack length from the numerical model.*

Two Abaqus input files have been included as examples in appendix A. The input file for DCB_CAF_18 is provided in section A.I. The input file for DCB_SF_12 is provided in section A.II.

$$\delta = \delta_{max}\sqrt{(1-\alpha^2)} \tag{5.4}$$

For all DCB fatigue models the delamination length is extracted from the model by requesting a field output of BDSTAT using a line of nodes on the centreline of the fracture surface along the length of the specimen as shown in figure 5.6. This produces a two dimensional array of binary values indicating for every node if it is connected or if it has been released at every frame of output data. The data is post processed using Python 3.7 to count the number of bonded nodes at every frame which, together with the mesh pitch, gives the instantaneous delamination length. Combining this with cycle count known for every frame allows the delamination length to be plotted against the number of fatigue cycles. This approach will lead to stair stepping in the delamination growth curves since any delamination propagation that happens near the edges of the specimen will write an output for the nodes on the centreline without any apparent change to the delamination length. Any post processing to smooth out these curves is avoided as this would only serve to improve their appearance without improving their accuracy.

5.1.3 Corrected Beam Theory model

The quasi-static delamination growth DCB models will be verified against the Corrected Beam Theory (CBT) model. The CBT model by Williams [63] is an analytical fracture mechanics model that has been developed for a number of standard test specimens. The modelled specimens include the Double Cantilevered Beam specimen with pure mode I loading, the End Loaded Split specimen with pure mode II loading, and the Asymmetric End Loaded Split specimen with mixed mode I/II loading. Only the DCB specimen model is of interest for this research. This CBT DCB model has been adopted for the ASTM standard [4] to determine mode I interlaminar fracture toughness through experimental testing of DCB specimens.

For the Corrected Beam Theory model of the Double Cantilevered Beam specimen a regular beam theory model is combined with a correction factor for transverse shear deformation and root elasticity. The compliance of a DCB specimen C is adjusted by the adding the correction factor χh to the delamination length a as

$$C = \frac{\delta}{P} = \frac{8\,(a+\chi h)^3}{BE_{11}h^3} \tag{5.5}$$

here C is the specimen compliance in [mm/N], δ is the specimen displacement in [mm], P is the applied load in [N], a is the delamination length in [mm], h is the beam thickness in [mm], B is the beam width in [mm], and E_{11} is the Longitudinal modulus of the specimen material in [MPa].

The mode I Strain Energy Release Rate (SERR) is adjusted the same way and is given as

$$G_I = \frac{12P^2(a+\chi h)^2}{B^2 E_{11} h^3} \tag{5.6}$$

where G_I is the mode one SERR in $[kJ/mm^2]$, P is the applied load in [N], a is the delamination length in [mm], h is the beam thickness in [mm], B is the beam width in [mm], and E_{11} is the longitudinal modulus of the specimen material in [MPa].

The correction factor χ is given as

$$\chi = \sqrt{\left(\frac{E_{11}}{11G_{12}}\right)\left\{3-2\left(\frac{\Gamma}{1+\Gamma}\right)^2\right\}} \tag{5.7}$$

where E_{11} is the longitudinal modulus of the specimen material in [MPa], G_{12} is the shear modulus of the specimen material in [MPa], and Γ is given as

$$\Gamma = 1.18\sqrt{\frac{E_{11}E_{22}}{G_{12}}} \tag{5.8}$$

and E_{22} is the lateral modulus of the specimen material in [MPa].

To find the load displacement curves of a DCB specimen the critical mode I SERR G_{Ic} is substituted into equation 5.6 and the equation is rewritten to

$$P = \sqrt{\frac{G_{Ic}B^2E_{11}h^3}{12(a+\chi h)^2}} \tag{5.9}$$

and equation 5.5 is rewritten to

$$\delta = \frac{8P(a+\chi h)^3}{Bh^3E_{11}} \tag{5.10}$$

5.2 MMB model

The Mixed Mode Bending (MMB) models were constructed similar to the DCB models. MMB model specimen dimensions were chosen to correspond to available verification data by Krueger [9, 10]. A schematic representation of an MMB specimen is shown in figure 5.7. The model dimensions, shown in table 5.6, were the same for quasi-static and fatigue delamination propagation.

The mode mixity applied at the delamination front of the MMB specimen is varied by changing the lever length c. Three lever lengths are specified for a $\frac{mode\ II}{mode\ I+mode\ II}$ mode mixity of 20%, 50%, and 80% in table 5.6. Because the only changes made to the model to switch between these different mode mixities are the change in lever length and the magnitude of the applied displacement, it has been decided to verify one mode mixity value through quasi-static delamination propagation to verify the modelling approach. Only the 20% mode mixity model was used for quasi-static delamination propagation. All three mode mixities were used for the fatigue delamination propagation.

The layup of all the modelled specimens was $[0]_{24}$ where the initial delamination was located at the centre of this layup. Material properties for IM7/8552 were used and can be found in table 5.7.

The same coarse mesh was used as for the DCB models for both the quasi-static and the fatigue delamination propagation models. The fine mesh used for the fatigue delamination was also identical to the fine mesh used for the DCB fatigue models. However, the fine mesh for the quasi-static delamination growth differs as shown in figure 5.8. The mesh density was reduced just as for the quasi-static DCB model, but the fine mesh was extended so that it continued until just beyond the sliding support of the lower test fixture. The first two thirds of the specimen length were meshed with an equidistant 25x200 element mesh and the remaining third was meshed with an equidistant mesh

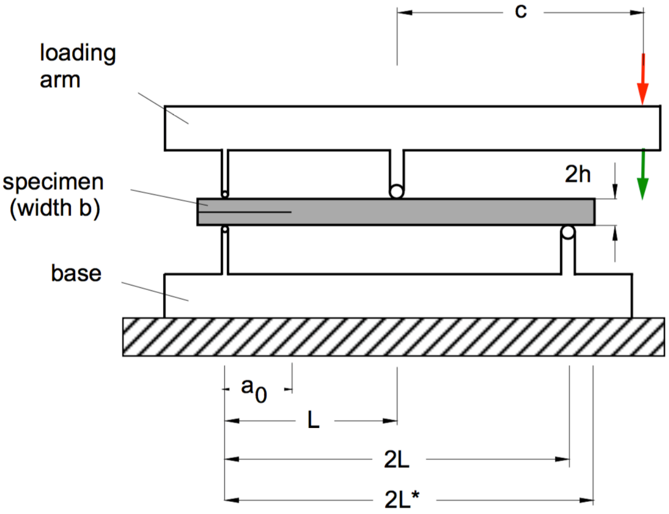

Figure 5.7: *Mixed Mode Bending (MMB) specimen geometry. From [10, Fig. 1].*

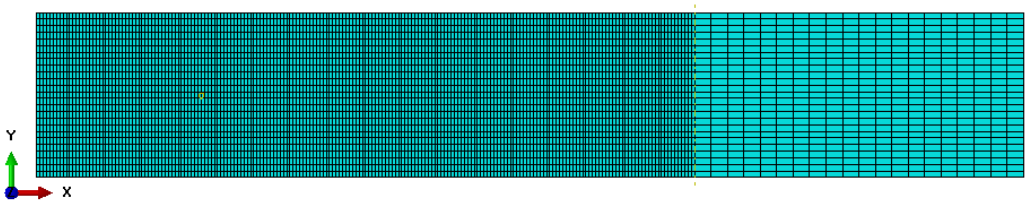

Figure 5.8: *Fine DCB mesh for quasi-static delamination propagation models. Equidistant 25x120 mesh for the 60 mm of the specimen length with an equidistant 25x90 mesh for the remaining 90 mm. Element length 0.5 mm in the propagation zone.*

of 25x20 elements. With the MMB specimen dimensions this resulted in an element length in the delamination propagation zone of 1.27 mm and 0.508 mm for the coarse and fine mesh respectively.

Both the bottom and the top fixture were modelled using R3D4 discrete rigid elements. An SC8R MMB model including the fixtures is shown in figure 5.9. The number of elements across the width of the fixtures was 25 to match the MMB specimen mesh. Only one element was used along the length of any feature of the fixtures. The bottom fixture was encasted and a tie constraint was used to pin the loaded edge of the specimen to the fixture. A hard contact frictionless surface to surface contact interaction was defined for the other side of the fixture to bear on the bottom side of the lower beam of the specimen. The bottom surface of the lower beam was defined as the master surface and the edge of the fixture was defined as the slave surface. The bottom surface of the lower beam was included in a geometrical surface definition and the sliding edge of the fixture was included in a geometrical set. A finite sliding formulation was adopted. Similarly the top fixture was pinned to the loaded edge of the specimen and the surface-to-surface contact interaction between the sliding edge of the fixture and the top surface of the upper beam was defined.

5.2.1 MMB quasi-static delamination propagation

For the quasi-static delamination propagation MMB model the critical strain energy release rates and the Benzeggagh-Kenane exponent used are for IM7/8552, shown in table 5.8, and were taken from [9, Table II]. These properties were chosen to match the available verification data from the same

Table 5.6: *MMB model dimensions.*

Parameter	Value
B [mm]	25.4
2L [mm]	100.8
2L* [mm]	152.4
2h [mm]	4.5
a [mm]	25.4
$c_{0.2}$[mm]	92.9
$c_{0.5}$ [mm]	41.3
$c_{0.8}$ [mm]	27.3

Table 5.7: *IM7/8552 material properties from [9, Table 1].*

Parameter	Value
E_{11} [GPa]	161
E_{22} [GPa]	11.38
E_{33} [GPa]	11.38
ν_{12} [-]	0.32
ν_{13} [-]	0.32
ν_{23} [-]	0.45
G_{12} [GPa]	5.2
G_{13} [GPa]	5.2
G_{23} [GPa]	3.9

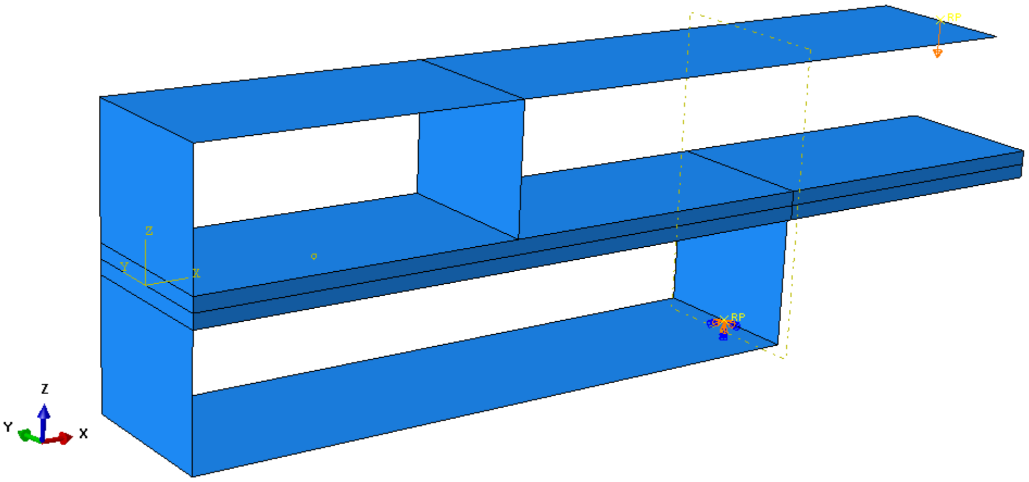

Figure 5.9: *View of an SC8R MMB model. Displacement boundary conditions have been applied to the loaded end of the top fixture and the bottom fixture has been encasted.*

Table 5.8: *IM7/8552 Critical Strain Energy Release Rates for mode 1 and mode 2, as well as the Benzeggagh-Kenane fracture criterion exponent from [9, Table 1].*

Parameter	Value
G_{Ic} [$\frac{kJ}{m^2}$]	0.212
G_{IIc} [$\frac{kJ}{m^2}$]	0.774
η [-]	2.1

Table 5.9: *IM7/8552 fatigue delamination propagation parameters for three mode mixity ratios. From [10, Table II].*

Parameter	20% mode II	50% mode II	80% mode II
c1	$1.8 \cdot 10^{-6}$	$9.0 \cdot 10^{-5}$	$5.6 \cdot 10^{-3}$
c2	-11.1	-9.71	-8.0
c3	2412	6.79	4.5788
c4	8.4	5.4	5.1
r1	0.264	0.186	0.11
r2	0.9	0.9	0.9

publication.

5.2.2 MMB fatigue delamination propagation

For the fatigue delamination propagation MMB models IM7/8552 fatigue parameters were used, as shown in table 5.9. The parameters vary with mode mixity and three separate sets have been specified for the three mode mixity values used. To determine the lower and upper fatigue delamination growth thresholds the critical SERR values from table 5.8 were used. The minimum and maximum displacements used to load the models were chosen to correspond to the displacements used for the verification benchmark. The maximum displacements were originally calculated to produce a fatigue load at the delamination front of 60% of G_c in this benchmark. Due to the change in lever length between the mode mixities and due to the change in G_c with mode mixity three distinct values shown in table 5.10 were used. The minimum displacements were determined by taking 10% of the corresponding maximum for a load ratio R of 0.1.

Table 5.10: *MMB fatigue displacements corresponding to a load of where the SERR reaches 60% of G_c. From [10, Table I].*

Parameter	20% mode II	50% mode II	80 % mode II
δ_{max} [mm]	1.27	1.04	1.28
δ_{min} [mm]	0.127	0.104	0.128
R [-]	0.1	0.1	0.1

Chapter 6

Quasi-static delamination propagation results

The results for the quasi-static delamination propagation of the DCB and MMB models are presented and discussed in this chapter. DCB results are discussed first in section 6.1 followed by the results for the MMB models 6.2.

6.1 DCB results

Several Double Cantilevered Beam (DCB) specimen models have been constructed and analysed with two main aims. Firstly, to compare the use of two element types and secondly to verify the modelling approach for the subsequent fatigue analyses. The specimen has been modelled using both S4R conventional shell elements as well as with SC8R continuum shell elements for comparison. Both element type models have been meshed at two mesh densities, using either 1.3 mm elements or 0.5 mm elements in the delamination propagation zone. The model construction is discussed in detail in section 5.1. For the SC8R element models, at both mesh densities, the influence of the release tolerance used for the Virtual Crack Closure Technique (VCCT) is evaluated.

The load displacement behaviour of the analysed Double Cantilevered Beam (DCB) models are presented along with the results of the DCB benchmark by Krueger [7] and the Corrected Beam Theory model by Williams [63] used in the ASTM standard [4] for mode one interlaminar fracture toughness and shown in section 5.1.3.

In the test standard the mode one critical strain energy release rate is computed by fitting the corrected beam theory model with a least squares fit to test data obtained from DCB specimens. It can be argued that the correlation of any numerical model based on the mode I strain energy release rate to DCB test data is at best equal to the correlation of the corrected beam theory model to that same test data due to the least squares fit. The best any numerical model could do in this case would be to replicate exactly the corrected beam theory model. As such, how well the numerical results presented here correspond to the corrected beam theory model is a direct measure of how close they are to the best correlation to experimental data that may be achieved.

The load displacement behaviour of S4R and SC8R DCB models are shown in figures 6.1 and 6.2 respectively for an element length of 0.5 mm and 1.3 mm. Both models show a linear response until the delamination begins to propagate at the peak reaction force. This is as expected although the stiffness of the specimen is slightly overestimated in all cases. Compared to the Corrected Beam Theory model error in the reaction force of the S4R model is at worst 4.3% at the 0.5 mm element size and 5.3 % at the 1.3 mm element size. The error of the SC8R model is at most 2.0% at the 0.5 mm element size and 3.6% at the 1.3 mm element size. Both element types show improved agreement of the stiffness to the corrected beam theory model with a reduction in element size, indicating that the mesh isn't fully converged yet. As such, it is expected that a minor improvement of a few percentage

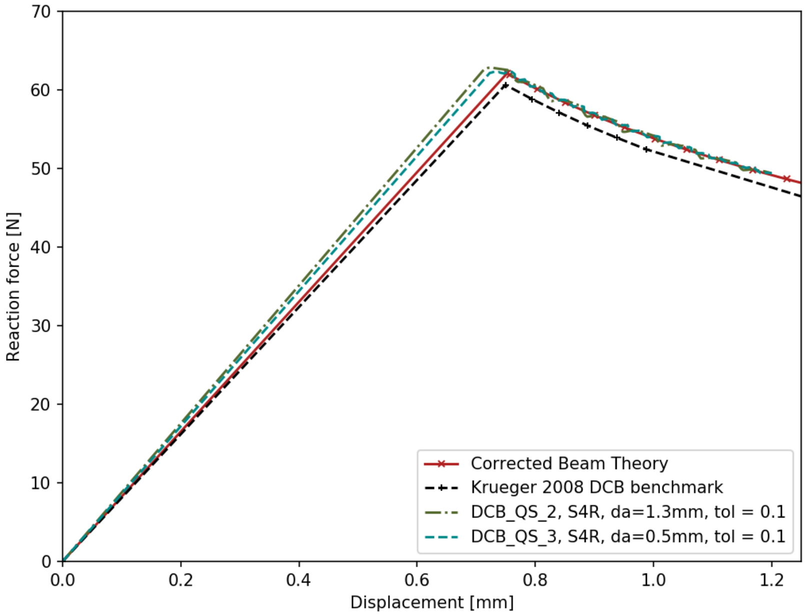

Figure 6.1: *Load against displacement for quasi-static delamination growth of a DCB model with S4R elements at an element length of 1.3 mm and 0.5 mm.*

points may still be achieved with further element size reduction.

The 0.5 mm SC8R and S4R results are compared directly to each other in figure 6.3 with a detailed view provided in figure 6.3b. The stiffness of the SC8R model corresponds slightly better to the corrected beam model than the S4R model at the same element size with around half the relative error. In the detailed view slight oscillation about the corrected beam theory model results during delamination propagation can still be seen for both element types where the SC8R model shows higher amplitude oscillations. These oscillations are a product of the ramp release specified for the VCCT, the ramp release appears not to perfectly match the model stiffness when the delamination front is progressing from one boundary of an element to the opposite boundary. That being said, the overall trend matches very well and errors are within a few percentage points which is good enough for practical application.

Because both the numerical results and the corrected beam theory results were generated for this thesis and many parameters were carried across from one to another they are compared to the benchmark results captured from literature to ensure that no systematic errors are present. At the peak load of the benchmark results the CBT load is 1.9% higher. This is close enough to rule out any major mistakes. The remaining differences may be caused by the different element type used for the benchmark, C3D8I solid elements, or by the differences in meshing. The benchmark model uses a very coarse mesh for most of the specimens with strong refinement for a 5 mm section around the delamination front where 20 elements are located. The outer two millimeters on either longitudinal side of the specimen have also been strongly refined. There is also some uncertainty associated with the data capture, as the load displacement data was acquired by re-digitising a published figure.

For the VCCT a tolerance must be specified that controls the convergence limit on the actual peak SERR at the crack front relative to the critical SERR. The default value of this tolerance is 0.3. The load displacement behaviour of the SC8R and S4R models with three tolerance values, 0.1, 0.01, and 0.001 are shown in figures 6.4a and 6.5a respectively with detailed views shown in figures 6.4b and 6.5b. From these figures only a tiny improvement is observed between a tolerance of 0.1 and 0.01 for both element types. No difference can be distinguished between a tolerance of 0.01 and

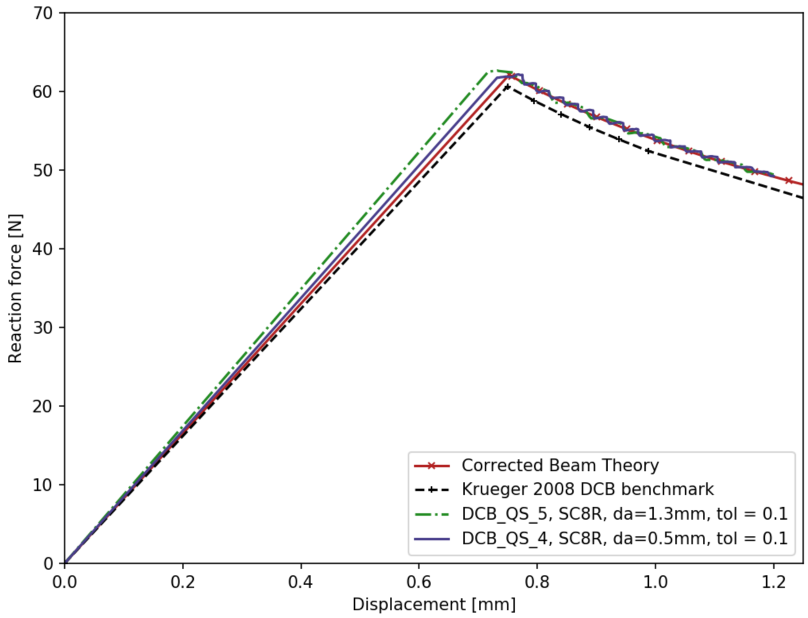

Figure 6.2: *Load against displacement for quasi-static delamination growth of a DCB model with SC8R elements at an element length of 1.3 mm and 0.5 mm.*

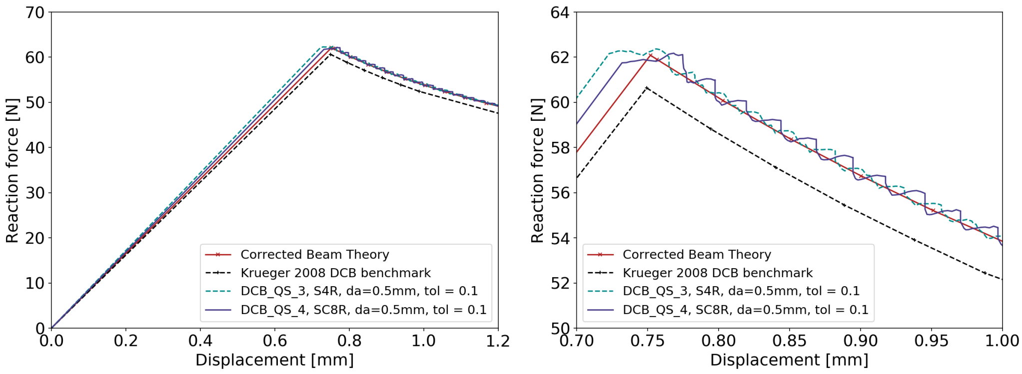

(a) *Full view.*

(b) *Detailed view.*

Figure 6.3: *Load against displacement for quasi-static delamination growth of a DCB model with S4R elements and SC8R elements at an element length of 0.5 mm.*

0.001. Consequently, a tolerance around 0.1 is enough for practical use. There is little to be gained by refining the tolerance to 0.01, and nothing to be gained with further refinement.

The delamination fronts at the end of the quasi-static delamination propagation step are shown for both the SC8R and S4R models with an element length of 0.5 mm in figure 6.6a and 6.6b. Both have a slightly rounded crack front with a large radius, as is expected from literature [9, 56], indicating that the ramp release captures the crack front behaviour encountered in experimental DCB specimen testing.

The computational time required for the presented analyses are shown in table 6.1. All jobs were executed on 10 Intel Xeon E5-2640 v4 CPU cores each. For the S4R models decreasing the

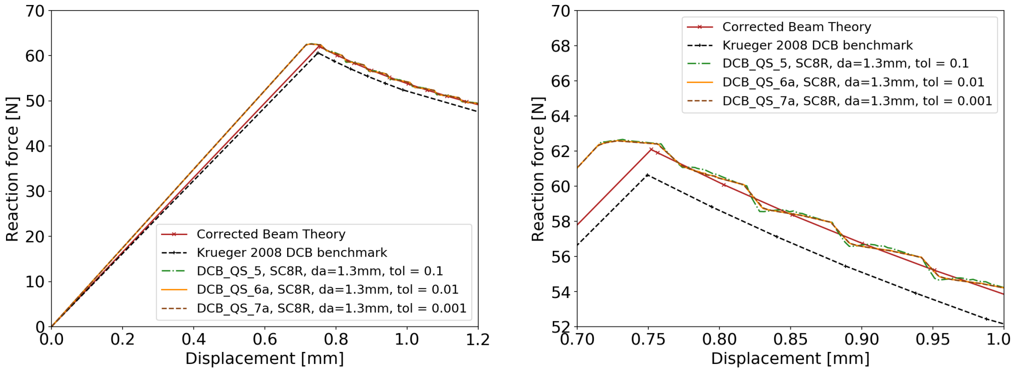

(a) *Full view.* **(b)** *Detailed view.*

Figure 6.4: *Load against displacement for quasi-static delamination growth of a DCB model with SC8R elements with a length of 1.3 mm and a VCCT tolerance of 0.1, 0.01, and 0.001.*

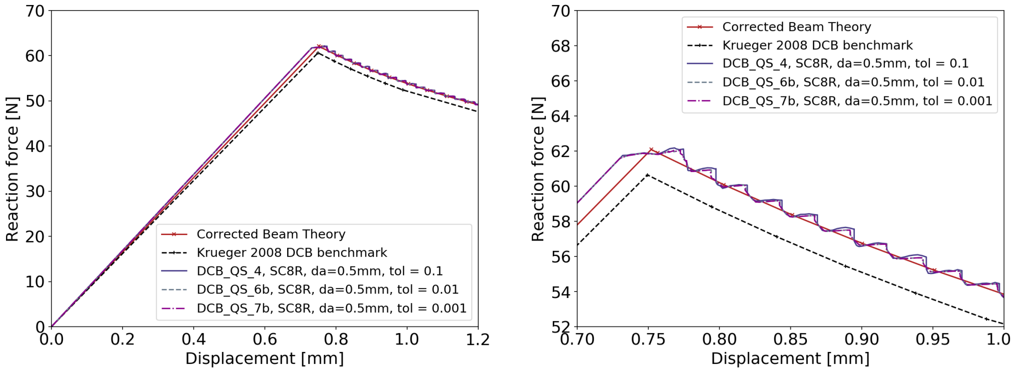

(a) *Full view.* **(b)** *Detailed view.*

Figure 6.5: *Load against displacement for quasi-static delamination growth of a DCB model with SC8R elements with a length of 0.5 mm and a VCCT tolerance of 0.1, 0.01, and 0.001.*

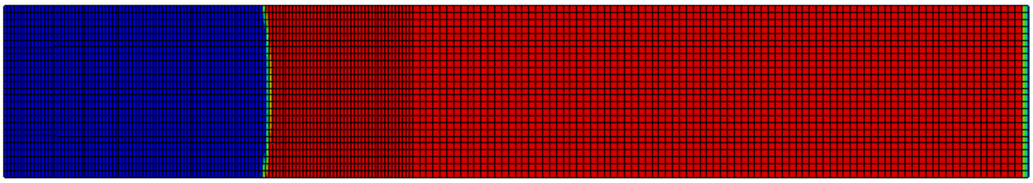

(a) *Delamination front of DCB_QS_3 at the end of the analysis. S4R elements*

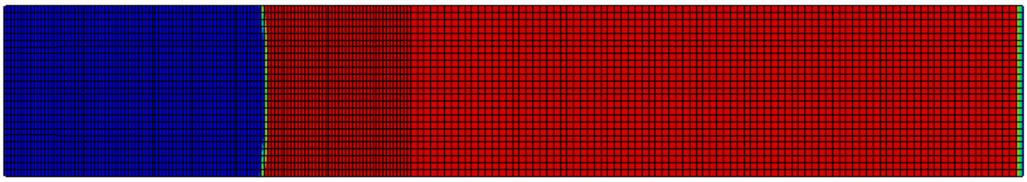

(b) *Delamination front of DCB_QS_4 at the end of the analysis. SC8R elements.*

Figure 6.6: *Delamination front of two DCB specimens at the end of the analysis. The element length is 0.5 mm. Blue (left) nodes are debonded, red (right) nodes are bonded.*

Table 6.1: *CPU time and wall time for the DCB analyses. Jobs executed on 10 cores each.*

Analysis	CPU time [hh:mm:ss]	Wall time [hh:mm:ss]	Details
DCB_QS_2	01:08:20	00:11:07	S4R, da=1.3 mm, tol = 0.1
DCB_QS_3	04:48:43	00:50:51	S4R, da=0.5 mm, tol = 0.1
DCB_QS_5	00:39:06	00:08:10	SC8R, da=1.3 mm, tol = 0.1
DCB_QS_4	05:13:55	01:01:38	SC8R, da=0.5 mm, tol = 0.1
DCB_QS_6	11:11:32	02:05:46	SC8R, da=0.5 mm and 1.3 mm, tol = 0.01. Aggregate time for both jobs.
DCB_QS_7	33:21:00	07:06:35	SC8R, da=0.5 mm and 1.3 mm, tol = 0.001. Aggregate time for both jobs.

element length from 1.3 mm to 0.5 mm in the crack growth zone increased the CPU time by 423% where the same decrease in element length led to an 803% increase in CPU time for the SC8R model. Comparing the CPU time across element types, the SC8R model needed 57% of the CPU time of the S4R model for the coarse mesh and 109% of the CPU time of the S4R model for the fine mesh. Jobs *DCB_QS_*6 and *DCB_QS_*7 contained both mesh sizes of the SC8R model and only an aggregate time is available. Comparing them to the aggregate of *DCB_QS_*4 and *DCB_QS_*5 shows that decreasing the tolerance by an order of magnitude resulted in 190 % of the CPU time being required. Using a tolerance value of 0.001 required 568% of the CPU time necessary for a tolerance of 0.1 and 298% of the CPU time necessary for a tolerance of 0.01.

Combined with the results presented before it is clear that a minor or negligible improvement in the results comes at a substantial cost in CPU time for reductions in the tolerance for pure mode I loading of DCB specimens. As such, refinement of the tolerance below 0.1 is not recommended. Which element type model was more computationally efficient depended on the mesh size, where the SC8R model outperformed the S4R model by a factor 1.7 using the 1.3 mm mesh and the SC8R model was 9% slower than the S4R model with the 0.5 mm mesh.

6.2 MMB results

Several Mixed Mode Bending specimen models have been constructed and analysed, both to compare the two used element types and to verify the modelling approach for the subsequent fatigue analyses. Just as for the DCB specimen models, the MMB specimen has been modelled using both S4R conventional shell elements and SC8R continuum shell elements. Both element type models have been meshed at two mesh densities, using either 1.3 mm elements or 0.5 mm elements in the delamination propagation zone. The model construction is discussed in detail in section 5.2. At both mesh densities, the influence of the release tolerance used for the Virtual Crack Closure Technique (VCCT) is evaluated.

Changing between the three mode mixity values of the MMB model used in the fatigue analyses involves changing only the length of the load application lever and the magnitude of the applied displacement. Since no substantial changes are made to the MMB models for different mode mixity values only the results for 20% mode II mode mixity are presented here.

The load versus displacement for the SC8R and S4R element models are shown in figures 6.7 and 6.8 respectively. A linear response is again observed until delamination propagation occurs. The MMB model stiffness agrees very well with the benchmark results in all cases. A small improvement is observed when the element length is reduced from 1.3 mm to 0.5 mm for both the SC8R and the S4R element types. The difference in load of the SC8R model reduces from 2.4% at 1.3 mm element size to essentially zero before the delamination propagates. The difference in load for the S4R model reduces from 2.6% at 1.3 mm element size to 1.9% at 0.5 mm element size.

From the detailed view it can be observed that during the quasi-static delamination propagation the SC8R model shows minor oscillations as the delamination front grows from one edge of a row of

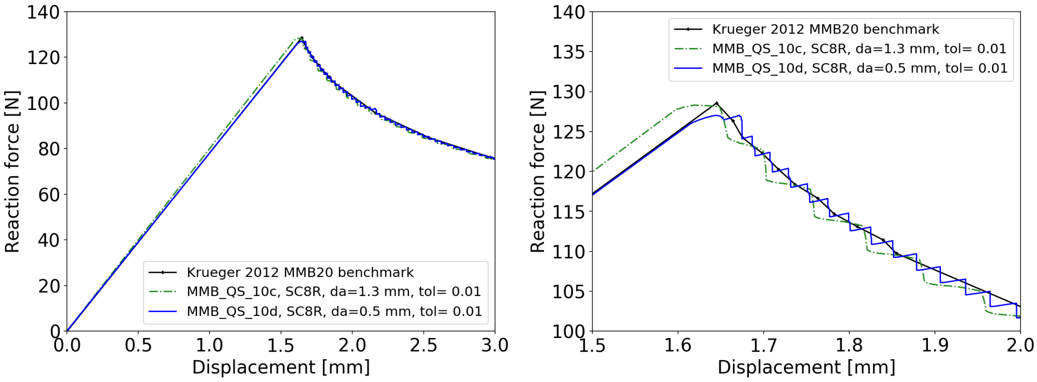

(a) *Full view.* **(b)** *Detailed view.*

Figure 6.7: *Load against displacement for quasi-static delamination growth of a 20% mode II MMB model with SC8R elements with a length of 1.3 mm and 0.5 mm and a VCCT tolerance of 0.01.*

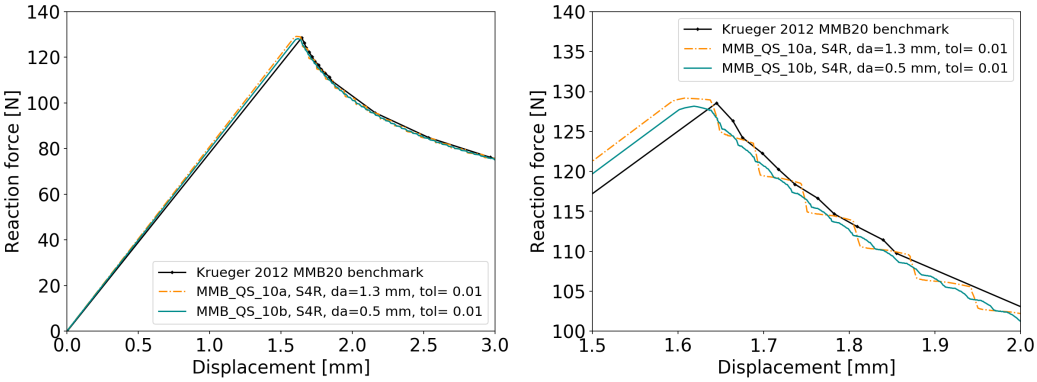

(a) *Full view.* **(b)** *Detailed view.*

Figure 6.8: *Load against displacement for quasi-static delamination growth of a 20% mode II MMB model with S4R elements with a length of 1.3 mm and 0.5 mm and a VCCT tolerance of 0.01.*

elements to the other edge. For the S4R model this oscillation is nearly indistinguishable. Despite the oscillations, the SC8R model follows the trend of the benchmark data very well where the S4R model appears to under predict the specimen stiffness during delamination propagation. The ramp release specified for all these analyses serves to reduce these oscillations, but it does not appear to perfectly match the response of a specimen with infinitesimally small elements. Overall the accuracy of the results for either element type is more than satisfactory for use in evaluating the CAF and SF methods as discussed in chapter 7.

The results for the SC8R element MMB model with a 0.5mm element length at a VCCT tolerance of 0.1 and 0.01 are shown in figure 6.9. Similar to the DCB results the difference in model response with smaller VCCT tolerances are negligible. Varying the tolerance for the S4R element model and for the other mesh sizes led to similarly tiny or indistinguishable results. For this reason these results are not presented here.

The computational time required for the presented analyses are shown in table 6.2. All jobs were computed using 10 Intel Xeon E5-2640 v4 CPU cores each. Just as for the DCB analyses, a major improvement in CPU time is associated with the SC8R model compared to the S4R model for the coarse mesh, although the computational time required for the fine mesh was about the same. The SC8R model required 47% of the CPU time that the S4R model did for the coarse mesh and 93% for the fine mesh. The penalty associated with reducing the tolerance from 0.1 to 0.01 is not as severe as

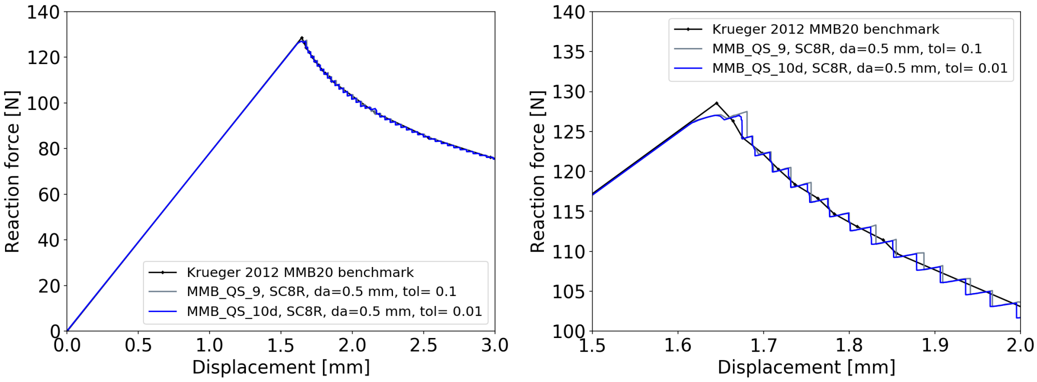

(a) *Full view.* **(b)** *Detailed view.*

Figure 6.9: *Load against displacement for quasi-static delamination growth of a 20% mode II MMB model with SC8R elements with a length of 0.5 mm and a VCCT tolerance of 0.1 and 0.01.*

Table 6.2: *CPU time and walltime for the presented MMB analyses. Jobs executed on 10 cores each.*

Analysis	CPU time [hh:mm:ss]	Wall time [hh:mm:ss]	Details
MMB_QS_11	05:07:14	00:57:04	S4R, da=1.3 mm, tol = 0.1
MMB_QS_12	18:04:17	03:01:42	S4R, da=0.5 mm, tol = 0.1
MMB_QS_8	02:24:04	00:26:43	SC8R, da=1.3 mm, tol = 0.1
MMB_QS_9	16:43:27	03:01:44	SC8R, da=0.5 mm, tol = 0.1
MMB_QS_10	88:54:46	14:58:47	Aggregate time for the 4 analyses specified above at tol = 0.01

for the DCB models as analysis *MMB_QS_*10 required 210% of the CPU time of the aggregate of analyses 8, 9, 11, and 12. Only the aggregate computational time is available for *MMB_QS_*10 as all four models with a tolerance of 0.01 were submitted as a single job.

It is expected that a tolerance around 0.1 will give excellent results for the SSCS models presented in subsequent chapters. It is not recommended to reduce the tolerance any further.

Overall the quasi-static delamination growth model of the simple DCB and MMB specimens produced excellent results. When compared to a CBT model for the DCB models and benchmark results for the MMB models errors were between 1 and 5.3% in all cases. The constructed models will serve as an solid foundation for the investigations of the fatigue delamination growth methods.

Chapter 7

Fatigue delamination propagation results

The results for the fatigue delamination propagation of the DCB and MMB models using both the Constant Amplitude Fatigue (CAF) and the Simplified Fatigue (SF) are presented and discussed in turn. DCB results are discussed first in section 7.1 followed by the results for the MMB models in section 7.2.

7.1 DCB results

The Double Cantilevered Beam (DCB) specimen models verified through quasi-static delamination growth analyses in chapter 6 have been used to investigate two fatigue delamination propagation methods: the Constant Amplitude Fatigue (CAF) method and the Simplified Fatigue (SF) method. The two fatigue methods have been evaluated at two mesh densities, using element lengths of 1.3 mm and 0.5 mm, and at three tolerance values used for the fatigue methods. Only the SC8R element models have been used as they outperformed the S4R element models in the required computational time for the quasi-static analyses.

In the CAF routine a load cycle is applied to the specimen, the number of cycles required to fail the weakest node on the delamination front is calculated, the weakest node is released and the cycle count and accumulated damage for the other delamination front nodes are updated. The damage extrapolation tolerance governs how close any other nodes on the delamination front must be to being released for them to be released together with the weakest node. A less stringent tolerance serves to speed up the analyis, since more nodes can be released for a single applied load cycle calculation and hence fewer load cycle calculations are required during the analysis.

The delamination length at the centre of the specimen is shown against the fatigue cycle count for the CAF method with an element length of 1.3 mm in figure 7.1 for three different damage extrapolation tolerances. The initial delamination of the analysed specimen was 30.0 mm. This was the nearest available initial delamination length for the 1.3 mm element length mesh compared to the initial delamination length of 30.5 mm used for the benchmark results. This affects the accuracy of the results for low cycle counts, but due to the logarithmic axis for the cycle count the effect of this quickly reduces. The delamination length increased gradually from 30.0 mm to 38.7 mm over the course of $1 \cdot 10^7$ fatigue cycles. Overall the results agree well at all three tolerance values and the predicted delamination length falls within a 2% margin of the benchmark results over the entire length.

One of three approaches may be adopted to post-process the analysis results to produce the delamination length against fatigue cycle count plots such as figure 7.1. The first is to measure the delamination length along only the specimen centre line directly, as is done here. When multiple nodes are released, and the node along the centreline of the specimen is among them, a diagonal can be observed in the figure. The stairstepping visible for the first two instances of delamination growth is an artefact of the delamination length measurement. The length is measured only along the centreline of the specimen and any nodes that are released elsewhere along the delamination front write an output value with no apparent change in the middle of the specimen.

Because the delamination length is measured only at a single point along the front there may also be some offset compared to the benchmark results, which have been calculated using straight delamination fronts at an interval of 0.1 mm. This offset may be caused because the delamination length at the measured point may be leading or lagging behind the overall delamination front depending on whether it is the first or the last node to be released for a particular delamination length increment. Since the measure may be leading or lagging, an uncertainty of at most 2 element lengths exists between the presented delamination length and the overall delamination length along the entire delamination front due to this.

Another approach would be use the compliance of the model as a measure for the delamination length. A corrected beam theory model may then be used to estimate an averaged delamination length. Although this would avoid the stairstepping and lead/lag discussed before, it is also a less direct measure. While this approach would give more aesthetically pleasing results, it may hide certain numerical issues such as the retreating delamination front visible in figure 7.9b discussed later. It also introduces uncertainty by estimating the delamination length using an analytical corrected beam theory model. Finally, this approach may give a false sense of certainty by abstracting the behaviour of the numerically prediction delamination front to an averaged delamination length.

A third approach would be to compute the delamination length by measuring the delamination length along the entire delamination front, and computing the average. Making the assumption that the relation between the numerically predicted delamination front and the model compliance as well as the relation between the model compliance and the delamination length estimated by the corrected beam theory model may be linearised for small delamination length increments, the increment in the estimated delamination length depends linearly on the percentage of the nodes that have been released along the delamination front for any particular increment in the overall delamination front. In other words, if half of the nodes along the delamination front are released, the estimated delamination length would be halfway to what it would be when all the nodes along a particular delamination front have released. With this assumption the complication of the corrected beam theory model may as well be neglected and the estimated delamination length may by found directly by averaging the delamination length along the entire delamination front.

All three of these approaches would be valid, each with their own up- and downsides, and none of them change anything about the actual delamination front predicted by the numerical model. Additionally, the differences between all three approaches reduce with mesh refinement. It was chosen here to use the first approach because it is the most direct measure and avoids hiding numerical issues. The stairstepping and lead/lag uncertainty are accepted as a trade-off. To verify that the fatigue methods are working as expected it is enough to know that the delamination length they predict is within one or two element lengths of the benchmark case.

In figure 7.1 the cut-off at the end of the analysis occurs at a higher delamination length than for the bechmark results. The analyses were conducted under displacement control with a constant peak displacement to match the benchmark results and to avoid quasi-static delamination propagation. Because of the displacement control the SERR at the delamination front reduces with increasing delamination length, slowing the delamination growth rate. At a certain point the SERR drops below the lower growth threshold and the delamination stops propagating. The cut-off occurs at a higher delamination length than the benchmark because at the last instance of delamination growth the calculated SERR is just above the threshold and the smallest increment is 1.3 mm. After this 1.3 mm delamination increment the SERR is below the threshold. This difference in cut-off reduces with mesh refinement as smaller increments are available for the last instance of delamination growth.

In this figure, no difference is observed between a damage extrapolation tolerance of 0.1 and 0.01. This indicates that the nodes along the delamination front have a fairly small spread in the calculated growth rate. Only for a tolerance of 0.001 is a difference observed where the first two increments in delamination length show stair-stepping indicating that the delamination front nodes were released

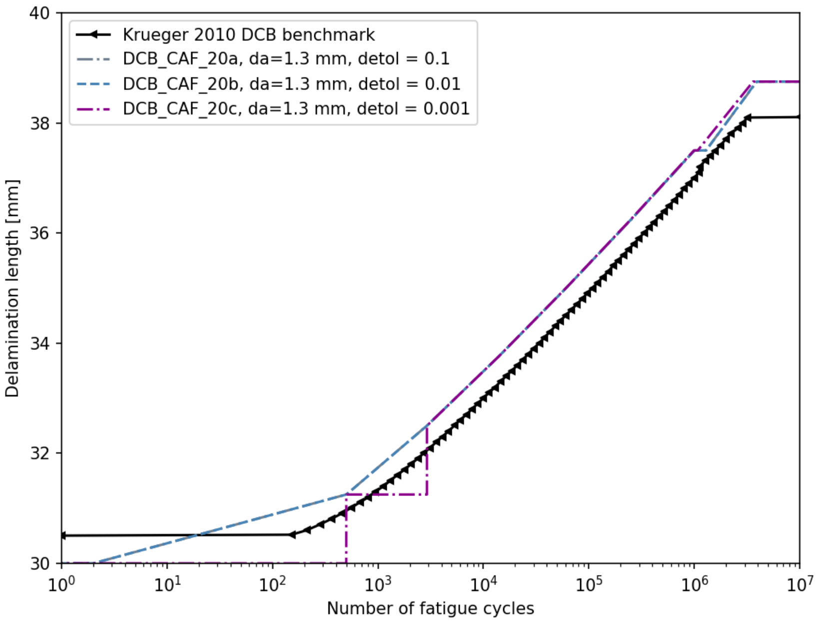

Figure 7.1: *Delamination length against fatigue cycle count for a CAF analysis of a DCB specimen model with an element length of 1.3 mm and a damage extrapolation tolerance of 0.1, 0.01 and 0.001.*

consecutively. For the rest of the delamination growth, even at this tolerance, the delamination advances across the whole front at the same time by concurrently releasing the delamination front nodes.

The results for the CAF method with a 0.5 mm element length are presented in figure 7.2. The results agree very well with the benchmark results, with an error within 1% for most of the analysis and peaks of around 1.5% error for the first two stair steps. Results for the damage extrapolation tolerance of 0.1 and 0.01 are indistinguishable except at $1 \cdot 10^6$ cycles, where the larger tolerance shows concurrent node release and the tighter tolerance shows consecutive node release. The results at a tolerance of 0.001 show more stair stepping, indicating that the delamination growth rate across the delamination front nodes is no longer close enough for all of them to be released concurrently, although some of them still are.

A view of the delamination front is provided for only two CAF analyses, as they are representative of the behaviour observed for all DCB specimen models. The delamination front of a DCB model with 0.5 mm elements and a tolerance of 0.1 is shown at two successive time increments in figure 7.3. It can be seen that the delamination front propagates by releasing a approximately half of the nodes at the front concurrently in a single time increment. The delamination progression for six successive time increments of a 0.5 mm element length model with a tolerance of 0.001 is shown in figure 7.4. It can be seen that the delamination increment starts at the centre of the specimen and is pushed outward to the sides of the specimen by releasing one or two nodes consecutively for every time increment until the delamination growth increment has propagated over the entire width of the specimen.

The results obtained with the SF method for the 1.3mm element length mesh are shown in figure 7.5. The error between the results and the benchmark falls within a 3% margin for al three tolerances. No difference is observed between a tolerance of 0.1 and 0.01 and the delamination front is propagated by concurrently releasing the delamination front nodes. Reducing the tolerance to 0.001 results in stairstepping for the first three element lengths of delamination growth indicating that the nodes are no longer released concurrently but are now released consecutively.

Initially, the analyses propagated to approximately $2.6 \cdot 10^6$ cycles without issue and then

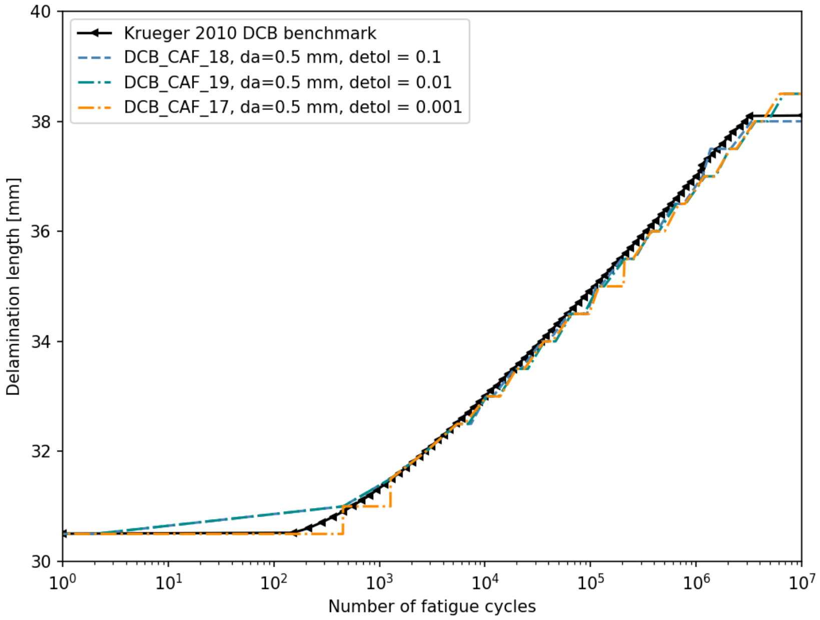

Figure 7.2: *Delamination length against fatigue cycle count for a CAF analysis of a DCB specimen model with an element length of 0.5mm and a damage extrapolation tolerance of 0.1, 0.01 and 0.001.*

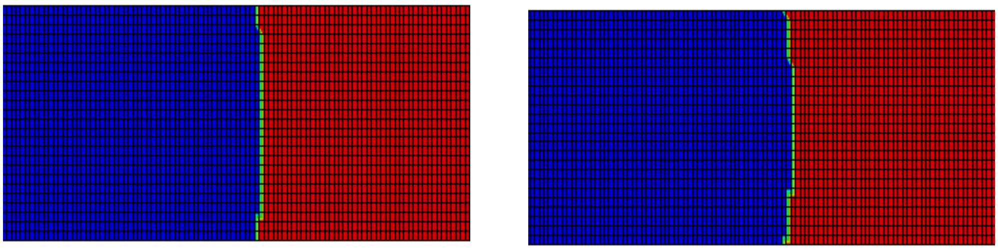

(a) *The fatigue cycle count is 42 354 cycles.*

(b) *The fatigue cycle count is 62 239 cycles.*

Figure 7.3: *DCB specimen delamination front at two successive time increments for a CAF analysis with a damage extrapolation tolerance of 0.1.*

proceeded with very small increments in the cycle count without releasing any nodes. This continued until the analyses were manually terminated. To avoid this the cycle limit was adjusted to $1 \cdot 10^6$ cycles for these three analyses compared to a limit of $1 \cdot 10^7$ cycles for the analyses presented in figures 7.1, 7.2, and 7.6.

The results obtained with the SF method for the 0.5mm element length mesh are shown in figure 7.5. They show no difference between a tolerance of 0.1 and 0.01 below $1 \cdot 10^6$ cycles. Above $1 \cdot 10^6$ cycles the larger tolerance results deviate from the benchmark and the results computed with tighter tolerances. Just as for the results presented before, the tip over point where the delamination front nodes are no longer released concurrently is between 0.01 and 0.001.

Taking all these results together it appears that for a DCB specimen practically no difference may be expected for either the CAF or the SF method by reducing the tolerance to 0.01. Only when the tolerance is reduced to 0.001 and beyond will any differences occur. A tolerance of 0.1 appears to already be sufficient to achieve good agreement between the analysis results and the benchmark results and is expected to give excellent results when the CAF and SF methods are used to analyse

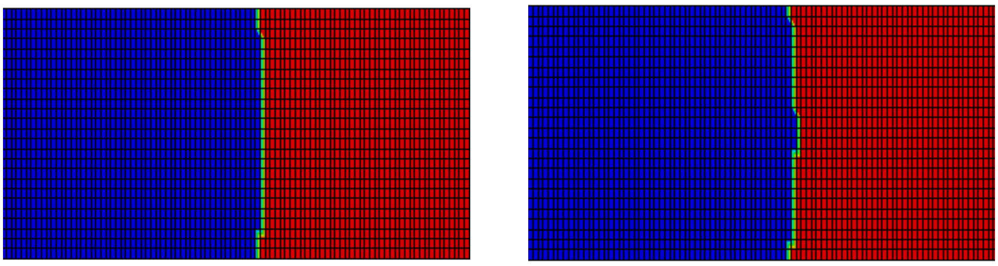

(a) *The fatigue cycle count is 43 766 cycles.* **(b)** *The fatigue cycle count is 65 894 cycles.*

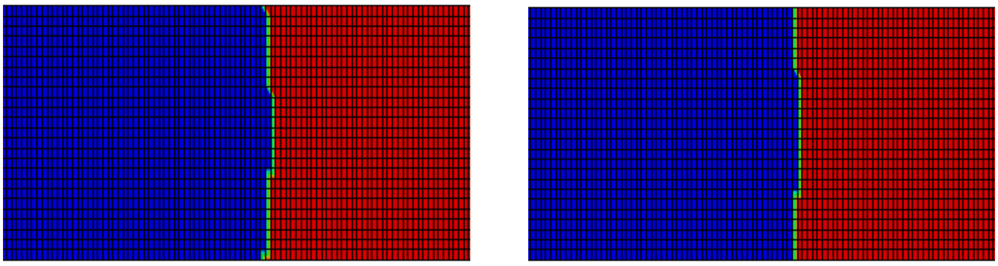

(c) *The fatigue cycle count is 66 704 cycles.* **(d)** *The fatigue cycle count is 68 424 cycles.*

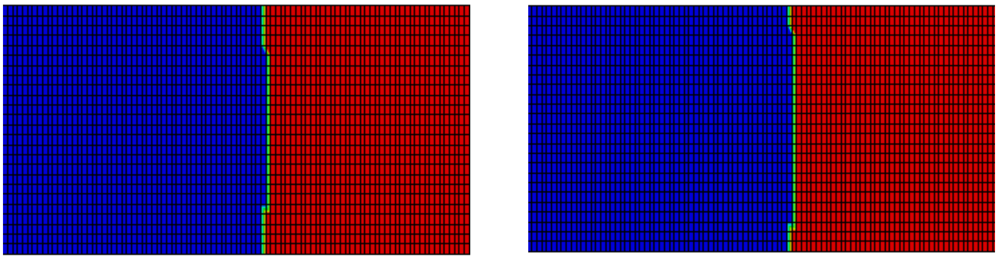

(e) *The fatigue cycle count is 71 460 cycles.* **(f)** *The fatigue cycle count is 78 768 cycles.*

Figure 7.4: *DCB specimen delamination front at six successive cycle count increments for a CAF analysis with a damage extrapolation tolerance of 0.001.*

the SSCS. Should it be desired to reduce the number of nodes released concurrently the tolerance will likely have to be reduced substantially, to less than 0.01 or even below 0.001.

Comparing the CAF and SF results for the DCB specimen models, both track within a single element length of the benchmark results. Due to the lead/lag uncertainty discussed before neither can be said to work better than the other, although the accuracy of either ought to be high enough for practical applications at 1.3 mm element length since they fall within 3% of the benchmark. A minor improvement in accuracy can be observed for both methods when the element length is reduced to 0.5 mm.

As an indication of the computational load of these models the CPU time and wall time are reported for the presented analyses in table 7.1. The number of cores was not kept constant for these analyses as it was adjusted based on the availability of computational resources limiting the comparisons that can be made. Comparing DCB_SF_15 to DCB_CAF_20 shows that the SF analyses took 54% of the CPU time for the CAF analyses at an element length of 1.3 mm. Comparing DCB_SF_14 to DCB_CAF_19 shows that the SF analysis took 74% of the CPU time of the CAF analysis at an element length of 0.5 mm. Comparing DCB_CAF_18 to DCB_CAF_19 indicates that these small models may not benefit from additional computational power after a few cores as doubling the number of cores resulted in approximately the same CPU and wall time being used. This may mean that the analysis time is dominated by overhead that does not scale with the computational resources available, or it may mean that the computational time is limited by memory or storage bandwidth rather than by computational power.

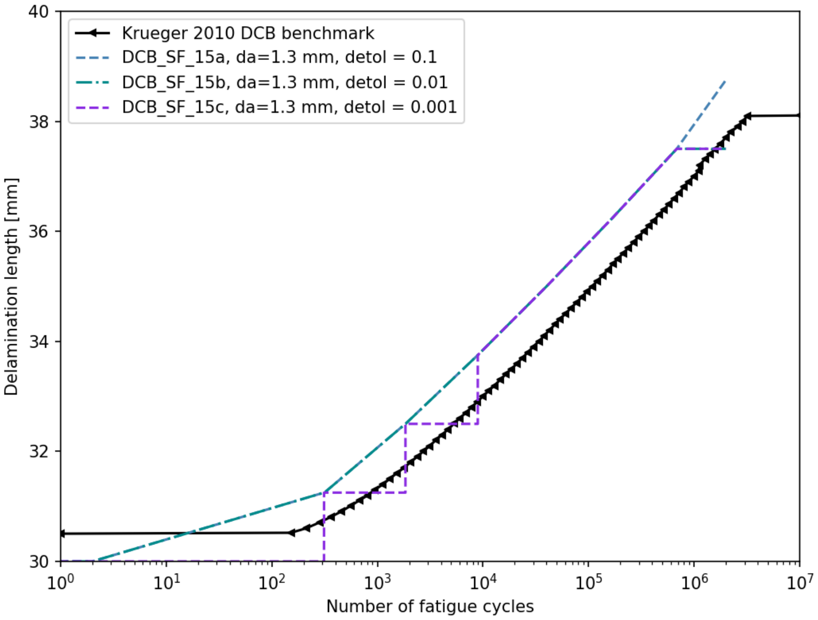

Figure 7.5: *Delamination length against fatigue cycle count for a SF analysis of a DCB specimen model with an element length of 1.3mm and a damage extrapolation tolerance of 0.1, 0.01 and 0.001.*

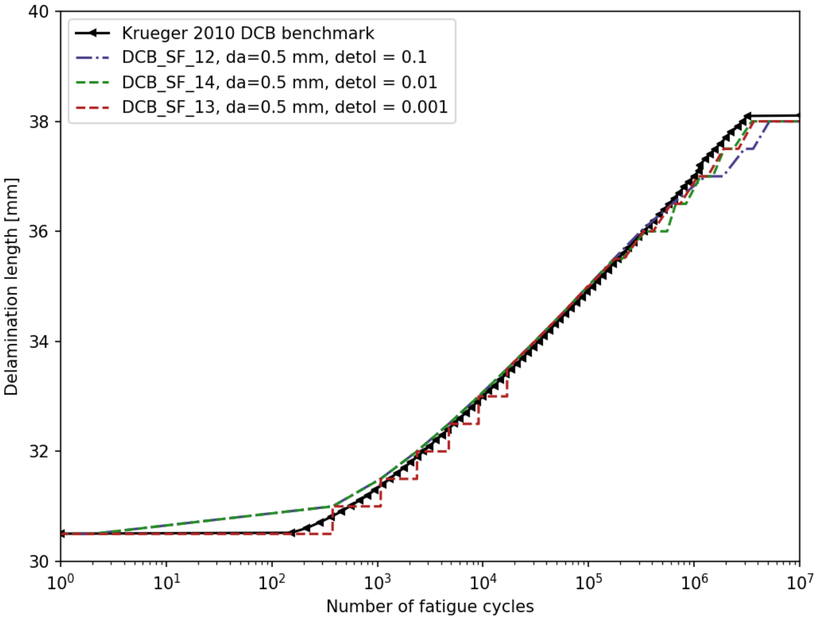

Figure 7.6: *Delamination length against fatigue cycle count for a SF analysis of a DCB specimen model with an element length of 0.5mm and a damage extrapolation tolerance of 0.1, 0.01 and 0.001.*

Table 7.1: *CPU time and walltime for the presented DCB fatigue analyses. Jobs executed on the number of cores specified.*

Analysis	CPU time [hh:mm:ss]	Wall time [hh:mm:ss]	Cores	Details
DCB_CAF_18	01:17:44	00:13:51	20	SC8R, da=0.5 mm, detol=0.1
DCB_CAF_19	01:13:37	00:15:26	10	SC8R, da=0.5 mm, detol=0.01
DCB_CAF_17	02:12:19	00:20:27	20	SC8R, da=0.5 mm, detol=0.001
DCB_SF_12	00:22:51	00:10:16	6	SC8R, da=0.5 mm, detol=0.1
DCB_SF_14	00:54:28	00:12:36	10	SC8R, da=0.5 mm, detol=0.01
DCB_SF_13	00:59:12	00:23:10	6	SC8R, da=0.5 mm, detol=0.001
DCB_CAF_20	00:57:29	00:12:40	10	SC8R, da=1.3 mm, detol=0.1, 0.01, 0.001 aggregate for all three values
DCB_SF_15	00:31:20	00:09:35	10	SC8R, da=1.3 mm, detol=0.1, 0.01, 0.001 aggregate for all three values

7.2 MMB results

The Mixed Mode Bending (MMB) specimen models verified through quasi-static delamination growth analyses in chapter 6 have been used to investigate two fatigue delamination propagation methods: the Constant Amplitude Fatigue (CAF) method and the Simplified Fatigue (SF) method. The two fatigue methods have been evaluated at two mesh densities, using element lengths of 1.3 mm and 0.5 mm, and at three tolerance values used for the fatigue methods. Only the SC8R element models have been used as they outperformed the S4R element models in the required computational time for the quasi-static analyses. The MMB fatigue analysis results are presented for mode II mode mixity values of 20%, 50%, and 80%. For the CAF analyses a triangular waveform has been used for the applied displacement, which is ramped linearly from the minimum applied displacement to the maximum applied displacement from step time 0 to 0.5 and is then linearly ramped back down to the minimum from step time 0.5 to 1. For the SF method a constant displacement proportional to the peak displacement used for the CAF method is applied.

It seemed reasonable to assume for the CAF analyses, considering that the specimen response is geometrically linear, the material is linear elastic, and the applied displacement varies linearly, that the response of the specimen only needed to be evaluated at three time points: 0, 0.5 and 1, provided that the solution convergence allowed for time increments of 0.5. Although this was the case for the DCB specimen models, this turned out not to be the case for the MMB models. It also seemed reasonable that time increments of 1 would be sufficient for the SF method due to the constant load. This also turned out not to be the case for the MMB specimen models.

For the CAF method the maximum time increment was set to 0.5 with the assumption that if the model converged, this would be adequate to determine the minimum and maximum SERR and hence to predict the delamination propagation. For an element length of 1.3 mm this was the case, but the assumption did not hold when the element size was reduced to 0.5 mm as shown in figures 7.7a, 7.7b, and 7.7c for mode II mode mixities of 20%, 50%, and 80% respectively. When using a maximum time increment of 0.5 the fine mesh models converged, but did not correctly predict the delamination growth. They under predicted the delamination length in all cases. The analyses converged without warnings or complaints and even though automatic time incrementation was enabled, the time increment was not reduced. Manually limiting the time increment by reducing the maximum time increment to 0.1 resolved the observed under prediction for the 0.5 mm element length models with 50% and 80% mode II mode mixity.

The delamination fronts for the fine mesh 50% and 80% mode II mode mixity models with a maximum time increment of 0.5 are shown in figure 7.8. The delamination fronts are not symmetric with respect to the specimen centreline, as would be expected. The 80% mode II mode mixity front especially shows a raggedness, where connected and unconnected nodes alternate across the width of the specimen. This behaviour is not observed in any other specimen analyses and disappears when the maximum time increment is reduced to 0.1.

No results are presented for the MMB specimen model with 20% mode II mode mixity, an element length of 0.5 mm, and a maximum time increment of 0.1. During this analysis 3581 load cycles were applied to the model for which no nodes were released, each followed by a small increment in the cycle count. The analyses was manually terminated after 319 hours of CPU time, at which time no nodes had been released.

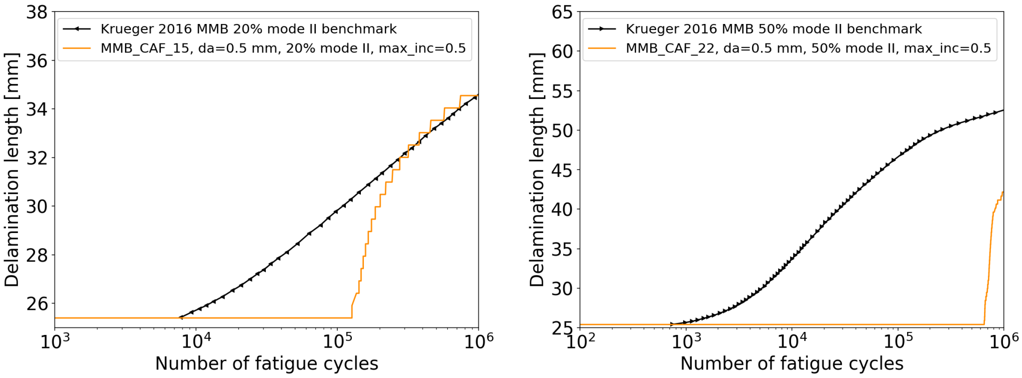

(a) *20% mode II mode mixity.* **(b)** *50% mode II mode mixity..*

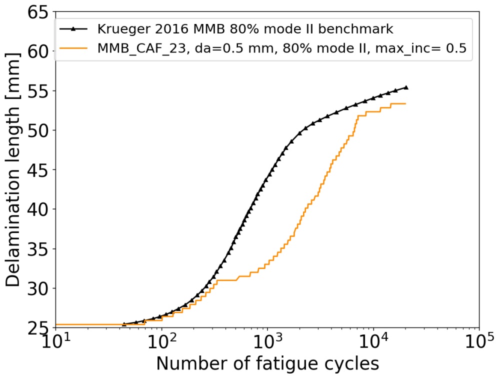

(c) *80% mode II mode mixity.*

Figure 7.7: *Delamination length against fatigue cycle count for three CAF analyses of MMB specimen models at 20%, 50%, and 80% mode II mode mixity. The element length was 0.5mm. The maximum time increment of 0.5 clearly produced incorrect results.*

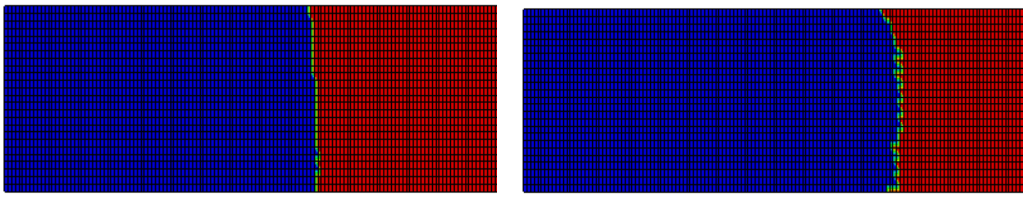

(a) *50% mode II mode mixity model. The fatigue cycle count is* $1.1 \cdot 10^6$ *cycles.* **(b)** *80% mode II mode mixity model. The fatigue cycle count is* $2 \cdot 10^4$ *cycles.*

Figure 7.8: *Delamination front of CAF analyses of two MMB specimen models with an element length of 0.5mm and a maximum time increment of 0.5.*

For the SF analyses it was assumed that a maximum time increment of 1 would be sufficient due to the constant load being applied. For all 20% and 50% mode II mode mixity models this assumption held, but it did not hold for the 80% mode II mode mixity models. The results for two SF analyses at 80% mode II mode mixity with an element length of 1.3 mm are shown in figure 7.9a with a detailed view in figure 7.9b. The overall trend of the results agrees well with the benchmark results. However, curiously, on several occasions the delamination front was advanced by releasing a node only for the node to be reconnected shortly after, effectively causing the delamination front to retreat. The most obvious occurrence of this is just before 2000 cycles, but closer inspection reveals that this occurred for most instances of delamination propagation such as at 900, 1000, 1200, and 1300 cycles. The results for a 0.5 mm element length mesh shown in figure 7.9c show 4 occurrences of the nodes being reconnected and the delamination front retreating. Additionally behaviour similar to the CAF analyses is observed, where the delamination length is severely under predicted. All of these oddities disappeared when the maximum allowed time increment was reduced from 1 to 0.1.

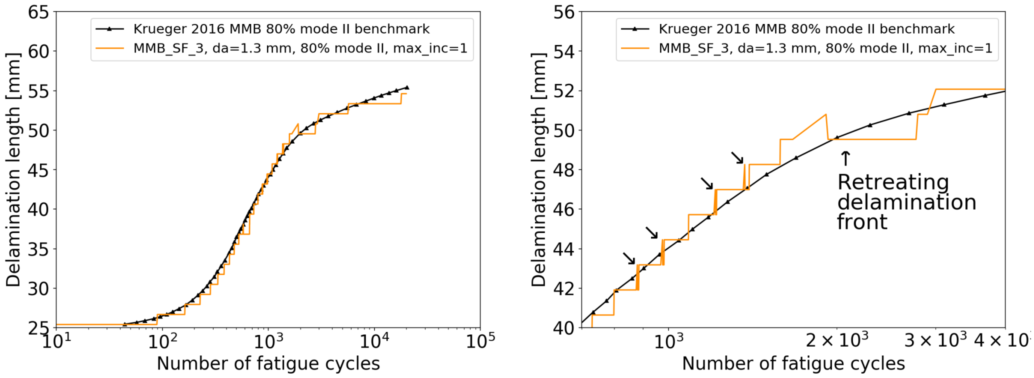

(a) *Full view. The element length was 1.3 mm*

(b) *Detailed view. The element length was 1.3 mm*

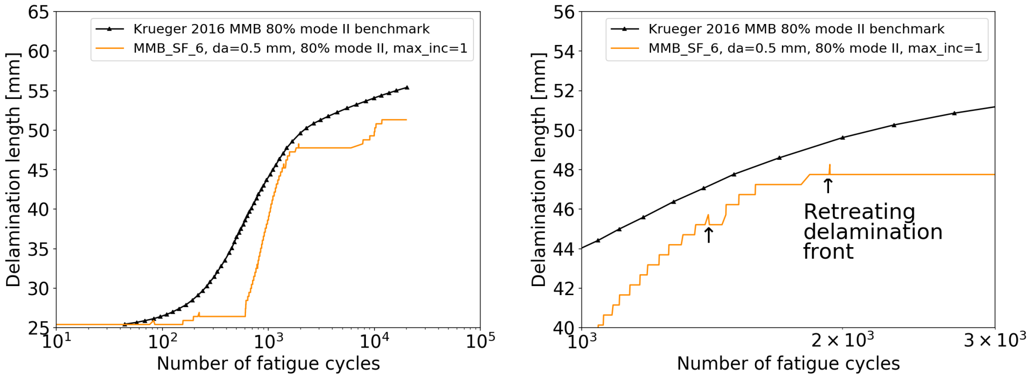

(c) *Full view. The element length was 0.5 mm*

(d) *Detailed view. The element length was 0.5 mm*

Figure 7.9: *Delamination length against fatigue cycle count for two SF analyses of MMB specimen models at 80% mode II mode mixity. The element length was 1.3 mm and 0.5 mm. The maximum time increment of 1 clearly produced incorrect results.*

The results of CAF analyses for both the 1.3 mm and 0.5 mm element length meshes at mode mixities of 20%, 50%, and, 80% are shown in figure 7.10 with the exception of the fine mesh 20% results as discussed before. At the reduced maximum time increments the achieved results are an excellent match to the benchmark results for all three mode mixity ratios. Errors were at worst around 5% for the coarse mesh results and occurred early in the analyses where the delamination length is still close to the initial delamination length. These errors reduce by a factor two towards the end of the analyses not because their absolute magnitude has reduced but because the delamination length has doubled. The increase in error at the end of the analyses after they reach the lower SERR threshold is expected since they will maintain a constant delamination length to any cycle count after the threshold

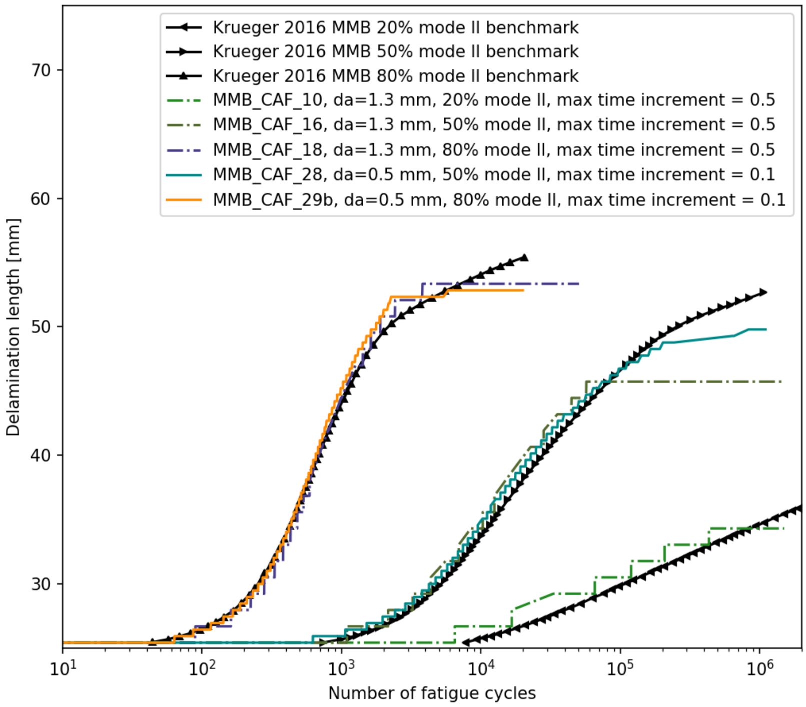

Figure 7.10: *Delamination length against fatigue cycle count for CAF analyses of MMB specimen models at 20%, 50% and 80% mode II with an element length of 1.3 mm and 0.5 mm.*

has been reached. Unexpectedly large errors are observed at the end of the analysis for the fine mesh 50% mode II mode mixity results. The difference in threshold behaviour between the coarse and the fine mesh 50% mode II mode mixity cannot be explained at this time.

The results for the SF analyses presented in figure 7.11 show similar performance. In fact, comparing the fine mesh results for the CAF and SF methods as shown in figure 7.12 shows nearly indistinguishable results.

The delamination front progression for a CAF analysis with 50% mode II mode mixity and an element length of 0.5 mm is shown in figure 7.13. The figure shows the delamination front for six successive time increments. The delamination front of only one analysis at a particular point during the analysis is shown here because it is representative of the behaviour observed in the other analyses. In figure 7.13a two instances of delamination propagation can be observed. In the next frame these instances have grown out towards the sides of the specimen by a few nodes each. In the subsequent frames it can be observed that the delamination increment propagates all the way out to the sides of the specimen by releasing a few nodes at a time. In the last frame the next delamination increment can be seen. The delamination front is symmetric with respect to the specimen centreline, as is expected. Delamination front straightening can clearly be seen: the sharp corner nodes in the delamination front fail preferentially, keeping the delamination front mostly straight. It was not expected that the rate at which the delamination increment propagates to the edges of the specimen is slow enough that a new increment starts before the previous increment has propagated all the way out. In a way, this also somewhat approximates a slightly curved delamination front as can be seen in figure 7.13c.

As an indication of the computational load of these models the CPU time and walltime are reported for the presented analyses in table 7.2. The number of cores was constant at 6 Intel Xeon E5-2640 v4 CPU cores per job. An increase in CPU time is associated with increasing mode II

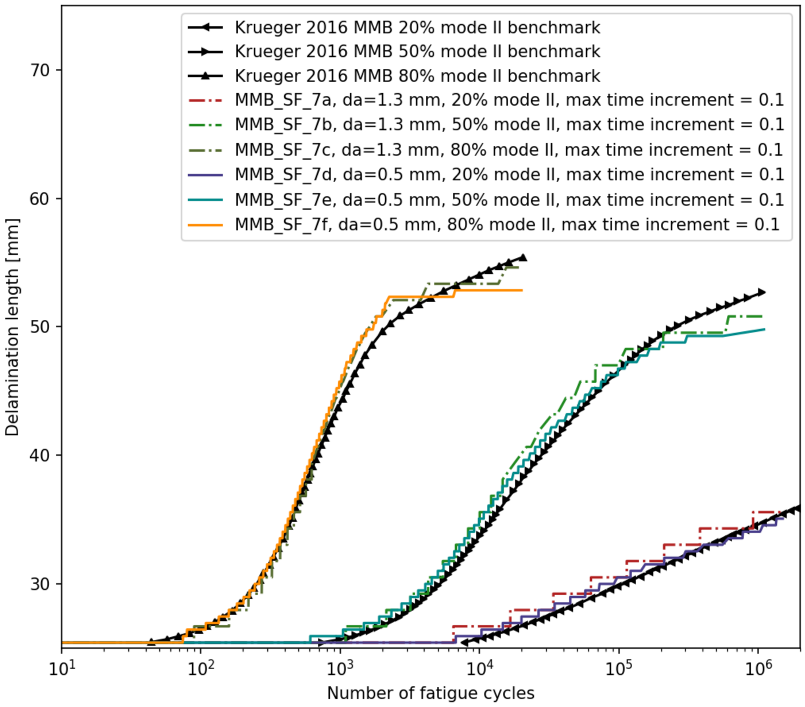

Figure 7.11: *Delamination length against fatigue cycle count for SF analyses of MMB specimen models at 20%, 50% and 80% mode II with an element length of 1.3 mm and 0.5 mm.*

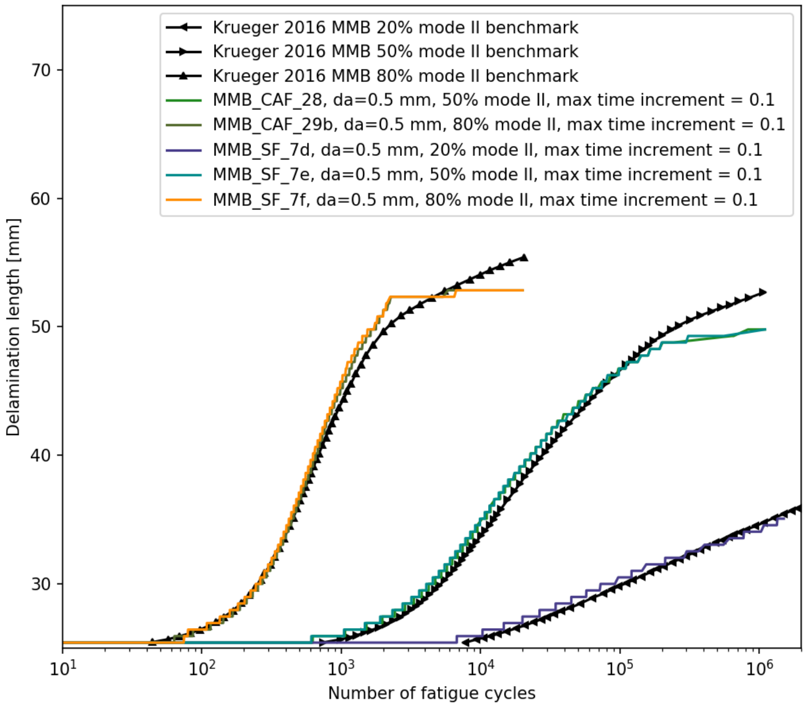

Figure 7.12: *Delamination length against fatigue cycle count for CAF and SF analyses of MMB specimen models at 20%, 50% and 80% mode II with an element length of 0.5 mm.*

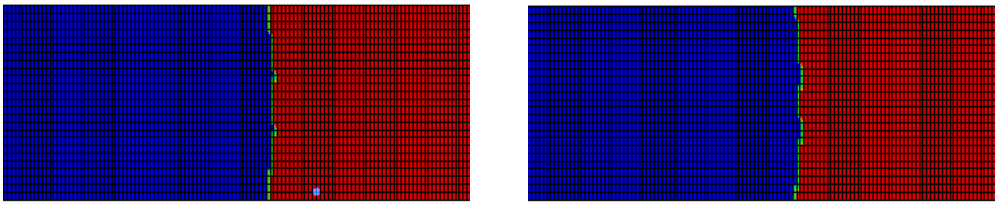

(a) *The fatigue cycle count is 49 268 cycles.* **(b)** *The fatigue cycle count is 49 482 cycles.*

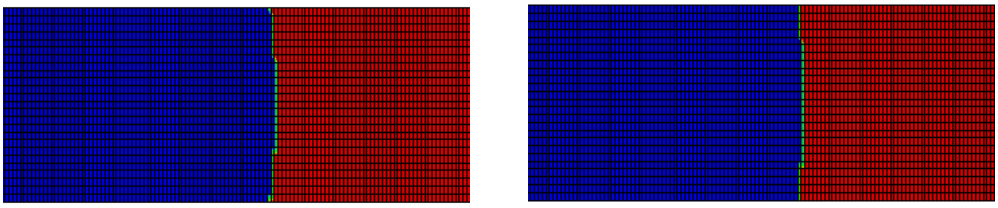

(c) *The fatigue cycle count is 50 384 cycles.* **(d)** *The fatigue cycle count is 52 222 cycles.*

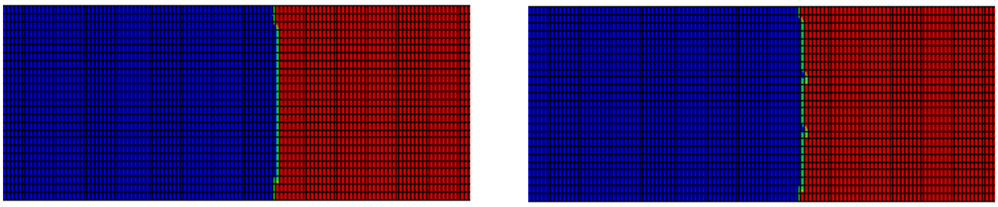

(e) *The fatigue cycle count is 53 641 cycles.* **(f)** *The fatigue cycle count is 55 177 cycles.*

Figure 7.13: *Bonded nodes at six subsequent time increments for a CAF analysis with 0.5 mm element length, 50% mode II mode mixity, and a damage extrapolation tolerance of 0.001.*

loading, with an especially large increase between the 50 and 80% mode two mode II mode mixity models. For the 1.3 mm mesh this resulted in 636% of the CPU time being required and for the 0.5 mm mesh 337% of the CPU time was used. At 50% mode II mode mixity the coarse mesh model took 34% of the CPU time required for the fine mesh model. A smaller difference is observed for the 80% mode II mode mixity model where the coarse mesh took 64% of the CPU time of the fine mesh model.

The large increase in computational load compared to the DCB model results may be ascribed to two causes. The first is the reduction in maximum time increment for the fine mesh CAF analyses from 0.5 to 0.1 necessitating at least five times more increments per applied load cycle than for the DCB models. This does not, however, account for the change in the computational load of the coarse mesh CAF models and only explains part of the increase for the fine mesh models. The main cause driving the computational time up seems to be failure of the cycle jumping mechanism in the CAF method.

The cycle jumping mechanism implemented in the CAF method is supposed to calculate, using the SERR and a Paris type fatigue relation, which node on the delamination front is the weakest and how many cycles are required to fail this node. The weakest node is then released and the total cycle count and the damage accumulation parameters of the other delamination front nodes are then updated with this increase in cycle count. This is supposed to avoid repeatedly applying load cycles to the model without any nodes being released.

Unfortunately, this behaviour is exactly what is observed for the six CAF analyses presented in this section. During analysis MMB_CAF_16, for example, all delamination propagation occurs in the first 200 load cycles applied to the model. This is followed by a further 900 load cycles which are applied to the model without any nodes being released before a cycle count of 1 500 000 cycles is reached and the analysis is terminated. The other analyses appear to go back and forth between sections where good cycle jumping is observed and sections where small increments in cycle count

Table 7.2: *CPU time and walltime for the presented MMB fatigue analyses. Jobs executed on 6 cores each.*

Analysis	CPU time [hh:mm:ss]	Wall time [hh:mm:ss]	Details
MMB_CAF_10	11:04:39	03:22:59	SC8R, da=1.3 mm, 20% mode II, detol=0.001
MMB_CAF_16	13:55:59	04:14:35	SC8R, da=1.3 mm, 50% mode II, detol=0.001
MMB_CAF_18	89:06:10	26:50:12	SC8R, da=1.3 mm, 80% mode II, detol=0.001
MMB_CAF_29a	319:11:44	75:44:02	SC8R, da=0.5 mm, 20% mode II, detol=0.001 Manually terminated, only one node released
MMB_CAF_28	41:06:45	11:53:57	SC8R, da=0.5 mm, 50% mode II, detol=0.001
MMB_CAF_29b	138:14:37	39:37:03	SC8R, da=0.5 mm, 80% mode II, detol=0.001
MMB_SF_7	44:23:38	12:32:03	SC8R, aggregate for all three mode mixities, detol=0.001 at both element lengths

without any node release are observed. The worst of these six analyses was MMB_CAF_29a where 3581 load cycles were applied to the model, and no nodes were released before the analysis was terminated manually. The analysis reached a cycle count of 20 885 cycles, which means that on average the cycle count was incremented with just 6 cycles for every applied load cycle. The SF analyses did not show this issue in the cycle jumping and performed excellently.

From the DCB specimen model results it would appear that the SF method is substantially less computationally expensive than the CAF method, with a 50% reduction of the required CPU time. No such conclusions can be derived from the MMB model results due to the failure of the cycle jumping mechanism in the CAF analyses. The nearly identical accuracy of the results between the two methods would indicate that the SF method is the preferred method for all cases where its assumptions, detailed in section 3.2.2, hold. Due to the proportionality assumption the method is limited to geometrically linear specimens, and is not expected to produce accurate results for geometrically non-linear specimens such as post-buckled Single Stringer Compression Specimens.

The Constant Amplitude Fatigue method produces excellent results for both the DCB and MMB specimen models. Provided that the maximum time increment was limited to 0.1, errors were within 5% compared to the benchmark results. The main issue encountered with the method for these analyses is the occasional failure of the cycle jumping mechanism. No pattern to these failures has been established and they cannot be explained at this time. Besides this, the performance of the method is sufficient for the application of the method to single stringer compression specimens to be warranted.

Part III

Single Stringer Compression Specimen (SSCS) analyses

Chapter 8

SSCS models

The Single Stringer Compression Specimen (SSCS), discussed in detail in chapter 4 , was modelled with dimensions and material properties chosen to correspond to previously manufactured test specimens [57, 58]. Two geometries were used, one for the quasi-static delamination propagation and another with a different stiffener flange width for the fatigue delamination propagation, to correspond to the geometries used in experimental campaigns. The quasi-static geometry is shown in figure 8.1a and the fatigue geometry is shown in figure 8.1b, where the only differences are in the stiffener flange width and flange spacing. Material properties are for IM7/8552 taken from [57] shown in table 8.1. Note that these are distinct from the IM7/8552 material properties in table 5.7 used for the MMB specimen models. The differences in the values may be explained by the fact that there is a US and an EU version of the material [64, 65] although the data sheets report the same stiffness properties for both versions or they may have been derived from tests of a different batch of material from the same source. It should be noted that neither dataset corresponds directly to the values reported in the data sheet although all are fairly close. For the dynamic implicit steps the density is also required; the nominal laminate density of IM7/8552 with a value of $1.57 \cdot 10^{-6}$ [kg/mm^3] [64] has been used.

8.1 Layup

An 8 ply quasi-isotropic $[45/90/\text{-}45/0]_s$ unidirectional layup has been used for the skin and a 7 ply [-45/0/45/0/45/0/-45] unidirectional layup was used for the stiffener where all angles are relative to the longitudinal axis of symmetry of the specimen. An initial delamination with a width of 40 mm was modelled in between one stiffener flange and the skin. It was located at the middle of the length of the specimen as shown in figure 8.1b.

Table 8.1: *IM7/8552 material properties from [57, Table 1].*

Parameter	Value
E_{11} [GPa]	150
E_{22} [GPa]	9.08
E_{33} [GPa]	9.08
ν_{12} [-]	0.32
ν_{13} [-]	0.32
ν_{23} [-]	0.42
G_{12} [GPa]	5.29
G_{13} [GPa]	5.29
G_{23} [GPa]	3.40

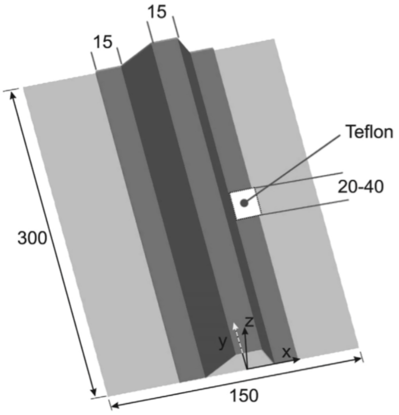

(a) *Quasi-static delamination propagation model dimensions. From [58].*

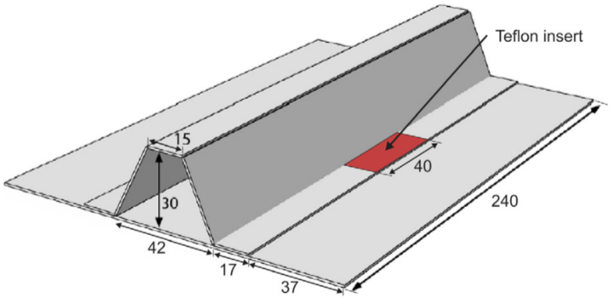

(b) *Fatigue delamination propagation model dimensions. From [57]*

Figure 8.1: *Single Stringer Compression Specimen dimensions.*

8.2 Meshing

Two equidistantly spaced meshes, with square elements of 3 mm and 1 mm nominal length, were used for the quasi-static delamination propagation models. Only a 1 mm nominal element size was used for the fatigue delamination propagation model. The exact element dimensions varied slightly depending on their location in the specimen model to ensure that the nodes used for the VCCT were coincident on the skin and stiffener, and to ensure that the potting length and initial delamination length were replicated closely.

The skin of the quasi-static specimen geometry was partitioned into three sections longitudinal to the specimen, along the outer edges of the stiffener, for the 1 mm pitch mesh as shown in figure 8.2a. For the middle section, 73 elements with a width of exactly 1 mm were used, and the outer two sections used 39 elements each, with an element length of 0.987 mm. The skin of the 3 mm pitch quasi-static model was partitioned into twenty five sections as shown in figure 8.2b. In the delamination propagation zone on either side of the initial delamination, 33 elements with a length of 3.03 mm were used along the length. Five elements with a width of exactly 3 mm were used across the width of the delamination propagation zone. The rest of the sections were meshed with whichever integer number of elements brought them closest to the 3 mm nominal element size. The skin of the fatigue specimen model was not partitioned and used a uniform mesh with elements of exactly 1 mm length.

The stiffener was partitioned into five sections along its length: two flanges, two side walls and one top section. The flanges were meshed to match the skin mesh, and the other three sections were meshed with the integer number of elements that gave the closest element size to the nominal mesh pitch.

The quasi-static delamination propagation specimen was modelled using both S4R conventional shell elements and SC8R continuum shell elements. For the S4R element model the geometry was defined through reference planes. The reference plane of the skin was located at the top of the part and the reference plane of the stiffener was located at the bottom of the part to ensure that the nodes used for the VCCT coincided. The SC8R element model was modelled with solid geometry with one element through the thickness for all parts. For all partitioned cells of the SC8R model a stacking direction was assigned before meshing to ensure correct element orientation. The fatigue delamination propagation specimen was modelled using only SC8R continuum shell elements.

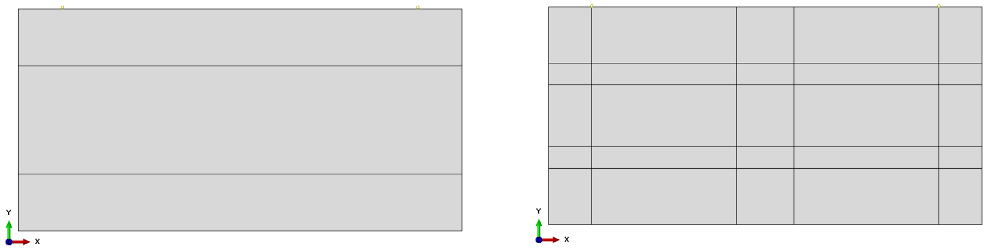

(a) *Partitions of the 1 mm element pitch mesh.* **(b)** *Partitions of the 3 mm element pitch mesh.*

Figure 8.2: *Skin partitions of the quasi-static delamination propagation models.*

8.3 VCCT definition

A ’Debond using VCCT’ type crack was specified between the skin and the two stiffener flanges with a ramp debonding force for the quasi-static delamination propagation and a step debonding force for the fatigue analyses. The ramp debonding force was adopted for improved solution convergence. Additionally, the ramp debonding force is better able to capture delamination front rounding than a step debonding force. Ramp debonding is not currently supported for fatigue analyses and a step debonding force is the only available option. This is expected to cause delamination front straightening because sharp corners in the debonded delamination front created by releasing a node tend to attract load and fail shortly after the initial node failure that advanced the delamination front. This will continue until the nodes all the way out to the edge of the stiffener flange have failed. The improved solution convergence of the ramp release would not be expected to benefit the fatigue propagation analysis since no quasi-static delamination growth occurs; the nodes are failed at the minimum displacement defined in the fatigue cycle and the load is redistributed over the new delamination front nodes before the displacement is increased in the subsequent fatigue cycle.

A surface to surface contact interaction was defined where the top surface of the skin served as the master surface and the bottom surface of the stiffener flanges served as the slave surface. A small sliding formulation is adopted as the finite sliding surface to surface contact formulation is not supported for VCCT. Slave adjustment is specified to prevent initial over or under closure, but normally no nodes need to be adjusted since the specimen is modelled with flat surfaces which are assembled such that no under or over closure exists. An initial clearance of $1.0 \cdot 10^{-8}$ mm is specified to prevent numerical round-off issues. A node set is specified on the slave surface and the bonding of the slave nodes is limited to this subset.

Automatic contact stabilisation was specified through standard contact controls with a value of $1.0 \cdot 10^{-4}$. Without any contact stabilisation the models struggled with solution convergence, adding the contact stabilisation helped them to converge. Increasing the contact stabilisation by an order of magnitude to a value of $1.0 \cdot 10^{-3}$ did not affect the overall response of the specimen, but did reduce some ringing observed after sharp load drops. Although by no means definite proof, this is at least an indication that the accuracy of the results is not substantially affected by the introduction of contact stabilisation.

The viscosity was set to 0. The tolerance for quasi-static VCCT delamination propagation was increased from a default of 0.1 to 0.3 with the aim to reduce the computational load associated with the model, without substantially affecting the accuracy of the results. The damage extrapolation tolerance for the fatigue VCCT was set to 0.1.

Two Abaqus input files have been included as examples in appendix A. The input file for SSCS_QS_80 is provided in section A.III. The input file for SSCS_CAF_54 is provided in section A.IV.

8.4 Initial imperfection

To ensure that the panel buckles in the desired buckling mode shape, and to help the panel transition through the buckling bifurcation point, an initial imperfection is applied. An eigenmode analysis is used to generate the initial imperfection for a particular model geometry. The first eigenmode is imposed on the model with a magnitude of -0.01.

For the first eigenmode both free edges of the specimen buckle with a three half wave pattern as shown in figure 8.3. This corresponds to the buckling mode observed in experimental testing, which showed the same three half wave buckling mode. Contrary to the experimental buckling mode shape, where the middle half wave served to close the initial delamination, the numerical buckling mode shape is applied with a negative magnitude as this results in a more critical delamination opening mode. For comparison to experimental testing the imperfection has also been inverted, back to the mode shape predicted by the eigenmode analysis and observed in experimental testing, for select analyses. Besides this eigenmode imperfection, no additional specimen imperfections were modelled.

8.5 Boundary conditions

Two reference points were defined, one at the displaced end of the specimen and one at the stationary end of the specimen. The nodes on the edge of the specimen shown in figure 8.4a were constrained to their respective reference point with rigid body ties, tying both displacement and rotation degrees of freedom for the S4R models and only displacement degrees of freedom for the SC8R models.

The reference point at the stationary end of the specimen was encasted. For the reference point at the displaced end of the specimen all rotation degrees of freedom and both the lateral and out-of-plane displacement degrees of freedom were set to zero with a displacement boundary condition, leaving this reference point free only to displace along the longitudinal axis of the specimen. Both displacement and load control options were implemented in the model, through either a displacement boundary condition or a load specified for the reference point on the previously unconstrained degree of freedom. For the quasi-static delamination propagation displacement control was used to match available experimental data and to avoid any unstable delamination propagation. For the fatigue delamination propagation load control was used to match available experimental test data.

The potting of the specimen is simulated through a displacement boundary condition constraining all rotation and lateral and out-of-plane displacement of the nodes in the potted regions, shown in figure 8.4b, leaving them free to displace only in the longitudinal axis of the specimen. In effect, this boundary condition entails the assumption of a potting compound with infinite stiffness for all displacements and rotations except for the longitudinal displacement, for which zero stiffness is assumed. This is, of course, only an approximation of the real potting compound which has neither infinite nor zero stiffness.

Initially the potted sections of the specimen were not modelled, but the specimen length was reduced to the length in between the pottings and clamped boundary conditions were applied to the edge nodes. Although the buckling load and mode shape were not affected, the overall specimen compliance was. Modelling these pottings, perhaps obviously in hindsight, was essential to bring the specimen compliance into agreement with both verification and validation data.

The peak displacement for the quasi-static delamination propagation steps was set to 1 mm. At this displacement the delamination has propagated to several times its original length, and this displacement is just beyond the displacement at which final failure occurred for the experimental

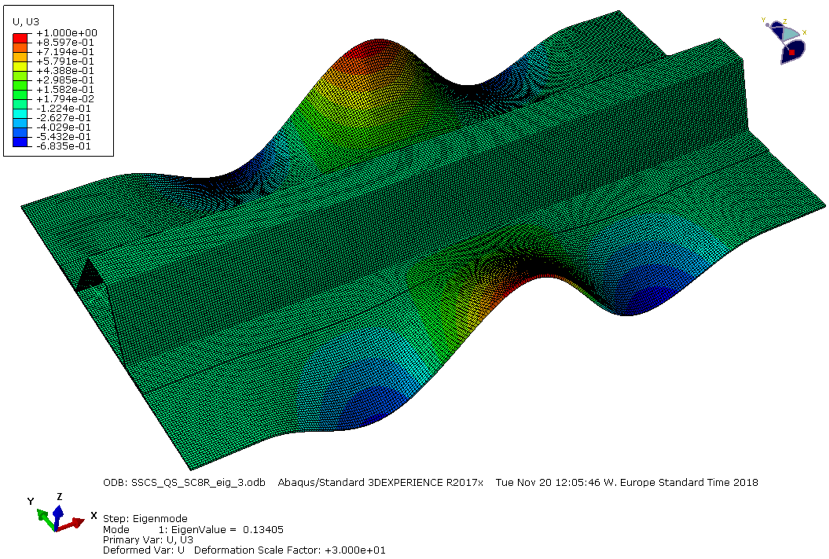

(a) *Three dimensional view.*

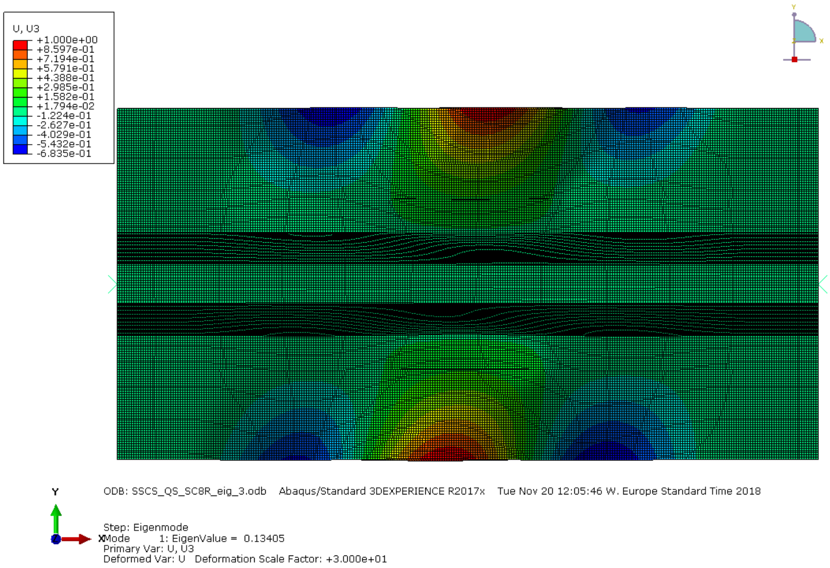

(b) *Top down view.*

Figure 8.3: *First eigenmode of the SSCS used as initial imperfection.*

results.

For the fatigue delamination propagation a triangular load waveform has been defined, the same as for the DCB and MMB specimen models. The load is ramped linearly from the minimum to the maximum load from step time 0 to 0.5 and is ramped linearly back to the minimum from step time 0.5 to 1. Three time points have been defined, at 0, 0.5, and 1, to ensure that both the minimum and the maximum load are captured. If these are not defined the automatic time incrementation may place increments just before and just after, but not right on, the peak applied displacement. A pre-load step is used to bring the specimen up to the minimum applied load before cycling is commenced.

A load ratio R of 0.1 was used for the load applied to the specimen as a whole. Due to the geometric non-linearity this no longer translates to a displacement ratio of 0.1 as it does for the DCB and MMB specimens. Due to the global buckling modeshape and potential local buckling of the stiffener flange or the skin, this also no longer necessarily translates to a load ratio of 0.1 at the delamination front. Due to the buckling bifurcation the load ratio becomes practically 0 if the specimen is cycled in and out of post buckling; before the specimen buckles the out-of-plane displacement is zero and therefore the load on the delamination front is zero making the load ratio at the delamination front zero as well regardless of the applied load ratio.

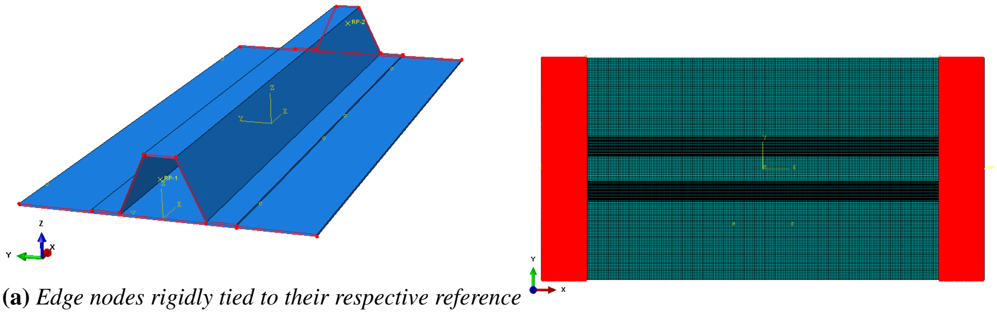

(a) *Edge nodes rigidly tied to their respective reference points.*

(b) *Potted nodes.*

Figure 8.4: *Boundary conditions*

8.6 Steps

To aid solution convergence of the quasi-static delamination propagation model, a dynamic implicit type step was used. The model compliance was identical for a static general step and a dynamic implicit step as shown in figure 8.5, but the static general step would not converge after delamination propagation commenced. A step time of 20 was used to limit dynamic loading effects. With a peak displacement of 1 mm for the analyses this translated to a loading rate of 0.05 mm per unit time. The initial time increment was set to 0.01 and the maximum time increment was limited to 0.1. The minimum time increment was set to $1.0 \cdot 10^{-12}$. The numerical artificial damping control α for the dynamic implicit time stepping scheme was set to -0.10 to give some numerical damping for improved convergence. The value was reduced from the peak numerical damping at $\alpha = -0.333$ because a substantial improvement in solution time was observed for this reduction.

For the fatigue analyses the Constant Amplitude Fatigue (CAF) method was used. Due to the assumptions made for the Simplified Fatigue (SF) method it is limited to geometrically linear analyses and it is not expected to produce satisfactory results for the SSCS loaded in the post-buckling regime. The time of a single load step has been set to 1, with an initial time increment of 0.05 and a maximum time increment of 0.1. The minimum time increment has been set to $1.0 \cdot 10^{-8}$.

8.7 Solution controls

The Abaqus solution controls were adjusted for the the quasi-static and for the fatigue analyses to improve solution convergence. For the quasi-static delamination propagation analyses the time incrementation controls, the displacement field controls, and the line search controls were adjusted. The time incrementation controls used for the quasi-static delamination propagation analyses are shown in table 8.2. I_0 and I_R were increased to 10 to push back convergence checks and give the analysis more iterations before it might be terminated due to expected non-convergence. I_P was reduced from 9 to 4 to make the analysis switch to the larger residual tolerance quicker, although since later both R_n and R_p were both increased and set to the same value this no longer affects the results. I_C was increased to 500 to disable termination due to the predicted logarithmic rate of convergence. I_S was increased to 30 to allow more contact state changes to occur during equilibrium iterations. I_A was increased to 35 to make sure that the minimum allowed time increment could be reached. I_J was increased from 6 to 10 to allow the time increment to be increased even in the presence of some

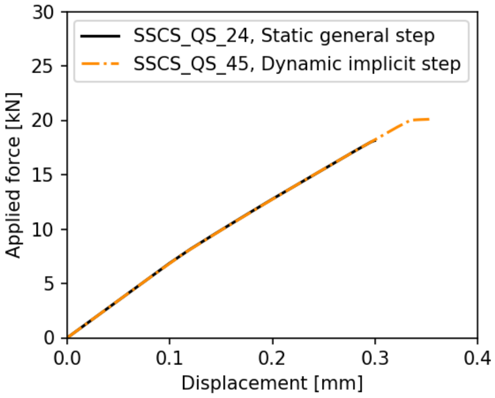

Figure 8.5: *Load against displacement for SSCS analyses with a static general step and a dynamic implicit step.*

contact state changes during equilibrium iterations. Finally I_T was increased from 3 to 10 to prevent the time increment from being raised back up too quickly.

The displacement field convergence criteria were relaxed to reduce analysis time as shown in table 8.3. The line search algorithm is turned on by setting the number of line search iterations to 4 as is shown in table 8.4. The line search algorithm helps when ”many nonlinear iterations and/or cutbacks are needed to resolve sharp discontinuities in the solution” [51, Convergence criteria for nonlinear problems].

For the fatigue delamination propagation analyses only the time incrementation controls were adjusted. The time incrementation controls used for the fatigue delamination propagation analyses are shown in table 8.5. They are more conservative than the controls used for the quasi-static propagation analyses as they do not need to deal with the sudden release of nodes while the specimen is highly loaded. Failed nodes are released below the buckling load and the panel is loaded back up gradually with the updated delamination front.

I_C was increased to 20 to allow for a few more equilibrium equations before the analysis was terminated, should they be needed. I_G was halved and I_T was almost doubled to prevent the time increment from being increased prematurely. I_A was increased to 30 to allow the analysis to reach the minimum allowed time increment.

Table 8.2: *Time incrementation parameters. Default values and values used for the quasi-static delamination propagation analyses. Descriptions from [51, Customizing general solution controls].*

Parameter	Default value	used value	Description
I_0	4	10	Number of equilibrium iterations (without severe discontinuities) after which the check is made whether the residuals are increasing in two consecutive iterations.
I_R	8	10	Number of consecutive equilibrium iterations (without severe discontinuities) at which logarithmic rate of convergence check begins.
I_P	9	4	Number of consecutive equilibrium iterations (without severe discontinuities) after which the residual tolerance R_p is used instead of R_n.
I_C	16	500	Upper limit on the number of consecutive equilibrium iterations (without severe discontinuities), based on prediction of the logarithmic rate of convergence.
I_L	10	10	Number of consecutive equilibrium iterations (without severe discontinuities) above which the size of the next increment will be reduced.
I_G	4	4	Maximum number of consecutive equilibrium iterations (without severe discontinuities) allowed in consecutive increments for the time increment to be increased.
I_S	12	30	Maximum number of severe discontinuity iterations allowed in an increment if CONVERT SDI=NO. This parameter is not used if CONVERT SDI=YES.
I_A	5	35	Maximum number of attempts allowed for an increment.
I_J	6	10	Maximum number of severe discontinuity iterations allowed in two consecutive increments for the time increment to be increased if CONVERT SDI=NO. This parameter is not used if CONVERT SDI=YES.
I_T	3	10	Minimum number of consecutive increments in which the time integration accuracy measure must be satisfied without any cutbacks to allow a time increment increase.

Table 8.3: *Displacement field parameters. Default values and values used for the quasi-static delamination propagation analyses. Descriptions from [51, Customizing general solution controls].*

Parameter	Default value	Used value	Description
R_n^α	$5 \cdot 10^{-3}$	$1 \cdot 10^{-1}$	Convergence criterion for the ratio of the largest residual to the corresponding average flux norm for convergence.
C_n^α	$1 \cdot 10^{-2}$	1	Convergence criterion for the ratio of the largest solution correction to the largest corresponding incremental solution value.
$\tilde{q}_0^\alpha$	$1 \cdot 10^{-2}$	-	Initial value of the time average flux for this step. The default is the time average flux from previous steps or $1\ cdot 10^{-2}$ if this is Step 1.
$\tilde{q}_u^\alpha$	-	-	User-defined average flux
R_P^α	$2 \cdot 10^{-2}$	$1 \cdot 10^{-1}$	Alternative residual convergence criterion to be used after I_P^α iterations.

Table 8.4: *Line search parameters. Default value and value used for the quasi-static delamination propagation analyses. Description from [51, Customizing general solution controls].*

Parameter	Default value	Used value	Description
N^{ls}	0	4	Maximum number of line search iterations. Default is 0 for steps that use the Newton method and 5 for steps that use the quasi-Newton method.

Table 8.5: *Time incrementation parameters. Default values and values used for the fatigue delamination propagation analyses. Descriptions from [51, Customizing general solution controls].*

Parameter	Default value	used value	Description
I_0	4	4	Number of equilibrium iterations (without severe discontinuities) after which the check is made whether the residuals are increasing in two consecutive iterations.
I_R	8	8	Number of consecutive equilibrium iterations (without severe discontinuities) at which logarithmic rate of convergence check begins.
I_P	9	9	Number of consecutive equilibrium iterations (without severe discontinuities) after which the residual tolerance R_p is used instead of R_n.
I_C	16	20	Upper limit on the number of consecutive equilibrium iterations (without severe discontinuities), based on prediction of the logarithmic rate of convergence.
I_L	10	10	Number of consecutive equilibrium iterations (without severe discontinuities) above which the size of the next increment will be reduced.
I_G	4	2	Maximum number of consecutive equilibrium iterations (without severe discontinuities) allowed in consecutive increments for the time increment to be increased.
I_S	12	12	Maximum number of severe discontinuity iterations allowed in an increment if CONVERT SDI=NO. This parameter is not used if CONVERT SDI=YES.
I_A	5	30	Maximum number of attempts allowed for an increment.
I_J	6	6	Maximum number of severe discontinuity iterations allowed in two consecutive increments for the time increment to be increased if CONVERT SDI=NO. This parameter is not used if CONVERT SDI=YES.
I_T	3	5	Minimum number of consecutive increments in which the time integration accuracy measure must be satisfied without any cutbacks to allow a time increment increase.

Chapter 9

SSCS quasi-static delamination propagation results

The quasi-static delamination propagation results for the Single Stringer Compression Specimen (SSCS) are presented in this chapter. The analyses were conducted under displacement control. One of the potted ends of the specimen was displaced at a constant rate until a total compressive end displacement of 1 mm had been reached while the other end was kept stationary. The specimens buckled at an end displacement of around 0.13 mm, and were loaded in the post-buckling regime for the remainder of the analysis. After buckling, the specimens started to displace in the out-of-plane direction which in turn began loading the delamination front. At an end displacement around 0.3 mm the critical Strain Energy Release Rate (SERR) was reached at some locations along the delamination front and quasi-static delamination growth commenced.

Figure 9.1 shows the reaction force against the displacement applied to two SSCS models with 3 mm and 1 mm SC8R elements. For both analyses the panel buckles at a displacement between 0.12 and 0.14 mm for a buckling load between 6.5 kN and 7.9 kN. The buckling load cannot be determined with better precision for two reasons, the first is that output is only written every 5 increments for output data reduction. The second reason is that due to the initial imperfection the model transitions from pre- to post-buckling more gradually than it would without, making it challenging to pin down a particular step time at which buckling occurs. This gradual buckling is desired, it helps the analysis transition through the buckling bifurcation point without cutbacks in the time incrementation, and is one of the main reasons the imperfection is applied.

Initial delamination propagation for SSCS_QS_80 occurred at a displacement of 0.27 mm with a reaction force of 13.8 kN. A load drop occurred at a displacement of 0.37 mm with a reaction force of 18.2 kN. A second load drop occurred at a displacement of 0.49 mm with a reaction force of 20.2 kN. A third load drop occurred at a displacement of 0.62 mm with a reaction force of 23.2 kN. No further load drops occurred before the analysis was terminated.

These three load drops correlate with shifts in the buckling modeshape of the delaminated stiffener flange section. The out-of-plane displacement of the model is presented in figure 9.2, showing the buckling sequence. Initially the skin of the panel buckles in a three half wave mode where the half wave at the initial delamination buckles away from the stiffener as can be seen in figure 9.2a. This serves to open up the delamination and causes mode I loading to occur along the delamination front. This buckling mode shape corresponds to the imposed initial imperfection discussed in section 8.4. The magnitude of the eigenmode shape used as an imperfection has been inverted on purpose to force the more critical delamination opening to occur. If the skin had buckled towards the stiffener at the delamination it would have served to close the initial delamination and little to no mode I loading would have been present along the delamination front.

The first, and largest, load drop occurs when the delaminated section of the flange buckles locally into a single half wave buckling mode shape shown in figure 9.2c. Shortly thereafter the skin also shifts to a local single half wave buckling modeshape shown in figure 9.2e. In the same figure it can

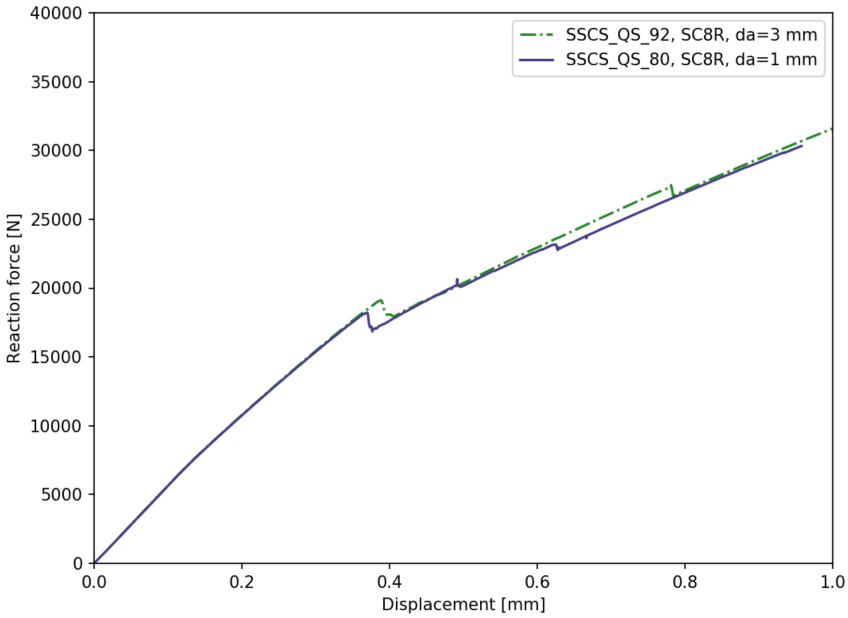

Figure 9.1: *Load against displacement for quasi-static delamination growth of an SSCS model with SC8R elements with a length of 3 mm and 1 mm.*

be observed that the buckling modeshape on the other side of the specimen has inverted. The second load drop correlates with the locally buckled section of the stiffener flange snapping from a single half wave buckling modeshape to a two half wave buckling modeshape shown in figure 9.2g. The third and last load drop occurs when the flange snaps from a two to a three half wave buckling mode shape. This buckling mode is maintained until the end of the analysis shown in figure 9.2i. At the end of the analysis, extensive buckling of the sides and top of the stiffener can be observed.

The delamination growth progression in the specimen is shown in figure 9.2 interleaved with the out-of-plane displacement figures. In each case the out-of-plane displacement at a particular moment during the analysis is shown first followed by the delamination state at that same moment.The delamination is viewed from the skin side of the specimen, compared to the stiffener side view used for the displacement figures. The same area of the stiffener flange is shown at the same scaling in all five figures allowing direct comparison of the extent of the delamination. The upper edge of the figures corresponds to the inside edge of the stiffener flange, and the lower edge corresponds to the outside edge.

Up to an applied displacement of 0.37 mm the delamination grows on both sides at the same time. After this the delamination growth alternates between the sides, where one side is stationary and only the other side grows.

Substantial delamination front rounding is observed at a delamination length of 50.8, 75.1, and 95.1 mm. The rounding is characterised by the edges leading the overall delamination front. This is opposite to the rounding observed in the DCB and MMB specimens where the edges lagged behind the overall delamination front. The initial rounding of the front indicates that the Strain Energy Release Rate distribution is not constant across the delamination front. After the initial rounding, the front shape is fairly consistent for most of the analysis. Only towards the end of the analyses is a substantial deviation in the delamination front shape observed, where for the left side in particular the front sharpens into two straight sections almost aligned with the diagonal of the elements.

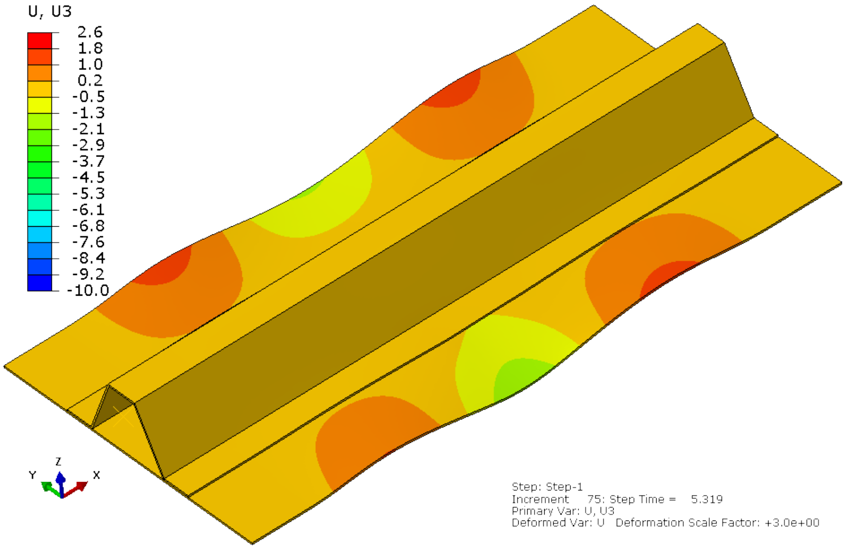

(a) *Out-of-plane displacement before any delamination growth has occurred. The applied displacement is 0.27 mm.*

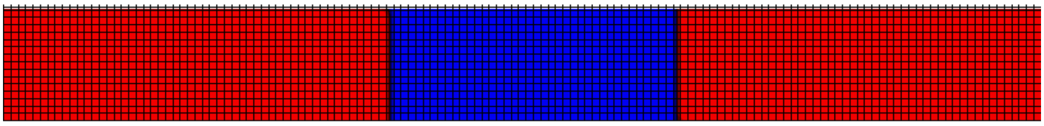

(b) *Initial delamination. The applied displacement is 0.27 mm. The delamination length is 40 mm.*

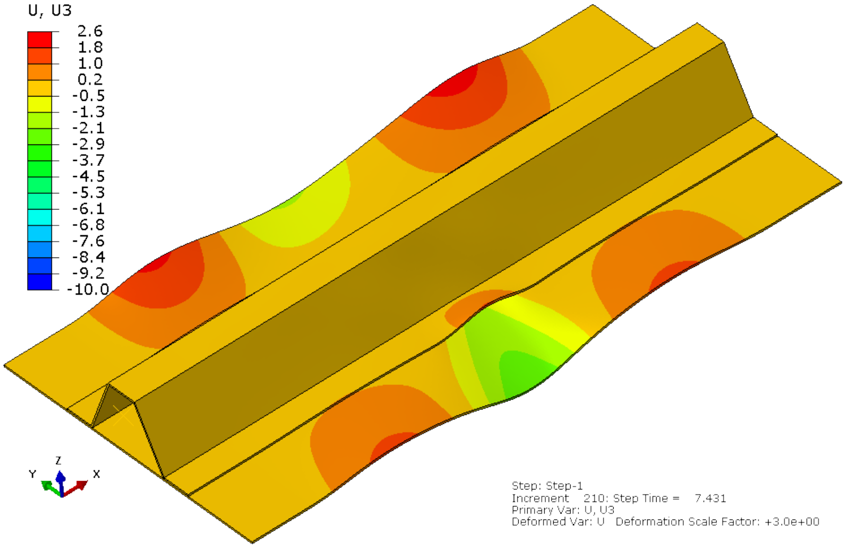

(c) *Out-of-plane displacement at the first load drop, stiffener flange has just developed local buckling. The applied displacement is 0.37 mm.*

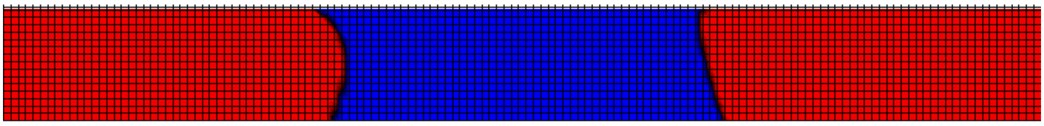

(d) *Delamination at the first load drop. The applied displacement is 0.37 mm. The delamination length is 50.8 mm.*

Figure 9.2: *Out-of-plane displacement and delamination front of SSCS_QS_80 at five moments of the analysis. Displacement in mm. The displacement scaling factor is 3. For the delamination blue (centre) nodes are released, red (outer) nodes are tied. The delamination is viewed from the skin side of the specimen. The top edge of the delamination is the inside edge of the stiffener flange.*

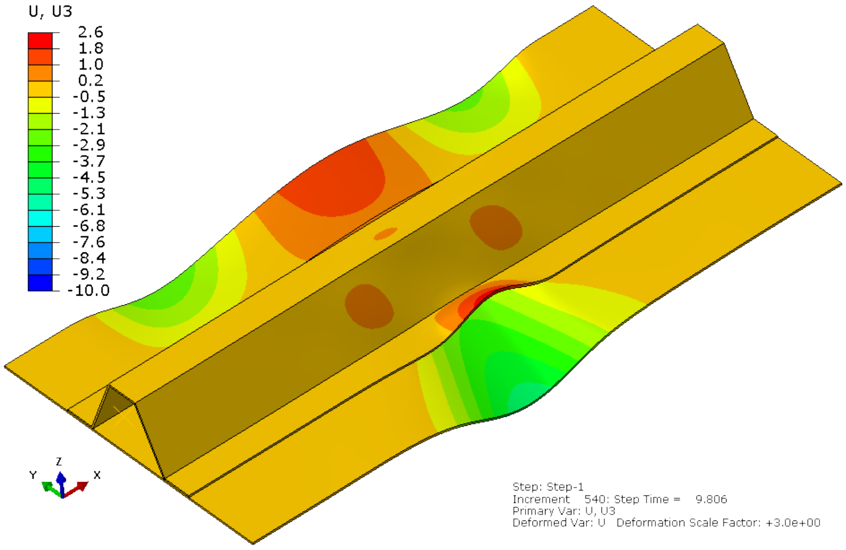

(e) *Out-of-plane displacement at the second load drop, stiffener flange is about to transition to a two half wave buckling mode. The applied displacement is 0.49 mm.*

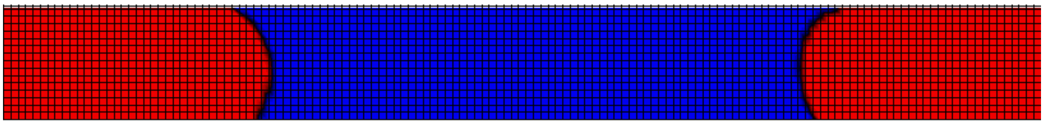

(f) *Delamination at the second load drop. The applied displacement is 0.49 mm. The delamination length is 75.1 mm.*

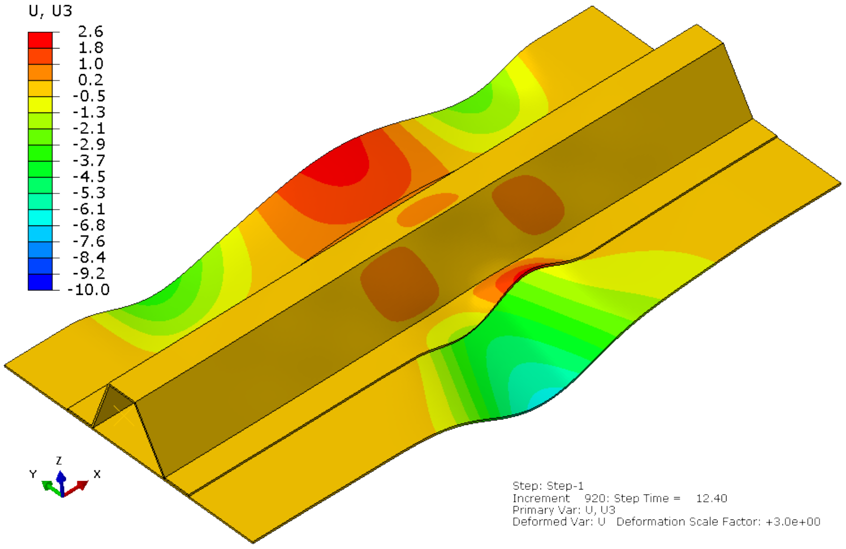

(g) *Out-of-plane displacement at the third load drop, stiffener flange is about to transition to a three half wave buckling mode. The applied displacement is 0.62 mm.*

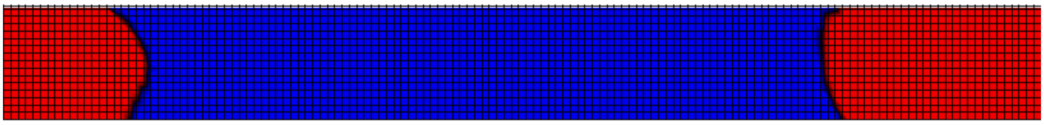

(h) *Delamination at the third load drop. The applied displacement is 0.62 mm. The delamination length is 95.1 mm.*

Figure 9.2: *(cont.) Out-of-plane displacement and delamination front of SSCS_QS_80 at five moments of the analysis. Displacement in mm. The displacement scaling factor is 3. For the delamination blue (centre) nodes are released, red (outer) nodes are tied. The delamination is viewed from the skin side of the specimen. The top edge of the delamination is the inside edge of the stiffener flange.*

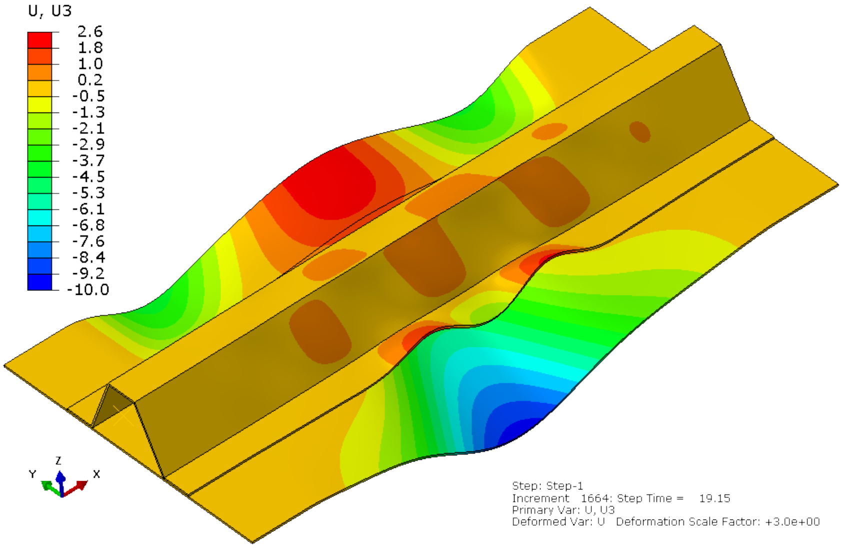

(i) *Out-of-plane displacement at the termination of the analysis. The applied displacement is 0.97 mm.*

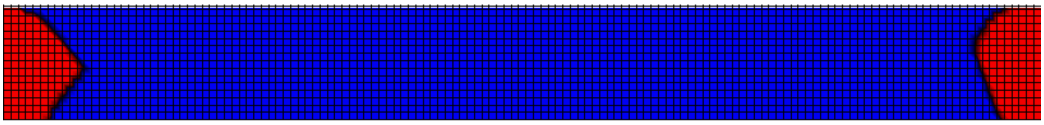

(j) *Delamination at the termination of the analysis. The applied displacement is 0.97 mm. The delamination length is 126.5 mm.*

Figure 9.2: *(cont.) Out-of-plane displacement and delamination front of SSCS_QS_*80 *at five moments of the analysis. Displacement in mm. The displacement scaling factor is 3. For the delamination blue (centre) nodes are released, red (outer) nodes are tied. The delamination is viewed from the skin side of the specimen. The top edge of the delamination is the inside edge of the stiffener flange.*

9.1 Strain Energy Release Rate distribution

The Strain Energy Release Rate (SERR) distribution along the delamination front has been extracted from the analysis results and has been plotted in figure 9.3 for all three delamination opening modes. The SERR is calculated during the analysis as discussed in section 2.4. When the calculated value exceeds the critical SERR value, the node at which the critical value is exceeded is released and the delamination is propagated. The four moments at which the SERR distribution is shown correspond to the last four moments for which the displacement and delamination figures were shown before. The SERR distribution is only shown for one side of the delamination, corresponding to the right hand side of the delamination figures shown before. The distribution is shown over the width of the stiffener flange, where 0 mm corresponds to the outside edge of the flange, and 15 mm corresponds to the inside edge.

The SERR results shown in figure 9.3 show some sharp peaks and dips. Partly these are caused by corners in the delamination front and are a correct representation of the data. However, to some extent these are caused by the data processing. Gradual nodal release is enabled and the load is transferred from a failing node at the delamination front to the following node over a few increments. This gradual 'hand-over' of the load is not included fully in the data output. For the failing node the peak load value is written out for the rest of the analysis and never decreases. To avoid summing the gradual load increase of the subsequent node to the peak load of the failing node the gradual increases of load are filtered out of the data. The value of the failing node is shown until the next node has ramped up completely. Only then is the value at the next node used. This leads to some dips and peaks in the displayed SERR values across the width of the flange. When the delamination front propagates some nodes along the delamination front may have already ramped up fully while some other nodes are still ramping up. When this occurs some of the values along the previous delamination front are still shown together with some of the values along the subsequent delamination front.

Figure 9.3a shows the Strain Energy Release Rate (SERR) distribution when the first load drop occurs. The distribution is fairly constant over the width of the flange except for the inside corner, where the mode I contribution drops and the mode II and III contributions increase. At the middle of the flange the mode I SERR is around 0.27 kJ/m^2 and the mode II contribution is around 0.12 kJ/m^2 for a mode II mode mixity of 30%.

The delamination front loading at the second load drop, shown in figure 9.3b, has shifted to being mode II and mode III dominated. The delamination front at the outer half of the stiffener flange sees a mode I SERR around 0.17 kJ/m^2, a mode II contribution around 0.42 kJ/m^2, and negligible mode III loading for a mode II mode mixity of 70%. The inner half of the flange is loaded predominantly in mode III, with a mode III mixity around 70%.

At the third load drop the mode I loading is comparable to the mode I loading at the second load drop, but the magnitude of the second and third mode has increased as shown in figure 9.3c. Over the outer half of the flange the mode II mode mixity peaks at 83%. Towards the inner half of the flange the mode mixity shifts to 50% mode II and 40% mode III. The mixity becomes dominated by mode III at the inside corner of the flange.

At the end of the analysis the mode III SERR has risen to around $0.9 kJ/m^2$, for an 80% mode III mode mixity on the inner half of the stiffener flange, as shown in figure 9.3d. The outer half of the stiffener flange has returned to the mode I dominated loading that was present at the first load drop. Here the mode II mode mixity is around 20%.

Clearly, the mode mixity is not constant along the delamination front. Furthermore, the mode mixity changes quite dramatically as the delamination grows. Substantial mode III components are present for a large part of the analysis. In the Benzeggagh-Kenane relation used to determine the mixed mode critical SERR in these models the mode III contributions are lumped together with mode II and are not accounted for separately. This may be acceptable when mode III components are small or negligible, but it may not suffice when mode III loading becomes dominant.

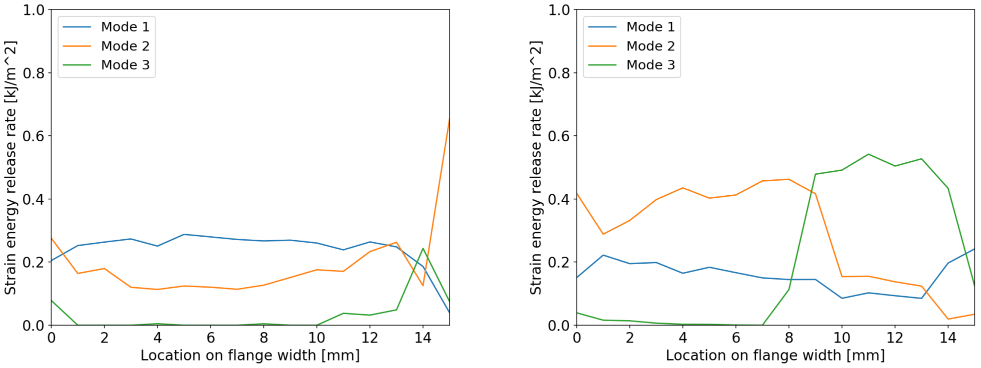

(a) *Strain energy release rate distribution along the delamination front at the first load drop. The distribution is shown at a delamination length of 50.8 mm.*

(b) *Strain energy release rate distribution along the delamination front at the second load drop. The distribution is shown at a delamination length of 75.1 mm.*

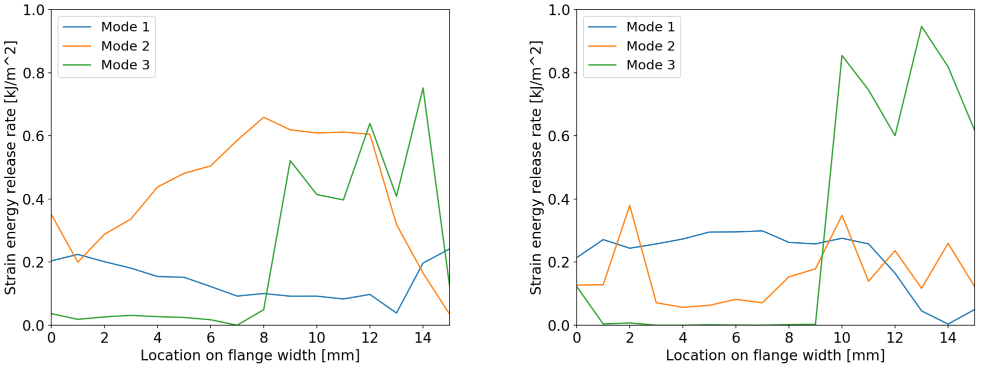

(c) *Strain energy release rate distribution along the delamination front at the third load drop. The distribution is shown at a delamination length of 95.1 mm.*

(d) *Strain energy release rate distribution along the delamination front at the end of the analysis. The distribution is shown at a delamination length of 126.5 mm.*

Figure 9.3: *Strain energy release rate distribution along delamination front of SSCS_QS_*80 *at four moments during the analysis. The distribution is shown over the width of the stiffener flange. 0 mm is the outside edge of the flange, 15 mm is the inside edge of the stiffener flange. The distribution on one side of the delamination is shown. The side shown corresponds to the right hand side of the delamination as shown in figure 9.2.*

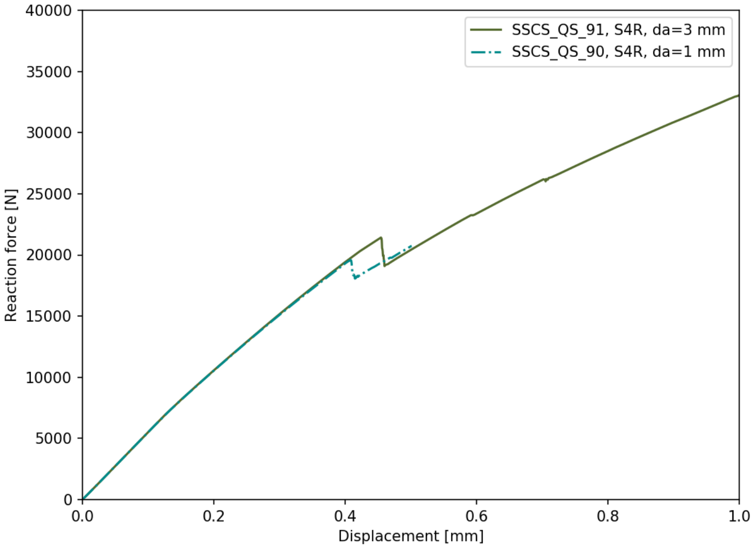

Figure 9.4: *Load against displacement for quasi-static delamination growth of an SSCS model with S4R elements with a length of 3 mm and 1 mm.*

9.2 Effect of mesh density and element type

For the 3 mm pitch SC8R model the first load drop occurs at a displacement of 0.39 mm with a reaction load of 19.1 kN. Compared to the finer 1 mm pitch mesh the load is 4.9% higher and the displacement is 5.4% higher. For the coarser model the same correlation between the shifts in buckling mode of the delaminated stiffener flange section and the load drops is observed. The shift from a single half wave buckling mode shape to a two half wave mode shape occurs earlier, at a displacement of 0.42 mm. This shift is not visible as a load drop in figure 9.1 at this magnification; the flange buckles initially in a single half wave and shifts to the second mode before the whole model has settled from the first load drop. The shift to the three half wave mode correlates with the last load drop which occurs much later, at a displacement of 0.78 mm with a reaction force of 27.5 kN, than for the finer mesh model.

Both the 1 mm and 3 mm pitch model geometries have been replicated with S4R elements and the results are shown in figure 9.4. Using identical steps and settings as for the SC8R models the solution of the fine mesh S4R model did not converge beyond a displacement of 0.50 mm. The first and only load drop occurred at a displacement of 0.41 mm with a reaction force of 19.6 kN. The coarse mesh does show three load drops, although the latter two are very small. For the coarse mesh the first load drop occurred at a displacement of 0.45 mm with a reaction force of 21.4 kN. The second load drop occurred at 0.59 mm with a reaction force of 23.3 kN. The third load drop occurred at a displacement of 0.71 mm with a reaction force of 26.3 kN. The buckling mode shape behaviour differed from that observed for the SC8R model. The first load drop still correlates with the occurrence of local buckling in the stiffener flange, but the buckle deflects towards the skin rather than away from it as for the SC8R models. The second load drop corresponds to a shift from a one half wave buckling mode to a two half wave buckling mode as for the SC8R models. However, the third load drop correlates with an inversion of the two half wave buckling mode shape. No three half wave buckling mode shape is observed for the delaminated stiffener flange.

The results for both S4R and SC8R element types with the 1 mm pitch mesh can be compared in figure 9.5. The S4R load drop occurs at a 10.8% higher displacement and a 7.7% higher load compared to the SC8R model. The model compliance agrees well between element types both before

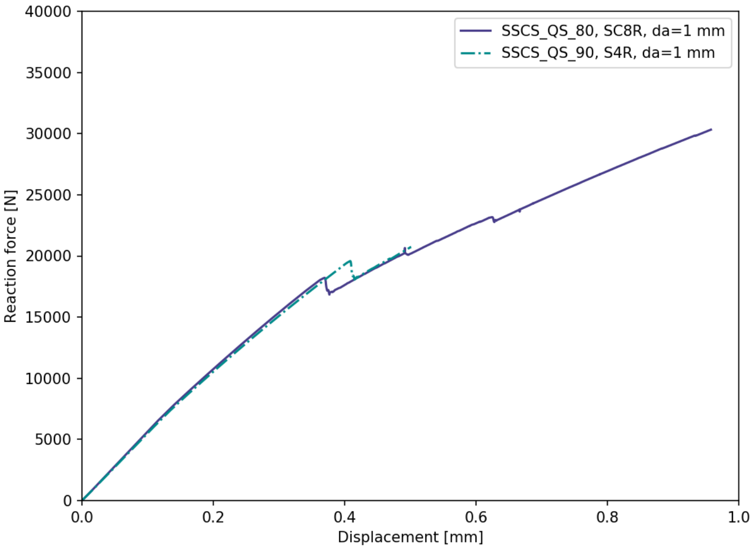

Figure 9.5: *Load against displacement for quasi-static delamination growth of an SSCS model with SC8R elements and S4R elements with a length of 1 mm.*

and after the first load drops.

From both the S4R and SC8R models it appears that mesh refinement is associated with a reduction in the load and displacement at which the first load drop occurs. If the mesh convergence observed for the DCB and MMB specimens holds it may be argued that the SC8R model is likely to have better mesh convergence at any particular mesh size than the S4R model. The SC8R model results are then expected to be more accurate than the S4R results for the 1 mm pitch mesh. Additionally, if the mesh convergence results of the DCB and MMB specimens may be generalised it would be expected that the first load drop reduces by a further few percentage points with a reduction of the mesh size to 0.5 mm.

The CPU time required for the coarse and fine mesh SC8R and S4R models are shown in table 9.1 to indicate the relative computational load. The models were computed on 20 Intel Xeon E5-2640 v4 CPU cores each. The 1 mm pitch mesh S4R model terminated at 50% step time. Because substantially smaller increments are required during delamination propagation the computational effort is not equally distributed over the step time and the 1 mm pitch mesh results cannot be compared to each other directly for the two element types. Comparing the 3 mm pitch mesh results shows an 46% decrease in CPU time for the SC8R model relative to the S4R model. Taken together with the accuracy of the SC8R and S4R models discussed before it would appear that using SC8R elements is preferred for Single Stringer Compression Specimens .

A 49 fold increase in CPU time is associated with reducing the mesh pitch from 3 mm to 1 mm for the SC8R models. If a similar increase would be required to reduce the mesh pitch to 0.5 mm or smaller increase in computational expense is not worth the improvement in accuracy, which is expected to be at most a few percentage points as discussed before. This means that further mesh refinement with uniform meshes is not advised. To limit the increase in computational expense, or potentially even to reduce the computational expense, but still improve the mesh convergence associated with the VCCT a biased or locally refining meshing approach may be explored where the mesh is refined preferentially in the delamination propagation zone.

Table 9.1: *CPU time and walltime for the selected SSCS analyses. Jobs executed on 20 cores each.*

Analysis	CPU time [hh:mm:ss]	Wall time [hh:mm:ss]	Details
SSCS_QS_80	166:43:22	15:32:34	SC8R, da=1 mm
SSCS_QS_90	78:13:56	09:10:25	S4R, da=1 mm, terminated at 50% step time
SSCS_QS_92	03:07:01	00:19:12	SC8R, da=3 mm
SSCS_QS_91	05:46:28	00:56:20	S4R, da=3 mm

9.3 Verification

For verification the model results have been compared to an available parametric S4R based SSCS model, referred to as the reference model. The properties used for the reference model and the presented S4R and SC8R model were matched to generate comparable results. Since this parametric model as provided had been set up at a mesh pitch of 3 mm, this same nominal pitch was used for the presented models. Shown here are only the final results for the presented models which match quite well with the reference model as discussed below. As may be deduced from the index in the analysis names, a few attempts were required before satisfactory results were obtained.

Some small differences exist in the model construction of the reference model relative to the presented models, mainly due to the parametrisation of the reference model. Originally only an SC8R SSCS model had been constructed which was being compared to the reference model. The S4R model was constructed specifically to be able to separate the effect of the modelling differences between the SC8R model and the reference model from the differences caused by the use of the different element types.

Comparing the reference model to the S4R model it can be seen that the compliance is well matched, both before and after the first load drop. The first load drop of the reference model occurred at a displacement of 0.47 mm with a reaction force of 22.1 kN. This displacement was 4.4% higher than for the S4R model and the load was 3.3% higher. The reference model showed the same buckling behaviour during the first load drop as the S4R model, where the delaminated section of the stiffener flange buckled towards the skin in a single half wave mode and then shifted to a two half wave mode before the model settled. Contrary to the S4R model the reference model did show a load drop that corresponded to a shift from a two half wave buckling mode to a three half wave buckling mode for the delaminated stiffener flange section. Because the same properties, parameter values, and element type were used for both the S4R and the reference model it could be argued that only the modelling differences between the models are responsible for the difference in results. Because the modelling approach was consistent for the presented S4R and SC8R models in addition to the material properties and parameter values it could then also be argued that this leaves only the difference in element type as the cause for the different results of the presented models.

The specimen compliance of the 3 mm pitch models is well matched between the S4R and SC8R models before the first load drop occurs, just as for the 1 mm mesh pitch models discussed before. The first load drop of the SC8R model occurs before the first load drop of the S4R model at an applied displacement of 0.39 mm and a reaction force of 18.9 kN. The first load drop of the S4R model occurred at an applied displacement of 0.45 mm, 15% higher, and at a reaction force of 21.2 kN, 12% higher. The model compliance is less well matched after the first load drop. Just after the S4R load drop the compliance of the models is the same, but at the end of the analysis the reaction force of the S4R model is 5% higher than the reaction force of the SC8R model.

9.4 Validation

For validation the models are compared to experimental test data from a quasi-static delamination growth test campaign [58]. In this campaign six Single Stringer Compression Specimens were tested, two pristine specimens, two specimens with an initial delamination of 20 mm and two specimens

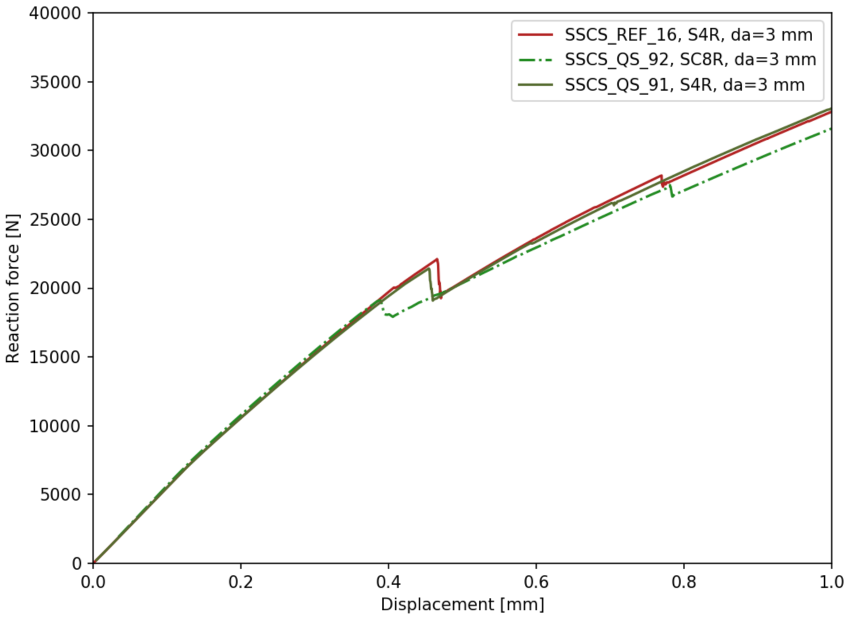

Figure 9.6: *Load against displacement for quasi-static delamination growth of an SSCS model with SC8R elements and S4R elements with a length of 3 mm and an S4R reference model.*

with an initial delamination of 40 mm. Only the test data for the specimens with a 40 mm initial delamination is shown here, in figure 9.7. The experimental results are compared to the 1 mm element size results of both the SC8R and S4R models. The global buckling mode shape of these analyses is inverted compared to the global buckling mode shape of the experimental results because this creates a more critical delamination opening mode as explained in section 8.4. To compare the numerical results to the experimental results with matching global buckling mode shapes results from SSCS_QS_83 are presented, for which the initial imperfection has been inverted relative to SSCS_QS_80 and 90 making it the same as the experimentally observed buckling modeshape.

SSCS_QS_83 failed to converge after the first load drop which occurs at a displacement of 0.50 mm with a reaction force of 23.8 kN. The convergence issue correlates with the occurrence of contact closure at three nodes. Improving the convergence of this model has not been pursued since having the initial load drop is enough to make a comparison.

The overall trend of the analysis results matches the experimental results, although a difference in stiffness between the numerical results and the experimental results can be observed in figure 9.7 both before and after the first load drops. This may be due to one or a combination of several of the following causes. The test specimens have geometrical imperfections compared to the nominal specimen dimensions used for the model. The measured imperfections [58] include variation in the potting length, the overall specimen length, the alignment of the loaded surfaces of the pottings, the alignment of the skin and the stiffener to each other, the alignment of the specimen to the loaded surfaces, and the flatness of the specimen. Potential other sources of this stiffness difference may be the misalignment of plies in the skin and the stiffener, taper at the sides of the stiffener flanges, or scatter in the material properties of the batch of material used in the specimen production. In addition to these imperfections part of the difference may also be caused by the assumed boundary conditions. The modelled pottings have infinite stiffness for lateral and out-of-plane displacements and all rotations, and have no stiffness for longitudinal displacements. The difference in rotational stiffness compared to the actual pottings especially may influence the stiffness of the specimen in post-buckling; the real boundary condition will be somewhere between a pinned and a clamped

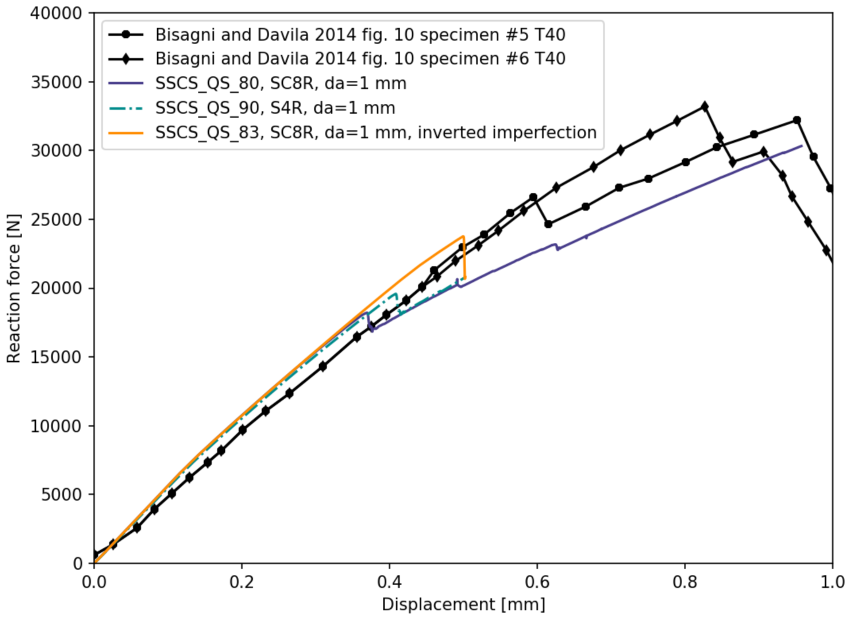

Figure 9.7: *Load against displacement for quasi-static delamination growth. Experimental results and numerical results of an SSCS model with SC8R elements and S4R elements with a length of 1 mm.*

boundary condition due to elasticity at the root whereas the numerical boundary condition simulates a pure clamped condition.

Comparing the load drop of SSCS_QS_83 to the experimental results shows a 20% increase in the displacement with a 12% increase in load for specimen #5 and a 66 % increase in displacement with a 40% increase in load for specimen # 6. This difference may be due to residual adhesion at the initial delamination in the test specimens. This residual adhesion may have a substantial spread considering the differences between the two test results, although too few results are available to make any statistical claims. For the numerical results it has been assumed that no residual adhesion is present. Additionally a frictionless interface between the delaminated stiffener flange section and the skin is assumed.

The remaining difference in the first load drop between SSCS_QS_83 and SSCS_QS_80 is due only to the inversion of the initial imperfection, and with that the inversion of the global buckling mode shape.

The collapse of the experimental specimens, visible by the sharp drop in reaction force at the end of the graph, is not captured by the numerical models presented here. This is because no failure criterion has been implemented. It was chosen not to implement such a criterion because the regime of interest for this research starts at the buckling point and ends just before final failure, where the delamination growth occurs in the specimen. Capturing the final failure of the specimen was outside the scope of this research.

The out-of-plane deformation of the SC8R model (SSCS_QS_80) is compared to the out-of-plane deformation of test specimen QS-40 from [57] in figure 9.8. Although the nominal specimen geometry is slightly different between these, the models have stiffener flange widths of 15 mm and the test specimen has stiffener flange widths of 17 mm, their displacement can still be compared qualitatively. The legend of the numerical results has been matched to the convention used for the experimental results. In all cases the specimen is viewed from the skin side.

The displacement before any delamination growth has occurred is shown in figures 9.8a and 9.8b. As discussed before, the magnitude of the buckling mode shape is inverted between this numerical model and the experimental specimen. Otherwise, the buckling mode shape matches well. The two free edges of the skin have buckled in a three half wave buckling mode, as has the skin at the centre of the specimen in between the two stiffener flanges. This same shape is observed for both the numerical and experimental results.

The buckling mode shape after the initial delamination has opened up is shown in figures 9.8c and 9.8d. The numerical model is shown at the same applied load as the test specimen, at 24.5 kN. The buckling mode shape agrees rather well between them, both in overall shape and in the direction in which the skin has buckled. On the delamination side of the specimen the skin has buckled in a large single half wave buckling mode, which extends for nearly the full length of the specimen. The skin on the other side of the specimen still has a three half wave buckling mode shape, but has inverted for the numerical results compared to the mode shape present before any delamination growth occurred.

The buckling mode shape of the experimental specimen at the end of the experiment is shown in figure 9.8e. The delamination has spread to the other flange of the stiffener and the skin has formed a tunnel. The skin is completely detached from the stiffener over the middle third of the specimen. A corresponding numerical result is not available. The Virtual Crack Closure Technique used for this research can only propagate an existing delamination. No delamination is able to initiate between the skin and the other stiffener flange. As a consequence this behaviour cannot be captured.

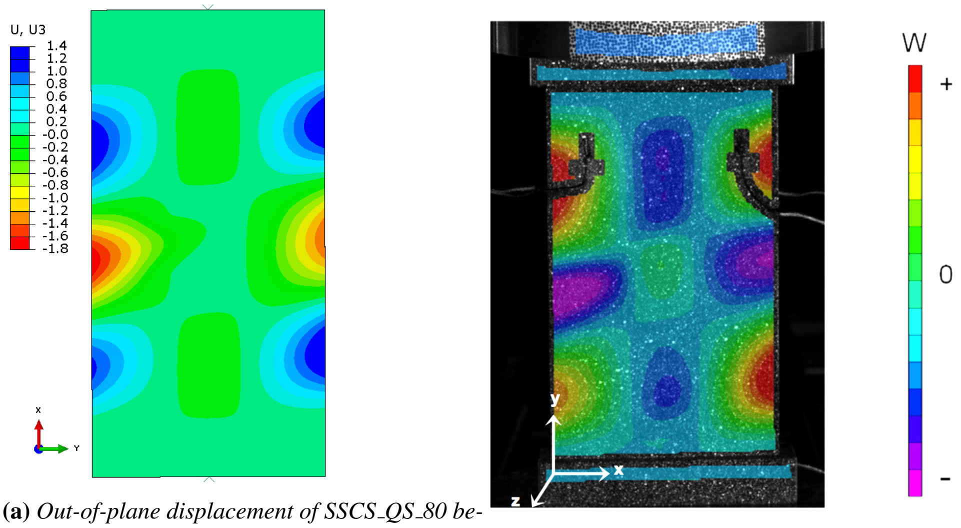

(a) *Out-of-plane displacement of SSCS_QS_80 before delamination growth has occurred. Displacement in mm. Delamination length is 40 mm.*

(b) *Out-of-plane displacement of test specimen QS-40 from [57] before the initial delamination opened up.*

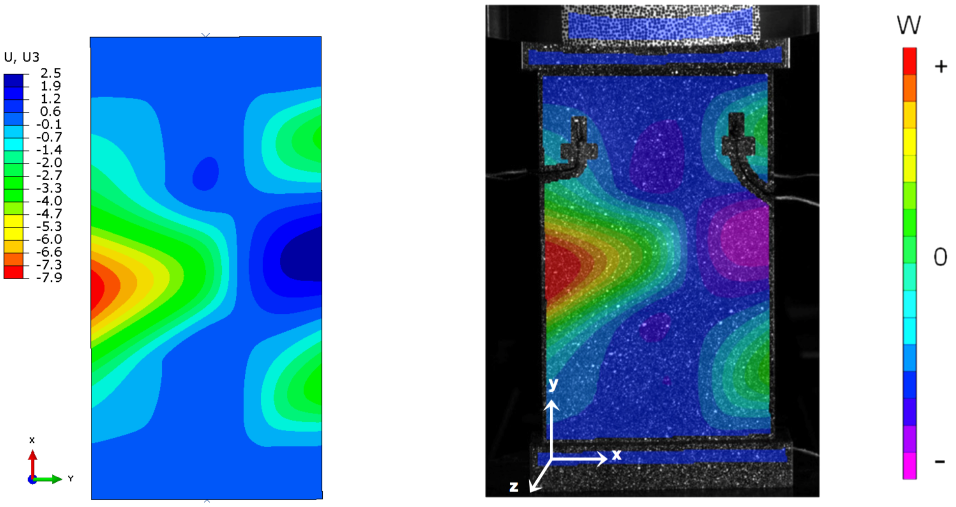

(c) *Out-of-plane displacement of SSCS_QS_80 at the end of the analysis. Displacement in mm. Delamination length is 126.5 mm.*

(d) *Out-of-plane displacement of test specimen QS-40 from [57] after the initial delamination opened up.*

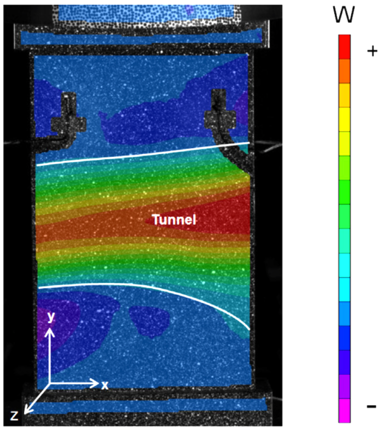

(e) *Out-of-plane displacement of test specimen QS-40 from [57] after the delamination propagated to the other stiffener flange.*

Figure 9.8: *Out-of-plane displacement for analysis SSCS_QS_80 and test specimen QS-40 from [57] at selected moments during the delamination growth. All are viewed from the skin side of the specimen. The colouring of the legend of the numerical results has been inverted to match the convention used for the experimental results.*

Chapter 10

SSCS fatigue delamination propagation results

The Single Stringer Compression Specimen (SSCS) model described in chapter 8 has been analysed under fatigue load conditions. A triangular load cycle definition was used to define the load applied to the model. The model was analysed with a number of fatigue loads to check if the behaviour of the method met expectations at each of the loads. The lowest selected load was 7 kN, where the panel has just entered the post-buckling regime and the delamination front is starting to see loading from the out-of-plane displacement of the specimen. The other three selected loads were based on a scaling of the critical load at which quasi-static delamination growth occurs. The critical load was determined using the quasi-static growth models discussed in the previous chapter and was 16.4 kN for the fatigue Single Stringer Compression Specimen geometry. The specimen was loaded at 67 % of the critical load (11 kN), 80% of the critical load (13.14 kN), and 85% of the critical load (13.94 kN). For all four loads the load ratio was 0.1. The model geometry was the same for all analyses.

When setting up the analysis a set of delamination initiation and propagation parameters must be chosen for the Paris relation used to calculate the delamination growth rate. These parameters vary with mode mixity and four sets are available from the DCB and MMB models discussed before, shown in tables 5.4 and 5.9. The chosen set of parameters cannot be updated during the analysis at this time, effectively meaning that a single fixed mode mixity value must be assumed for the entire analysis. Results using the 20% and 50% mode II mode mixity parameter sets are reported.

10.1 Fatigue load at 43 % critical load

At a load of 43% of the critical load, or 7 kN, the panel has just entered the post buckling regime at the peak of the applied load cycle. At a load of 7 kN the panel had just entered the post-buckling regime and fully formed three half wave buckling mode shapes could be observed in the skin. The delamination front is starting to see load due to the out-of-plane displacement of the specimen. 50% mode II propagation parameter values were used. No fatigue delamination growth occurred. Instead the first load cycle was re-applied over and over again until the analysis was terminated manually.

This behaviour is unexpected. If the applied load is too low for fatigue delamination growth to occur it would be expected that the analysis jumps to the fatigue cycle limit set for the analysis without releasing any nodes after the first load cycle is applied. At this point it would be expected that the analysis is terminated due to reaching the fatigue cycle limit. Instead the first load cycle is applied again and again indefinitely. Explaining this behaviour is difficult; reviewing the manual has not been beneficial. It is currently unclear why this behaviour occurred.

10.2 Fatigue load at 67 % critical load

With a fatigue load of two thirds of the critical load (11 kN), only a single node was released before the analysis terminated. This behaviour was observed in two separate analyses using either 20 % mode II (SSCS_CAF_51) or 50% mode II (SSCS_CAF_46) delamination growth parameters. A total of 42 load cycles were applied to the 20% mode II analysis. Because of the cycle jumping mechanism implemented in the routine a fatigue cycle count of 4617 cycles was reached before the analysis terminated. In figure 10.1 the applied load is plotted against the fatigue cycle count. This shows at which fatigue cycle counts the load cycles were applied to the model. It also shows the cycle jumping that occurred. The first applied load cycle is followed by a cycle jump where the fatigue cycle count is increased from 1 to 858 cycles. During this first cycle jump the first and only node release occurs. A second load cycle is applied and subsequently the fatigue cycle count is incremented to 4079 cycles. At this point 40 load cycles are applied with small increments in fatigue cycle count between them until the analysis terminates.

For the analysis using 50% mode II delamination propagation parameters a total of 41 load cycles were applied and a fatigue cycle count of 50559 was reached before it terminated. In figure 10.2 the applied load is plotted against the fatigue cycle count which shows the cycle jumping that occurred. After the first load cycle was applied the cycle count jumped to 106 cycles. Subsequently 12 load cycles were applied for which the fatigue cycle count was increased from 106 to 130 cycles. The first and only node release occurred in the cycle jump from a cycle count of 130 to 1845 cycles. A single load cycle was applied at a cycle count of 1845 followed by a jump to a cycle count of 48 708 cycles. A further 27 load cycles were applied before the analysis was terminated at a cycle count of 50 559 cycles.

The behaviour is unexpected, more than one node should have been released. Unlike the analysis results obtained at 7 kN discussed before, at least one node is released. This indicates that the load is not too low for any delamination growth to occur at the start of the analysis. Because the analysis is conducted under load control and because the specimen stiffness reduces with increasing delamination length the peak displacement applied to the end of the specimen will increase with delamination extension. Due to this increasing end displacement the out-of-plane displacement is expected to increase as the delamination grows. Because the delamination growth rate is driven by the delamination opening which increases with increasing out-of-plane displacement, the delamination growth rate increases after the first node is released and hence the delamination growth should not be arrested at this point. The load is also not high enough to cause quasi-static delamination growth, indicated by the analysis results obtained at higher load levels discussed later. At present, it cannot be explained why the analysis is terminated with only a single released node.

The cycle jumping behaviour that can be observed is also unexpected. For 40 of the load cycles applied to the model no nodes were released. This means that nothing about the model has changed between these load cycles. Re-applying the load cycles is a duplication of effort as the calculated Strain Energy Release Rate is the same every time. According to the manual the express purpose of the cycle jumping routine is to prevent this duplication of effort. It cannot be explained why the cycle jumping mechanism failed to work for these analyses. Changing only the magnitude of the applied load for analyses discussed later produced much better cycle jumping behaviour. Similar failure of the cycle jumping mechanism was observed for some of the Mixed Mode Bending specimen analyses discussed in section 7.2. Also unclear is what caused the analyses to terminate when they did. Both analyses were terminated because the minimum time increment was reached, i.e. the solution failed to converge. There is no readily apparent difference between any of the last 40 load cycles. No explanation why the solution convergence failed in the last load cycle, rather than in any of the others has been found.

10.3 Fatigue load at 80 % critical load

The fatigue load was increased to 80% of the quasi-static delamination propagation load (SSCS_CAF_53), or 13.14 kN. This scaling matches the scaling used for the experimental results discussed later. 20%

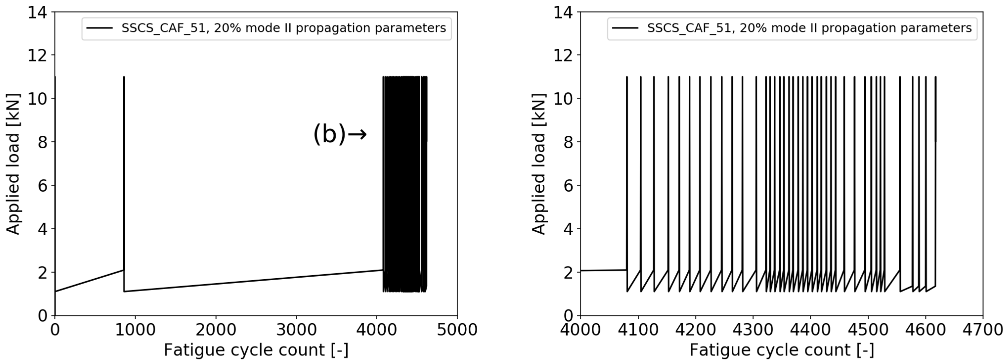

(**a**) *Full view.* (**b**) *Detailed view of the last 40 applied load cycles.*

Figure 10.1: *Applied load cycles against fatigue cycle count for SSCS_CAF_51. Peak load was 11 kN, minimum load was 1.1 kN. Propagation parameters for 20% mode II loading.*

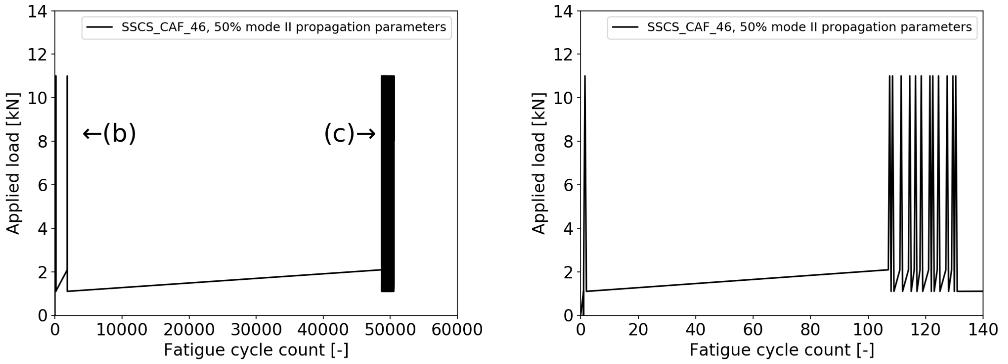

(**a**) *Full view.* (**b**) *Detailed view of the first 13 applied load cycles.*

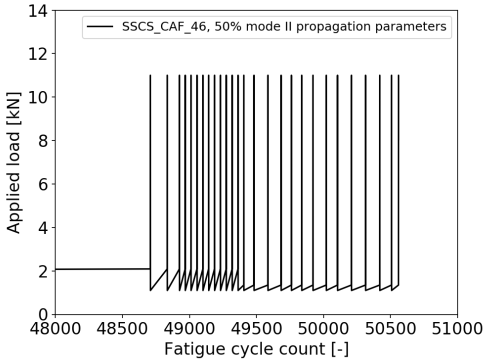

(**c**) *Detailed view of the last 27 applied load cycles.*

Figure 10.2: *Applied load cycles against fatigue cycle count for SSCS_CAF_46. Peak load was 11 kN, minimum load was 1.1 kN. Propagation parameters for 50% mode II loading.*

mode II delamination propagation parameters were used. A total of 43 load cycles were applied to the model before the analysis was terminated. In figure 10.3 the applied load is plotted against the fatigue cycle count showing the cycle jumping that occurred. Good cycle jumping is observed, without large clusters of applied load cycles for which no nodes were released.

The out-of-plane displacement of the specimen at an applied load of 13.14 kN before any delamination growth has occurred is shown in figure 10.4. For every load cycle applied during the

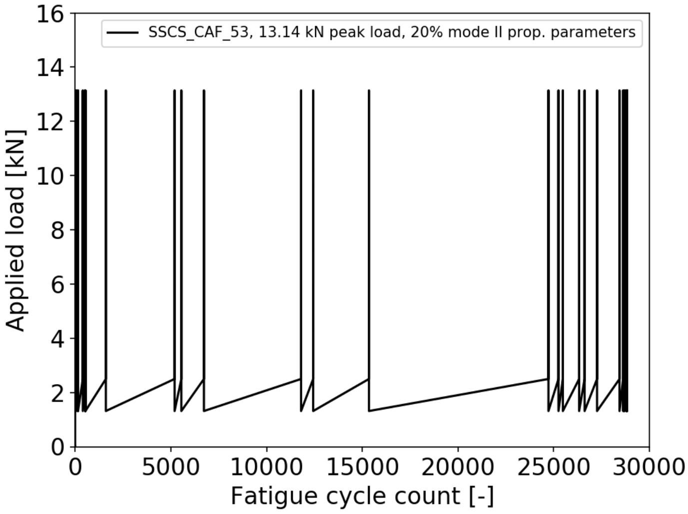

Figure 10.3: *Applied load cycles against fatigue cycle count. Peak load was 13.14 kN, minimum load was 1.314 kN. Propagation parameters for 20% mode II loading.*

analysis the skin buckles in a three half wave buckling mode shape. The same buckling mode shape was observed in the quasi-static analyses discussed in chapter 9 before any delamination growth occurred.

The delaminated section of the stiffener flange does not buckle locally at any point during the analysis until a fatigue cycle count of 28 830 cycles is reached. From a cycle count of 28 830 to the final cycle count of 28 836 cycles the delaminated section of the stiffener flange begins to buckle locally at the peaks of the applied load cycles. The out-of-plane displacement of the stiffener flange is plotted in figure 10.5a against the fatigue cycle count for the last eight applied load cycles. As a load cycle is applied to the specimen, the global buckling mode shape of the skin serves to pull the stiffener flange downwards. At the peak load the stiffener flange suddenly buckles upwards, visible as the sharp upward peaks in the figure. The magnitude of the out-of-plane displacement of the local buckle in the stiffener flange at peak load increases over the last few load cycles. On the plot the red dot marks the moment at which the out-of-plane displacement of the delaminated flange section is shown in figure 10.5. A modest upward buckle may be observed in the stiffener flange.

The delamination between the stiffener flange and the skin is shown in figure 10.6 at four fatigue cycle counts. The delamination is viewed from the skin side of the specimen. The delamination grew from an initial length of 40 mm to a length of 53.4 mm averaged over the width of the flange before the analysis was terminated. The delamination growth started at the three of the four corners of the tied stiffener flange sections. It grew slowly in these three corners over the course of the first 26 329 cycles. At this cycle count 45 nodes have been released. Since the stiffener flange is discretised with 18 nodes across the width, this results in an average delamination growth rate of $9.4 \cdot 10^{-5}$ mm per fatigue cycle. The delamination propagation rate increased after this cycle count. In the cycle count interval from 26 329 to 28 803 cycles an additional 81 nodes were released, which brings the average rate up to$1.8 \cdot 10^{-3}$ mm per fatigue cycle. In the last 33 fatigue cycles, from 28 803 to 28 836 cycles, from an additional 116 nodes were released, for an average growth rate of $2.0 \cdot 10^{-1}$ mm per fatigue cycle. This sharp increase in delamination growth rate correlates with the local stiffener flange buckling which also starts at a fatigue cycle count of 28 803. The analysis was terminated because the critical strain energy release rate was reached, beyond which the delamination grows quasi-statically.

Changing to 50% mode II delamination propagation parameters, at a fatigue load of 13.14 kN (SSCS_CAF_45), a total of 72 load cycles were applied to the model before the analysis was terminated. The fatigue cycle count was 2550 cycles at termination. A total of six nodes were released during the analysis. For the majority of the applied load cycles, no nodes were released. The applied

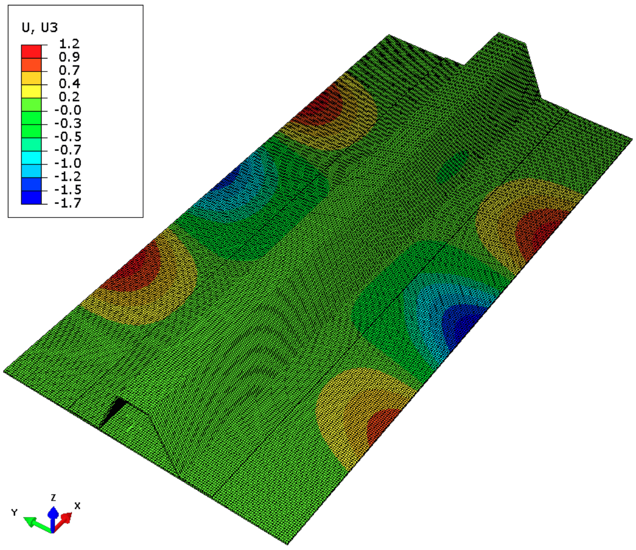

Figure 10.4: *Out-of-plane displacement in mm of the specimen from analysis SSCS_CAF_53 at the peak load application in the first load cycle. The applied load at this time was 13.14 kN.*

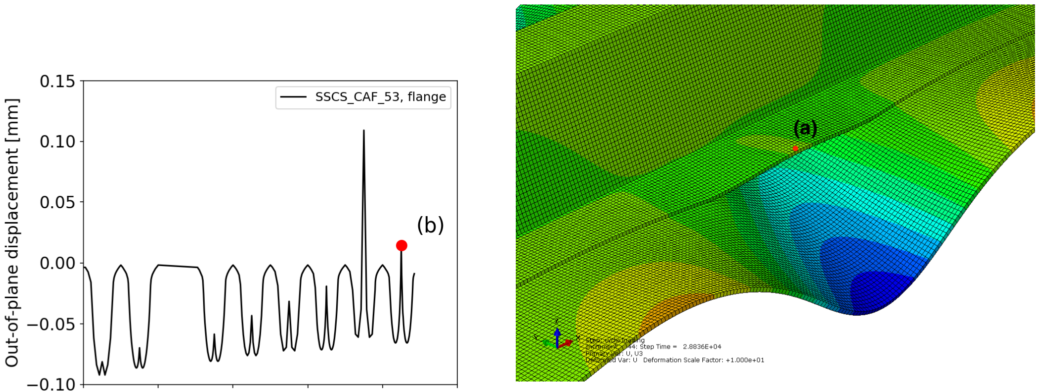

(a) *Out-of-plane displacement of the stiffener flange against the fatigue cycle count of SSCS_CAF_53. The red dot indicates the moment at which the out-of-plane displacement is plotted in (b).*

(b) *Detailed view of the out-of-plane displacement of the delaminated stiffener section of the specimen from analysis SSCS_CAF_53. The applied load at this time was 13.14 kN and the fatigue cycle count was 28836. The red dot indicates the location of which the displacement is plotted in (a).*

Figure 10.5: *Local buckling of the stiffener flange. The out-of-plane displacement is plotted for the last eight load cycles applied to the model in (a). For every load cycle the flange is first pulled downwards by the global buckling of the skin. At every load peak the flange buckles locally in the positive out-of-plane direction. The magnitude of the local buckling increases with increasing fatigue cycle count. The displacement of the flange is shown in figure (b) at the peak applied load of the last load cycle, as indicated in (a).*

load cycles are plotted against the fatigue cycle count in figure 10.7. Good cycle jumping is not observed. Three clusters of applied load cycles can be seen. The first is a cluster of 9 cycles at the start of the analysis. The second cluster is a cluster of 12 cycles starting at a fatigue cycle count of 579 cycles. The third cluster contains the last 48 cycles applied to the model. The remaining three cycles out of the total of 72 were not clustered together with any others. It is currently unclear why

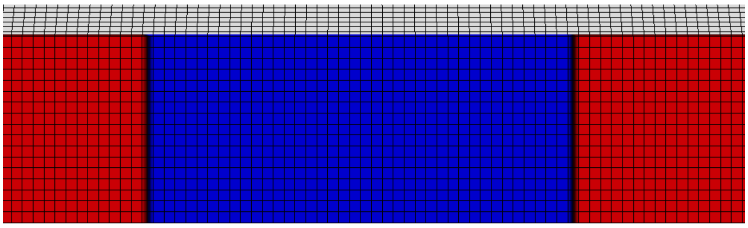

(a) *Initial delamination with a length of 40 mm.*

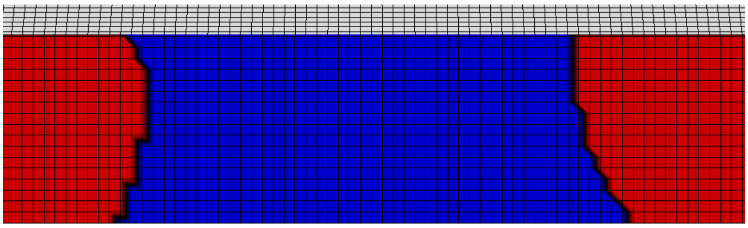

(b) *Delamination at a fatigue cycle count of 26 329 cycles. The average delamination length is 42.5 mm.*

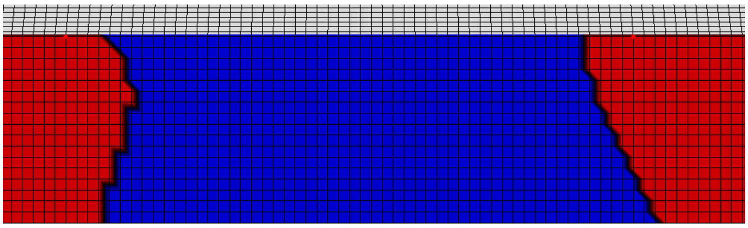

(c) *Delamination at a fatigue cycle count of 28 803 cycles. The average delamination length is 47.0 mm.*

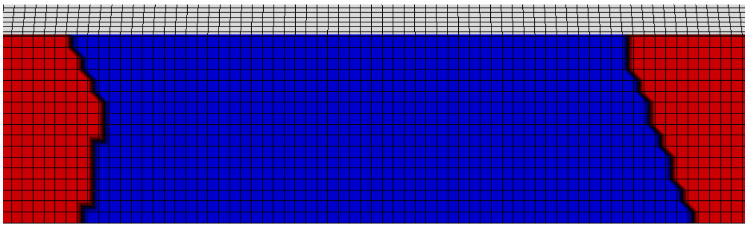

(d) *Delamination at a fatigue cycle count of 28 836 cycles. The average delamination length is 53.4 mm. The analysis was terminated at the end of this cycle.*

Figure 10.6: *Delamination front of SSCS_CAF_53 at four fatigue cycle counts. Peak load was 13.14 kN. Blue (centre) nodes are released, red (outer) nodes are tied.*

changing from 20 % to 50% mode II propagation parameters would cause the cycle jumping to fail. For the MMB specimen analyses discussed in section 7.2 the opposite was observed. There the cycle jumping failed with 20% mode II mode mixity parameters and changing to 50% mode II parameters caused the cycle jumping mechanism to resume operation.

Nodes that have failed are released in a step release fashion for all of the presented fatigue Single Stringer Compression Specimen analyses. The tie that holds the nodes together is pristine until a node has failed, at which point the tie is released. For this application the step release seems to work reasonably well. It appears to be able to capture non-orthogonal and curved delamination fronts to some extent, although more delamination front rounding was observed in the quasi-static analyses which used a gradual nodal release approach. The step release approach may be working fairly well because the delamination is not growing in a self-similar manner. The growth is driven predominantly by global and local buckling mode shapes opening the delamination. These buckling mode shapes

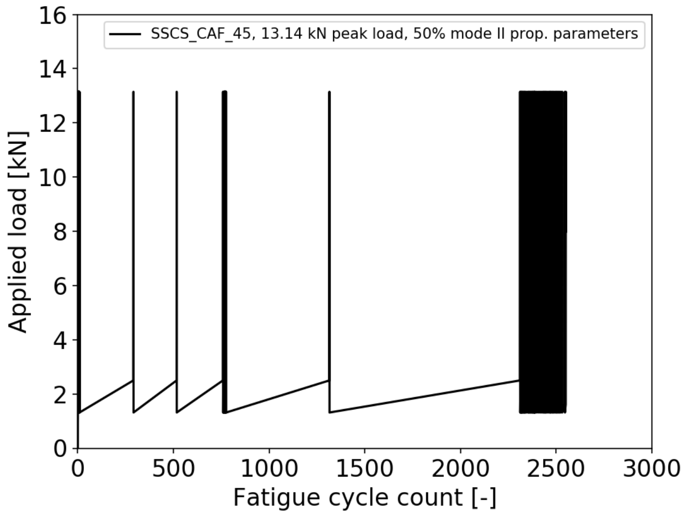

Figure 10.7: *Applied load cycles against fatigue cycle count. Peak load was 13.14 kN, minimum load was 1.314 kN. Propagation parameters for 50% mode II loading.*

are affected by the overall length of the delamination but not by the exact shape of the delamination front. As such, the shape of the delamination front is largely decoupled from the displacement driving the delamination growth. Improvement may still be attained by moving to a gradual nodal release approach, but the current step release approach seems to function well as is.

10.4 Fatigue load at 85 % critical load

An increase in the fatigue load from 13.14 kN to 13.96 kN (SSCS_CAF_54) , or 85% of the quasi-static delamination propagation load, produced results similar to those obtained at 13.14 kN using the delamination propagation parameters for 20% mode II mode mixity. The main differences were that the delamination grew faster, that the delaminated section of the stiffener flange buckled earlier and that quasi-static propagation was reached sooner. The analysis was terminated at a fatigue cycle count of 4687 cycles, at which point 31 load cycles had been applied. A total of 226 nodes were released before the analysis was terminated for a total of 12.6 mm of delamination growth compared to a total of 13.4 mm of delamination growth (242 released nodes) at a load of 13.14 kN (SSCS_CAF_53).

The delamination between the stiffener flange and the skin at a fatigue load of 13.96 kN is shown in figure 10.6 at three fatigue cycle counts. Just as for a fatigue load of 13.14 kN the delamination grows slowly at the start of the analysis and the growth rate increases as nodes are released. At a fatigue cycle count of 4216 cycles 41 nodes have been released, for a an average delamination growth rate of $5.4 \cdot 10^{-4}$ mm per cycle. In the fatigue cycle increment from 4216 cycles to 4673 cycles an additional 39 nodes are released for an average rate of $4.7 \cdot 10^{-3}$ mm per cycle. In the last 14 fatigue cycles an additional 146 nodes are released for an average growth rate of $5.8 \cdot 10^{-1}$ mm per cycle. The delamination has grown from an initial length of 40 mm to a length of 52.6 mm averaged over the width of the stiffener flange when the analysis terminates.

The out-of-plane displacement of the delaminated stiffener flange is shown in figure 10.9 at a scaling factor of 10. Two moments are shown; the left hand image shows the displacement of the flange at the peak load of cycle 4674. No local buckling of the stiffener flange is observable. The displacement at the peak load of cycle 4687 is shown in the right hand image. Local buckling of the stiffener flange is clearly visible. The stiffener flange begins to buckle in load cycle 4675 and the magnitude of the out-of-plane displacement increases in every subsequent load cycle. This local flange buckling correlates with the increase in delamination growth rate from $4.7 \cdot 10^{-3}$ mm per cycle to $5.8 \cdot 10^{-1}$ mm per cycle.

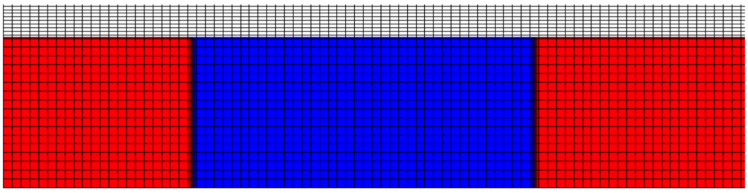

(a) *Initial delamination with a length of 40 mm.*

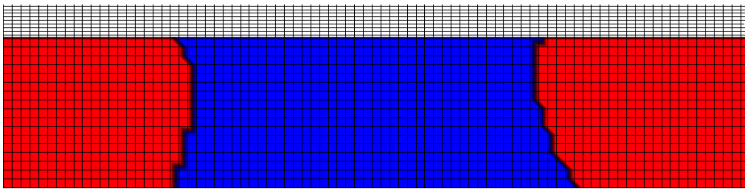

(b) *Delamination at a fatigue cycle count of 4 216 cycles. The average delamination length is 42.3 mm.*

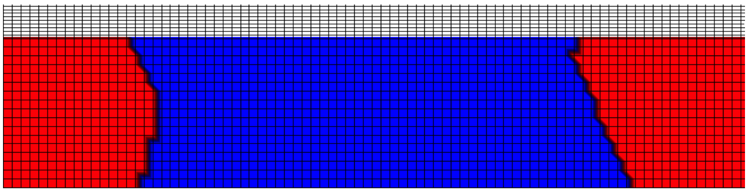

(c) *Delamination at a fatigue cycle count of 4 687 cycles. The average delamination length is 52.6 mm. The analysis was terminated at the end of this cycle.*

Figure 10.8: *Delamination front of SSCS_CAF_54 at three fatigue cycle counts. Peak load was 13.96 kN. Blue (centre) nodes are released, red (outer) nodes are tied.*

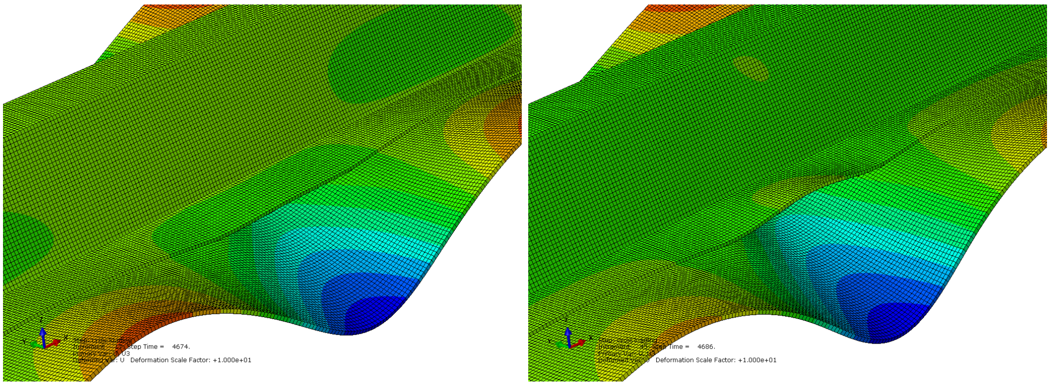

(a) *Out-of-plane displacement at the peak load of cycle 4674. No local buckling of the stiffener flange.* **(b)** *Out-of-plane displacement at the peak load of cycle 4686. Local buckling of the stiffener flange.*

Figure 10.9: *Detailed views of the out-of-plane displacement of the delaminated section of the stiffener flange. SSCS_CAF_54. Peak load was 13.96 kN, minimum load was 1.4 kN. Propagation parameters for 20% mode II loading.*

The increased delamination growth rate compared to a fatigue load of 13.14 kN is due to the increase in the opening of the delamination. The overall delamination growth rate was $4.7 \cdot 10^{-4}$ mm per fatigue cycle at 13.14 kN fatigue load and $2.7 \cdot 10^{-3}$ mm per fatigue cycle at 13.96 kN fatigue load: a 5.7 fold increase. A small part of this is attributable to the increased out-of-plane displacement of the skin. In the first load cycle, before any delamination growth has occurred, the peak out-of-plane displacement of the skin buckle located at the initial delamination is 1.694 mm at a load of 13.14 kN. At a load of 13.96 kN the displacement is 1.782 mm, an increase of 5.2 %. The remainder of the increase in growth rate may be attributed to the increased local buckling of the stiffener flange.

A fatigue analysis is terminated when the critical Strain Energy Release Rate (SERR) is reached and quasi-static growth would occur. For the analysis a threshold is set to determine when this happens. The upper threshold for analysis SSCS_CAF_54 was set to 0.98 times the critical SERR. Increasing the threshold allows additional delamination growth to occur before the analysis is terminated. Increasing the threshold to 0.999 (SSCS_CAF_55) resulted in substantially more delamination growth. In total 94 load cycles were applied and 1278 nodes were released before the analysis was terminated manually. The delamination had grown by 71 mm from an initial length of 40 mm to a final length of 111 mm compared to 13.44 mm of growth with the lower threshold.

For the analysis with the increased upper threshold (SSCS_CAF_55) the delamination initiation criterion had also been disabled. Because of this change in initiation criterion, nodes failed at lower cycle counts and the fatigue cycle count is much lower than for SSCS_CAF_54. Analysis SSCS_CAF_55 was terminated at a fatigue cycle count of 363 cycles. The delamination growth is shown in figure 10.10. In figure 10.10b the delamination front is shown at a cycle count of 277 cycles. 50 nodes have been released for a delamination growth rate of $1.0 \cdot 10^{-2}$ mm per cycle. From a fatigue cycle count of 277 cycles to 300 cycles an additional 301 nodes are released for a growth rate of $7.2 \cdot 10^{-1}$ mm per cycle. At a fatigue cycle count of 277 cycles the delaminated section of the stiffener flange begins to buckle locally at peak load. At a fatigue cycle count of 291 cycles fully established local buckling of the flange is observed. The increase in delamination growth rate follows a similar pattern to SSCS_CAF_54, where a substantial jump occurs at the same time that the stiffener flange begins to buckle locally. For the last 63 applied load cycles no cycle jumping occurred, the fatigue cycle count was increased by 1 cycle for every applied load cycle. 927 nodes were released in these last 63 cycles, for a delamination growth rate of $8.2 \cdot 10^{-1}$ mm per cycle.

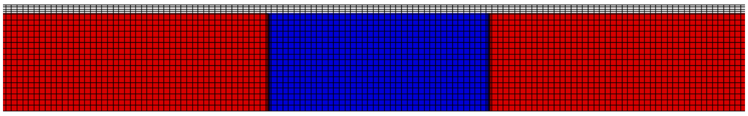

(a) *Initial delamination with a length of 40 mm.*

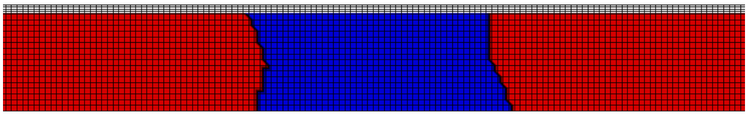

(b) *Delamination at a fatigue cycle count of 277 cycles. The average delamination length is 42.8 mm.*

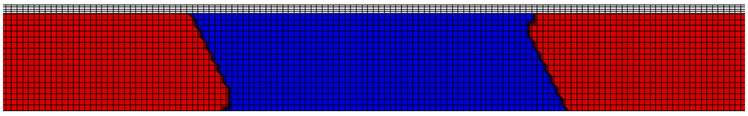

(c) *Delamination at a fatigue cycle count of 300 cycles. The average delamination length is 59.5 mm.*

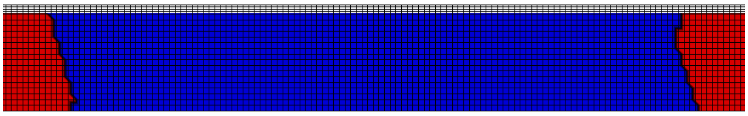

(d) *Delamination at a fatigue cycle count of 363 cycles. The average delamination length is 111 mm. The analysis was terminated at the end of this cycle.*

Figure 10.10: *Delamination front of SSCS_CAF_55 at four fatigue cycle counts. Peak load was 13.96 kN. Blue (centre) nodes are released, red (outer) nodes are tied.*

The out-of-plane displacement of SSCS_CAF_55 at the peak load of the last applied load cycle is shown in figure 10.11. The delamination has fully opened up, and the skin has shifted to a single half wave buckling mode shape. The stiffener flange has buckled into a two half wave mode shape. The stiffener initially buckled into a single half wave mode from a fatigue cycle count of 277 cycles when the delamination length reached 42.8 mm. It shifted to a two half wave buckling mode at a fatigue cycle count of 326 cycles when the delamination length reached 84.1 mm. The buckling mode shape of the skin on the opposite side of the initial delamination reversed in sign when the initial delamination opened up, where the middle buckle now buckles towards the stiffener side of the specimen instead of away from it.

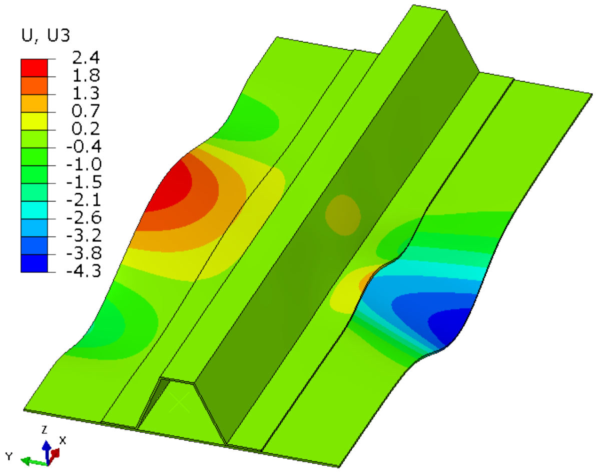

Figure 10.11: *Out-of-plane displacement of SSCS_CAF_55 at the peak load of the last load cycle. Applied load is 13.96 kN. Delamination length is 111 mm. Displacement is in mm.*

Substantial computational resources were required to calculate the results of analysis SSCS_CAF_55. On 20 Intel Xeon E5-2640 v4 CPU cores 605 CPU hours were required. A total of 7558 load increments were computed for a rate of 4.8 minutes per increment. For comparison, 1282 load increments were computed for SSCS_CAF_54 at a total CPU time 97 hours for a rate of 4.5 minutes per increment.

10.5 Comparison to experimental results.

The behaviour of Single Stringer Compression Specimens with a 40 mm initial delamination under fatigue loading was investigated experimentally by Dávila and Bisagni [57]. The experimental campaign is discussed in detail in chapter 4. Three specimens were tested, one under quasi-static loading to determine an appropriate fatigue load followed by two specimens, F40A and F40B, which were tested under fatigue load. The nominal specimen geometry used for the experimental campaign was the same as the geometry that has been used for the numerical analysis results presented in this chapter.

At this time, the data of these two specimens are the only test data available of post-buckled Single Stringer Compression Specimens with a 40 mm initial delamination loaded in fatigue. This limited dataset makes validation of any numerical results difficult. Exacerbating the challenge is that the delamination growth rates observed in the experiment have substantial scatter; the average delamination growth rates were $2.5 \cdot 10^{-3}$ and $1.6 \cdot 10^{-2}$ mm per fatigue cycle for the two specimens. Nevertheless, by comparing the obtained numerical results to these experimental results it can be determined if the growth rates are of a similar order of magnitude. Furthermore, the overall behaviour of the delamination can be compared to see if they are qualitatively similar.

The out-of-plane displacement of specimen F40A is shown in figure 10.12b. The displacement was recorded during the fatigue test before the initial delamination had opened up. The applied load was 12.88 kN at the moment this displacement was recorded. Three half wave buckling mode shapes may be observed in the experimental results which are qualitatively similar to the numerical results of SSCS_CAF_53 shown in figure 10.12a . The main difference is that the buckling mode shape of the numerical results is symmetric about the longitudinal axis of the specimen where the experimental results are antisymmetric. The initial delamination is located towards the left hand side of the panel for both the numerical and the experimental results. The delamination is opened by the buckling mode used for the numerical analysis, leading to a mode I loading component at the delamination front in addition to any mode II and mode III loading. For the experimental specimen the initial delamination is being closed, and little to no mode I loading is expected along the delamination front. As a consequence the delamination propagation rate would be expected to be higher for the numerical specimen than for the experiment specimen. The buckling mode shape of the numerical analysis was chosen on purpose to investigate the more critical delamination front loading, instead of prioritising agreement with the experimental buckling mode shape.

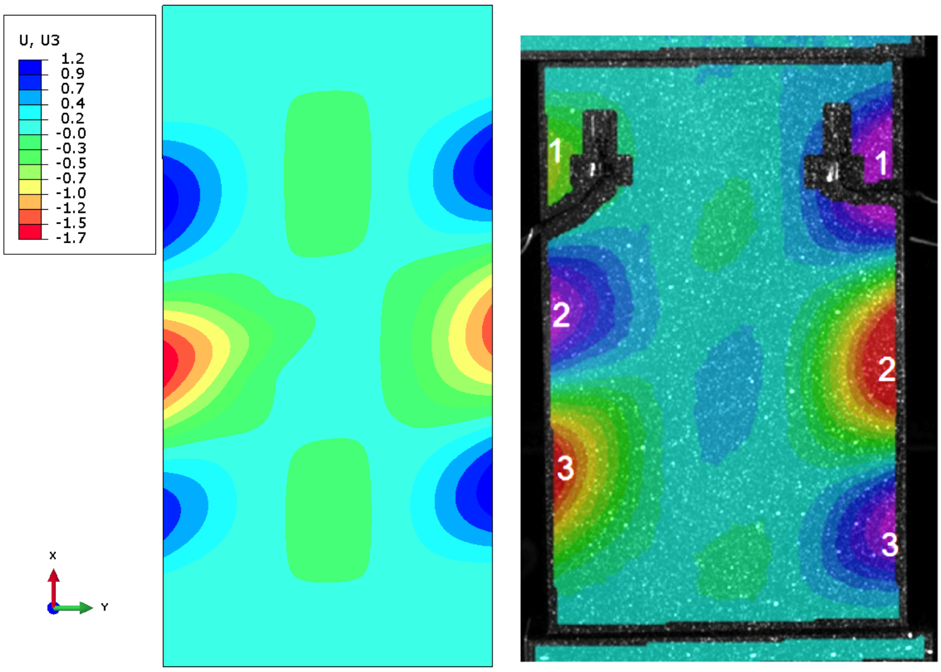

(a) *Out-of-plane displacement of SSCS_CAF_53 at 13.14 kN load before any delamination growth has occurred. Displacement is in mm. Legend has been inverted to match the convention used for the F40B experimental results. Initial delamination located left of centre.*

(b) *Out-of-plane displacement of the fatigue test specimen F40A from [57] at 12.88 kN load before the initial delamination has opened. Initial delamination located left of centre.*

Figure 10.12: *Out-of-plane displacement of the fatigue analysis SSCS_CAF_53 and of the experimental fatigue specimen F40B from [57]. Viewed from the skin side of the specimen.*

The out-of-plane displacement of specimen F40B is shown in figure 10.13b viewed from the skin side of the specimen. The displacement was recorded during the fatigue test after the initial delamination had opened up. The applied load was 23 kN at the moment this displacement was recorded. The delamination length was between 62 and 92 mm. The out-of-plane displacement of the analysis that showed extensive delamination growth (SSCS_CAF_55) is presented in figure 10.13a. The displacement is shown at the end of the analysis, when the delamination had extended from 40 mm to 111 mm in length. Overall the out-of-plane displacement behaviour is qualitatively similar between the numerical results and the experimental results. A large single half wave buckle can be observed in the skin on the left hand side of both specimens, at the location of the delamination. The other side of the skin has buckled in a three half wave buckling mode for both specimens where the middle buckle extends towards the stiffener side of the specimen. The buckles of the experimental results seem to extend further than the numerical results. In particular, the outer two half waves on the right hand of the specimen extend further towards the centreline of the specimen and the large buckle on the left hand side extends further towards the top and bottom of the experimental specimen. This difference is likely the results of the lower applied load, 13.96 kN for the numerical results versus 23 kN for the experimental results. The magnitude of the out-of-plane displacement of the experimental results is not available and cannot be compared to the numerical results.

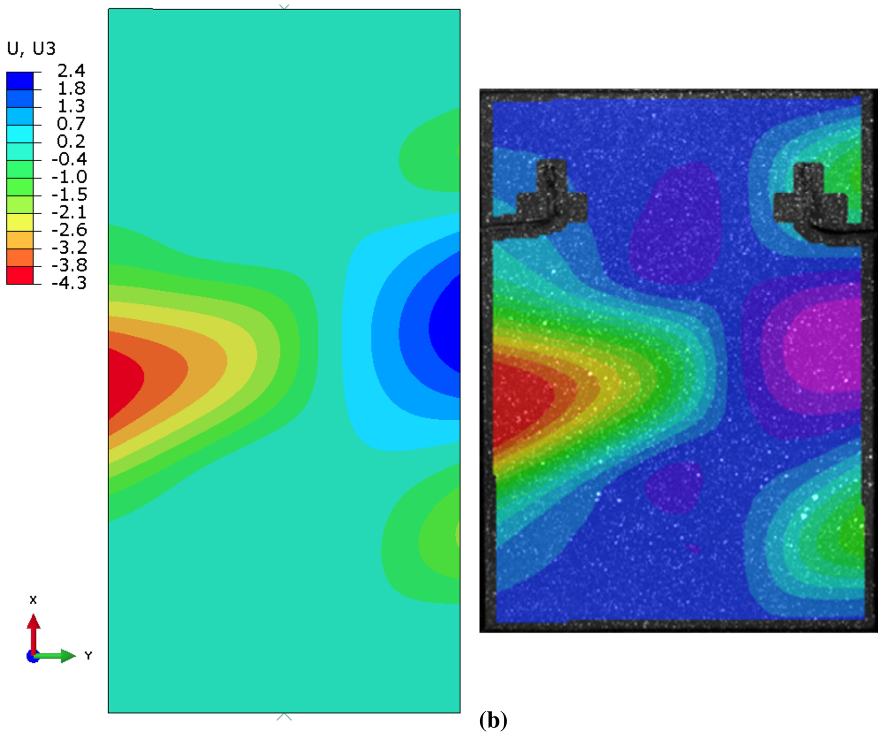

(a) *Out-of-plane displacement of SSCS_CAF_55 at 13.96 kN load during the last load cycle of the analysis. The delamination has extended from 40 mm to 111 mm in length. Displacement is in mm. Legend has been inverted to match the convention used for the F40B experimental results. Initial delamination located left of centre.*

(b) *Out-of-plane displacement of the fatigue test specimen F40B from [57] after the initial delamination has opened. Applied load is 23 kN. Initial delamination located left of centre.*

Figure 10.13: *Out-of-plane displacement of the fatigue analysis SSCS_CAF_55 and of the experimental fatigue specimen F40B from [57]. Viewed from the skin side of the specimen.*

The delamination growth measured by Dávila and Bisagni is shown in figure 10.14. In the experiment a Single Stringer Compression Specimen was subjected to a 23 kN fatigue load. The measured delamination length was 62 mm at 2002 fatigue cycles, 92 mm at 11 850 fatigue cycles and 99 mm at 24 000 fatigue cycles. The delamination extension was characterised by long stretches of load cycling where little delamination growth occurred interspersed by sudden delamination extensions.

The delamination growth rate of the numerical results, averaged over the entire analysis, are $4.6 \cdot 10^{-4}$ mm per fatigue cycle at a fatigue load of 13.14 kN for SSCS_CAF_53 and $2.7 \cdot 10^{-3}$ mm per fatigue cycle at a fatigue load of 13.96 kN for SSCS_CAF_54. The delamination growth rates observed in the experimental tests by Dávila and Bisagni varied from $2.5 \cdot 10^{-3}$ to $1.6 \cdot 10^{-2}$ mm per fatigue cycle. Four causes may be identified to explain the lower growth rates of these numerical analyses. This first is that the experimental tests were conducted at a fatigue load of 23 kN, around 10

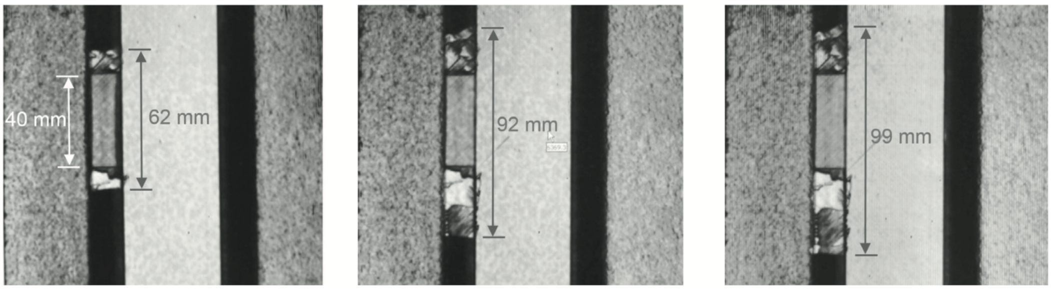

(a) (b) (c)

Figure 10.14: *Damage propagation data measured by UT scan during a fatigue experiment conducted by Dávila and Bisagni [57]. Specimen F-40B. a) at 2002 cycles; b) at 11850 cycles; c) at 24000 cycles.*

kN higher than the numerical analyses. Because this load exceeds the critical load of the numerical model and would cause quasi-static delamination growth, it cannot be used for the numerical fatigue delamination propagation analyses.

The second cause that may be identified is the absence of the occurrences of quasi-static growth in the numerical analyses. occurrences of sudden, rapid delamination growth were observed during the experiments. Their presence would serve to increase the average delamination growth rate. Thirdly, the buckling mode shape of the specimen changes substantially after the opening of the delamination. This directly changes the delamination opening and hence affects the growth rate. Because these fatigue analyses stop before this happens, the condition is not accounted for.

Finally, the set of delamination growth parameters assumed for the Paris relation in the numerical analysis may not be sufficient to capture the delamination growth behaviour. These parameters vary with mode mixity. A single set must be selected when setting up the analysis and they cannot be changed as the analyses runs. A single set valid for 20% or 50% mode II mode mixity does not adequately describe the growth behaviour when the mode mixity varies along the delamination front, and as the delamination grows. Because the out-of-plane displacement and therefore the delamination opening was similar between the quasi-static and fatigue models, similar Strain Energy Release Rates distributions may be expected. For the quasi-static analyses the mode mixity was far from constant along the delamination front. This distribution along the delamination front also varied with the delamination length. Additionally, only the influence of the mode I/Mode II mode mixity was taken into account. The influence of the mode III mode mixity was not accounted for in the Paris relation parameters. Substantial components of all three opening modes were observed in the quasi-static Single Stringer Compression Specimen results. As such, the mode III influence should have been accounted for in the Paris relation parameters.

The amount of delamination growth observed in analysis SSCS_CAF_55, to a total length of 111 mm, is comparable to the amount of growth observed in the experimental results. The delamination in experimental specimen F40A reached a length of 88 mm after 6750 fatigue cycles and the delamination in specimen F40B reached a length of 99 mm after 24 000 cycles. The cycle count of the numerical results, at 363 fatigue cycles, is one to two orders of magnitude lower than the experimental cycle counts. The delamination growth rate is correspondingly higher at $2.0 \cdot 10^{-1}$mm per fatigue cycle for the numerical results compared to $2.5 \cdot 10^{-3}$ to $1.6 \cdot 10^{-2}$ mm per fatigue cycle for the experimental results. The main cause of this increased growth rate was the disabled delamination growth initiation criterion. This criterion should not have been disabled. Re-enabling the criterion would slow down the analysis and bring it more in to line with the experimental results.

The numerical delamination growth rates are one to three orders of magnitude lower than the experimentally obtained growth rates. Although the results are qualitatively similar, the accuracy of the numerical analyses is not satisfactory. The limitations of the present model will need to be addressed to improve the accuracy of the results to the point that they may be relied on with confidence. In particular, the reliability of the cycle jumping mechanism included to speed up the analyses must be improved. Additionally, the mode-mixity ratio used for the fatigue delamination growth relation should not be fixed for the duration of the analysis. Instead the mode mixity should be accounted for in the delamination growth relation, it should be based on the actual mode mixity distribution at the delamination front, and it should be updated during the analysis as the delamination front grows. Finally, the influence of the mode III component in the mode mixity should be taken into account in the delamination growth calculation, as it is not negligible in a post-buckled Single Stringer Compression Specimen. In addition to addressing these limitations more experimental data of fatigue delamination growth in post-buckled Single Stringer Compression Specimens is needed to validate numerical results. Test data of only two specimens was available, and these exhibit substantial scatter in the observed delamination growth rates.

Chapter 11

Conclusions

To investigate the delamination growth behaviour of a Single Stringer Compression Specimen with an initial delamination loaded in post-buckling a number of test specimens models have been constructed and analysed. First, simple Double Cantilevered Beam and Mixed Mode Bending specimen models were analysed under quasi-static delamination growth conditions. Subsequently, two fatigue delamination growth methods were evaluated using these simple specimen models. After these simple specimen analyses were completed the quasi-static and fatigue delamination growth behaviour of Single Stringer Compression Specimens loaded in post-buckling was investigated.

Two fatigue delamination growth methods available in Abaqus FEA 2017 have been evaluated: the Constant Amplitude Fatigue method and the Simplified Fatigue method. Both methods were evaluated at the simple specimen level with Double Cantilevered Beam and Mixed Mode Bending specimen models and the Constant Amplitude Fatigue method was evaluated at the more complex Single Stringer Compression Specimen level.

Both the Constant Amplitude Fatigue and Simplified Fatigue methods produced excellent results when used to predict fatigue delamination growth in Double Cantilevered Beam and Mixed Mode Bending specimen models. At an element size of 1 mm the error when compared to benchmark data was less than 3% for the Double Cantilevered Beam specimen results and less than 5% for the Mixed Mode Bending specimen results. The Constant Amplitude Fatigue and Simplified Fatigue methods produced results with similar accuracy for a given element size. Using the Simplified Fatigue method a 25 to 50% reduction in computational time was observed compared to the Constant Amplitude Fatigue method. A minor improvement in accuracy was observed for a reduction of the element size from 1 mm to 0.5 mm for both methods, at a four to five fold increase in the required computational time.

Two element types have been used to construct the specimen models: S4R conventional shell elements and SC8R continuum shell elements. Their performance has been evaluated at the simple specimen level using the Double Cantilevered Beam and Mixed Mode Bending specimen models and at the structural element level of complexity using the Single Stringer Compression Specimen models. SC8R elements exhibited better solution convergence and better mesh convergence than S4R elements for the analysis of quasi-static delamination growth. The improved solution convergence translates to the need for fewer load or displacement increments and hence improved computation time at the same mesh density. The improvement in the required computational time was on the order of a factor 2 to 3 for the 1 mm and 3 mm element sizes evaluated.

The Single Stringer Compression Specimen models have been analysed under both quasi-static and fatigue loading in the post-buckling regime. They featured a 40 mm long initial delamination between the skin and one of the two stiffener flanges. In the quasi-static delamination growth analyses of the Single Stringer Compression Specimen a clear correlation has been observed between the local buckling of the stiffener flange, the first sudden delamination extension, and the first load drop. When the load at which the first load drop occurs is reached the delaminated section of the stiffener flange suddenly buckles locally. This is followed shortly by a shift from a global three half wave buckling mode to a single half wave buckling mode for the skin. As this shift occurs a rapid delamination extension is observed. When the shift in buckling modes has settled the delamination continues to grow, but at a substantially reduced pace compared to the pace during the shift.

Under further quasi-static loading a correlation has been observed between shifts in the buckling mode of the stiffener flange, sudden delamination extensions and load drops. If the load on the specimen is increased after the first load drop, a second and a third load drop occur. The locally buckled delaminated stiffener flange section shifts from a one half wave to a two half wave buckling mode at the second load drop. As this shift occurs another rapid delamination extension is observed. At the third load drop the stiffener flange shifts from a two to a three half wave buckling mode shape.

In the fatigue delamination growth analyses of the Single Stringer Compression Specimen a correlation has been observed between local buckling of the stiffener flange and a sharp increase in the delamination growth rate. Initially, the stiffener flange does not buckle locally at the maximum applied load. The rate at which the delamination propagates starts around $9.4 \cdot 10^{-5}$ to $5.4 \cdot 10^{-4}$ mm per fatigue cycle, and slowly increases with delamination length. When the stiffener flange begins to buckle locally at the peak applied load the delamination growth rate jumps to 0.6 to 0.8 mm per fatigue cycle.

The Constant Amplitude Fatigue method is in principle capable of predicting delamination growth in post-buckled Single Stringer Compression Specimens. Several limitations have been encountered that reduce the usability of the method for this application at this time. These limitations are listed as follows:

- The coefficient and exponent of the fatigue delamination propagation relation used vary with mode mixity. At present the value of these parameters must be fixed in advance of the analysis and a single mode mixity value must assumed to determine these parameters. The assumed mode mixity cannot accurately represent the mode-mixity present at any particular node along the delamination front of a post-buckled SSCS as the mode mixity varies both along the delamination front at a particular delamination length, and varies as the delamination grows.

- A single parameter fatigue delamination propagation relation is used. The coefficient and exponent of such a relation depend on the load ratio. Coefficient and exponent values were used that corresponded to the applied load ratio. However, the applied load ratio is not proportional to the load ratio present at the delamination front of the post-buckled Single Stringer Compression Specimen.

- The cycle jumping mechanism implemented in the Constant Amplitude Fatigue method does not always work as expected. The mechanism is intended to accelerate analyses by preventing repeated application of load cycles without releasing any nodes. If no nodes have been released, nothing has changed about the model geometry. In this situation applying repeated load cycles means duplicate work is performed. In some instances, repeated load cycles without any node release are observed. Presently, no pattern has been discerned as to when the mechanism works as expected and when it does not.

- When the Single Stringer Compression Specimen is loaded at a low load, where the specimen has barely buckled at the peak load, the Constant Amplitude Fatigue method behaves unexpectedly. The method keeps applying the first load cycle until the analysis is terminated manually. If the applied load is too low for fatigue delamination growth to occur it would be expected that the analysis jumps to the fatigue cycle limit set for the analysis without releasing any nodes after the first load cycle is applied.

- The Constant Amplitude Fatigue method terminates when quasi-static delamination growth is encountered. This behaviour is logical, since it is a method to predict fatigue growth. However, the opening up of the delamination of a Single Stringer Compression Specimen may be accompanied by quasi-static growth. This quasi-static growth could arrest shortly after the delamination has opened up completely, due to changes in the buckling mode shape of the specimen. The analyses are terminated before the initial delamination opens up fully unless the quasi-static growth threshold is increased to 0.999. Because of this, the fatigue life of the specimen after the initial delamination has opened up cannot readily be explored.

The Simplified Fatigue method available in Abaqus FEA 2017 has not been successfully used for the prediction of delamination growth in post-buckled Single Stringer Compression Specimens at this time. For the method a constant load is applied to the model to calculate the Strain Energy Release Rate. The maximum and minimum Strain Energy Release Rates used to predict delamination growth are assumed to be proportional to the calculated value. This proportionality assumption does not hold for geometrically non-linear structural responses, such as those of post-buckled Single Stringer Compression Specimens.

For this research, only the influence of the mode I/Mode II mode mixity was taken into account. The influence of mode III delamination opening is not taken into account in the mode mixity used for either the quasi-static or the fatigue delamination growth models. For the quasi-static growth the Benzeggagh-Kenane relation is used to interpolate the mode I and mode II critical Strain Energy Release Rates. Mode III is treated as if it were mode II and the contributions for mode II and III are summed. For the fatigue delamination growth the mode III component was not accounted for in the Paris relation parameters. For the Double Cantilevered Beam and Mixed Mode Bending specimen models this worked well, since they are subjected to pure mode I and mixed mode I/mode II delamination opening respectively. For the Single Stringer Compression Specimen models this was not the case. Substantial components of all three opening modes were observed in the Single Stringer Compression Specimen results. As such, the influence of mode III delamination opening on the Paris relation should not have been neglected.

Predicting fatigue delamination growth in post-buckled Single Stringer Compression Specimen using the Virtual Crack Closure Technique is, in principle, achievable. However, the accuracy of the numerical results obtained for this research is not satisfactory. The results are similar to experimentally obtained results in a qualitative sense, but quantitatively the predicted delamination growth rates were off by one to three orders of magnitude. The limitations discussed before will need to be addressed to improve the accuracy of the obtained results. Only then might sufficient confidence in the calculated results be attained for industrial application. In particular, the reliability of the cycle jumping mechanism included to speed up the analyses must be improved. Additionally, the mode-mixity ratio used for the fatigue delamination growth relation should not be fixed for the duration of the analysis. Instead the mode mixity should be accounted for in the growth relation, it should be based on the actual mode mixity at the delamination front, and it should be updated during the analysis as the delamination front grows. Finally, the influence of the mode III component in the mode mixity should be taken into account in the delamination growth calculation, as it is not negligible in a post-buckled Single Stringer Compression Specimen. In addition to addressing these limitations more experimental data of fatigue delamination growth in post-buckled Single Stringer Compression Specimens is needed to validate numerical results. Test data of only two specimens was available, and these exhibit substantial scatter in the observed delamination growth rates.

Chapter 12

Recommendations

Based on the experience gathered over the course of this research a number of recommendations for future work can be made:

Investigate the use of the local delamination front mode mixity in the fatigue growth relation. The parameters of the Paris type relation used for this research vary with mode mixity. Their values must be selected before the start of the analysis. Effectively this means that a single constant mode mixity value is assumed for every node along the delamination front during the entire analysis.

Investigate the influence of mode III mode mixity components on fatigue delamination propagation in post-buckled Single Stringer Compression Specimens. For this study only mode I/mode II mode mixity was considered.

Investigate incorporating the local delamination front load ratio into the fatigue growth relation. Due to the geometric non-linearity of the Single Stringer Compression Specimen loaded in post-buckling the applied load ratio is not proportional to the load ratio at the delamination front. The coefficient and exponent of the Strain Energy Release Rate range based Paris type relation used at present vary with load ratio. The values of these parameters must be selected before the start of the analysis. The applied load ratio was used as a proxy for the present research.

Investigate if the SF method can be modified to disable the proportionality assumption. For this method a constant load is applied to the model and the maximum and minimum Strain Energy Release Rates used for the delamination propagation are estimated through this proportionality assumption. The assumption does not hold for post-buckled Single Stringer Compression Specimens due to the geometric non-linearity of the specimen. However, when the minimum applied load is below the buckling load the load ratio at the delamination front effectively becomes zero for any applied load ratio. In this case the minimum Strain Energy Release Rate will be zero. If the proportionality assumption can be disabled the Simplified Fatigue method may be used to determine the maximum Strain Energy Release Rate which can then be used for the delamination growth rate prediction.

Investigate dynamically switching between fatigue and quasi-static delamination growth. At present, the fatigue analysis is terminated when an upper Strain Energy Release Rate threshold is reached. Experimental fatigue results from literature indicate that intermittent rapid delamination growth occurs, with stretches of slow or no growth in between the occurrences of rapid growth. The rapid delamination growth may be quasi-static in nature. To get substantial delamination growth the upper threshold had to be increased from 0.98 to 0.999. At such high subcritical Strain Energy Release Rates, instead of stretching the threshold, it may be better to simply switch over to quasi-static delamination growth.

Investigate the fatigue delamination growth behaviour of the Single Stringer Compression Specimen under displacement controlled conditions. Only load controlled conditions were used to investigate the fatigue delamination growth behaviour of the specimen for this study. When load control is used there is a potential for unstable delamination propagation to occur. Switching to displacement control would avoid this.

Bibliography

[1] C.-W. Kong, I.-C. Lee, C.-G. Kim, and C.-S. Hong. “Postbuckling and failure of stiffened composite panels under axial compression”. In: *Composite Structures* 42.1 (1998), pp. 13–21.

[2] F. Smith. *The use of composites in aerospace: past, present and future challenges*. Retrieved on: 05/08/2018. Avalon Consultancy Services Ltd. 2013. URL: `https://avaloncsl.files.wordpress.com/2013/01/avalon-the-use-of-composites-in-aerospace-s.pdf`.

[3] C. Bisagni and C.G. Dávila. “Single-stringer compression specimen for the assessment of damage tolerance of postbuckled structures”. In: *Journal of Aircraft* 48.2 (2011), pp. 495–502.

[4] *Standard test method for mode I interlaminar fracture toughness of unidirectional fiber-reinforced polymer matrix composites*. ASTM D5528-13. Standard. ASTM. 2013, pp. 1–13.

[5] *Standard test method for mode I fatigue delamination growth onset of unidirectional fiber-reinforced polymer matrix composites*. ASTM D6115-97. Standard. Re-approved 2011. ASTM. 1997, pp. 1–7.

[6] *Standard test method for mixed mode I-mode II interlaminar fracture toughness of unidirectional fiber reinforced polymer matrix composites*. D6671/D6671M—13. Standard. ASTM. 2013, pp. 1–15.

[7] R. Krueger. *An approach to assess delamination propagation simulation capabilities in commercial finite element codes*. Tech. rep. NASA/TM-2008-215123. NASA, Apr. 2008.

[8] R. Krueger. *Development of a benchmark example for delamination fatigue growth prediction*. Tech. rep. NASA/CR-2010-216723. NASA, July 2010.

[9] R. Krueger. *Development and application of benchmark examples for mixed-mode I/II quasi-static delamination propagation predictions*. Tech. rep. NASA/CR-2012-217562. NASA, Apr. 2012.

[10] R. Krueger and N. Carvalho. *In search of a time efficient approach to crack and delamination growth prediction in composites*. Tech. rep. Paper 2606. NASA, 2016.

[11] A.A. Griffith. “The phenomena of rupture and flow in solids”. In: *Philosophical Transactions of the Royal Society A* 221.582-593 (1921), pp. 163–198.

[12] G.R. Irwin. “Analysis of stress and strain near the end of a crack traversing a plate”. In: *Journal of Applied Mechanics* 24 (1957), pp. 361–364.

[13] G.C. Sih, P.C. Paris, and G.R. Irwin. “On cracks in rectilinear anisotropic bodies”. In: *International Journal of Fracture* 3.1 (1965), pp. 189–203.

[14] P.C. Paris, M. P. Gomez, and W. E. Anderson. “A rational analytic theory of fatigue”. In: *The Trend in Engineering* 13 (9 1961), pp. 9–14.

[15] F. Paris P.C. Erdogan. “A critical analysis of crack propagation laws”. In: *Journal of basic engineering* 85 (4 1963), pp. 528–533.

[16] J.A. Pascoe, R.C. Alderliesten, and R. Benedictus. “Methods for the prediction of fatigue delamination growth in composites and adhesive bonds.” In: *Engineering Fracture Mechanics* 112-113 (2013), pp. 72–96.

[17] J. Schijve. *Fatigue of structures and materials*. 2nd ed. Springer Science + Business media, 2009. ISBN: 978-1-4020-6807-2.

[18] J.A. Pascoe, R.C. Alderliesten, and R. Benedictus. "On the physical interpretation of the R-ratio effect and the LEFM parameters used for fatigue crack growth in adhesive bonds". In: *International Journal of Fatigue* 97 (2017), pp. 162–176.

[19] C. Rans, R.C. Alderliesten, and R. Benedictus. "Misinterpreting the results: how similitude can improve our understanding of fatigue delamination growth". In: *Composites Science and Technology* 71 (2011), pp. 230–238.

[20] R. Jones, A.J. Kinloch, and W. Hu. "Cyclic-fatigue crack growth in composite and adhesively-bonded structures: the FAA slow crack growth approach to certification and the problem of similitude". In: *International Journal of Fatigue* 88 (2016), pp. 10–18.

[21] R. Khan, R. Alderliesten, S. Badshah, and R. Benedictus. "Effect of stress ratio or mean stress on fatigue delamination growth in composites: critical review". In: *Composite Structures* 124 (2015), pp. 214–227.

[22] N. Blanco, E.K. Gamstedt, L.E. Asp, and J. Costa. "Mixed-mode delamination growth in carbon–fibre composite laminates under cyclic loading". In: *International Journal of Solids and Structures* 41 (2004). pp. 4219 – 4235.

[23] L. Yao, R.C. Alderliesten, M. Zhao, and R. Benedictus. "Discussion on the use of strain energy release rate for fatigue delamination characterisation". In: *Composites: Part A* 66 (2014), pp. 65–72.

[24] T. Takeda, M. Miura, Y. Shindo, and F. Narita. "Fatigue delamination growth in woven glass/epoxy composite laminates under mixed-mode II/III loading conditions at cryogenic temperatures". In: *Cryogenics* 58 (2013), pp. 55–61.

[25] M. Miura, Y. Shindo, T. Takeda, and F. Narita. "Mixed-mode I/III fatigue delamination growth in woven glass/epoxy composite laminates at cryogenic temperatures". In: *Journal of Composite materials* 48.10 (2014). pp. 1251 – 1259.

[26] L.R. Deobald, G.E. Mabson, S. Engelstad, M. P. Rao, M. Gurvich, W. Seneviratne, S. Perera, T. K. O'Brien, G. Murri, J. Ratcliffe, C. Davila, N. Carvalho, and R. Krueger. *Guidelines for VCCT-based interlaminar fatigue and progressive failure finite element analysis*. Tech. rep. NASA/TM-2017-219663. NASA, 2017.

[27] L. Amaral, R. Alderliesten, and R. Benedictus. "Understanding mixed-mode cyclic fatigue delamination growth in unidirectional composites: an experimental approach". In: *Engineering Fracture Mechanics* 180 (2017), pp. 161–178.

[28] J.A. Pascoe, R.C. Alderliesten, and R. Benedictus. "On the relationship between disbond growth and the release of strain energy". In: *Engineering Fracture Mechanics* 133 (2015), pp. 1–13.

[29] J.A. Pascoe, R.C. Alderliesten, and R. Benedictus. "Towards understanding fatigue disbond growth via cyclic strain energy". In: *Procedia Materials Science*. Vol. 3. 20th European Conference on Fracture (ECF20). 2014, pp. 610–615.

[30] J.A. Pascoe, D.S. Zarouchas, R.C. Alderliesten, and R. Benedictus. "Using acousic emission to understand fatigue crack growth within a single load cycle". In: *Engineering Fracture Mechanics* 194 (2018), pp. 281–300.

[31] L. Yao, Y. Sun, L. Guo, M. Shao, L. Jia, R.C. Alderliesten, and R. Benedictus. "A modified Paris relation for fatigue delamination with fibre bridging in composite laminates". In: *Composite Structures* 176 (2017), pp. 556–564.

[32] L. Yao, Y. Sun, R.C. Alderliesten, R. Benedictus, and M. Zhao. "Fibre bridging effect on the Paris relation for mode I fatigue delamination growth in composites with consideration of interface configuration". In: *Composite Structures* 159 (2017), pp. 471–478.

[33] K.B. Broberg. "On stable crack growth". In: *Journal of the Mechanics and Physics of Solids* 23 (3 1975), pp. 215–237.

[34] L. Amaral, D. Zarouchas, R. Alderliesten, and R. Benedictus. "Energy dissipation in mode II fatigue crack growth". In: *Engineering Fracture Mechanics* 173 (2017), pp. 41–54.

[35] E.F. Rybicki and E.F. Kanninen. "A finite element calculation of stress intensity factors by a modified crack closure integral". In: *Engineering Fracture Mechanics* 9 (4 1977), pp. 931–938.

[36] G.R. Irwin. "Elasticity and plasticity / elastizität und plastizität". In: ed. by S. Flügge. Vol. 6. Encyclopedia of Physics/ Handbuch der Physik. Springer Berlin Heidelberg, 1958, pp. 551–590. ISBN: 978-3-642-45887-3.

[37] R. Krueger. "Virtual crack closure technique: history, approach, and applications". In: *Appl.Mech. Rev* 57.2 (Apr. 2004), pp. 109–143.

[38] J.D. Whitcomb and K.N. Shivakumar. "Strain-energy release rate analysis of plates with postbuckled delaminations". In: *Journal of Composite Materials* 23.7 (1989), pp. 714–734.

[39] J. Wang, I. Raju, C. Dávila, and D. Sleight. "Computation of strain energy release rates for skin-stiffener debonds modeled with plate elements". In: *34th Structures, Structural Dynamics and Materials Conference*. American Institute of Aeronautics and Astronautics, 1993.

[40] J.T. Wang and I.S. Raju. "Strain energy release rate formulae for skin-stiffener debond modeled with plate elements". In: *Engineering Fracture Mechanics* 54.2 (1996), pp. 211–228.

[41] N.V. De Carvalho and R. Krueger. *Modelling fatigue damage onset and progression in composites using an element-based virtual crack closure technique combined with the floating node method*. Tech. rep. Paper 1102. NASA, 2016.

[42] E.H. Glaessgen, W.T. Riddell, and I.S. Raju. "Effect of shear deformation and continuity on delamination modelling with plate elements". In: *39th AIAA/ASME/ASCE/AHS/ASC Structures, Structural Dynamics and Materials Conference*. 1998.

[43] E.H. Glaessgen, W.T. Riddell, and I.S. Raju. "Nodal constraint, shear deformation and continuity effects related to the modeling of debonding of laminates, using plate elements". In: *Computer Modelling in Engineering and Science* 3.1 (2002), pp. 103–116.

[44] R. Krueger, K.N. Shivakumar, and I.S. Raju. "Fracture mechanics analysis for interface crack problems - a review". In: *Collection of Technical Papers - 54th AIAA/ASME/ASCE/AHS/ASC Structures, Structural Dynamics and Materials Conference*. Apr. 2013. ISBN: 978-1-62410-223-3.

[45] S.A. Smith and I.S. Raju. "Evaluation of stress-intensity factors using general finite-element models". In: *Fatigue and Fracture mechanics* 29 (1999), pp. 176–200.

[46] L.R. Deobald, G.E. Mabson, B. Dopker, D.M. Hoyt, J. Baylor, and D. Graesser. "Interlaminar fatigue elements for crack growth based on virtual crack closure technique". In: *48th AIAA/ASME/ASCE/AHS/ASC Structures, Structural Dynamics, and Materials Conference*. 2007.

[47] G.E. Mabson, L.R. Deobald, B. Dopker, D.M. Hoyt, J.S. Baylor, and D.L. Graesser. "Fracture interface elements for static and fatigue analysis". In: *16th International Conference on Composite Materials*. Japan Society for Composite Materials. 2007.

[48] N.V. De Carvalho and R. Krueger. *Modeling fatigue damage progression and onset in composites using an element-based virtual crack closure technique combined with the floating node method*. 31st ASC Technical conference. 2016.

[49] R. Krueger. *Development and application of benchmark examples for mode II static delamination propagation and fatigue growth predictions*. Tech. rep. NASA/CR-2011-217305. NASA, Nov. 2011.

[50] S.C. Saunders. *A review of miner's rule and subsequent generalisations for calculating expected fatigue life*. Technical report D1-82-1019. Boeing Scientific Research Laboratories, Dec. 1970.

[51] *Abaqus analysis guide*. Dassault Systemes. 2018.

[52] N.V. De Carvalho, R. Krueger, G.E. Mabson, and L.R. Deobald. “Combining progressive nodal release with the virtual crack closure technique to model fatigue delamination growth without re-meshing”. In: *2018 AIAA/ASCE/AHS/ASC Structures, Structural Dynamics, and Materials Conference*. 2018.

[53] I. Di Memmo. “Fatigue simulation for damage propagation in composite structures”. MA thesis. Politecnico di Milano, 2017.

[54] I. Di Memmo and C. Bisagni. “Fatigue simulation for damage propagation in composite structures”. In: *Proceedings of the American Society for Composites Thirty-Second Technical Conference*. 2017.

[55] J.G. Ratcliffe and W.M. Johnston jr. *Influence of mixed mode I-mode II loading on fatigue delamination growth characteristics of a graphite epoxy tape laminate*. Tech. rep. Paper 663. NASA, 2014.

[56] *Modeling delamination in postbuckled composite structures under static and fatigue loads*. (The Society for Advancement of Materials and Process Engineering’s spring conference and exhibition). Document ID: 20130013696, Report Number: NF1676L-15330. Long Beach, CA, United States of America, 2013.

[57] C.G. Dávila and C. Bisagni. “Fatigue life and damage tolerance of postbuckled composite stiffened structures with initial delamination”. In: *Composite Structures* 161 (2017), pp. 73–84.

[58] C. Bisagni and C.G. Dávila. “Experimental investigation of the postbuckling response and collapse of a single-stringer specimen”. In: *Composite Structures* 108 (2014), pp. 493–503.

[59] C.G. Dávila and C. Bisagni. “Fatigue life and damage tolerance of postbuckled composite stiffened structures with indentation damage”. In: *Journal of Composite Materials* 52.7 (2018), pp. 931–943.

[60] A. J. Brunner, N. Murphy, and G. Pinter. “Development of a standardized procedure for the characterization of interlaminar delamination propagation in advanced composites under fatigue mode I loading conditions”. In: *Engineering Fracture Mechanics* 76 (18 Dec. 2009), pp. 2678–2689.

[61] S. Stelzer, A.J. Brunner, A. Argüelles, N. Murphy, and G. Pinter. “Mode I delamination fatigue crack growth in unidirectional fiber reinforced composites: development of a standardized test procedure”. In: *Composites Science and Technology* 72 (10 June 2012), pp. 1102–1107.

[62] M.L. Benzeggagh and M. Kenane. “Measurement of mixed-mode delamination fracture toughness of unidirectional glass/epoxy composites with mixed-mode bending apparatus”. In: *Composites Science and Technology* 56 (1996), pp. 439–449.

[63] J. G. Williams. “The fracture mechanics of delamination tests”. In: *Journal of Strain Analysis* 24.4 (1989), pp. 207–214.

[64] *Hexply 8552 product data sheet, EU version*. Hexcel Corporation. 2016. URL: `https://www.hexcel.com/user_area/content_media/raw/HexPly_8552_eu_DataSheet.pdf`.

[65] *Hexply 8552 product data sheet, US version*. Hexcel Corporation. 2016. URL: `https://www.hexcel.com/user_area/content_media/raw/HexPly_8552_us_DataSheet.pdf`.

Appendices

Appendix A

Example Abaqus input files

A.I DCB_CAF_18 input file

```
*Heading
** Job name: DCB_CAF_18 Model name: 7500 DCB SC8R
** Generated by: Abaqus/CAE 2017
*Preprint, echo=NO, model=NO, history=NO, contact=NO


*parameter
** load
d_max = 0.67
R=0.1
***
*** Fatigue parameters ***
***
** time of a single load cycle. If set to one the analysis timestep corresponds to
    the number of fatigue cycles that have been applied.
T = 1
** Initial time increment, If neither CETOL or DELTMX are specified for the fatigue
    step the timestepping will be constant and use the initial time increment only.
    The minimum and maximum time increment allowed parameters are ignored.
t_ini = 0.5
** Minimum time increment allowed. Ignored if neither CETOL or DELTMX are specified.
t_min = 1E-9
** Maximum time increment allowed. Ignored if neither CETOL or DELTMX are specified.
t_max = 0.5
** Minimum increment in number of cycles over which the damage is extrapolated
    forward. Must be greater than 0, default is 100.
n_incmin = 50
** Maximum increment in number of cycles over which the damage is extrapolated
    forward. Must be greater than 0, default is 1000.
n_incmax = 500
** Total number of cycles allowed in a step. If it is 0 a value of 1 + n_incmax/2 is
     used.
n_max = 10000000
** tolerance for the least number of cycles to fracture and element. Default is 0.1
d_e_tol = 0.1
***
*** Fracture toughness ***
***
** Mode I critical strain energy release rate
```

```
GIc  =0.17030
** Mode II critical strain energy release rate
GIIc =0.49360
** Mode III critical strain energy release rate
GIIIc=0.49360
***
*** B-K parameter ***
***
** Benzeggagh-Kenane mixed mode interpolation law exponent
eta = 1.62
*** fatigue crack growth data
** Crack initiation law coefficient
c1 = 2.8461E-9
** Crack initiation law exponent
c2 = -12.415
** Paris law coefficient
c3 = 2.44E+06
** Paris law exponent
c4 = 10.61

r1 = 0.353
r2 = 0.9

***
*** amplitude
***
*amplitude,name="load 1",definition=TABULAR
0.,0., 0.5,1., 1, <R>
*amplitude,name="cyclic_load", definition=TABULAR
0., <R>, 0.5, 1., 1, <R>
***
*** MATERIALS
***
*Material, name="T300/1076 Krueger 2010"
*Elastic, type=ENGINEERING CONSTANTS
139400.,10160.,10160., 0.3,  0.3, 0.436, 4600., 4600.
 3540.,
**
** INTERACTION PROPERTIES
**
*Surface Interaction, name="VCCT interaction Krueger 2010"
1.,
*Clearance, master="Top Flange-1"."Master surface", slave="Bottom Flange-1"."Slave
    surface", value=1e-08
**
** BOUNDARY CONDITIONS
**
** Name: Bottom flange encast Type: Symmetry/Antisymmetry/Encastre
*Boundary
"Bottom Flange-1"."Fixed edge", ENCASTRE
** Name: Top flange encast Type: Symmetry/Antisymmetry/Encastre
*Boundary
"Top Flange-1"."Fixed edge", ENCASTRE
**
** INTERACTIONS
**
** Interaction: VCCT interaction
*Contact Pair, interaction="VCCT interaction Krueger 2010", small sliding, Adjust="
```

```
    Bottom Flange-1"."Bonded nodes"
"Bottom Flange-1"."Slave surface", "Top Flange-1"."Master surface"
*Initial Conditions, type=CONTACT
"Bottom Flange-1"."Slave surface", "Top Flange-1"."Master surface", "Bottom Flange
    -1"."Bonded nodes"
*** --------------------------------------------------------------
***
*** STEP 1: Static pre-load
***
*Step, name="Static pre-load", nlgeom=YES, INC=100
** turn on nonlinear geometry, leave the maximum number of increments per step at
    the default of 100.
*Static
0.1, 1., 1e-10, 0.1
***
*** BOUNDARY CONDITIONS
***
** Name: Bottom flange preload Type: Displacement/Rotation
*Boundary, amplitude="load 1"
"Bottom Flange-1"."Loaded edge", 3, 3, -<d_max>
** Name: Top flange preload Type: Displacement/Rotation
*Boundary, amplitude="load 1"
"Top Flange-1"."Loaded edge", 3, 3, <d_max>
**
** OUTPUT REQUESTS
**
*Restart, write, frequency=0
**
** FIELD OUTPUT: F-Output
**
*Output, field
*Node Output
RF, U
*Element Output, directions=YES
S
*Contact Output
BDSTAT, CDISP, CSTRESS, DBS, EFENRRTR, ENRRT
**
** HISTORY OUTPUT: H-Output
**
*Output, history
*Node Output, nset="Bottom Flange-1"."Disp output"
RF3, U3
*Node Output, nset="Top Flange-1"."Disp output"
RF3, U3
**
*Debond, slave="Bottom Flange-1"."Slave surface", master="Top Flange-1"."Master
    surface", frequency=1
*Fracture Criterion, type=VCCT, mixed mode behavior=BK
<GIc>, <GIIc>, <GIIIc>, <eta>,
*End Step
** --------------------------------------------------------------
**
** STEP: cyclic loading
**
*Step, name="cyclic loading", nlgeom=YES, inc=100
** turn on nonlinear geometry, leave the maximum number of increments per step at
    the default of 100.
```

```
*fatigue, type=constant amplitude
<t_ini>, <T>, <t_min>, <t_max>
<n_incmin>, <n_incmax>, <n_max>, ,<d_e_tol>
**
** BOUNDARY CONDITIONS
**
** Name: Bottom flange displacement Type: Displacement/Rotation
*Boundary, amplitude="cyclic_load"
"Bottom Flange-1"."Loaded edge", 3, 3, -<d_max>
** Name: Top flange displacement Type: Displacement/Rotation
*Boundary, amplitude="cyclic_load"
"Top Flange-1"."Loaded edge", 3, 3, <d_max>
**
** OUTPUT REQUESTS
**
**
** FIELD OUTPUT: F-Output
**
*Output,field,freq=1
*Node Output
U
*Element Output, directions=YES
S
*contact output,slave="Bottom Flange-1"."Slave surface", master="Top Flange-1"."
    Master surface"
cstress, cdisp, BDSTAT, EFENRRTR, ENRRT
*contact output,slave="Bottom Flange-1"."Slave surface", master="Top Flange-1"."
    Master surface", nset="Bottom Flange-1"."Crack growth output"
BDSTAT
**
** HISTORY OUTPUT: H-Output
**
*output, history,freq=1
*Node Output, nset="Bottom Flange-1"."Disp output"
RF3, U3
*Node Output, nset="Top Flange-1"."Disp output"
RF3, U3
**
*Debond, slave="Bottom Flange-1"."Slave surface", master="Top Flange-1"."Master
    surface", frequency=1
*Fracture Criterion, type=fatigue, mixed mode behavior=BK
 <c1>,<c2>,<c3>,<c4>,<r1>,<r2>,<GIc>, <GIIc>
 <GIIIc>, <eta>
*End Step
```

A.II DCB_SF_12 input file

```
*Heading
** Job name: DCB_SF_12 Model name: 7500 DCB SC8R
** Generated by: Abaqus/CAE 2017
*Preprint, echo=NO, model=NO, history=NO, contact=NO


*parameter
***
*** load ***
***
** Maximum applied displacement
d_max = 0.67
** Applied load ratio
R=0.1
** the constant load used for the simplified fatigue calculation is the peak applied
     load adjusted based on the applied load ratio as per the manual ("Linear
    elastic fatigue crack growth analysis")
d_constant = d_max * sqrt(1-R**2)
***
*** Fatigue parameters ***
***
** time of a single load cycle
T = 1
** Initial time increment
t_ini = 0.5
** Minimum time increment allowed
t_min = 1E-9
** Maximum time increment allowed
t_max = 0.5
** Minimum increment in number of cycles over which the damage is extrapolated
    forward. Must be greater than 0, default is 100.
n_incmin = 50
** Maximum increment in number of cycles over which the damage is extrapolated
    forward. Must be greater than 0, default is 1000.
n_incmax = 500
** Total number of cycles allowed in a step. If it is 0 a value of 1 + n_incmax/2 is
     used.
n_max = 10000000
** tolerance for the least number of cycles to fracture and element. Default is 0.1
d_e_tol = 0.1
***
*** quasi static damage and tolerance parameters ***
***
tol = 0.1
***
*** Fracture toughness ***
***
** Mode I critical strain energy release rate
GIc  =0.17030
** Mode II critical strain energy release rate
GIIc =0.49360
** Mode III critical strain energy release rate
GIIIc=0.49360
***
*** B-K parameter ***
***
```

```
** Benzeggagh-Kenane mixed mode interpolation law exponent
eta = 1.62
*** fatigue crack growth data
** Crack initiation law coefficient
c1 = 2.84E-15
** Crack initiation law exponent
c2 = -12.415E-15
** Paris law coefficient
c3 = 2.44E+06
** Paris law exponent
c4 = 10.61

r1 = 0.353
r2 = 0.9
***
*** amplitude ***
***
*amplitude,name="load 1",definition=TABULAR
0.,0., 0.5,1., 1, <R>
*amplitude,name="cyclic_load", definition=TABULAR
0., <R>, 0.5, 1., 1, <R>
***
*** MATERIALS
***
*Material, name="T300/1076 Krueger 2010"
*Elastic, type=ENGINEERING CONSTANTS
139400.,10160.,10160., 0.3,  0.3, 0.436, 4600., 4600.
 3540.,
***
*** INTERACTION PROPERTIES
***
*Surface Interaction, name="VCCT interaction Krueger 2010"
1.,
*Clearance, master="Top Flange-1"."Master surface", slave="Bottom Flange-1"."Slave
    surface", value=1e-08
***
*** BOUNDARY CONDITIONS
***
*** Name: Bottom Flange encast Type: Symmetry/Antisymmetry/Encastre
*Boundary
"Bottom Flange-1"."Fixed edge", ENCASTRE
** Name: Top Flange encast Type: Symmetry/Antisymmetry/Encastre
*Boundary
"Top Flange-1"."Fixed edge", ENCASTRE
***
*** INTERACTIONS
***
*** Interaction: VCCT interaction
*Contact Pair, interaction="VCCT interaction Krueger 2010",type=SURFACE TO SURFACE,
    small sliding, Adjust="Bottom Flange-1"."Bonded nodes"
** use adjust to remove underclosure before analysis starts
"Bottom Flange-1"."Slave surface", "Top Flange-1"."Master surface"
*Initial Conditions, type=CONTACT
"Bottom Flange-1"."Slave surface", "Top Flange-1"."Master surface", "Bottom Flange
    -1"."Bonded nodes"
*** ---------------------------------------------------------------
***
*** STEP 1: Static pre-load
```

```
***
*Step, name="Static pre-load", nlgeom=YES, INC=100
** turn on nonlinear geometry, leave the maximum number of increments per step at
    the default of 100.
*Static
0.1, 1., 1e-10, 0.1
***
*** BOUNDARY CONDITIONS
***
*** Name: Bottom Flange preload Type: Displacement/Rotation
*Boundary, amplitude="load 1"
"Bottom Flange-1"."Loaded edge", 3, 3, -<d_max>
** Name: Top Flange preload Type: Displacement/Rotation
*Boundary, amplitude="load 1"
"Top Flange-1"."Loaded edge", 3, 3, <d_max>
***
*** OUTPUT REQUESTS
***
*Restart, write, frequency=0
***
*** FIELD OUTPUT: F-Output
***
*Output, field
*Node Output
RF, U
*Element Output, directions=YES
S
*Contact Output
BDSTAT, CDISP, CSTRESS, DBS, EFENRRTR, ENRRT
***
*** HISTORY OUTPUT: H-Output
***
*Output, history
*Node Output, nset="Bottom Flange-1"."Disp output"
RF3, U3
*Node Output, nset="Top Flange-1"."Disp output"
RF3, U3
**
*Debond, slave="Bottom Flange-1"."Slave surface", master="Top Flange-1"."Master
    surface", debonding force=STEP, frequency=1
*Fracture Criterion, type=VCCT, mixed mode behavior=BK
<GIc>, <GIIc>, <GIIIc>, <eta>,
*End Step
*** ----------------------------------------------------------------
***
*** STEP: cyclic loading
***
*Step, name="cyclic loading", nlgeom=YES, inc=100
** turn on nonlinear geometry, leave the maximum number of increments per step at
    the default of 100.
*fatigue, type=simplified
<t_ini>, <T>, <t_min>, <t_max>
<n_incmin>, <n_incmax>, <n_max>, ,<d_e_tol>
***
*** BOUNDARY CONDITIONS
***
*** Name: Bottom Flange displacement Type: Displacement/Rotation
*Boundary
```

```
"Bottom Flange-1"."Loaded edge", 3, 3, -<d_constant>
** Name: Top Flange displacement Type: Displacement/Rotation
*Boundary
"Top Flange-1"."Loaded edge", 3, 3, <d_constant>
***
*** OUTPUT REQUESTS
***
***
*** FIELD OUTPUT: F-Output
***
*Output,field,freq=1
*Node Output
U
*Element Output, directions=YES
S
*contact output,slave="Bottom Flange-1"."Slave surface", master="Top Flange-1"."
    Master surface"
cstress, cdisp, BDSTAT, EFENRRTR, ENRRT
*contact output,slave="Bottom Flange-1"."Slave surface", master="Top Flange-1"."
    Master surface", nset="Bottom Flange-1"."Crack growth output"
BDSTAT
***Contact Print
**BDSTAT
***
*** HISTORY OUTPUT: H-Output
***
*output, history,freq=1
*Node Output, nset="Bottom Flange-1"."Disp output"
RF3, U3
*Node Output, nset="Top Flange-1"."Disp output"
RF3, U3
**
*Debond, slave="Bottom Flange-1"."Slave surface", master="Top Flange-1"."Master
    surface", frequency=1
*Fracture Criterion, type=fatigue, mixed mode behavior=BK
 <c1>,<c2>,<c3>,<c4>,<r1>,<r2>,<GIc>, <GIIc>
 <GIIIc>, <eta>
*End Step
```

A.III SSCS_QS_80 input file

```
*Heading
** Job name: SSCS_QS_80 Model name: SSCS QS SC8R load control mesh offset
** Generated by: Abaqus/CAE 2017
*Preprint, echo=NO, model=NO, history=NO, contact=NO


**
** ELEMENT CONTROLS
**
*Section Controls, name=EC-1, hourglass=ENHANCED, second order accuracy=YES
1., 1., 1.
** Change the hourglass control from the default total stiffness approach to the
    enhanced assumed strain method.
*parameter
** load controlled
** peak applied load in N
**f_max = 35E3
**Displacement controlled
** peak applied displacement in mm
d_max = 1.00
** tolerance
tol = 0.30
***
*** Step controls ***
***
initial_timestep = 0.010
step_timeperiod = 20.00
minimum_timestep = 1.0E-12
maximum_timestep = 0.10
***
*** Fracture toughness ***
***
** Mode I critical strain energy release rate
GIc  =0.277
** Mode II critical strain energy release rate
GIIc =0.788
** Mode III critical strain energy release rate
GIIIc=0.788
***
*** B-K parameter ***
***
** Benzeggagh-Kenane mixed mode interpolation law exponent
eta = 1.63
***
*** amplitude
***
***amplitude,name="Ramp", definition=TABULAR
**0., 0., <step_timeperiod>, 1
***Amplitude, name=Cyclic_load
**           0.,             0.,            0.5,             1.,             1.,
               0.
***Amplitude, name=Preload
**           0.,             0.,            0.5,            0.1
**
** MATERIALS
**
```

```
*Material, name="IM7/8552 - Davila & Bisagni 2017"
*Elastic, type=ENGINEERING CONSTANTS
150000.,9080.,9080., 0.32, 0.32, 0.42,5290.,5290.
3400.,
*density
 1.57e-6
** 1.57E-6 for nominal laminate density, 1.77E-6 is the nominal fibre density and
    1.3E-6 is the nominal resin density.
**
** INTERACTION PROPERTIES
**
*Surface Interaction, name="VCCT interaction Davila & Bisagni 2017"
1.,
*Friction
0.,
*Surface Behavior, pressure-overclosure=HARD
*Clearance, master=Skin-1.Master, slave=Stringer-1.Slave, value=1.0e-08
**
** BOUNDARY CONDITIONS
**
** Name: Lower clamp Type: Symmetry/Antisymmetry/Encastre
*Boundary
"Reference point lower boundary", ENCASTRE
** Name: Lower potting Type: Displacement/Rotation
*Boundary
"Lower potted nodes", 2, 2
"Lower potted nodes", 3, 3
"Lower potted nodes", 4, 4
"Lower potted nodes", 5, 5
"Lower potted nodes", 6, 6
** Name: Upper clamp Type: Displacement/Rotation
*Boundary
"Reference point upper boundary", 2, 2
"Reference point upper boundary", 3, 3
"Reference point upper boundary", 4, 4
"Reference point upper boundary", 5, 5
"Reference point upper boundary", 6, 6
** Name: Upper potting Type: Displacement/Rotation
*Boundary
"Upper potted nodes", 2, 2
"Upper potted nodes", 3, 3
"Upper potted nodes", 4, 4
"Upper potted nodes", 5, 5
"Upper potted nodes", 6, 6
**
** INTERACTIONS
**
** Interaction: VCCT interaction
*Contact Pair, interaction="VCCT interaction Davila & Bisagni 2017", small sliding,
    type=SURFACE TO SURFACE,
adjust=Stringer-1."Bonded nodes uncracked"
Stringer-1.Slave, Skin-1.Master
*Initial Conditions, type=CONTACT
Stringer-1.Slave, Skin-1.Master, Stringer-1."Bonded nodes cracked"
*IMPERFECTION, FILE=SSCS_QS_SC8R_eig_3,STEP=1
1,-0.01
2,0.000
3,0.000
```

```
4,0.000
5,0.000
6,0.000
7,0.000
8,0.000
** ----------------------------------------------------------------
**
** STEP: Displacement
**
*Step, nlgeom, UNSYMM=YES, increment=10000
*Dynamic, alpha=-0.10, HAFTOL=5000
<initial_timestep>, <step_timeperiod>, <minimum_timestep>, <maximum_timestep>
** 1 - Suggested initial time increment
** 2 - Time period of the step
** 3 - Minimum time increment allowed
** 4 - Maximum time increment allowed
** alpha specifies the numerical artificial damping control from 0 ( no damping) to
    -0.5. Max damping at -0.333.
**
** Controls
**
** change the maximum number of cutbacks allowed for an increment to 30, to prevent
    the analysis from erroring out on "too many cutbacks for this increment", and to
     allow it to actually reach small increments
** Change the minimum number of consecutive increments without cutbacks required
    before a time increment increase is allowed to 10, from a default of 3, to
    prevent the analysis from increasing the step size too quickly and losing track
    of the converged response.
***Controls, parameters=time incrementation
**, , , , , , , 30, , 10, , ,
**
***CONTROLS,PARAMETERS=FIELD
**1.0E-2, , , , 5.0E-2
** 1 - convergence criterion for the ratio of the largest residual to the average
    force. Default: 5E-3
** 5 - Alternative redidual convergence criterion to be used after Iap iterations.
    Default: 2E-2
*CONTROLS,PARAMETERS=TIME INCREMENTATION
10, 10, 4, 500, 10, 4, 30, 35, 10, 10
** 1 - default: 4, minimum: 3 - number of iterations after which a check is made
    whether the residuals increase in two consecutive iterations
** 2 - default: 8 - Number of iterations after which a logarithmic convergence check
     is performed in each iteration.
** 3 - default: 9 - Number of iterations after which the residual tolerance Rap is
    used instead of Ran
** 4 - default: 16 - Maximum number of iterations allowed
** 5 - default: 10 - Number of iterations after which the size of the subsequent
    increment will be reduced.
** 6 - default: 4 - Maximum number of iterations allowed in two consecutive
    increments for the size of the next increment to be increased.
** 7 - default: 12 - Maximum number of severe discontinuity iterations allowed in an
     increment
** 8 - default 5 - Maximum number of attempts allowed for an increment.
** 9 - default 6 - Maximum number of severe discontinuity iterations allowed in two
    consecutive increments for the time increment to be increased if CONVERT SDI=NO
** 10 - default 3, maximum: 10 - Minmimum number of consecutive increments in which
    the time integration accuracy measure must be satisfied without any cutbacks to
    allow a time increment increase.
```

```
** 11 - default: 50 - Maximum number of equilibrium and severe discontinuity
    iterations allowed in an icrement if CONVERT SDI=YES. Unused if CONVERT SDI=NO
** 12 - default: 50 - Maximum number of equilibrium and severe discontinuity
    iterations allowed in two consecutive increments for the time increment to be
    increased ig CONVERT SDI=YES. Unused if CONVERT SDI=NO
** 13 - default: 50 - Maximum number of allowed contact augmentations if the
    augmented Lagrange contact constraint enforcement method is specified.
*CONTROLS,PARAMETERS=FIELD,FIELD=DISPLACEMENT
.10, 1., , , 0.10
** 1 - convergence criterion for the ratio of the largest residual to the average
    flux norm for convergence.
** 2 - Convergence criterion for the rsation of the largest solution correction to
    the largest corresponding incremental solution value.
** 3 - Initial value of the time average flux for this step.
** 4 - User defined average flux
** 5 - Alternative redidual convergence criterion to be used after Iap iterations
*CONTROLS,PARAMETERS=LINE SEARCH
4,,,,
**4, 4, 0.25, 0.25, 0.15
** 1 - Mximum number of line search iterations. Default is 0 for steps that use the
    Newton method and 5 for steps that use the quasi-Newton method.
** 2 - Maximum correction scale factor. Default: 1.0
** 3 - Minimum correction scale factor. Default: 0.0001
** 4 - Residual reduction factor at which line searching terminates. Default: 0.25
** 5 - ratio of new to old correction scale factors below which line searching
    terminates. Default: 0.10

**
** BOUNDARY CONDITIONS
**
** Name: Lower clamp Type: Symmetry/Antisymmetry/Encastre
*Boundary, op=NEW
"Reference point lower boundary", ENCASTRE
** Name: Lower potting Type: Displacement/Rotation
*Boundary, op=NEW
"Lower potted nodes", 2, 2
"Lower potted nodes", 3, 3
"Lower potted nodes", 4, 4
"Lower potted nodes", 5, 5
"Lower potted nodes", 6, 6
** Name: Upper clamp Type: Displacement/Rotation
*Boundary, op=NEW
"Reference point upper boundary", 2, 2
"Reference point upper boundary", 3, 3
"Reference point upper boundary", 4, 4
"Reference point upper boundary", 5, 5
"Reference point upper boundary", 6, 6
** Name: Upper potting Type: Displacement/Rotation
*Boundary, op=NEW
"Upper potted nodes", 2, 2
"Upper potted nodes", 3, 3
"Upper potted nodes", 4, 4
"Upper potted nodes", 5, 5
"Upper potted nodes", 6, 6
*** DISPLACEMENT CONTROL ***
** For displacement controlled analysis disable the load boundary condition below
    and the f_max parameter
** Name: Displacement Type: Displacement/Rotation
```

```
*Boundary, op=NEW
"Reference point upper boundary", 1, 1, -<d_max>
**
** LOADS
**
*** LOAD CONTROL ***
** For load controlled analysis disable the displacement boundary condition and the
    d_max parameter
***Cload
**"Reference point upper boundary", 1, -<f_max>
**
** INTERACTIONS
**
** Contact Controls for Interaction: VCCT interaction
*Contact Controls, master=Skin-1.Master, slave=Stringer-1.Slave, reset
*Contact Controls, master=Skin-1.Master, slave=Stringer-1.Slave, stabilize=1e-04

** OUTPUT REQUESTS
**
***Restart, write, frequency=0
**
** FIELD OUTPUT: F-Output
**
*Output, field,freq=5
*Node Output
U
*Element Output, directions=YES
S, ELEN, ENER
*contact output,slave=Stringer-1.Slave, master=Skin-1.Master
cstress, cdisp, BDSTAT, EFENRRTR, ENRRT
*contact output,slave=Stringer-1.Slave, master=Skin-1.Master, nset=Stringer-1."Crack
     growth output"
BDSTAT
**
** HISTORY OUTPUT: H-Output
**
*Output, history,freq=5
*Node Output, nset="Reference point upper boundary"
U
*Node Output, nset="Reference point upper boundary"
TF1
*Energy Output
ALLAE, ALLCD, ALLDMD, ALLEE, ALLFD, ALLIE, ALLJD, ALLKE, ALLKL, ALLPD, ALLQB, ALLSD,
     ALLSE, ALLVD, ALLWK, ETOTAL
*Debond, slave=Stringer-1.Slave, master=Skin-1.Master,debonding force=RAMP,
    frequency=5
*Fracture Criterion, type=VCCT, mixed mode behavior=BK, tolerance=<tol>, viscosity
    =0.0
<GIc>, <GIIc>, <GIIIc>, <eta>
*End Step
```

A.IV SSCS_CAF_54 input file

```
*Heading
** Job name: SSCS_CAF_54 Model name: SSCS F SC8R load control
** Generated by: Abaqus/CAE 2017
*Preprint, echo=NO, model=NO, history=NO, contact=NO


**
** ELEMENT CONTROLS
**
*Section Controls, name=EC-1, hourglass=ENHANCED, second order accuracy=YES
1., 1., 1.
**
** Parameters
**
*parameter
** use either a load controlled or a displacement controlled analysis by setting one
     of these two parameters.
**
** !! When switching between load or displacement control make sure to switch the
    applied boundary condition.
**
** load controlled
** peak applied load in N
f_max = 13.96E3
**Displacement controlled
** peak applied displacement in mm
**d_max = 1.00
**
** load/displacement ratio, expressed as fraction of f_max or d_max
R=0.1
***
*** Fatigue parameters ***
***
** time of a single load cycle. If set to one the analysis timestep corresponds to
    the number of fatigue cycles that have been applied.
T = 1
** Initial time increment
t_ini = 0.05
** Minimum time increment allowed.
t_min = 1E-8
** Maximum time increment allowed.
t_max = 0.1
** Minimum increment in number of cycles over which the damage is extrapolated
    forward. Must be greater than 0, default is 100.
n_incmin = 100
** Maximum increment in number of cycles over which the damage is extrapolated
    forward. Must be greater than 0, default is 1000.
n_incmax = 2200000
** Total number of cycles allowed in a step. If it is 0 a value of 1 + n_incmax/2 is
     used.
n_max = 100000
** tolerance for the least number of cycles to fracture and element. Default is 0.1
d_e_tol = 0.1
***
*** Fracture toughness ***
***
```

```
** Mode I critical strain energy release rate
GIc  =0.277
** Mode II critical strain energy release rate
GIIc =0.788
** Mode III critical strain energy release rate
GIIIc=0.788
***
*** B-K parameter ***
***
** Benzeggagh-Kenane mixed mode interpolation law exponent
eta = 1.63
*** fatigue crack growth data
** Crack initiation law coefficient
c1 = 1.8E-6
** Crack initiation law exponent
c2 = -11.1
** Paris law coefficient
c3 = 2412
** Paris law exponent
c4 = 8.4
**Ratio of energy release rate threshold used in the Paris law over the equivalent
    critical energy release rate.
r1 = 0.264
**Ratio of energy release rate upper limit used in the Paris law over the equivalent
     critical energy release rate.
r2 = 0.98
***
*** amplitude
***
*amplitude,name="Preload",definition=TABULAR
0.,0., 1, <R>
*amplitude,name="Cyclic_load", definition=TABULAR
0., <R>, 0.5, 1., 1, <R>
**
** Time points
**
*TIME POINTS, NAME=Time_points_trian
0
0.5
1
**
** MATERIALS
**
*Material, name="IM7/8552 - Davila & Bisagni 2017"
*Elastic, type=ENGINEERING CONSTANTS
150000.,9080.,9080., 0.32, 0.32, 0.42,5290.,5290.
3400.,
*density
 1.57e-6
 ** 1.57E-6 for nominal laminate density, 1.77E-6 is the nominal fibre density and
     1.3E-6 is the nominal resin density.
** Density is relevant for dynamic implicit steps, not for static general or fatigue
     steps.
**
** INTERACTION PROPERTIES
**
*Surface Interaction, name="VCCT interaction Davila & Bisagni 2017"
1.,
```

```
*Friction
0.,
*Surface Behavior, pressure-overclosure=HARD
*Clearance, master=Skin-1.Master, slave=Stringer-1.Slave, value=1.0e-08
**
** BOUNDARY CONDITIONS
**
** Name: Lower clamp Type: Symmetry/Antisymmetry/Encastre
*Boundary
"Reference point lower boundary", ENCASTRE
** Name: Lower potting Type: Displacement/Rotation
*Boundary
"Lower potted nodes", 2, 2
"Lower potted nodes", 3, 3
**"Lower potted nodes", 4, 4
**"Lower potted nodes", 5, 5
**"Lower potted nodes", 6, 6
** DOF 4, 5, and 6 are rotation DOFs which are undefinded for SC8R elements.
    Reactivate these when S4R elements are used.
** Name: Upper clamp Type: Displacement/Rotation
*Boundary
"Reference point upper boundary", 2, 2
"Reference point upper boundary", 3, 3
"Reference point upper boundary", 4, 4
"Reference point upper boundary", 5, 5
"Reference point upper boundary", 6, 6
** Name: Upper potting Type: Displacement/Rotation
*Boundary
"Upper potted nodes", 2, 2
"Upper potted nodes", 3, 3
**"Upper potted nodes", 4, 4
**"Upper potted nodes", 5, 5
**"Upper potted nodes", 6, 6
**
** INTERACTIONS
**
** Interaction: VCCT interaction
*Contact Pair, interaction="VCCT interaction Davila & Bisagni 2017", small sliding,
    type=SURFACE TO SURFACE,
adjust=Stringer-1."Bonded nodes uncracked"
Stringer-1.Slave, Skin-1.Master
*Initial Conditions, type=CONTACT
Stringer-1.Slave, Skin-1.Master, Stringer-1."Bonded nodes cracked"
** ----------------------------------------------------------------
**
** STEP:Preload
**
*IMPERFECTION, FILE=SSCS_F_SC8R_eig_1,STEP=1
1,-0.01
2,0.00
3,0.000
4,0.000
5,0.000
6,0.000
7,0.000
8,0.000
**
*Step, name=Pre-load, nlgeom=YES, inc=50
```

```
*Static
.02, 1., 1e-07, .2
** Controls
*CONTROLS,PARAMETERS=TIME INCREMENTATION
10, 10, 4, 500, 10, 4, 30, 35, 10, 10
** 1 - default: 4, minimum: 3 - number of iterations after which a check is made
    whether the residuals increase in two consecutive iterations
** 2 - default: 8 - Number of iterations after which a logarithmic convergence check
     is performed in each iteration.
** 3 - default: 9 - Number of iterations after which the residual tolerance Rap is
    used instead of Ran
** 4 - default: 16 - Maximum number of iterations allowed
** 5 - default: 10 - Number of iterations after which the size of the subsequent
    increment will be reduced.
** 6 - default: 4 - Maximum number of iterations allowed in two consecutive
    increments for the size of the next increment to be increased.
** 7 - default: 12 - Maximum number of severe discontinuity iterations allowed in an
     increment
** 8 - default 5 - Maximum number of attempts allowed for an increment.
** 9 - default 6 - Maximum number of severe discontinuity iterations allowed in two
    consecutive increments for the time increment to be increased if CONVERT SDI=NO
** 10 - default 3, maximum: 10 - Minmimum number of consecutive increments in which
    the time integration accuracy measure must be satisfied without any cutbacks to
    allow a time increment increase.
** 11 - default: 50 - Maximum number of equilibrium and severe discontinuity
    iterations allowed in an icrement if CONVERT SDI=YES. Unused if CONVERT SDI=NO
** 12 - default: 50 - Maximum number of equilibrium and severe discontinuity
    iterations allowed in two consecutive increments for the time increment to be
    increased ig CONVERT SDI=YES. Unused if CONVERT SDI=NO
** 13 - default: 50 - Maximum number of allowed contact augmentations if the
    augmented Lagrange contact constraint enforcement method is specified.
**
** BOUNDARY CONDITIONS
**
** Name: Upper clamp Type: Displacement/Rotation
** Name: Lower clamp Type: Symmetry/Antisymmetry/Encastre
*Boundary, op=NEW
"Reference point lower boundary", ENCASTRE
** Name: Lower potting Type: Displacement/Rotation
*Boundary, op=NEW
"Lower potted nodes", 2, 2
"Lower potted nodes", 3, 3
**"Lower potted nodes", 4, 4
**"Lower potted nodes", 5, 5
**"Lower potted nodes", 6, 6
** DOF 4, 5, and 6 are rotation DOFs which are undefinded for SC8R elements.
    Reactivate these when S4R elements are used.
** Name: Upper clamp Type: Displacement/Rotation
*Boundary, op=NEW
"Reference point upper boundary", 2, 2
"Reference point upper boundary", 3, 3
"Reference point upper boundary", 4, 4
"Reference point upper boundary", 5, 5
"Reference point upper boundary", 6, 6
** Name: Upper potting Type: Displacement/Rotation
*Boundary, op=NEW
"Upper potted nodes", 2, 2
"Upper potted nodes", 3, 3
```

```
***"Upper potted nodes", 4, 4
***"Upper potted nodes", 5, 5
***"Upper potted nodes", 6, 6

*** DISPLACEMENT CONTROL ***
** For displacement controlled analysis disable the load boundary condition below
    and the f_max parameter
** Name: Displacement Type: Displacement/Rotation
***Boundary, op=NEW amplitude="Preload"
**"Reference point upper boundary", 1, 1, -<d_max>
**
** LOADS
**
*** LOAD CONTROL ***
** For load controlled analysis disable the displacement boundary condition and the
    d_max parameter
*Cload, amplitude="Preload"
"Reference point upper boundary", 1, -<f_max>
**
** INTERACTIONS
**
** Contact Controls for Interaction: VCCT interaction
*Contact Controls, master=Skin-1.Master, slave=Stringer-1.Slave, reset
*Contact Controls, master=Skin-1.Master, slave=Stringer-1.Slave, stabilize=1.0e-03
**
** FIELD OUTPUT: F-Output
**
*Output, field,freq=1
*Node Output
U
*Element Output, directions=YES
S
*contact output,slave=Stringer-1.Slave, master=Skin-1.Master
cstress, cdisp, BDSTAT, EFENRRTR, ENRRT
*contact output,slave=Stringer-1.Slave, master=Skin-1.Master, nset=Stringer-1."Crack
     growth output"
BDSTAT
**
** HISTORY OUTPUT: H-Output
**
*Output, history,freq=1
*Node Output, nset="Reference point upper boundary"
U
*Node Output, nset="Reference point upper boundary"
TF1
*Debond, slave=Stringer-1.Slave, master=Skin-1.Master, frequency=1
*Fracture Criterion, type=fatigue, mixed mode behavior=BK
 <c1>,<c2>,<c3>,<c4>,<r1>,<r2>,<GIc>, <GIIc>
 <GIIIc>, <eta>
*End Step
**
**
**
** Cyclic loading step
**
**
**
*Step, name="cyclic loading", nlgeom=YES, inc=100
```

```
** turn on nonlinear geometry, leave the maximum number of increments per step at
    the default of 100.
*fatigue, type=constant amplitude, TIME POINTS=Time_points_trian
<t_ini>, <T>, <t_min>, <t_max>
<n_incmin>, <n_incmax>, <n_max>, ,<d_e_tol>
**
** Controls
**
*Controls, parameters=time incrementation
4, 8, 9, 20, 10, 2, 12, 30, 6, 5
** 1 - Number of iterations after which a check is made whether the residuals
    increase in two consecutive iterations. Default: 4, minimum: 3
** 2 - Number of iterations after which a logarithmic convergence check is performed
     in each iteration. Default: 8
** 3 - Number of iterations after which the residual tolerance Rap is used instead
    of Ran. Default: 9
** 4 - Maximum number of iterations allowed. Default: 16
** 5 - Number of iterations after which the size of the subsequent increment will be
     reduced. Default: 10
** 6 - Maximum number of iterations allowed in two consecutive increments for the
    size of the next increment to be increased. Default: 4
** 7 - Maximum number of severe discontinuity iterations allowed in an increment.
    Default: 12
** 8 - Maximum number of attempts allowed for an increment. Default: 5
** 9 - Maximum number of severe discontinuity iterations allowed in two consecutive
    increments for the time increment to be increased if CONVERT SDI=NO. Default: 6
** 10 - Minmimum number of consecutive increments in which the time integration
    accuracy measure must be satisfied without any cutbacks to allow a time
    increment increase. Default: 3, maximum: 10
** 11 - Maximum number of equilibrium and severe discontinuity iterations allowed in
     an increment if CONVERT SDI=YES. Unused if CONVERT SDI=NO. Default: 50
** 12 - Maximum number of equilibrium and severe discontinuity iterations allowed in
     two consecutive increments for the time increment to be increased ig CONVERT
    SDI=YES. Unused if CONVERT SDI=NO. Default: 50
** 13 - Maximum number of allowed contact augmentations if the augmented Lagrange
    contact constraint enforcement method is specified. Default: 50
**
** BOUNDARY CONDITIONS
*** DISPLACEMENT CONTROL ***
** For displacement controlled analysis disable the load boundary condition below
    and the f_max parameter
** Name: Displacement Type: Displacement/Rotation
***Boundary, op=NEW amplitude="Cyclic_load"
**"Reference point upper boundary", 1, 1, -<d_max>
**
** LOADS
**
*** LOAD CONTROL ***
** For load controlled analysis disable the displacement boundary condition and the
    d_max parameter
*Cload, amplitude="Cyclic_load"
"Reference point upper boundary", 1, -<f_max>
**
** FIELD OUTPUT: F-Output
**
*Output, field,freq=1
*Node Output
U
```

```
*Element Output, directions=YES
S
*contact output,slave=Stringer-1.Slave, master=Skin-1.Master
cstress, cdisp, BDSTAT, EFENRRTR, ENRRT
*contact output,slave=Stringer-1.Slave, master=Skin-1.Master, nset=Stringer-1."Crack
     growth output"
BDSTAT
**
** HISTORY OUTPUT: H-Output
**
*Output, history,freq=1
*Node Output, nset="Reference point upper boundary"
U
*Node Output, nset="Reference point upper boundary"
TF1
*End Step
```